

AD/A-004 771

A METHOD FOR PREDICTING THREE-DEGREE-
OF-FREEDOM STORE SEPARATION TRAJECTO-
RIES AT SPEEDS UP TO THE CRITICAL SPEED

Frederick K. Goodwin, et al

Nielsen Engineering and Research,
Incorporated

Prepared for:

Air Force Flight Dynamics Laboratory

July 1971

DISTRIBUTED BY:

NTIS

National Technical Information Service
U. S. DEPARTMENT OF COMMERCE

Best Available Copy

UNCLASSIFIED

Security Classification

AD/A-004771

DOCUMENT CONTROL DATA - R & D

(Security classification of title, body of abstract and indexing annotation must be entered when the cover report is classified)

1. ORIGINATING ACTIVITY (Corporate author) Nielsen Engineering & Research, Inc. 850 Maude Avenue Mountain View, California 94040		2a. REPORT SECURITY CLASSIFICATION Unclassified	
		2b. GROUP N/A	
3. REPORT TITLE A Method for Predicting Three-Degree-of-Freedom Store Separation Trajectories at Speeds up to the Critical Speed			
4. DESCRIPTIVE NOTES (Type of report and inclusive dates) Final technical report - December 1968 to January 1971			
5. AUTHOR(S) (First name, middle initial, last name) Frederick K. Goodwin, Jack N. Nielsen, and Marnix F. E. Dillenius			
6. REPORT DATE July 1971		7a. TOTAL NO. OF PAGES 206	7b. NO. OF REFS 17
8a. CONTRACT OR GRANT NO. F33615-60-C-1337		8a. ORIGINATOR'S REPORT NUMBER(S) NEAR Report TR-26	
b. PROJECT NO. 8219		9b. OTHER REPORT NO(S) (Any other numbers that may be assigned this report)	
c. Task No. 821902		AFFDL-TR-71-81	
d.			
10. DISTRIBUTION STATEMENT Approved for public release; distribution unlimited.			
11. SUPPLEMENTARY NOTES None		12. SPONSORING MILITARY ACTIVITY Air Force Flight Dynamics Lab. Wright-Patterson Air Force Base Ohio 45433	
13. ABSTRACT This report is the final technical report which describes a combined theoretical-experimental program which has been conducted with the aim of developing a computer program to predict three-degree-of-freedom trajectories of stores when dropped from fighter-bomber type aircraft at speeds up to the critical speed. Both single store and multiple store installations are treated. The report first describes the mathematical models used to represent the various aircraft components. Then the calculation of the flow field, accounting for primary interference effects, using these models is described followed by the method of calculating the normal force and pitching moment from this flow field. A method of accounting for additional interference between the wing, pylon, and store is next presented. Comparisons between the calculated results and available experimental data and data obtained during the present program are included for all aspects of the analysis. Good overall agreement is obtained. A comparison between one sample calculated trajectory and an experimental trajectory is presented. The agreement is quite good.			

Reproduced by
NATIONAL TECHNICAL
INFORMATION SERVICE
US Department of Commerce
Springfield, VA 22151

PRICES SUBJECT TO CHANGE

DD FORM 1473
NOV 66

REPLACES DD FORM 1473, 1 JAN 64, WHICH IS
OBSOLETE FOR ARMY USE.

UNCLASSIFIED

Security Classification

UNCLASSIFIED

Security Classification

14 KEY WORDS	LINK A		LINK B		LINK C	
	ROLE	WT	ROLE	WT	ROLE	WT
External stores						
Aerodynamic interference						
Subsonic flow						
Transonic flow						
Aerodynamic loads						
Flow fields						

UNCLASSIFIED

Security Classification

1a

A METHOD FOR PREDICTING
THREE-DEGREE-OF-FREEDOM STORE
SEPARATION TRAJECTORIES AT
SPEEDS UP TO THE CRITICAL SPEED

Frederick K. Goodwin
Jack N. Nielsen
Marnix F. E. Dillenius

Approved for public release; distribution unlimited.

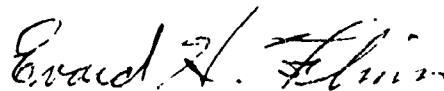
FOREWORD

This report, "A Method for Predicting Three-Degree-of-Freedom Store Separation Trajectories at Speeds up to the Critical Speed," describes a combined theoretical-experimental program directed toward developing a computer program for predicting the trajectory of an external store dropped from an aircraft of the fighter-bomber type at speeds up to the critical speed. The work was carried out by Nielsen Engineering & Research, Inc., 850 Maude Avenue, Mountain View, California 94040, under Contract No. F33615-69-C-1337. The contract was initiated under Project 8219, Task E21902, of the Air Force Flight Dynamics Laboratory. The Air Force Project Engineer on the contract was Mr. Jerry E. Jenkins, AFFDL/FGC. The report number assigned by Nielsen Engineering & Research, Inc. is NEAR TR 26.

The authors wish to thank Mr. Jenkins for his assistance in solving some of the technical and administrative problems which arose during the course of the investigation. Also, they would like to thank Mr. John C. Marshall and Mr. Willard E. Summers of the 4T Projects Branch, Propulsion Wind-Tunnel Facility, Arnold Engineering Development Center, for the timely performance of the experimental test program.

The work documented in this report was started on December 1, 1968 and was effectively concluded with the submission of this report. The report was released by the authors in January 1971.

This technical report has been reviewed and is approved.



E. H. FLINN
Control Criteria Branch
Flight Control Division

ABSTRACT

This report is the final technical report which describes a combined theoretical-experimental program which has been conducted with the aim of developing a computer program to predict three-degree-of-freedom trajectories of stores when dropped from fighter-bomber type aircraft at speeds up to the critical speed. Both single store and multiple store installations are treated. The report first describes the mathematical models used to represent the various aircraft components. Then the calculation of the flow field, accounting for primary interference effects, using these models is described followed by the method of calculating the normal force and pitching moment from this flow field. A method of accounting for additional interference between the wing, pylon, and store is next presented. Comparisons between the calculated results and available experimental data and data obtained during the present program are included for all aspects of the analysis. Good overall agreement is obtained. A comparison between one sample calculated trajectory and an experimental trajectory is presented. The agreement is quite good.

TABLE OF CONTENTS

<u>Section</u>	<u>Page No.</u>
1. INTRODUCTION	1
2. GENERAL METHOD OF APPROACH	2
3. COMPRESSIBILITY CORRECTION	4
4. MATHEMATICAL MODELS FOR DETERMINING FLOW FIELD	8
4.1 Axisymmetric Bodies at Zero Degrees Angle of Attack	9
4.1.1 Fundamental equations	9
4.1.2 Conditions used to obtain source strengths	10
4.1.3 Calculative examples	12
4.2 Wing Thickness at Zero Degrees Angle of Attack	13
4.2.1 Fundamental equations	13
4.2.2 Conditions used to obtain source strengths	14
4.2.3 Calculative example	15
4.2.4 Calculation of the velocity field about wings with sweep and taper	15
4.3 Wing Angle of Attack; Lifting-Surface Theory	18
4.3.1 Description of method	18
4.3.2 Effect of the number of vortices on the calculated flow field	19
5. CALCULATION OF FLOW FIELD	20
5.1 Interference Effects	20
5.2 Method of Calculation	23
5.2.1 Single store under the wing	23
5.2.2 Single store under fuselage centerline	23
5.2.3 Multiple store under the wing or fuselage	24
5.3 Comparison of Calculated and Experimental Flow Fields	24
5.3.1 Comparison with data from NACA RM 156J19 (ref. 5)	24
5.3.2 Comparison with data from NEAR TR 2. (ref. 1)	28
6. PRIMARY INTERFERENCE FORCE AND MOMENT	31
6.1 Buoyancy Force and Moment	34
6.2 Angle of Attack Force and Moment	36
6.2.1 Slender-body force and moment	37
6.2.2 Viscous crossflow force and moment	40
6.3 Empennage Force and Moment	41

<u>Section</u>	<u>Page No.</u>
7. ADDITIONAL INTERFERENCE FORCE AND MOMENT	43
7.1 Axes and Conventions	45
7.2 Formulation of the Interference Problem	46
7.3 Store Normal-Force Distribution	48
7.4 Boundary Condition for Store Under Pylon of Wing-Body Combination	51
7.5 Application of the Method to Conical Configurations	54
7.5.1 Boundary conditions	54
7.5.2 Calculative example	59
8. COMPARISON OF CALCULATED LOAD DISTRIBUTION, FORCE, AND MOMENT WITH EXPERIMENT	65
8.1 Single Store Under Wing of Wing-Fuselage Combination	66
8.2 Single Store Under Wing of Wing-Fuselage-Pylon Combination	68
8.3 TER Stores Under Wing of Wing-Fuselage-Pylon-Rack Combination	73
9. EXPERIMENTALLY DETERMINED MER INTERFERENCE EFFECTS	74
10. STORE TRAJECTORIES	77
10.1 Equations of Motion	78
10.2 Description of Computer Program	83
10.3 Sample trajectory	84
11. CONCLUDING REMARKS	85
TABLE 1	88
FIGURES 1 THROUGH 46	89
APPENDIX I - INTEGRATION OF THE LOADING EQUATION	163
APPENDIX II - CALCULATION OF VORTEX STRENGTHS	173
REFERENCES	185
DD FORM 1473	

LIST OF ILLUSTRATIONS

<u>Figure</u>	<u>Page No.</u>
1.- Coordinate system for axisymmetric body.	89
2.- Wing-fuselage combination used in reference 1.	90
3.- Single store in the presence of the wing-fuselage combination of reference 1. (a) Store location.	91
3.- Concluded. (b) Store details.	92
4.- Comparison between actual and calculated shapes for two axisymmetric bodies. (Note differences in x^* and r^* scales.) (a) Fuselage in NACA RM L56J19 (ref. 5). (b) Cylinder with ellipsoidal ends.	93
5.- Coordinate system for two-dimensional wing.	94
6.- Comparison between actual and calculated shapes for NACA 65A006 airfoil. (Note difference in z/c and x/c scales.)	95
7.- Swept-wing configuration and flow velocities.	96
8.- Swept and unswept constant chord wings.	97
9.- Dimensions of wing-body configuration of references 5 and 6.	98
10.- Definitions of local angle of attack and sidewash angle. (a) Local angle of attack. (b) Sidewash angle. (c) Composite velocity diagram.	99
11.- Perturbation velocities due to angle of attack 10 percent of local chord beneath wing of example wing-body combination. (a) Upwash perturbation velocity.	100
11.- Concluded. (b) Sidewash perturbation velocity.	101
12.- Perturbation velocities due to angle of attack 5 percent of the local chord beneath wing of example wing-body combination. (a) Upwash perturbation velocity.	102
12.- Concluded. (b) Sidewash perturbation velocity.	103
13.- Comparison between calculated and experimental local angle of attack and sidewash angle under the mid-semispan of wing-body configuration of figure 9; $\alpha_w = -0.2^\circ$.	104
13.- Concluded. (b) Sidewash angle.	105
14.- Comparison between calculated and experimental local angle of attack and sidewash angle under wing-body configuration of figure 9 at the mid-semispan 17 percent of the local chord below the wing for various angles of attack. (a) Local angle of attack with $\alpha_w = -0.2^\circ$ and -4.3° .	106

LIST OF ILLUSTRATIONS (cont.)

<u>Figure</u>	<u>Page No.</u>
14.- Continued. (b) Local angle of attack with $\alpha_w = 6.1^\circ$ and 12.3° .	107
14.- Concluded. (c) Sidewash angle.	108
15.- Comparison between calculated and experimental local angle of attack and sidewash angle under wing-body configuration of figure 9 at the mid-semispan at an angle of attack of 6.1° . (a) Local angle of attack.	109
15.- Concluded. (b) Sidewash angle.	110
16.- Comparison between calculated and experimental local angle of attack and sidewash angle under wing-body configuration of figure 9 at 17 percent of the local chord below the wing at an angle of attack of 6.1° . (a) Local angle of attack.	111
16.- Concluded. (b) Sidewash angle.	112
17.- Comparison between calculated and experimental local angle of attack under the fuselage centerline of wing-body configuration of figure 9 for various distances below the fuselage. (a) $\alpha_w = -0.2^\circ$.	113
17.- Concluded. (b) $\alpha_w = 6.1^\circ$.	114
18.- Comparison between calculated and experimental velocity field at the 1/3 semispan of the left wing panel of wing-body configuration of figure 1; $M_\infty = 0.25$, $z/c = -0.30$. (a) $\alpha_p = 0^\circ$.	115
18.- Concluded. (b) $\alpha_p = 6^\circ$.	116
19.- Comparison between calculated and experimental velocity field at the 1/3 semispan of the left wing panel of wing- body configuration of figure 1; $M_\infty = 0.70$, $z/c = -0.30$. (a) $\alpha_p = 0^\circ$.	117
19.- Concluded. (b) $\alpha_p = 6^\circ$.	118
20.- TER grouping of stores in the presence of the wing-fuselage combination of reference 1.	119
21. Comparison between calculated and experimental velocity increments due to addition of two shoulder stores to TER rack; $M_\infty = 0.25$, $y/s = -0.333$, $z/c = -0.40$. (a) $\alpha_p = 0^\circ$.	120
21.- Concluded. (b) $\alpha_p = 6^\circ$.	121
22.- Coordinate system fixed in ejected store.	122

LIST OF ILLUSTRATIONS (cont.)

<u>Figure</u>	<u>Page No.</u>
23.- Axis systems used in mutual interference analysis.	123
24.- Effect of vortex spacing on calculated values of K_{α} for conical wing-store-pylon configuration.	124
25.- Variation of K_{α} with geometric parameters of conical wing-store-pylon configuration.	125
26.- Effect of vortex spacing on calculated values of K_{β} for conical wing-store-pylon configuration.	126
27.- Variation of normal force due to sidewash with geometric parameters of conical wing-store-pylon configuration.	127
28.- Primary interference normal force distribution on a single store below the left wing panel of a wing-fuselage combination; $M_{\infty} = 0.25$, $y/s = -0.333$, $z/c = -0.30$. (a) $\alpha_p = 0^{\circ}$, $\alpha_w = 1.25^{\circ}$.	128
28.- Concluded. (b) $\alpha_p = 6^{\circ}$, $\alpha_w = 6.75^{\circ}$.	129
29.- Effect of additional interference on normal-force distribution on a single store below the left wing panel of a wing-fuselage combination; $M_{\infty} = 0.25$, $y/s = -0.333$, $z/c = -0.30$. (a) $\alpha_p = 0^{\circ}$, $\alpha_w = 1.25^{\circ}$.	130
29.- Concluded. (b) $\alpha_p = 6^{\circ}$, $\alpha_w = 6.75^{\circ}$.	131
30.- Primary interference normal-force distribution on a single store below the left wing panel of a wing-fuselage combination; $M_{\infty} = 0.70$, $y/s = -0.333$, $z/c = -0.30$. (a) $\alpha_p = 0^{\circ}$, $\alpha_w = 0.96^{\circ}$.	132
30.- Concluded. (b) $\alpha_p = 6^{\circ}$, $\alpha_w = 6.79^{\circ}$.	133
31.- Primary interference normal force and pitching moment on a single store below the left wing panel of a wing-fuselage combination; $y/s = -0.333$, $z/c = -0.30$. (a) $M_{\infty} = 0.25$.	134
31.- Concluded. (b) $M_{\infty} = 0.70$.	135
32.- Details of pylons used in experimental investigation of reference 1.	136
33.- Incremental loading on single store at 1/3 semispan location caused by addition of pylon to wing-fuselage combination; $M_{\infty} = 0.25$, $z/c = -0.30$. (a) $\alpha_p = 0^{\circ}$.	137
33.- Concluded. (b) $\alpha_p = 6^{\circ}$.	138
34.- Swept-wing model of NACA RM L54B18 (ref. 15).	139

LIST OF ILLUSTRATIONS (cont.)

<u>Figure</u>	<u>Page No.</u>
35.- Distribution of the various components of normal force on a store in a nonuniform flow field. (a) $\alpha_w = \alpha_s = 0^\circ$.	140
35.- Continued. (b) $\alpha_w = \alpha_s = 2^\circ$.	141
35.- Continued. (c) $\alpha_w = \alpha_s = 4^\circ$.	142
35.- Concluded. (d) $\alpha_w = \alpha_s = 8^\circ$.	143
36.- Normal force and pitching moment on store without tail fins. (a) Buoyancy component.	144
36.- Continued. (b) Angle of attack component.	145
36.- Concluded. (c) Total force and moment.	146
37.- Total normal force and pitching moment on store with tail fins.	147
38.- Incremental loading on bottom store on TER rack at 1/3 semispan caused by addition of two side stores; $M_\infty = 0.25$, $z/c = -0.40$. (a) $\alpha_p = 0^\circ$.	148
38.- Concluded. (b) $\alpha_p = 6^\circ$.	149
39.- Incremental loading on store no. 2 on TER rack at 1/3 semispan caused by addition of store no. 3; $M_\infty = 0.25$, $z/c = -0.333$. (a) $\alpha_p = 0^\circ$.	150
39.- Concluded. (b) $\alpha_p = 6^\circ$.	151
40.- MER grouping of stores in the presence of the wing-fuselage combination of reference 1. (a) Store locations.	152
40.- Concluded. (b) Store details.	153
41.- MER rack details.	154
42.- Incremental interference force and moment on finless MER stores; $M_\infty = 0.40$, $z = -3.80$ inches. (a) Store number 1.	155
42.- Concluded. (b) Store number 4.	156
43.- Incremental interference force and moment on finned MER stores; $M_\infty = 0.40$, $z = -3.80$ inches. (a) Store number 1.	157
43.- Concluded. (b) Store number 4.	158
44.- Coordinate systems and angle definitions used in trajectory calculations.	159
45.- Forces acting on store.	160

LIST OF ILLUSTRATIONS (conc.)

<u>Figure</u>	<u>Page No.</u>
46.- Sample trajectory calculation. (a) Pitch angle.	161
46.- Concluded. (b) Vertical location of store center of gravity.	162

LIST OF SYMBOLS

a	local body radius
a_E	body radius at the axial location of the empennage centroid
a_{max}	maximum body radius
b	total wing span
c	local wing chord
C_{d_c}	section drag coefficient of a circular cylinder normal to air stream, taken equal to 1.2
$C_{D,0}$	zero-lift drag coefficient, zero-lift drag/ $q_{\infty_S} S_R$
C_m	pitching-moment coefficient, pitching moment/ $q_{\infty_S} S_R l_R$
$C_{m,\alpha}$	pitching-moment coefficient excluding buoyancy contribution
C_n	yawing-moment coefficient, yawing moment/ $q_{\infty_S} S_R l_R$
C_N	normal-force coefficient, normal force/ $q_{\infty_S} S_R$
$C_{N,\alpha}$	normal-force coefficient excluding buoyancy component
C_{N_s}	normal-force coefficient of store due to primary interference
$C_{N_s(\alpha)}$	normal-force coefficient of store alone due to angle of attack
$C_{N_s,pw(\alpha)}$	normal-force coefficient of store in presence of wing and pylon due to angle of attack
C_p	pressure coefficient, $(p - p_{\infty_S})/q_{\infty_S}$
$C_{p,l}$	pressure coefficient of lower surface of store
$C_{p,u}$	pressure coefficient on upper surface of store
ΔC_p	$C_{p,l} - C_{p,u}$
C_Y	side-force coefficient, side force/ $q_{\infty_S} S_R$
d	maximum store diameter

D_0	store alone drag at zero lift
F	resultant force in crossflow plane, $Y + iN$
F_ξ, F_η	sum of forces acting on store in ξ and η directions, respectively
g	gravitational acceleration
h	distance of store center beneath wing
h_p	distance from store center to top of pylon
$i_p(k)$	local incidence angle of pylon at k^{th} control point
i_s	store incidence angle relative to fuselage axis
i_w	wing incidence angle relative to fuselage axis
k	radius of gyration of store
K_B, K_E	interference lift ratios defined by equations (69) and (70)
K_α	interference coefficient denoting change in store-alone normal force associated with W component of interference field, equation (119)
K_B	interference coefficient denoting change in store-alone normal force associated with V component of interference field, equation (121)
l	pylon length
l_f	fuselage length
l_R	reference length; taken equal to store maximum diameter, d , everywhere except for section 4 and for C_m of figures 36 and 37, where it is taken equal to store length, l_s
l_s	store length
m	number of control points on pylon
m_s	store mass
M_∞	free-stream Mach number
M_g	sum of pitching moments acting on store taken about store center of gravity, positive nose up

n	number of control points on left panel, or direction normal to body surface
N	normal force
N_S	normal force acting on store due to primary interference
N_Γ	normal force acting on store due to additional interference vortex system
p	static pressure or number of control points on right panel
p_l	static pressure on lower surface of store
p_u	static pressure on upper surface of store
q	dynamic pressure
Q_k	strength of k^{th} point source
Q_k^*	$Q_k/4\pi l_R^2 V_\infty$ for bodies, $Q_k/2\pi c V_\infty$ for airfoils
r	radial distance in y - z plane
r^*	r/l_R
r_i	radial distance to i^{th} external vortex
s	wing semispan; in section 7, distance from pylon to right wing tip
s_E	empennage semispan
S	store cross sectional area, πa^2
S_n	area of store normal to sidewash velocity V
S_R	reference area taken equal to body frontal area, πa_{max}^2
t	time or wing thickness; also, in section 7, distance from pylon to left wing tip
u, v, w	perturbation velocities in x_s, y_s, z_s directions, respectively
$\bar{u}, \bar{v}, \bar{w}$	perturbation velocities in $\bar{x}, \bar{y}, \bar{z}$ directions, respectively (fig. 23)
u^*, v^*, w^*	$u/V_\infty, v/V_\infty, w/V_\infty$

u_i, v_i, w_i	values of u, v, w associated with vortex Γ_i including its image system
u_n	perturbation velocity in direction normal to line of constant percent thickness of swept wing
u_s, v_s, w_s	values of u, v, w due to store alone
$u_\Gamma, v_\Gamma, w_\Gamma$	sums of u_i, v_i, w_i over all external vortices
U, V, W	total velocities in x_s, y_s, z_s directions, respectively
$\bar{U}, \bar{V}, \bar{W}$	total velocities in $\bar{x}, \bar{y}, \bar{z}$ directions, respectively
U^*, V^*, W^*	$U/V_\infty, V/V_\infty, W/V_\infty$
U_s, V_s, W_s	total velocities in x_s, y_s, z_s directions, respectively, as seen from a point on the store
U_s^*, V_s^*, W_s^*	$U_s/V_{\infty_s}, V_s/V_{\infty_s}, W_s/W_{\infty_s}$
v_B, w_B	values of v and w for body alone of conical wing-body-pylon combination
$v_{p(s)}$	value of v on pylon due to store alone
$v_{p(k)}$	value of v to be cancelled by vortex system at k^{th} control point on pylon
V_c	crossflow velocity, $\sqrt{V_s^2 + W_s^2}$
V_c^*	V_c/V_{∞_s}
$V_{\text{hor}}, V_{\text{vert}}$	horizontal and vertical components of store velocity, respectively
V_r	radial velocity in y_s-z_s plane
V_r^*	V_r/V_∞
V_o	store ejection velocity
$V_{3D(k)}$	value of V associated with ϕ_{3D} at k^{th} pylon control point
V_∞	aircraft free-stream velocity
V_{∞_s}	ejected store free-stream velocity

$w_L(g)$	velocity w to be cancelled by vortex system at g^{th} control point on left panel
$w_R(j)$	velocity w to be cancelled by vortex system at j^{th} control point on right panel
$w_w(s)$	value of w on wing due to store alone
$W(\zeta)$	complex potential for flow around store in planes parallel to y_s-z_s plane
$W_s(\sigma)$	complex potential for store alone perturbation velocities
$W_\Gamma(\sigma)$	complex potential associated with N external vortices and their images including the center vortex
x, y, z	Cartesian coordinate system in compressible space
x', y', z'	Cartesian coordinate system in incompressible space; related to x, y, z by equation (2)
$\bar{x}, \bar{y}, \bar{z}$	Cartesian coordinate system with origin at store nose (see fig. 23)
x^*	x/ℓ_R for bodies, x/c for airfoils
x_k	x -location of k^{th} point source
x_k^*	x_k/ℓ_R for bodies, x_k/c for airfoils
x_s, y_s, z_s	Cartesian coordinate system with origin at nose of ejected store (see fig. 22)
$x_{s,0}$	separation location on store body
y	side force
Y_{cf}	side force on store alone due to viscous crossflow
z^*	z/c
$z_c(x)$	wing camber distribution in compressible space
$z_{th}(x)$	wing thickness distribution in compressible space measured from the camberline, positive upwards
α	angle of attack
α_B	angle of attack of fuselage

α_c	combined angle of attack at the axial location of the tail centroid; that is, angle between local velocity vector and store axis
α_L	local angle of attack, $\tan^{-1}(W/U)$
α_P	parent aircraft angle of attack; that is, angle between wind-tunnel longitudinal axis and fuselage axis
α_S	angle of attack of store
α_W	angle of attack of wing
B	$\sqrt{1 - M_\infty^2}$ or angle of sideslip
B_j	body or airfoil slope at the j^{th} point on the surface
γ_B	flight path angle of fuselage
γ_S	flight path angle of store
Γ_i	strength of vortex at $z = z_i$
θ	store pitch angle, positive nose up
$\dot{\theta}$	store pitching rate, $d\theta/dt$
$\ddot{\theta}$	store pitching acceleration, $d^2\theta/dt^2$
σ	s_E/a_E or expression given by equation (91)
λ	sweep angle or expression defined by equation (113)
x, y	coordinates of store center of gravity relative to fuselage nose, see figure 44
\dot{x}, \dot{y}	velocities of store center of gravity relative to fuselage
\ddot{x}, \ddot{y}	accelerations of store center of gravity relative to fuselage
ρ	mass density
σ	sidewash angle, $\tan^{-1}(V/U)$, or complex variable in $y_S - z_S$ plane, $\sigma = y_S + iz_S$
z_i	location of Γ_i vortex
ϕ	potential function in compressible space
ϕ_c	complete potential for airplane including store and pylon under consideration

ϕ_s	perturbation potential of store alone
ϕ_{SB}	part of potential ϕ_c due to presence of store and pylon
ϕ_{xx}	$\partial^2\phi/\partial x^2$
ϕ_{yy}	$\partial^2\phi/\partial y^2$
ϕ_{zz}	$\partial^2\phi/\partial z^2$
ϕ_{3D}	complete potential for aircraft except for store and pylon under consideration
ψ	stream function or algebraic expression given by equation (90)
ψ^*	ψ/l^2V_∞ for bodies, ψ/cV_∞ for airfoils

Subscripts

ATT	in the attached position
B	body
BY	due to buoyancy
CF	due to viscous crossflow
2D	two-dimensional (airfoil)
E	of the empennage
LE	leading edge
s	ejected store coordinate system
s,cg	store center of gravity
SB	due to slender-body theory
t,cen	tail centroid
th	thickness
T	of the tail alone (two tail panels joined together)
TE	trailing edge
TOT	total
vl	vortex lattice

- o initial conditions
- ∞ free-stream conditions
- α due to angle of attack

Superscripts

- * nondimensional quantities
- ' the value of the quantity at the corresponding point in the incompressible space

A METHOD FOR PREDICTING THREE-DEGREE-OF-FREEDOM STORE SEPARATION TRAJECTORIES AT SPEEDS UP TO THE CRITICAL SPEED

1. INTRODUCTION

This report is the final technical report describing a combined theoretical-experimental program which has been carried out with the objective of developing a computer program which will predict the trajectories of external stores dropped from aircraft of the fighter-bomber type. The speed range is limited to speeds below the critical. The stores can be placed either under the fuselage or the wing and may be single stores on pylons or groups of stores on racks. Only store motion in the vertical, or pitch, plane is considered.

The three principal tasks in the prediction of a store trajectory are: first, the determination of the nonuniform flow field in the neighborhood of the ejected stores; second, the determination of the forces and moments on the store in this flow field; and third, the integration of the equations of motion to determine the store trajectory. The first two tasks are the more difficult because they are complicated by interference effects.

The general methodology adopted in the present work is that the overall difficulty of the interference problem and the probable length of the computer program make it desirable to use the simplest possible methods consistent with accuracy. Thus, even though more precise methods may be known for handling some of the aerodynamic problems, simplified methods are used if they are deemed sufficiently accurate for the task at hand.

At each stage of development of the prediction method, comparisons will be made with experimental data to assess the accuracy of the method. It has been found that there is a general lack of data on external stores suitable for a critical check of a theory for predicting forces and moments on a store in a nonuniform flow field. Consequently, an experimental program has been conducted as part of the present investigation with the aim of obtaining such data. Data have been obtained for single stores and for triple ejection rack (TER) and multiple ejection rack (MER) groupings. A coordinated set of data has been obtained giving the flow-field velocity components where the store is to be located, forces and

moments on the store in this location, and in most cases, pressure distributions and thus load distributions on the store in this location. In order to isolate effects due to adding a component to the parent aircraft, the parent aircraft has been built up component by component and the tests repeated for each parent aircraft configuration.

The data obtained during this program are not presented in this report but are tabulated in reference 1. The complete test program is described in that reference. Representative data from this program are also presented in references 2 and 3.

2. GENERAL METHOD OF APPROACH

The accurate calculation of store separation trajectories requires that the forces and moments acting on the store be known at every point in the trajectory. If these forces and moments are to be calculated by theoretical means, then the velocity field in the vicinity of the ejected store relative to that store must first be determined. This field depends not only on the store free-stream velocity, but also the perturbation velocities induced by all of the aircraft components and any stores still attached to the aircraft. The determination of this velocity field requires that models for the aircraft components be developed and that the important interferences between components be accounted for. In the basic method presented in this report, models are developed for the fuselage, wing, and stores and the following flow-field components are accounted for in the primary interference method:

- (1) Fuselage volume
- (2) Fuselage angle of attack
- (3) Wing thickness
- (4) Wing angle of attack, camber, and twist
- (5) Wing-fuselage interference
- (6) Store volume
- (7) Wing-store interference

Pylon and rack effects are not included in the primary interference.

Fuselage volume is taken into account by approximating the shape by an axisymmetric body and representing this body by a series of point sources placed on the body axis. The volumes of all of the stores present are accounted for in the same manner. Fuselage angle of attack is taken into account as a simple Beskin upwash. Mutual interference

between wing, pylon, and store are accounted for in an additional interference method.

Wing thickness is accounted for by representing the airfoil section immediately above the store being ejected by a series of two-dimensional point sources. Simple sweep theory is then used to modify the velocities induced by this source distribution to account for wing sweep and taper.

The remaining three items: wing angle of attack, twist, and camber; wing-fuselage interference; and wing-store interference are accounted for in the following way. The wing is represented by a vortex lattice and the velocities induced by the fuselage and stores at the wing are computed and treated as an induced wing camber which is added to any geometric twist and camber. The wing model then accounts for this induced camber and the velocities induced by the wing on the store to be ejected are computed with the store in its initial position. After the store is ejected and moves relative to the wing, the velocities induced by it at the wing will change. To account precisely for these changing velocities would require calculating a new wing model at each point in the trajectory and would greatly increase computation time. Since the initial motion of the store is the most important, it is felt that any change in the wing model due to movement of the store is a second-order effect, and, hence, it is not accounted for at the present time. This assumption can be relaxed if proven necessary.

The wing also changes the flow field in the vicinity of the fuselage and stores in such a way as to cause them to operate in a nonuniform flow field. Since the basic fuselage and store models are derived for an assumed uniform flow field, the existence of the nonuniform flow causes additional changes in the wing loading not accounted for by the interference effects discussed thus far. At the present time, the modification of the wing loading due to this effect is not included in the primary interference but is included in the additional interference.

The fact that one store can induce velocities in the vicinity of another store such as to cause that store to be in a nonuniform flow field is neglected for single stores, but included for multiple stores. For single stores, each mounted on its own pylon, the distance between stores is such that this effect is felt to be a second-order effect. For stores grouped together, as on TER or MER racks, experiments show that this effect is important. For the cases tested, the store volume effects are dominant and have been included in the theory.

The general method being described in this report allows the trajectory of a store ejected from under the fuselage or the wing, either as a single store or one of a cluster on a TER or MER rack, to be calculated. In the preceding discussion, the method of accounting for the pylon or rack was not described. In order to investigate the importance of mutual interference between the wing, pylon, and store, an interference model has been developed for the special case of a single store mounted on a pylon beneath the wing. This interference calculation has not been carried out for MER and TER configurations, but the basic approach is applicable to any of the store locations and groupings of interest. The magnitude of the additional interference for three-degrees-of-freedom as calculated is generally negligible. This may not be the case for six-degree-of-freedom motion.

The determination of the trajectory of the ejected store requires that the forces and moments acting on the store, including damping, be calculated at each point in the trajectory. This is done by calculating the three-dimensional velocity field in which the store is operating as seen by the store. The free-stream velocity and all of the velocities induced by the wing, fuselage, and other stores are summed up together with that due to the angular velocity at the particular point on the store. The velocity field over the store length is calculated in this manner. The axial distribution of the forces and moments due to buoyancy, potential flow, and viscous crossflow are calculated from this velocity field and then integrated over the store length. At the present time, only normal force and pitching moment are calculated although the information for calculating the side force and yawing moment can be readily generated by the computer program.

3. COMPRESSIBILITY CORRECTION

Consider a wing-fuselage combination moving at Mach number M_∞ and angle of attack of the fuselage α_B and assume that the flow field for compressible subcritical flow is governed by a perturbation potential ϕ which satisfies

$$(1 - M_\infty^2) \phi_{xx} + \phi_{yy} + \phi_{zz} = 0 \quad (1)$$

where the x, y, z coordinate system is fixed in the fuselage (see fig. 1). The approach to be used in solving for the wing-fuselage flow field is to transform the wing-fuselage combination to an equivalent incompressible one,

determine the incompressible flow field for the equivalent combination, and then transform the flow field back to the compressible speed.

The transformation of the compressible space (x,y,z) to the incompressible space (x',y',z') can be done in a number of ways. For the present work let us use the following transformation:

$$x' = \frac{x}{\sqrt{1 - M_\infty^2}}, \quad y' = y, \quad z' = z \quad (2)$$

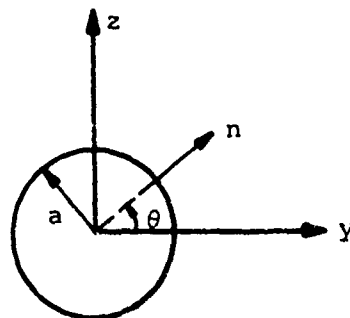
The coordinates (x,y,z) and (x',y',z') so related are termed corresponding points. Using this transformation, the configuration cross sections in corresponding planes are not changed, but the configuration is stretched in the x direction to make it more slender. Consequently, the surface slopes in planes parallel to the x -axis are reduced by the factor β , where $\beta = \sqrt{1 - M_\infty^2}$. That is,

$$\frac{dy'}{dx'} = \beta \frac{dy}{dx}, \quad \frac{dz'}{dx'} = \beta \frac{dz}{dx} \quad (3)$$

Let us now determine the boundary conditions on the wing and body. At any streamwise section, the wing is defined by a thickness distribution, $z_{th}(x)$, and a camber distribution, $z_c(x)$. The linearized wing boundary condition is then for $z = 0$

$$\frac{\partial \phi}{\partial z} = w = V_\infty \left(-\alpha_B + \frac{dz_{th}}{dx} + \frac{dz_c}{dx} \right) \quad (4)$$

The body boundary condition will be written with the aid of the following sketch:



If the body radius in any plane perpendicular to the body axis is $a(x)$, then the linearized body boundary condition is

$$V_{\infty} \left(-\alpha_B \sin \theta + \frac{da}{dx} \right) = \frac{\partial \phi}{\partial n} = \frac{\partial \phi}{\partial y} \cos \theta + \frac{\partial \phi}{\partial z} \sin \theta \quad (5)$$

Let us now write the potential and boundary conditions in the incompressible (x', y', z') plane. If ϕ' is the potential function which satisfies

$$\phi'_{x'x'} + \phi'_{y'y'} + \phi'_{z'z'} = 0 \quad (6)$$

then the boundary conditions in the $M_{\infty} = 0$ space which correspond to equations (4) and (5) are

$$\frac{\partial \phi'}{\partial z'} = V_{\infty} \left(-\alpha'_B + \frac{dz'_{th}}{dx'} + \frac{dz'_c}{dx'} \right) \quad (7)$$

and

$$V_{\infty} \left(-\alpha'_B \sin \theta' + \frac{da'}{dx'} \right) = \frac{\partial \phi'}{\partial n'} = \frac{\partial \phi'}{\partial y'} \cos \theta' + \frac{\partial \phi'}{\partial z'} \sin \theta' \quad (8)$$

If we now let

$$\alpha'_B = \beta \alpha_B \quad (9)$$

then the incompressible problem is completely defined by the boundary conditions given by equations (7), (8), and (9), together with the condition that the perturbation velocities vanish at infinity.

We must now show how the potential ϕ is related to ϕ' at corresponding points. From equations (2), (4), (7), and (9), we find on the wing

$$\frac{\partial \phi'}{\partial z'} = \beta V_{\infty} \left(-\alpha_B + \frac{dz_{th}}{dx} + \frac{dz_c}{dx} \right) = \beta \frac{\partial \phi}{\partial z} \quad (10)$$

On the body we have, from equations (2), (5), and (8),

$$\frac{\partial \phi'}{\partial n'} = v_{\infty} \left(-\alpha'_B \sin \theta' + \frac{da'}{dx'} \right) = \beta v_{\infty} \left(-\alpha_B \sin \theta + \frac{da}{dx} \right) = \beta \frac{\partial \phi}{\partial n} \quad (11)$$

Both equations (10) and (11) can be satisfied if, at corresponding points,

$$\phi = \frac{\phi'}{\beta} \quad (12)$$

Since the relationship given by equation (12) will satisfy both the wing and the body boundary conditions, and since ϕ will satisfy equation (1), we have the desired solution to the compressible problem.

The velocities in the compressible space, u , v , and w , are related to those in the incompressible space, u' , v' , and w' , as follows:

$$\left. \begin{aligned} u &= \frac{\partial \phi}{\partial x} = \frac{1}{\beta} \frac{\partial \phi'}{\partial x} = \frac{1}{\beta} \frac{\partial \phi'}{\partial x'} \frac{\partial x'}{\partial x} = \frac{1}{\beta^2} \frac{\partial \phi'}{\partial x'} = \frac{u'}{\beta^2} \\ v &= \frac{\partial \phi}{\partial y} = \frac{1}{\beta} \frac{\partial \phi'}{\partial y} = \frac{1}{\beta} \frac{\partial \phi'}{\partial y'} \frac{\partial y'}{\partial y} = \frac{1}{\beta} \frac{\partial \phi'}{\partial y'} = \frac{v'}{\beta} \\ w &= \frac{\partial \phi}{\partial z} = \frac{1}{\beta} \frac{\partial \phi'}{\partial z} = \frac{1}{\beta} \frac{\partial \phi'}{\partial z'} \frac{\partial z'}{\partial z} = \frac{1}{\beta} \frac{\partial \phi'}{\partial z'} = \frac{w'}{\beta} \end{aligned} \right\} \quad (13)$$

The procedure used to calculate the forces and moments acting on a store in the presence of a wing-fuselage combination for a compressible subcritical Mach number will now be described in detail. Consider the wing-fuselage combination shown in figure 2 and a single store located relative to it as shown in figure 3(a). The store geometry is shown in figure 3(b). The first step is to transform the wing-fuselage-store combination to an equivalent one for incompressible flow. This is done by using a coordinate system whose origin is at the fuselage nose as the x, y, z system. All of the configuration components are located in this system. The transformation given by equation (2) is used to determine the equivalent configuration. This results in a lengthening of the fuselage and store by a factor $1/\beta$. The methods to be presented in section 4.1 are then used to obtain source distributions to represent the volume distribution of these equivalent bodies.

The transformation also results in lengthening the wing chord by a factor $1/\beta$, which results in a thinner airfoil section. The methods to be presented in section 4.2 are used to obtain the source distribution to represent this thickness distribution.

The determination of the vorticity distribution to represent the wing surface is also done in the equivalent plane. In addition to the longer chord, the tangents of the wing leading- and trailing-edge sweep angles are increased by a factor $1/\beta$. If the wing is cambered, the slopes of the mean camber surface are reduced by a factor β as is the angle of attack of the wing. The vorticity distribution is determined by the methods to be described in section 4.3. Interference of the store on the wing is accounted for in the determination of the vorticity distribution.

The next step in the calculation of the forces and moments is to calculate the velocity field in the fuselage coordinate system in the vicinity of the store for the equivalent configuration. The perturbation velocities induced by the fuselage, wing thickness distribution, and wing vorticity distribution are calculated in the region that the incompressible store would occupy if it were present. They are added together and transformed back to the compressible space using equations (2) and (13). Finally, the free-stream velocity components are added to the compressible perturbation velocities. The example just considered is a case where the wing and store are at zero incidence relative to the fuselage axis. If they are at incidence, the incidence angles are reduced by a factor of β in the incompressible space.

It is important to point out that the incompressible perturbation velocity field must be calculated and resolved into velocity components in the fuselage coordinate system before transforming back to the compressible space. Since the transformation of the configuration was done in this coordinate system, the velocities must also be transformed in this system. Once in the compressible space, the velocities can be resolved into any desired coordinate system.

4. MATHEMATICAL MODELS FOR DETERMINING FLOW FIELD

The methods used to evaluate the forces on a released store require detailed knowledge of the flow field in the region of the store in its absence. Mathematical models of the aircraft components that influence

this flow field are described in this section. The methods used to account for mutual interference among the components are also described.

Models for the thickness or volume distributions of the isolated aircraft components at 0° angle of attack have been developed for the wing, fuselage, and stores. The wing thickness model is based on a distribution of two-dimensional point sources which represents the thickness distribution of the airfoil cut out of the wing by a vertical streamwise plane through the store axis. Adjustments to this model are applied which generalize it to three-dimensional wings with sweep and taper. The fuselage and stores at 0° angle of attack are approximated by axisymmetric bodies which are represented by a series of three-dimensional point sources distributed along the body axes. Body angle of attack effects are accounted for by doublets whose strengths are determined by slender-body theory.

A model composed of two superimposed planar arrays of horseshoe vortices is used to account for the effects of wing angle of attack, wing geometric camber and twist, and wing loading changes due to the presence of other aircraft components. The vortex strengths of the first vortex array or lattice are proportional to the angle of attack of the wing and account solely for the wing angle of attack effects. The second vortex lattice, assumed independent of angle of attack, accounts for the geometric twist and camber and the normal velocities induced at the wing by the fuselage and stores. The velocities induced by these bodies are treated as an "induced camber" which is added to the geometric twist and camber.

4.1 Axisymmetric Bodies at Zero Degrees Angle of Attack

4.1.1 Fundamental equations

The stream function ψ and the axial and radial velocity components, U and V_r , respectively, due jointly to a free-stream velocity V_∞ aligned with the body axis, the x -axis, and a series of N point sources distributed along the body axis are given in reference 4. With reference to figure 1, which shows the coordinate system, they can be written in dimensionless form as

$$\psi^*(x^*, r^*) = \frac{1}{2} r^{*2} - \sum_{k=1}^N Q_k^* \left\{ 1 + \frac{(x^* - x_k^*)}{[(x^* - x_k^*)^2 + r^{*2}]^{1/2}} \right\} \quad (14)$$

$$U^*(x^*, r^*) = \frac{1}{r^*} \frac{d\psi^*}{dr^*} = 1 + \sum_{k=1}^N \frac{Q_k^* (x^* - x_k^*)}{[(x^* - x_k^*)^2 + r^{*2}]^{3/2}} \quad (15)$$

$$V_r^*(x^*, r^*) = -\frac{1}{r^*} \frac{d\psi^*}{dx^*} = \sum_{k=1}^N \frac{Q_k^* r^*}{[(x^* - x_k^*)^2 + r^{*2}]^{3/2}} \quad (16)$$

where

$$x^* = \frac{x}{l_R}, \quad r^* = \frac{r}{l_R}$$

$$U^* = \frac{U}{V_\infty}, \quad V_r^* = \frac{V_r}{V_\infty}$$

$$Q^* = \frac{Q}{4\pi \beta^2 V_\infty}, \quad \psi^* = \frac{\psi}{l_R^2 V_\infty}$$

and where l_R is a reference length which for convenience will be taken as the length of the body. The quantities Q_k^* and x_k^* are the source strength and location, respectively, of the k^{th} point source, and the point (x^*, r^*) designates the field point in cylindrical coordinates.

4.1.2 Conditions used to obtain source strengths

A mathematical representation of the flow field about an axisymmetric body is obtained by imposing three conditions on equations (15) and (16). These equations, the velocity equations, are used to calculate the source strengths rather than the streamline equation because they were found to give a better shape representation. This is due to the fact that they require both body ordinates and surface slopes for their solution. For the first condition the flow directions at $(N - 2)$ points (x_j^*, r_j^*) , $j = 1, \dots, (N - 2)$, are specified by angles β_j with respect to the positive x^* -axis; that is,

$$\tan \beta_j = \frac{V_r^*(x_j^*, r_j^*)}{U^*(x_j^*, r_j^*)} \quad \text{for } j = 1, \dots, (N - 2) \quad (17)$$

or in terms of equations (15) and (16)

$$\tan \beta_j = \frac{\sum_{k=1}^N \frac{Q_k^* r_j^*}{[(x_j^* - x_k^*)^2 + r_j^{*2}]^{3/2}}}{1 + \sum_{k=1}^N \frac{Q_k^* (x_j^* - x_k^*)}{[(x_j^* - x_k^*)^2 + r_j^{*2}]^{3/2}}} \quad \text{for } j = 1, \dots, (N - 2) \quad (18)$$

The locations (x_j^*, r_j^*) where the flow angles β_j are specified lie on the surface of the axisymmetric body being represented, and the values of $\tan \beta_j$ correspond to the local body surface slopes, $dr^*(x_j^*, r_j^*)/dx^*$. For convenience, equation (18) is rearranged to give a set of linear algebraic equations in the Q_k^* 's

$$\tan \beta_j = \sum_{k=1}^N Q_k^* \frac{r_j^* - \tan \beta_j (x_j^* - x_k^*)}{[(x_j^* - x_k^*)^2 + r_j^{*2}]^{3/2}} \quad \text{for } j = 1, \dots, (N - 2) \quad (19)$$

The second condition is that the sum of all of the source strengths be zero. That is,

$$\sum_{k=1}^N Q_k^* = 0 \quad (20)$$

which insures that the surface described by $\psi^*(x^*, r^*) = 0$, the mathematical representation of the body surface, will be a closed surface.

The third condition is the existence of a stagnation point at the body nose; hence, $U^* = 0$, at the origin, $x^* = r^* = 0$. By substitution into equation (15) this condition becomes

$$\sum_{k=1}^N \frac{Q_k^*}{x_k^{*2}} = 1 \quad (21)$$

Since the sources are distributed along the positive x^* -axis only, the forward tip of the body is positioned at the origin and the $\psi^* = 0$ surface is the body surface. Upon selection of the N source positions, x_k^* , equations (19), (20), and (21) comprise a set of N linear equations in the N unknowns Q_k^* . After solving for these, equations (15) and (16)

can then be used to determine the velocities at any point in the flow field around the body.

4.1.3 Calculative examples

Several arbitrary choices remain in the application of equations (19) through (21) to particular bodies. In order to obtain adequate correspondence between the shape of the body that is to be represented and its mathematical representation, which is the surface $\psi^*(x^*, r^*) = 0$, a suitable selection is required for the number of sources and the $(N - 2)$ locations, (x_j^*, r_j^*) of equation (19), where the streamline direction constraints are to be imposed. Excellent "fits" of several bodies have been obtained to date and the selection of these parameters for two of these bodies is given below.

A comparison between the surface shape of a particular body (the fuselage of a wind-tunnel model described in ref. 5) and the $\psi^*(x^*, r^*) = 0$ surface is presented in figure 4(a). In examining this figure note that the r^* scale has been expanded over the x^* scale. A criterion that has been successfully used for this body, and for all reasonably smooth, pointed or slightly blunted, slender bodies, is that the distance between adjacent source points be proportional to the local body radius. For the specific case shown in figure 4(a), the distance between source points was 1.2 times the local radius. For proportionality factors of the order of 1.5, irregularities of undesirable magnitude in the $\psi^*(x^*, r^*) = 0$ surface tended to occur, whereas, no noticeable improvement resulted from factors less than 1.2. The most forward point source for the example shown is located at $x^* = 0.002$. For conically-tipped forebodies, distances of this order are required for satisfactory fitting. For values of the first source location significantly larger than 0.002, the foresection of the $\psi^*(x^*, r^*) = 0$ surface tends to be blunter than desired, whereas, smaller values, once again, show no noticeable improvement. For bodies whose aft sections are blunt, such as the example in figure 4(a), the procedure is to extend the aft section by a boattail. This procedure is based on the fact that in the real flow the body streamtube separates from the body at the base and converges to a point in the wake. The extreme aft point source is located at $x^* = 1.118$, and the number of sources used for this example is 37.

The axial locations of the $(N - 2)$ positions where the flow velocity directions, or surface slopes, are imposed have been chosen at positions midway between adjacent source positions. Since this would specify one too many slopes, a point in the middle of the body has been eliminated.

Results for a blunt axisymmetric body are presented in figure 4(b). The body is a cylinder with ellipsoidal ends and a length-to-maximum-diameter ratio of 10. The $(N - 2)$ axial locations at which the flow velocity directions, or surface slopes, were imposed are, as for the previous case, midway between source locations. For this case no precise criterion of source location was applied other than symmetry with respect to the body center since the fore and aft sections are identically shaped. Otherwise, the sources were concentrated in regions of high body curvature. The total number of point sources for this case was 18.

4.2 Wing Thickness at Zero Degrees Angle of Attack

The flow about a symmetrical airfoil at 0° angle of attack is the basic flow used to account for wing thickness. Its mathematical representation is obtained in much the same manner as that for the axisymmetric bodies. It is then extended to wings with sweep and taper. It should be noted that the flow parameters in this section that pertain to the symmetric airfoil at zero angle of attack are distinguished by the subscript "2D."

4.2.1 Fundamental equations

The stream function, ψ_{2D} , and the flow velocities, U_{2D} and W_{2D} , (fig. 5) due to a uniform flow of velocity V_∞ in the positive x direction with a series of N two-dimensional point sources distributed along the x -axis are given in dimensionless form (ref. 4).

$$\psi_{2D}^*(x^*, z^*) = z^* - \sum_{k=1}^N Q_k^* \left\{ - \tan^{-1} \left[\frac{z^*}{(x^* - x_k^*)} \right] \right\} \quad (22)$$

$$U_{2D}^*(x^*, z^*) = \frac{d\psi_{2D}^*}{dz^*} = 1 + \sum_{k=1}^N Q_k^* \frac{(x^* - x_k^*)}{(x^* - x_k^*)^2 + z^{*2}} \quad (23)$$

$$W_{2D}^*(x^*, z^*) = \frac{-d\psi_{2D}^*}{dx^*} = \sum_{k=1}^N \frac{Q_k^* z^*}{(x^* - x_k^*)^2 + z^{*2}} \quad (24)$$

where

$$x^* = \frac{x}{c}, \quad z^* = \frac{z}{c}$$

$$U^* = \frac{U}{V_\infty}, \quad W^* = \frac{W}{V_\infty}$$

$$Q_k^* = \frac{Q_k}{2\pi c V_\infty}, \quad \psi^* = \frac{\psi}{c V_\infty}$$

and where the reference length c is the chord. In these equations Q_k^* and x_k^* are the source strength and location, respectively, of the k th point source.

4.2.2 Conditions used to obtain source strengths

The flow field about a symmetrical airfoil is found by imposing three conditions on equations (23) and (24) analogous to those used for the axisymmetric case. First, at $(N - 2)$ points (x_j^*, z_j^*) , $j = 1, \dots, (N - 2)$, which correspond to airfoil surface locations, the flow direction is set equal to the corresponding local airfoil surface slope, $\tan \beta_j = dz^*(x_j^*, z_j^*)/dx^*$. Thus we obtain

$$\tan \beta_j = \frac{W_{2D}^*(x_j^*, z_j^*)}{U_{2D}^*(x_j^*, z_j^*)} \quad \text{for } j = 1, \dots, (N - 2) \quad (25)$$

The resulting expressions are

$$\tan \beta_j = \sum_{k=1}^N Q_k^* \frac{z_j^* - \tan \beta_j (x_j^* - x_k^*)}{(x_j^* - x_k^*)^2 + z_j^{*2}} \quad \text{for } j = 1, \dots, (N - 2) \quad (26)$$

The second condition, the sum of the source strengths equals zero, gives

$$\sum_{k=1}^N Q_k^* = 0 \quad (27)$$

The stagnation condition $U_{2D}^* = 0$ at the leading edge, $x^* = z^* = 0$, leads to the result

$$\sum_{k=1}^N \frac{Q_k^*}{x_k^*} = 1 \quad (28)$$

The resultant set of N linear equations given by equations (26) through (28) are solved for the N unknowns Q_k^* . The velocities at any point can then be calculated using equations (23) and (24).

4.2.3 Calculative example

The foregoing method has been applied to a NACA 65A006 airfoil and the results are shown in figure 6. The criterion used in selecting point-source locations is that the distance between adjacent sources be proportional to the local airfoil thickness. This is analogous to the criterion applied to the first axisymmetric body considered previously. The extreme fore and aft source locations are $x^* = 0.0006$ and $x^* = 0.996$, respectively, and the total number of sources is 43. The axial positions at which the $(N - 2)$ velocity direction conditions are imposed, were intermediate between adjacent source locations, omitting the position near the mid-chord. The comparison between the actual airfoil shape and the calculated shape shown in figure 6 shows good agreement. The velocity field around the airfoil can be calculated using equations (23) and (24).

4.2.4 Calculation of the velocity field about wings with sweep and taper

The calculation of the flow about a symmetrical swept tapered wing from knowledge of the flow about an airfoil following the method of reference 6 is briefly discussed in this section. The geometry associated with the problem is illustrated in figure 7. The circular symbols represent planform locations of points where the flow velocity is desired. Lines of constant percent chord are shown, together with normal lines that are perpendicular to the lines of constant percent chord at the circular symbols. Airfoil sections along the normal lines are called normal sections.

The calculation of the thickness-induced velocities for an infinite swept wing by simple sweep theory requires a knowledge of the thickness distribution of the normal airfoil section and the component of the free-

stream velocity normal to the leading edge. For swept and unswept wings of finite span, in regions sufficiently removed from the wing root and tip, the lines of constant pressure tend to be parallel to lines of constant percent thickness. Furthermore, for wings of constant thickness ratio and constant thickness distribution over the span these lines are parallel to lines of constant percent chord.

Referring to figure 7, the calculation by simple sweep theory of the perturbation velocities u_n and w (w is the vertical velocity below the point) requires that a source distribution be determined which represents the normal airfoil section through the point. Then the perturbation velocities can be determined for the component of the free-stream velocity parallel to this normal section, $V_\infty \cos \Lambda$ where Λ is the angle between the normal section and the local chord. The velocity $V_\infty \sin \Lambda$ perpendicular to the normal section does not enter the calculation of u_n . Once u_n is evaluated, then the perturbation velocities u and v in the x and y direction, respectively, are simply given by

$$u = u_n \cos \Lambda \quad (29)$$

$$v = u_n \sin \Lambda \quad (30)$$

Designating Λ_{LE} and Λ_{TE} , respectively, as the leading and trailing edge sweep angles, Λ is given by

$$\tan \Lambda = \tan \Lambda_{LE} + \frac{x}{c} (\tan \Lambda_{TE} - \tan \Lambda_{LE}) \quad \text{for } 0 \leq \frac{x}{c} \leq 1 \quad (31)$$

where x/c is a fraction of the local chord. For locations forward of the wing leading edge (or behind the trailing edge), Λ is taken as Λ_{LE} (or Λ_{TE}).

If the above method is to be used for tapered wings and velocities are required at a large number of points under the wing, then a large number of source distributions would be required, one for each point, since the normal airfoil section would be different at each point. A method for calculating the perturbation velocities without calculating a source distribution for each airfoil section is given in reference 6. It is assumed there that the flow over any normal section is related to that

over the streamwise section through the point and therefore, only one source distribution is required.

With regard to evaluating u_n , consider the two constant chord wings in figure 8. Both the swept and unswept wings have identical streamwise chords, streamwise thickness ratios, and thickness distributions. The thickness ratio of the normal section of the swept wing is larger than that of the streamwise airfoil (of either wing) by a factor $1/\cos \Lambda$. It is shown in reference 6, that, since the perturbation velocities depend linearly on thickness (for small thickness ratios), the effect of the larger thickness of the normal airfoil is offset by the smaller imposed velocity, $V_\infty \cos \Lambda$, in the normal direction. Thus, the perturbation velocities of normal sections of the swept wing are equal to those at corresponding points of the unswept wing. This result holds approximately for symmetrical tapered swept wings as well. Thus, the streamwise and lateral perturbation velocities for the swept and tapered wing, u and v of equations (29) and (30), may now be written in terms of the perturbation velocities of the streamwise airfoil section as

$$u^* = u_{2D}^* \cos \Lambda = (U_{2D}^* - 1) \cos \Lambda \quad (32)$$

$$v^* = u_{2D}^* \sin \Lambda = (U_{2D}^* - 1) \sin \Lambda \quad (33)$$

$$w^* = w_{2D}^* = W_{2D}^* \quad (34)$$

For tapered wings the local sweep angle, Λ , as given by equation (31) is used in equations (32) and (33).

In summary, flow equations for the velocity components applicable to swept and tapered wings with similar streamwise sections in the spanwise direction are given by

$$U^*(x^*, z^*) = 1 + \cos \Lambda \sum_{k=1}^N Q_k^* \frac{(x^* - x_k^*)}{(x^* - x_k^*)^2 + z^{*2}} \quad (35)$$

$$V^*(x^*, z^*) = \sin \Lambda \sum_{k=1}^N Q_k^* \frac{(x^* - x_k^*)}{(x^* - x_k^*)^2 + z^{*2}} \quad (36)$$

$$W^*(x^*, z^*) = \sum_{k=1}^N Q_k^* \frac{z^*}{(x^* - x_k^*)^2 + z^{*2}} \quad (37)$$

In these equations, the source strengths Q_k^* and their locations x_k^* correspond to the local streamwise airfoil section of the swept and tapered wing of interest. All quantities are made dimensionless on the basis of the local streamwise chord of the swept and tapered wing of interest.

4.3 Wing Angle of Attack; Lifting-Surface Theory

4.3.1 Description of method

The model used to account for wing angle of attack, wing geometric twist and camber, and interference-induced twist and camber is the method described in references 7 and 8. This method is a lifting-surface theory with the planform of the wing represented by two superimposed arrays of horseshoe vortices representing the basic and additional lift distributions. In contrast to a lifting-line theory, this method employs vortices distributed both chordwise and spanwise. The wing planforms handled by the method must be representable by a series of straight-line segments. The camber and twist distribution of the wing is arbitrary. The details of the method will not be repeated here, as they are contained in the above-mentioned references; however, the following paragraph will briefly describe the method.

The vortex lattice is determined by dividing the wing into area elements formed by lines of constant percent chord and lines parallel to the root chord. A horseshoe vortex is placed with the bound portion at the quarter chord on each of the area elements. The two semi-infinite trailing legs are in the plane of the wing and at the side edges of the area elements. The boundary condition of no flow through the wing is applied at the mid-span of the three-quarter chord of each area element. Two vorticity distributions are determined, one which is a function of angle of attack and the other which is not. The angle of attack

distribution cancels the component of the free-stream velocity normal to the wing planform. The zero angle-of-attack distribution accounts for the local angle of attack due to twist and camber when the wing root chord is at 0° angle of attack. The local angles of attack at the wing control points due to geometric twist and camber are input to the computer program and the induced camber due to interference of the fuselage and stores is calculated by the program and added to the geometric camber. Since both vorticity distributions are required to satisfy the boundary condition of no flow through the wing at the control points, they are obtained by solving two sets of simultaneous algebraic equations which differ only on the right-hand side. The computer program of reference 8 then uses these vorticity distributions as input to calculate the velocities induced by the wing at any point in its flow field.

4.3.2 Effect of the number of vortices on the calculated flow field

Since the wing is represented by a finite number of horseshoe vortices, the question arises as to how close to the wing the velocity field can be calculated within prescribed error limits. Stores are often sufficiently close to the wing that the number of vortices required to obtain accurate flow fields is quite large. The purpose of this section is to provide a notion of the lattice size required for reasonably accurate results at a given distance below the wing.

The calculations to be shown have been made for the swept wing geometry of references 5 and 6, as shown in figure 9. The wing is taken to be at 6° angle of attack. The calculations are made for downwash and sidewash due to angle of attack neglecting fuselage and wing thickness effects. The flow field results are presented in terms of the dimensionless perturbation velocities normal to the plane of the wing (w/V_∞) and in the lateral direction (v/V_∞) versus the chordwise distance (x/c) at the mid-semispan of the left wing panel for the two distances below the wing (z/c) of -0.10 and -0.05 . The coordinate system is shown in figure 10. The perturbation velocities u , v , and w are related to the components U , V , and W of the local velocity vector as follows:

$$U = V_\infty \cos \alpha_w + u$$

$$V = v$$

$$W = V_\infty \sin \alpha_w + w$$

The normal and lateral velocities at $z/c = -0.10$ for two combinations of chordwise and spanwise vortices are shown in figures 11(a) and 11(b). Cyclic chordwise variations evident for the 4 chordwise by 9 spanwise (4x9) array are imperceptible for the 10x9 array. Curves for a 7x9 array were indistinguishable from those for the 10x9 array except near the wing leading edge. It appears evident from the rapid convergence that curves from arrays with an increased number of chordwise vortices would coincide with those from the 10x9 array.

Velocities at $z/c = -0.05$ for the same two array, as above are presented in figures 12(a) and 12(b). For this case, small amplitude fluctuations persist for the 10x9 array. It is evident from the pattern of convergence, however, that the 10x9 curve closely approximates the ultimate curve, and that the cyclic variations would perhaps be imperceptible for a 13x9 array.

5. CALCULATION OF FLOW FIELD

5.1 Interference Effects

Methods have been presented for determining the flow fields of the fuselage or store alone and the wing alone. In the case of a wing-fuselage combination with stores, the flow field is the sum of the fields due to the various components plus one due to interference among the components. In terms of the potential functions, we have

$$\phi_{WB} = \phi_{w_t} + \phi_{w_\alpha} + \phi_{B_t} + \phi_{B_\alpha} + \phi_i$$

ϕ_{w_t} = potential due to wing thickness

ϕ_{w_α} = potential due to wing twist, camber, and angle of attack

ϕ_{B_t} = potential due to fuselage volume and external store volumes

ϕ_{B_α} = potential due to fuselage and external store angle of attack and sidewash

ϕ_i = potential due to wing-fuselage and wing-store interference

In order to determine ϕ_i , the only component not considered so far, we can use two means of approach; a noniterative approach and an iterative approach. In the noniterative approach singularities are placed on the fuselage and the wing, and the strength of the singularities are all calculated simultaneously using a large number of simultaneous equations. This approach requires large computer times and may be limited in accuracy by the number of simultaneous equations the computer can solve. In the iterative approach, adopted here, the computer time is kept reasonably short and the accuracy of calculation is adequate.

In the iterative approach to determine the flow under the wing of the wing-fuselage combination, consider first the wing alone at the airplane angle of attack. Now let the wing alone have velocities induced normal to it by the fuselage flow field. The wing boundary condition is no longer satisfied, but a wing-alone solution producing equal and opposite velocities to those induced at the wing by the fuselage can be found from the vortex-lattice program. This solution represents the first approximation of the interference solution in the vicinity of the wing.

To obtain the first approximation to the interference potential in the region of the fuselage, consider the fuselage alone, and then let its normal velocity distribution be modified by the induced flow field of the wing alone. The additional fuselage solution required to cancel these normal induced velocities is the first approximation to the interference field in the neighborhood of the body. It is clear that an iterative scheme can be set up to account for higher-order interactions. For our purposes only one iteration is required, as comparison between experiment and theory will show.

Some simplification has been found possible. Consider the application of the preceding equation to the flow field under the wing. For a high-wing monoplane the velocities associated with ϕ_{B_t} and ϕ_{B_α} both produce velocities normal to the wing, although for a midwing configuration, ϕ_{B_t} produces no such velocities. By considering the normal wing velocities associated with ϕ_{B_t} and ϕ_{B_α} , we can calculate interference potentials ϕ_{i_t} and ϕ_{i_α} using the vortex lattice program. These potentials would have the properties that

$$\frac{\partial}{\partial n} (\phi_{B_t} + \phi_{i_t}) = 0 \quad \text{on the wing}$$

$$\frac{\partial}{\partial n} (\phi_{B_\alpha} + \phi_{i_\alpha}) = 0 \quad \text{on the wing}$$

where n is normal to the wing surface. The physical argument could be made that if the sum of ϕ_{B_α} and ϕ_{i_α} produces zero normal velocity at the wing surface and dies away with distance from the surface, it will produce negligible velocities under the wing except in the neighborhood of the wing-fuselage juncture where the first approximation to the interference potential is not accurate. In this region the mutual interference problem must be solved. The same argument can be made for the sum of ϕ_{B_t} and ϕ_{i_t} .

A calculation was made to check this argument. The normal velocity at the wing associated with ϕ_{B_α} is the upwash produced by the doublet distribution representing the body at angle of attack, also termed Beskin upwash. A twist distribution equal and opposite to that due to the Beskin upwash was introduced into the wing, with zero twist in the region blanketed by the body, and the flow field associated with the resulting ϕ_{i_α} potential was calculated. The downwash and sidewash fields resulting from the combined effect of ϕ_{B_α} and ϕ_{i_α} was generally less than a degree. Accordingly, the assumption has been made that the combined effect of ϕ_{B_α} and ϕ_{i_α} can be neglected. A precise calculation is possible, but is not warranted at this time. While the $\phi_{B_\alpha} + \phi_{i_\alpha}$ effect has been neglected, the $\phi_{B_t} + \phi_{i_t}$ terms have been included. Both fuselage and external store effects have been included in these terms.

With regard to the flow field under the body, the sum of ϕ_{B_t} and ϕ_{B_α} satisfies the body boundary condition exactly. The sum $\phi_{w_t} + \phi_{w_\alpha} + \phi_i$ must produce zero normal velocity at the body. As we move downward from the body, the induced velocities due to this sum must decrease. Accordingly, we have neglected these induced velocities everywhere under the body.

The simplifications and approximations introduced in making the wing-body flow-field calculation greatly reduce the complexity of the analysis and the amount of computer time required at very little loss in accuracy. The adequacy of the above procedure is to be judged by the agreement between experiment and theory for downwash and sidewash subsequently to be presented.

5.2 Method of Calculation

5.2.1 Single store under the wing

The first step in calculating the flow field for the case of a single store under the wing of a wing-fuselage combination is to obtain source distributions to represent the volume distributions of the fuselage and store in the incompressible space as well as the wing thickness distribution in this plane. The next step is to calculate the vorticity distribution to represent the lifting wing. The velocities induced at the wing surface by the store, and also the fuselage if the wing is not a midwing, are treated as an induced camber and are added to any geometric twist and camber.

The flow field in the vicinity of the store is calculated by summing up the velocities induced by the fuselage and the wing. If additional stores are present, their influence on the wing is accounted for as are the velocities induced by their volume distributions in the vicinity of the ejected store.

5.2.2 Single store under fuselage centerline

In calculating the velocity field under the fuselage, the presence of the wing is ignored for the reasons discussed in section 5.1. Thus, the first step is to obtain a source distribution to represent the fuselage volume distribution in the incompressible space. For zero degrees angle of attack, the velocity field induced by this source distribution is the field which the store sees unless other stores are present in which case the fields induced by their volume distributions are additive. Fuselage angle-of-attack effects are treated as a Beskin upwash and given by

$$\frac{w'}{V_\infty} = \sin \alpha'_B \left[1 - \left(\frac{a}{z'} \right)^2 \right] \quad (38)$$

where w' is the velocity normal to the fuselage axis in the incompressible space a distance z' from the axis, a is the local fuselage radius, and α'_B is the fuselage angle of attack in the incompressible space. This velocity field is added to the volume-induced velocity field. Equation (38) is obtained from the complex potential for a circular cylinder in uniform flow given on page 29 of reference 9.

5.2.3 Multiple store under the wing or fuselage

The flow-field calculation for the case of a TER or MER installation is performed in a manner identical to that for the single store with the stores remaining on the rack treated as additional stores in the flow field. It is apparent from the close proximity of the stores on a rack that store-store interference may be important. At the present time, only body-volume effects are accounted for since they are the dominant effects as will be seen. The source distribution for each store is calculated as if the store were in a uniform flow by itself.

5.3 Comparison of Calculated and Experimental Flow Fields

References 1 and 5 contain the results of extensive experimental flow-field surveys. Those presented in reference 5 were taken in the vicinity of the wing-fuselage combination shown in figure 9. The wing-fuselage combination used in reference 1 is shown in figure 2. This model is a 40-percent scale model of that shown in figure 9. Reference 1 presents, in addition to data taken under the wing-fuselage combination, data taken with a pylon present at the 1/3 semispan location, a TER rack attached to the pylon, and, also, with stores mounted on the two shoulder positions of the rack. By building the configuration up component by component, as was done, interference effects can be isolated.

The majority of the data comparisons presented in this section will use the data of reference 5. A few comparisons with the data of reference 1 will be made primarily to show the importance of knowing the flow characteristics of the empty wind tunnel when comparing with wind-tunnel data. Since the primary interference flow-field calculation method does not include a model for the pylon or rack, comparisons with the data with these components present will not be made. A comparison will be made with the perturbation velocities induced by adding the two shoulder stores to the TER rack.

5.3.1 Comparison with data from NACA RM L56J19 (ref. 5)

Reference 5 contains extensive experimental flow-field surveys in the vicinity of a swept-wing fuselage configuration for a Mach number of about 0.15. The experimental wing-fuselage model is that shown in figure 9 with the coordinate system and angle definitions shown in figure 10. The positive directions of the local angles of attack and sidewash are as indicated in figure 10. It is noted that positive sidewash angle corresponds to flow coming in from the left when facing forward on the wing. This

sign convention agrees with that used in the present theory. The sign of the experimental sidewash angles taken from reference 5 has been changed to conform with the present sign convention.

Comparisons are made for a very small angle of attack at locations below the wing and remote from the fuselage to see how the two-dimensional point source model accounts for wing thickness effects. Comparisons under the wing at angle of attack serve principally to assess the vortex-lattice method. Finally, comparisons under the fuselage for both 0° and 6° angle of attack serve to evaluate the methods used to account for the fuselage.

For all experimental data used, estimates of the experimental accuracy are given in reference 5 as $\pm 1.0^\circ$ and $\pm 1.5^\circ$ for local angles of attack and sidewash, respectively. Included in the quoted experimental accuracy are estimates of probe alignment errors and wind-tunnel misalignment angles.

For all computations in this section involving the vortex-lattice model, a 10 chordwise by 12 spanwise array (on one wing panel) was used. All the flow angles were measured under the left wing panel.

The source strength and location distributions that have been obtained for the 65A006 airfoil (see section 4.2.3) have been used in conjunction with the method of extension to swept and tapered wings described in section 4.2.4 to evaluate the flow under the wing at 0° angle of attack for the swept wing configuration illustrated in figure 9. The calculated local angle of attack and sidewash angle results are compared with the data of reference 5 in figure 13 for three distances below the wing. The angles are plotted against axial distance from the local leading edge in percent local chord. The comparisons are at the mid-semispan. This location was chosen in order that the influence of the fuselage which was present for the measurements would be negligible and thus the accuracy of the wing thickness model could be assessed. The small influence of the fuselage is illustrated by including for the $z/c = -0.17$ case of each figure the calculated angle including and excluding the fuselage effects. As can be seen, they are very small.

It should be noted, also, that the measurements were made for a wing (and fuselage) angle of attack of -0.2° . The effect of this angle of

attack on the calculated results, shown for the $z/c = -0.17$ case, is not significant.

From figure 13 it can be seen that the computed and experimental flow parameters are in quite good agreement, with the largest differences tending to occur ahead of and behind the wing. These differences could be caused by any combination of the following things: inaccuracies in the modeling of the three-dimensional wing thickness effects, viscous effects which have been ignored, and wind-tunnel stream angles.

The combined effects of the vortex lattice and wing and fuselage thickness models were examined over a free-stream angle-of-attack range from -4.3° to 12.3° , and comparisons between prediction and experiment, in terms of the local angle of attack and the angle of sidewash versus chordwise distance, are presented in figure 14. These comparisons were made at the mid-semispan, 17 percent of the local chord below the wing and show how the accuracy of the method varies with angle of attack. Similar comparisons at 7, 17, and 27 percent of the local chord below the wing for a free-stream angle of attack of 6.1° are given in figure 15 and exhibit the accuracy as a function of distance from the wing. Finally, comparisons at the quarter, half, and three-quarter semispan locations for 6.1° angle of attack at 17 percent of the local chord below the wing are presented in figure 16. From these comparisons the accuracy as a function of semispan location can be assessed.

Figures 14 to 16 exhibit agreement between theory and experiment which is felt to be adequate for the present investigation. The largest differences tend to occur for the largest angle of attack of 12.3° (figs. 14(b) and 14(c)), the smallest distance below the wing of $z/c = -0.07$ (figs. 15(a) and 15(b)), and the most inboard location of $y/(b/2) = -0.25$ (figs. 16(a) and 16(b)). This behavior is as might be expected since the assumption of linearity becomes less accurate as the angle of attack increases. For instance, 12.3° is beyond the linear portion of the lift curve for the wing-fuselage combination, while there is an assumed linearity in the vortex-lattice model. In addition, the superposition of wing thickness effects and wing angle-of-attack effects is increasingly in error with increasing angle of attack. Some error is developed, also, by excluding fuselage angle-of-attack effects.

Some error arises through the approximate wing thickness model used. In figure 14 this error can be assessed by using the vortex lattice method together with experimental thickness effects to determine the local angle of attack and sidewash angle. These results are shown by the dashed lines of figure 14. These curves have been obtained by adding the difference between the experimental data and the calculation for $\alpha_w = -0.2^\circ$, where the flow angles are due principally to wing thickness, to the calculations made for the other angles of attack. As can be seen, the resulting curves agree better, in general, with the experimental data than the purely theoretical solid curve. This agreement can be taken as a measure of the accuracy of the vortex-lattice method.

Comparison of calculated and experimental local angle of attack at various distances under the fuselage axis for near zero degrees (-0.2°) and 6.1° free-stream angles of attack are presented in figure 17. As was discussed in section 5.1, the flow perturbations due to the wing thickness and the vortex lattice are not included. The computations for -0.2° angle of attack are based on fuselage thickness alone; that is, the small effect of the -0.2° angle of attack has been ignored. The fuselage angle-of-attack effects for the case of 6.1° angle of attack were calculated using equation (38). This velocity is added to the fuselage thickness velocity to obtain the local angle of attack.

From figure 17(a), a reasonable agreement between the calculated and experimental results can be seen for the case of -0.2° angle of attack. In the region adjacent to the cylindrical portion of the fuselage, a fluctuation in the computed values of about 0.2° amplitude occurs for the case $z/a_{\max} = -1.16$. The quantity a_{\max} is the maximum fuselage radius. The amplitude is reduced for $z/a_{\max} = -1.55$ to less than 0.1° , and is imperceptible for $z/a_{\max} = -2.21$. The origin of this variation is, of course, the fuselage thickness model. The magnitudes of the point sources representing the fuselage thickness are such that the calculated body shape has a slight "ripple" in the cylindrical section (which is imperceptible at the scale of the $\psi^* = 0$ sketch given in figure 4(a)), and the adjacent velocity field of course has a corresponding ripple which diminishes with distance from the fuselage. The field points at $z/a_{\max} = -1.16$ are 16 percent of the fuselage radius from its surface in the cylindrical portion, and a small fluctuation is therefore not surprising. While the amplitude of the present variation is only 0.2° ,

this case does indicate the desirability of an accurate fuselage representation when stores in the immediate vicinity of the fuselage are under consideration. On the basis of the source distributions that have been obtained for axisymmetric bodies with cylindrical sections, fluctuations in the cylindrical region appear to be characteristic, and the best procedure is to minimize their magnitude by increasing the number and varying the locations of the sources.

Considering still the case of -0.2° angle of attack, figure 17(a), the data lie slightly above the computed values in the region behind the wing, $x/c > 1.0$. This is due to small deviations between the analytic representation of the fuselage shape and its actual shape in this region. Both the data and calculated values will commence to rise in this region since the fuselage radius beginning at $x/c = 1.5$ decreases with increasing x/c . It is indicated on figure 4(a) that the $\psi^* = 0$ surface contracts more gradually than the actual surface, and the calculated angle of attack will be low as a consequence.

For the 6.1° angle-of-attack case (fig. 17(b)), the agreement is about as good as that at -0.2° except at the most remote distance of $z/a_{\max} = -2.21$.

5.3.2 Comparison with data from NEAR TR 24 (ref. 1)

Figure 18 presents a comparison between the calculated flow field and the measured flow field using data from Volume IV of reference 1. The wing-fuselage model used in the tests is shown in figure 2 and the data presented in figure 18 were taken under the left wing panel at the 1/3 semispan location 30 percent of the local wing chord or 2.12 inches below the wing. No pylon was present on the wing. The Mach number is 0.25.

The region of the survey can be seen more clearly by examining figure 3(a). The purpose of the survey was to measure the velocity field in the region the axis of the store shown in figure 3(a) would occupy if it were inserted one store diameter, 0.75 inch, below the location shown in the figure. The data in figure 18 are plotted against $(x/l)_s$ where l_s is the length of the store shown in figure 3 and x_s is measured from the position the store nose would occupy if it were present. The directions of the positive velocities are shown in figure 10.

Data are presented in figure 18 for two angles of attack, α_p , of the wing-fuselage combination. This angle, α_p , is the angle between the fuselage axis and the wind-tunnel longitudinal axis. Figure 18(a) is for $\alpha_p = 0^\circ$ and figure 18(b) is for $\alpha_p = 6^\circ$. Two theoretical curves are shown on the figure. One assumes an angle of attack equal to α_p and the other assumes an angle of attack different from α_p . This second case takes into account the wind-tunnel stream angles indicated by the tunnel-empty survey made and reported in Volume IV of reference 1. These data were analyzed in Volume I of reference 1 and it was found that for $\alpha_p = 0^\circ$ a tunnel-empty upwash angle of 1.25° existed in the portion of the tunnel where the survey of figure 18(a) was taken. Likewise, a tunnel-empty upwash angle of 0.75° was indicated for $\alpha_p = 6^\circ$ (fig. 18(b)). The difference in the tunnel-empty upwash angle for the two values of α_p is due to the fact that as α_p is changed testing is done in a different part of the tunnel test section. Since tunnel-empty surveys were only taken at the one spanwise location, a uniform correction was made to the wing angle of attack used in the vortex-lattice calculation rather than using a wing twist distribution due to stream angle of the wind tunnel.

Figure 18(a) for $\alpha_p = 0^\circ$ indicates that better overall agreement with the experimental data is obtained when the tunnel-empty stream angle is accounted for, particularly in the region below the wing leading edge, $(x/l)_s = 0.05$. This same conclusion cannot necessarily be drawn from figure 18(b) for $\alpha_p = 6^\circ$. In some regions the agreement is improved and in others it is made worse. On the basis of these comparisons, it is felt that to make precise comparisons with experimental flow-field data a knowledge of the angle of attack which the wing actually sees in the wind tunnel is required. The spanwise variation should also be taken into account by imposing a twist distribution on the wing in the vortex lattice calculation. In the tests reported in Volume IV of reference 1, tunnel-empty tests were not performed anywhere but at the 1/3 semispan location nor were they performed in the region the wing chord plane would occupy if it were in the tunnel. If these data had been taken and used in the theoretical calculations, the overall agreement may have been improved. The agreement exhibited in figure 18 is still quite good for the upwash, W/V_∞ , and sidewash, V/V_∞ , velocities; it is of the order of ± 0.01 . In terms of local flow angle, this is $\pm 0.58^\circ$.

Figure 19 presents a comparison between experiment and theory for the same conditions as those of figure 18 except that the Mach number is 0.70. Figure 19(a) is for $\alpha_p = 0^\circ$ and figure 19(b) is for $\alpha_p = 6^\circ$. In the theoretical calculations, the tunnel-empty stream angles as given in Volume I of reference 1 for these test conditions have been included in the wing angle of attack. The overall agreement between experiment and theory is not quite as good as exhibited in figure 18 for a Mach number of 0.25. In this case, the velocity ratios are predicted within ± 0.02 or in terms of local flow angle, $\pm 1.2^\circ$. This difference may be caused by not knowing what free-stream flow the wing actually saw or by inaccuracies in the method used to account for compressibility effects.

Since the primary interference flow-field calculation method does not incorporate models for a pylon and a rack, comparisons with flow-field data taken with these components present will not be made. Their presence will be accounted for by slender-body theory. The method does, however, include models for other stores present in the flow field as in the case of a TER or MER rack. Consider the TER grouping shown in figure 20 which was tested in reference 1. The pylon and TER rack are not shown in the figure, although they were present during the tests. The wing-fuselage combination is shown in figure 2 and the store geometry in figure 3(b). By subtracting the data obtained without stores 2 and 3 present on the TER rack from the data obtained with these two stores present, the velocity increments due to the addition of the two stores can be determined. These increments have been determined for one axial survey at two angles of attack and the data are plotted in figure 21. The survey was conducted in the region the axis of store 1 in figure 20 would occupy if it was one diameter below the location shown in the figure, that is, -2.83 inches below the wing chord plane. The velocities are plotted in figure 21 against $(x/l)_s$ where l_s is the length of the store shown in figure 20 and x_s is measured from the position the nose would occupy if it was present.

Also shown in figure 21 are the results of theoretical calculations. These curves were obtained by subtracting the velocity field calculated under the wing-fuselage combination from that calculated under the wing-fuselage with stores 2 and 3 present including wing camber induced by these stores. By doing this, perturbation velocities associated with wing angle of attack and fuselage volume are subtracted out and only perturbation velocities associated with the volumes of stores 2 and 3 and wing camber

induced by these stores remain. Since these are not functions of angle of attack, the theoretical curves for both figures 21(a) and 21(b) are the same. A comparison of the data plotted in the two parts of the figure also indicates little effect of angle of attack. The agreement between experiment and theory is quite good. The theoretical lateral velocity increment, $\Delta V/V_\infty$, is zero, as is borne out by the data, since stores 2 and 3 induce equal and opposite lateral velocities. In addition, because of the large distance from the wing, the vorticity distribution in the wing which cancels the small amount of store-induced camber contributes nothing.

6. PRIMARY INTERFERENCE FORCE AND MOMENT

The calculation of the trajectory of a store being ejected from an aircraft requires the determination of the forces and moments acting on the store at any point in its trajectory. To calculate these forces and moments accurately, the nonuniform nature of the flow field must be accounted for. In the previous sections of this report, mathematical models have been presented for the various components of the aircraft which allow the calculation of the perturbation velocities induced at any point in the flow field by these components. The effect of these velocities in changing the forces and moments acting on the store are the known dominant effects and will be termed primary interference. The term additional interference will be used to identify the additional change due to mutual interference between the wing, pylon, and store. This section of the report will describe the calculation of the primary interference force and moment. Additional interference will be discussed in section 7. Generally, it is the aim to put the dominant interference effects into primary interference so that the additional interference can be neglected.

By summing up the perturbation velocities due to the aircraft components and adding them to the free-stream velocity, the total velocities at any point in the field where the store will be located can be calculated. By performing this calculation for various points over the length of the store, the complete nonuniform flow field can be calculated. Pitch, yaw, and roll damping can be easily accounted for by adding the angular velocities of the store to the calculated flow field. From the resulting nonuniform velocity field, the load distribution on the store can be calculated, and the forces and moments can then be obtained by integrating over the store length.

This section of the report describes the methods used to calculate the forces and moments from the known velocity field. Store forces and moments due to buoyancy, slender-body theory (potential flow), and viscous crossflow are determined as well as the force and moment due to the store empennage if present. The empennage is restricted to triform or cruciform tail arrangements. The forces and moments thus do not depend on the roll attitude of the store provided that vortex separation is not present. This restriction is not made of necessity, but because it includes nearly all of the cases of interest. The damping due to the pitching motion of the store is accounted for by adding to the velocity field increments due to pitching rate. The velocity field at any point on the store is, thus, that seen from the store.

Figure 22 shows the x_s, y_s, z_s coordinate system fixed in the store with the origin at the store nose. The velocities $U_s, V_s,$ and W_s are positive in the x_s, y_s, z_s directions. The store velocity relative to the atmosphere is V_{∞_s} and the store angle of attack is α_s . The velocity components, U_s, V_s, W_s are calculated at points which would be on the store surface or axis if the store were present. They are

$$\left. \begin{aligned} U_s &= V_{\infty_s} \cos \alpha_s + u_{vl} + u_{th} \\ V_s &= v_{vl} + v_{th} \\ W_s &= V_{\infty_s} \sin \alpha_s + w_{vl} + w_{th} + \dot{\theta}(x_s - x_{s,cg}) \end{aligned} \right\} \quad (39)$$

The quantities $V_{\infty_s} \cos \alpha_s$ and $V_{\infty_s} \sin \alpha_s$ are free-stream components. The terms with subscript vl are velocities induced at the point by the vorticity distribution representing the wing. Those with the subscript th are the sum of the velocities induced by the thickness distributions of the wing, fuselage, and any other stores present on the aircraft. The term $\dot{\theta}(x_s - x_{s,cg})$ in the expression for W_s accounts for the pitching motion of the store. For points off the body axis, a $\dot{\theta}$ term should appear in the expression for U_s . This term, being very small, has been neglected in the present work. Yawing motion can be accounted for by adding a similar term to V_s . The velocities of equation (39) are made dimensionless by V to obtain

$$\left. \begin{aligned}
 U_s^* &= \frac{U_s}{V_{\infty s}} = \cos \alpha_s + u_{vl}^* + u_{th}^* \\
 V_s^* &= \frac{V_s}{V_{\infty s}} = v_{vl}^* + v_{th}^* \\
 W_s^* &= \frac{W_s}{V_{\infty s}} = \sin \alpha_s + w_{vl}^* + w_{th}^* + \frac{\dot{\theta}(x_s - x_{s,cg})}{V_{\infty s}}
 \end{aligned} \right\} \quad (40)$$

It is noted that $\dot{\theta}$ is positive for nose-up motion. These expressions, along with the work of the preceding sections of this report, allow the velocity field at any point which would lie on the store surface or axis, if the store were present, to be calculated. The pitching rate of the store, $\dot{\theta}$, is determined as a function of time during the integration of the equations of motion.

The calculation of the forces and moments on an external store in a nonuniform flow field is basically a difficult problem which can be significantly simplified by the assumption of slenderness valid for all sections of the store except the fins (or blunt noses). The method used herein is similar to that of McKinney and Polhamus (ref. 10). For the purpose of understanding the method used herein, consider the variation of downwash and sidewash angles along the centerline of a store. Let the store be cambered in both the vertical and lateral directions so that its axis now conforms to a streamline of the flow with its downwash and sidewash components. Any lift or side force due to the downwash or sidewash velocities will be eliminated in this fashion, and the pressure field acting on the body will be, to the first order, the sum of its own thickness pressure distribution plus the static pressure field acting in the nonuniform flow. The resultant forces (excluding drag) and moments of the doubly-cambered body will be due solely to the static pressure field of the nonuniform flow. These components of the total forces and moments are thus due to buoyancy.

The assumption concerning the camber of the store can now be relaxed, and downwash and sidewash velocities can be considered to act over the length of the axisymmetric store. It is an easy matter using slender-

body theory and apparent-mass methods to evaluate the normal- and side-force distributions on the store together with their resulting moments. For stores subject to a large value of the combined angle resulting from downwash and sidewash, separation of the body boundary layer may occur. Beyond this point, slender-body theory is not continued. In the present calculative method, we have assumed that simple viscous crossflow theory is applicable downstream of the separation location.

6.1 Buoyancy Force and Moment

The equations for the buoyancy normal force and pitching moment will now be derived for compressible flow. If the pressure coefficient is defined as

$$C_p = \frac{p - p_{\infty s}}{q_{\infty s}} \quad (41)$$

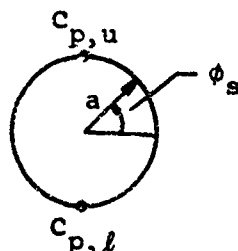
then it can be expressed in terms of Mach number and velocity for subsonic compressible flow as (see for example ref. 11, page 30, eq. (3.33)),

$$C_p = [1 - (U_s^{*2} + V_s^{*2} + W_s^{*2})] \left\{ 1 + \frac{M_{\infty s}^2}{4} [1 - (U_s^{*2} + V_s^{*2} + W_s^{*2})] + \dots \right\} \quad (42)$$

Only the first Mach number term is shown since successive terms are much smaller. Since in the present work $M_{\infty s}$ is less than 1.0 and the perturbation velocities in equation (40) are small compared to the free-stream velocity, this first Mach number term is much less than one. Consequently, in the present work it has been ignored and the following incompressible expression used for the pressure coefficient

$$C_p = 1 - (U_s^{*2} + V_s^{*2} + W_s^{*2}) \quad (43)$$

Consider the following sketch



which is the cross section of the store at any x_s . The quantity $C_{p,u}$ is the pressure coefficient at the location of the upper surface of the store ($\phi_s = \pi/2$) and $C_{p,l}$ is the pressure coefficient at the location of the lower surface ($\phi_s = -\pi/2$) of the store. Let the assumption be made that the vertical pressure gradient is linear and that there is no lateral gradient. Thus, as a function of ϕ_s

$$\Delta C_p = (C_{p,l} - C_{p,u}) \sin \phi_s \quad (44)$$

and the buoyancy normal-force coefficient acting on an element of surface area is

$$d(C_N)_{BY} = d\left(\frac{N_{BY}}{\frac{1}{2} \rho_\infty V_\infty^2 S_R}\right) = \frac{\Delta C_p \sin \phi_s a d\phi_s dx_s}{S_p} \quad (45)$$

From equations (44) and (45)

$$\begin{aligned} \frac{d(C_N)_{BY}}{dx_s} &= \frac{a(C_{p,l} - C_{p,u})}{S_R} 2 \int_0^{\pi/2} \sin^2 \phi_s d\phi_s \\ &= \frac{a}{2} \frac{a(C_{p,l} - C_{p,u})}{S_R} \end{aligned} \quad (46)$$

and finally

$$(C_N)_{BY} = \frac{\pi}{2S_R} \int_0^{l_s} (C_{p,l} - C_{p,u}) a dx_s \quad (47)$$

In a similar manner the pitching-moment coefficient due to buoyancy is found to be

$$(C_m)_{BY} = \frac{\pi}{2S_R \ell_R} \int_0^{\ell_s} (x_{s,cg} - x_s) (C_{p,l} - C_{p,u}) a \, dx_s \quad (48)$$

These two integrals are to be evaluated numerically using calculated values of $C_{p,l}$ and $C_{p,u}$ as a function of x_s .

6.2 Angle of Attack Force and Moment

Let us now derive the normal force and pitching moment due to angle of attack. To do this, use will be made of the method presented in reference 12. In that work it was found that for axisymmetric bodies in uniform flow the gross normal force and pitching moment could be calculated quite accurately for a wide range of shapes by assuming that potential flow applies over the forward portion of the body up to a location where viscous forces become important. This location did not change with angle of attack and is correlated in reference 12 as a function of the position of the maximum negative rate of change of cross sectional area. This correlation is for a body in uniform flow. No correlation of this type for axisymmetric bodies in nonuniform flow is known.

Using the method of reference 12 but accounting for the nonuniform flow field, the normal force and pitching moment are made up of two terms, the first calculated by slender-body theory, or potential flow, and the second calculated by viscous crossflow theory. Slender-body theory is assumed to apply over the forward portion of the body to some point, $x_{s,0}$, where the viscous forces are important. From this point to the end of the body, the force and moment are calculated by viscous crossflow theory. Thus, the normal force due to angle of attack $C_{N,\alpha}$ is

$$C_{N,\alpha} = \int_0^{x_{s,0}} \frac{d(C_N)_{SB}}{dx_s} dx_s + \int_{x_{s,0}}^{\ell_s} \frac{d(C_N)_{CF}}{dx_s} dx_s \quad (49)$$

$$= (C_N)_{SB} + (C_N)_{CF} \quad (50)$$

A similar expression can be written for the pitching moment. The expressions for the force and moment will now be derived.

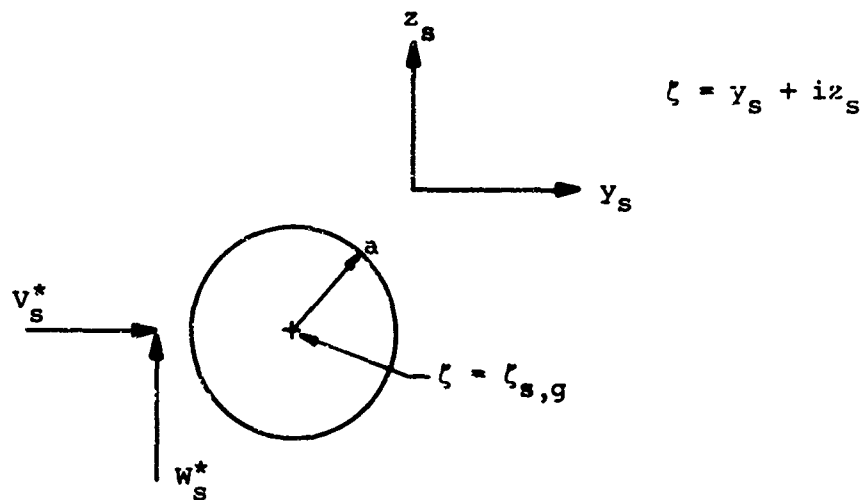
6.2.1 Slender-body force and moment

It is not difficult to determine the forces and moments on a slender body in a nonuniform flow field using slender-body theory. We have determined the buoyancy contributions for the case wherein the body is cambered to conform to the streamlines of the nonuniform flow field. The flow field can now be made uniform retaining the cambered body, and the forces and moments associated with apparent-mass effects can be calculated. Let us consider the shape of the cambered body.

The local angle of attack in the vertical plane is W_s^* , and the local sidewash angle is V_s^* within the small-angle assumption. Let x_s be the distance to a point on the body axis and let $\zeta_{s,g} = y_{s,g} + iz_{s,g}$ be the location of the body axis at distance x_s . Then we have

$$\zeta_{s,g} = -i \int_0^{x_s} W_s^*(x_s) dx_s - \int_0^{x_s} V_s^*(x_s) dx_s \quad (51)$$

The flow pattern is then as depicted in the following sketch.



The complex potential can be written for the flow following the results of reference 9, page 29

$$W(\zeta) = -iW_s \left[(\zeta - \zeta_{s,g}) - \frac{a^2}{(\zeta - \zeta_{s,g})} \right] + V_s \left[(\zeta - \zeta_{s,g}) + \frac{a^2}{(\zeta - \zeta_{s,g})} \right] + aV_\infty \frac{da}{dx_s} \log (\zeta - \zeta_{s,g}) \quad (52)$$

The complex force $Y + iN$ can be very simply determined from the foregoing complex potential by use of the following result from reference 9, page 50. (The development in reference 9 assumes a unit free-stream velocity, V_∞ . Hence, the $1/V_\infty$ factor in the first term of the following equation.)

$$\frac{Y + iN}{q_\infty} = 4\pi \frac{a_1}{V_\infty} + -S'(x_s) \zeta_{s,g}'(x_s) + 2S(x_s) \zeta_{s,g}''(x_s) \quad (53)$$

wherein

$$S(x_s) = \pi a^2 \quad (54)$$

and a_1 is the coefficient of the ζ^{-1} term (simple pole) in the Laurent expansion of the complex potential.

It is easy to show that

$$a_1 = iW_s a^2 + a^2 V_s - a \frac{da}{dx_s} V_\infty \zeta_{s,g} \quad (55)$$

$$S' = 2a \frac{da}{dx_s} \quad (56)$$

$$\zeta_{s,g}' = -(V_s^* + iW_s^*) \quad (57)$$

With these relationships equation (53) yields

$$\frac{Y + iN}{q_\infty} = 2ia^2 W_s^* + 2a^2 V_s^* \quad (58)$$

so that

$$(C_N)_{SB} = \frac{N}{q_\infty S_R} = \frac{2a^2}{S_R} a^2 W_s^* \quad (59)$$

$$(C_Y)_{SB} = \frac{Y}{q_\infty S_R} = \frac{2\pi}{S_R} a^2 v_s^* \quad (60)$$

In simple terms, the normal force up to axial distance x_s depends only on the body radius and local angle of attack at that station with a similar result for side force. The values of the foregoing quantities for the store can therefore be determined easily by evaluating equations (59) and (60) at the separation location. It is of interest that no coupling exists between normal force and side force. The pitching-moment coefficient and yawing-moment coefficient associated with the slender-body theory require a knowledge of the distribution of normal force and side force along the external store and require an integration along the body for their determination.

$$\begin{aligned} (C_m)_{SB} &= \frac{1}{l_R} \int_0^{x_{s,o}} \frac{d(C_N)_{SB}}{dx_s} (x_{s,cg} - x_s) dx_s \\ &= \frac{2\pi}{S_R l_R} \int_0^{x_{s,o}} (x_{s,cg} - x_s) \frac{d(a^2 W_s^*)}{dx_s} dx_s \end{aligned} \quad (61)$$

Similarly for yawing moment, we have

$$(C_n)_{SB} = \frac{2\pi}{S_R l_R} \int_0^{x_{s,o}} (x_{s,cg} - x_s) \frac{d(a^2 v_s^*)}{dx_s} dx_s \quad (62)$$

The integrations in equations (61) and (62) will normally be taken from the store nose to the separation location, $x_{s,o}$.

It is noted that a positive normal-force increment in front of the store center of gravity causes a nose-up pitching moment, and a positive side force in front of the center of gravity causes a nose-right yawing moment. The directions of these moments correspond to their positive directions.

A further point of interest is worth noting. It would have been possible to consider that the flow in planes perpendicular to the axis

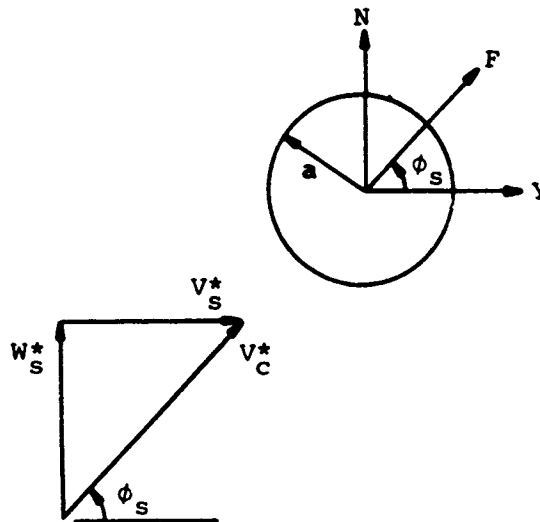
of the store obeys Laplace's equation, and that the upwash and sidewash velocities vary along the store length. If the potential is constructed on this basis and the body pressure coefficients determined from the unsteady Bernoulli equation, integration of the body pressures to obtain the forces yield both the slender-body results just obtained plus the buoyancy results. In this case the buoyancy force is given by

$$(C_N)_{BY} = \frac{2\pi}{S_R} \int_0^{l_s} a^2 \frac{dW_s^*}{dx_s} dx_s \quad (63)$$

Equation (47) has been used in the buoyancy calculation rather than equation (63).

6.2.2 Viscous crossflow force and moment

Let us now derive the crossflow normal-force and pitching-moment coefficients. It should be pointed out that for nonuniform flow fields this method is untried. For the present application it may have to be modified when data become available to check the method.



Referring to the sketch, we have from crossflow theory (ref. 9, p. 85) that

$$\frac{dF_{CF}}{dx_s} = \frac{1}{2} \rho_\infty V_\infty^2 V_c^{*2} c_{d_c} \quad (64)$$

where c_{d_c} is the section-drag coefficient of a cylinder normal to the free stream. That is,

$$c_{d_c} = \frac{\text{drag per unit length}}{q_\infty (2a)}$$

so that in coefficient form

$$\begin{aligned} \frac{d(C_N)_{CF}}{dx_s} &= \frac{1}{\frac{1}{2} \rho_\infty V_\infty^2 S_R} \frac{dF_{CF}}{dx_s} \sin \phi_s \\ &= \frac{c_{d_c}}{S_R} 2aV_c^*W_s^* \end{aligned}$$

Thus, integrating from the separation location to the end of the store

$$(C_N)_{CF} = \frac{2c_{d_c}}{S_R} \int_{x_{s,0}}^{l_s} aV_c^*W_s^* dx_s \quad (65)$$

and similarly

$$(C_m)_{CF} = \frac{2c_{d_c}}{S_R l_R} \int_{x_{s,0}}^{l_s} (x_{s,cg} - x_s) aV_c^*W_s^* dx_s \quad (66)$$

In the present work c_{d_c} has been taken equal to 1.2.

6.3 Empennage Force and Moment

The remaining forces and moments acting on the store are those produced by the empennage. The components of these quantities due to angle of attack and damping are not calculated separately. As was done for the body damping, the pitching rate of the store is added to the velocity field and the total forces and moments calculated. The velocities at the x_s location of the store empennage centroid are calculated using equation (40). The combined angle of attack, the angle between the store's longitudinal axis and the local velocity vector, at the empennage centroid is

$$\alpha_c = \tan^{-1} \left(\frac{\sqrt{V_s^{*2} + W_s^{*2}}}{U_s^*} \right)_E \quad (67)$$

The slender-body theory normal force is

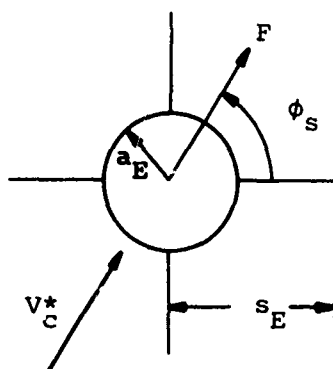
$$(C_N)_E = (K_E + K_B) \left(\frac{\partial C_N}{\partial \alpha} \right)_T \alpha_c \sin \phi_s \quad (68)$$

where K_E and K_B are interference lift ratios. The quantity K_E is the ratio of normal force developed on the tail panels in the presence of the body to that developed by the tail alone. The quantity K_B is an analogous ratio to specify the normal force developed by the body in the presence of the tail panels. These ratios from reference 9, pages 119 and 120, are given by

$$K_E = \frac{1}{\pi(\lambda - 1)^2} \left[\frac{\pi}{2} \left(\frac{\lambda^2 - 1}{\lambda} \right)^2 + \left(\frac{\lambda^2 + 1}{\lambda} \right)^2 \sin^{-1} \left(\frac{\lambda^2 - 1}{\lambda^2 + 1} \right) - 2 \frac{(\lambda^2 - 1)}{\lambda} \right] \quad (69)$$

$$K_B = \left(1 + \frac{1}{\lambda} \right)^2 - K_E \quad (70)$$

where $\lambda = s_E/a_E$. The quantity s_E is the empennage semispan and a_E is the body radius at the x_s location of the empennage centroid. The quantity $(\partial C_N/\partial \alpha)_T$ is the lift curve slope of the tail alone and is to be specified. The tail alone is two tail panels joined together without the intervening body. The angle ϕ_s is shown in the following sketch.



Equation (68) can be written

$$(C_N)_E = (K_E + K_B) \frac{W_S^*}{V_C^*} \left(\frac{dC_N}{d\alpha} \right)_T \alpha_c \quad (71)$$

The pitching moment due to the empennage is

$$(C_m)_E = \frac{(x_{s,cg} - x_{t, cen})}{l_R} (C_N)_E \quad (72)$$

In the above expressions

$$\frac{d}{d\alpha} (C_N)_T = \frac{d}{d\alpha} \left(\frac{N_T}{\frac{1}{2} \rho_\infty V_\infty^2 S_R} \right) \quad (73)$$

7. ADDITIONAL INTERFERENCE FORCE AND MOMENT

In section 6, primary interference forces and moments on a store under an aircraft have been calculated from slender-body theory using the calculated downwash and sidewash of the wing-body combination at the store axis. The interference effect of the store source distribution on the wing was accounted for in the attached condition and was not changed thereafter during the trajectory. The effect of the wing on the store was thus accounted for as in the first step of an iterative procedure. There is additional interference due to the presence of the pylon and due to the velocities induced at the wing by the store flow fields associated with downwash and sidewash. There is presently no simple method for determining the additional interference loading. Accordingly, a numerical method is developed herein for determining the additional interference effects, which are directly additive to the effects already calculated. Only the case of a single store under the wing is considered, although the techniques employed can be used to treat other cases. The additional interference is expected to be small so that slender-body theory should be sufficiently accurate for its determination.

The methods available for solving the additional interference problem include conformal mapping techniques and numerical vortex methods. It is probable that with a considerable analytical effort, some exact solutions

can be obtained using conformal mapping and slender-body theory. However, we have chosen to use numerical vortex methods because of their compatibility with the computer program of the previous sections, the simpler analysis required, and the possibility of applying them more easily to a wide range of interference problems.

The basic approach to the present interference problem is to consider first the nonuniform flow field which exists near an airplane at the store location with the store absent. If we now imagine the store to appear, its flow field induces velocities normal to the pylon and the wing which can be cancelled by bound vortices in all components. The forces on the store due to the bound vortices represent the additional interference effect. Since we have computed the forces on the store alone in the nonuniform flow field using slender-body theory, it is consistent to use slender-body theory to determine the interference effects. This approach allows solution of the interference problem without iteration. The flow is solved in crossflow planes normal to the store axis, and as many planes can be used as necessary to determine the store load distribution accurately. As opposed to a three-dimensional approach which tries to account for all such crossflow planes simultaneously, the present approach has the distinct advantages of less computing time and less computer storage.

In the theory to be developed in this section, both primary and additional interference terms are included so that the theory is complete. The present approach is applicable to a finless store in its entirety or to a finned store up to the beginning of the empennage. The empennage is to be handled as described in section 6.3. In case flow separation occurs on the store, there is the possibility in the present method of including the resulting shed vortices in the calculation as free vortices which induce additional interference forces on the store. The only question is with respect to the strength and position of the store vortices. In the present analysis, only normal force distributions are determined, although side-force distributions can easily be obtained from the method.

Not all of the mathematical details of the derivation will be included. They are contained in reference 13.

7.1 Axes and Conventions

In the analysis several different axis systems will be used. First consider a plane fixed in the stationary fluid normal to the velocity of the store as it passes through the plane (fig. 23). The cross section of the store in the plane at any time t is an ellipse, the center of which is the origin of the x, y, z coordinates. The x coordinate is aligned with the velocity, V_∞ , and the axes y, z lie in a plane normal to x . Let the store nose pierce the plane at $t = 0$ at the origin of the axes $\bar{x}_0, \bar{y}_0, \bar{z}_0$, which are fixed to the plane and coincide with the positions of x, y, z at $t = 0$. The $\bar{x}, \bar{y}, \bar{z}$ axes are attached to the nose of the store with \bar{x} aligned in the V_∞ direction and \bar{y} and \bar{z} being parallel to \bar{y}_0 and \bar{z}_0 .

Another set of axes used in the analysis is a set of axes x_s, y_s, z_s which are symmetry axes of the store. These axes are obtained by pitching the system about \bar{y} by an angle α , and then yawing the system about the new vertical axis by $-\beta$ as described in reference 9, page 4. The cross section of the store as seen in the y_s-z_s plane is a true circle for a body of revolution.

It is noted that the store cross section in the fixed plane has a vertical downward speed $+W$, and a lateral speed V to the left given by (for small angles)

$$W = \alpha V_\infty$$

$$V = -\beta V_\infty$$

The sign conventions of α and β are such that the store shown in figure 23 is at positive angle of attack and negative angle of sideslip.

Let the velocity components in the $\bar{x}, \bar{y}, \bar{z}$ system be $\bar{U}, \bar{V}, \bar{W}$ with corresponding perturbation components $\bar{u}, \bar{v},$ and \bar{w} . Let $u, v,$ and w be the perturbation velocity components in the x_s, y_s, z_s system. If the pressure coefficient is defined as

$$C_P = \frac{P - P_\infty}{q_\infty} \quad (74)$$

then the pressure coefficient on the basis of slender-body theory is

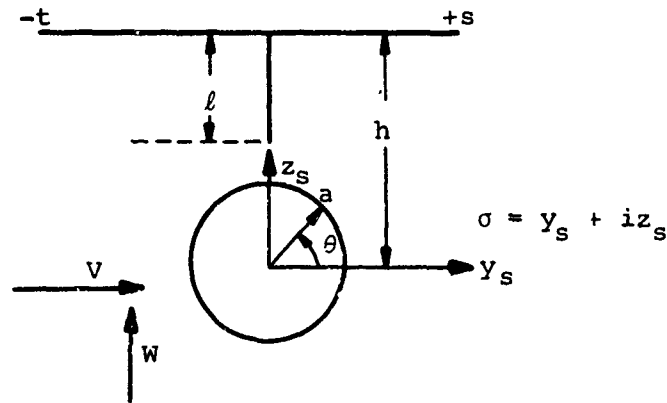
$$C_p = -2 \left(\frac{\bar{u}}{V_\infty} \right) - \left(\frac{\bar{v}^2}{V_\infty^2} + \frac{\bar{w}^2}{V_\infty^2} \right) \quad (75)$$

or in the x_s, y_s, z_s system

$$C_p = -2 \frac{(u - \beta v + \alpha w)}{V_\infty} - \frac{(v^2 + w^2)}{V_\infty^2} \quad (76)$$

7.2 Formulation of the Interference Problem

Consider a wing-body configuration which may have a single pylon-mounted store beneath a wing panel. Take a cross section through the store normal to its axis of rotation shortly after drop. The cross section will have the following appearance.



For the short pylons on which such stores are mounted, we will neglect sweep of the pylon leading and trailing edges so that we are dealing principally with cross sections of the type depicted above. The portions of the wing panel extending to the left and right of the store will generally be of unequal span. The velocities V and W are related to the local angle of attack and sideslip of the store in the crossflow plane in question. These angles of attack and sideslip are due in part to the downwash and sidewash induced at the store by the wing-body combination (without the pylon and store present) and to the angles of pitch and yaw

of the store itself. These latter angles are due to the store dynamical motion or to its orientation on the pylon in the attached position.

In section 6 of the present study, the lift and moment on the store were determined by placing the store in the wing-body flow field and calculating its reaction by slender-body theory. The empennage was handled by linear theory. The store thickness effect was represented by a distribution of three-dimensional point sources on its axis, and the effects of V and W were handled by slender-body theory. Most of the effects of the wing on the store are properly accounted for in this manner. However, neither pylon interference nor the interference on the wing due to the store flow fields associated with V and W are accounted for. In this section we will account for these additional components of the total interference field in a way which avoids iteration. Also in the analysis we will include store source effects in a way which will permit accounting for them as a function of distance from the wing without redoing the entire wing loading calculation at each step.

The basic flow around the store is due to the nonuniformity associated with the distributions of V and W along the store and the sources associated with changing body cross section. To fix ideas, let us write down the complex potential for this flow field in terms of the complex variable σ . The complex potential for the perturbation velocities v and w is

$$W_s(\sigma) = i \frac{Wa^2}{\sigma} + \frac{Va^2}{\sigma} + aV_\infty \left(\frac{da}{dx_s} \right) \log \sigma \quad (77)$$

The perturbation velocities in the y_s - z_s plane due to this flow are

$$v_s - iw_s = \frac{dW_s}{d\sigma} = -i \frac{Wa^2}{\sigma^2} - \frac{Va^2}{\sigma^2} + aV_\infty \left(\frac{da}{dx_s} \right) \frac{1}{\sigma} \quad (78)$$

These are thus components of the store velocity field associated with V , W , and da/dx_s which produce velocities normal to wing and pylon.

Because of the normal velocities, a distribution of bound vorticity is produced in the wing and pylon which just overcomes the velocity components of equation (78). At the same time an image vortex system is introduced inside the store to maintain its cross sectional shape unchanged.

Consider only one vortex external to the body at point σ_i . It requires an image vortex of opposite sense at a point internal to the circle, $a^2/\bar{\sigma}_i$. In addition, an image vortex of the same sign is placed at the center of the circle to keep the circulation at infinity unchanged. As a result the complex potential for N external vortices is

$$W_{\Gamma}(\sigma) = \frac{i}{2\pi} \sum_{i=1}^N \Gamma_i \left[\log(\sigma - \sigma_i) - \log\left(\sigma - \frac{a^2}{\bar{\sigma}_i}\right) + \log \sigma \right] \quad (79)$$

The Γ_i vortices are placed over the wing and pylon in such a way as to counteract the velocities as obtained from equation (78) at certain control points.

On the wing and pylon equation (78) yields the following perturbation velocities due to the store. On the wing $\sigma = y_s + ih$ so that

$$w_w(s) = \frac{a^2 W(y_s^2 - h^2)}{(h^2 + y_s^2)^2} - \frac{2a^2 v_h y_s}{(h^2 + y_s^2)^2} + \frac{a v_{\infty} h \frac{da}{dx_s}}{(h^2 + y_s^2)} \quad (80)$$

On the pylon $\sigma = iz_s$ so that

$$v_p(s) = \frac{Va^2}{z_s^2} \quad (81)$$

These velocity distributions on the wing and pylon are to be cancelled by the vortices associated with $W_{\Gamma}(\sigma)$.

7.3 Store Normal-Force Distribution

To obtain the force on the store, we determine the pressure coefficient through the use of equations (75) and (76) and integrate the component of the surface pressure force over the surface of the store. It is convenient to consider various components in the pressure distribution. Let u_s , v_s , and w_s be the perturbation components due to the store and u_{Γ} , v_{Γ} , and w_{Γ} be those due to the N external vortices,

$$u_{\Gamma} = \sum_{i=1}^N u_i ; \quad v_{\Gamma} = \sum_{i=1}^N v_i ; \quad w_{\Gamma} = \sum_{i=1}^N w_i \quad (82)$$

From reference 9, page 48,

$$\left(\frac{\bar{v}}{V_\infty}\right)^2 + \left(\frac{\bar{w}}{V_\infty}\right)^2 = \left(\frac{v}{V_\infty}\right)^2 + \left(\frac{w}{V_\infty}\right)^2 \quad (83)$$

so that the pressure coefficient (eqs. (75) and (76)) can be written in a mixed system as

$$\begin{aligned} c_p = & -2 \frac{\bar{u}_s}{V_\infty} \cdot \frac{v_s^2 + w_s^2}{V_\infty^2} - 2 \sum_{i=1}^N \left(\frac{u_i}{V_\infty}\right) \\ & + 2 \sum_{i=1}^N \left(\frac{\beta v_i - \alpha w_i}{V_\infty}\right) - 2 \sum_{i=1}^N \left(\frac{v_i}{V_\infty} \frac{v_s}{V_\infty} + \frac{w_i}{V_\infty} \frac{w_s}{V_\infty}\right) \\ & - \sum_{i=1}^N \frac{v_i^2 + w_i^2}{V_\infty^2} - \sum_{i=1}^N \sum_{\substack{j=1 \\ i \neq j}}^N \left(\frac{v_i v_j + w_i w_j}{V_\infty^2}\right) \end{aligned} \quad (84)$$

The rate of change of normal force with x_s can then be obtained by integrating the above equation around the surface. Thus,

$$\frac{dN}{dx_s} = - \left(\frac{1}{2} \rho_\infty V_\infty^2\right) a \int_0^{2\pi} c_p \sin \theta \, d\theta \quad (85)$$

or

$$\begin{aligned} \frac{1}{\rho_\infty V_\infty^2 a} \frac{dN}{dx_s} \int_0^{2\pi} \left(\frac{\bar{u}_s}{V_\infty}\right) \sin \theta \, d\theta + \frac{1}{2} \int_0^{2\pi} \left(\frac{v_s^2 + w_s^2}{V_\infty^2}\right) \sin \theta \, d\theta \\ + \sum_{i=1}^N \int_0^{2\pi} \left(\frac{u_i}{V_\infty}\right) \sin \theta \, d\theta + \sum_{i=1}^N \int_0^{2\pi} \left(\frac{\alpha w_i - \beta v_i}{V_\infty}\right) \sin \theta \, d\theta \end{aligned}$$

(eq. (86) cont. on next page)

$$\begin{aligned}
& + \sum_{i=1}^N \int_0^{2\pi} \left[\left(\frac{v_i}{V_\infty} \right) \left(\frac{v_s}{V_\infty} \right) + \left(\frac{w_i}{V_\infty} \right) \left(\frac{w_s}{V_\infty} \right) \right] \sin \theta \, d\theta \\
& + \frac{1}{2} \sum_{i=1}^N \int_0^{2\pi} \left[\left(\frac{v_i}{V_\infty} \right)^2 + \left(\frac{w_i}{V_\infty} \right)^2 \right] \sin \theta \, d\theta \\
& + \frac{1}{2} \sum_{i=1}^N \sum_{\substack{j=1 \\ i \neq j}}^N \int_0^{2\pi} \left[\left(\frac{v_i}{V_\infty} \right) \left(\frac{v_j}{V_\infty} \right) + \left(\frac{w_i}{V_\infty} \right) \left(\frac{w_j}{V_\infty} \right) \right] \sin \theta \, d\theta \quad (86)
\end{aligned}$$

The first two terms in this equation are the primary interference associated with the nonuniform flow field and the last five are the additional interference due to the vortex system.

The integration of equation (86) with respect to θ is carried out in Appendix I. The resulting normal-force distribution is

$$\frac{1}{\rho_\infty V_\infty^2 a} \frac{dN}{dx_s} = \frac{1}{\rho_\infty V_\infty^2 a} \frac{dN_s}{dx_s} + \frac{dN_\Gamma}{dx_s} \quad (87)$$

The first term on the right-hand side is given by equation (I-13) as

$$\frac{1}{\rho_\infty V_\infty^2 a} \frac{dN_s}{dx_s} = 2\pi \frac{d}{dx_s} \left(\frac{Wa}{V_\infty} \right) \quad (88)$$

The second term, from equations (I-36) through (I-38), is

$$\begin{aligned}
\frac{1}{\rho_\infty V_\infty^2 a} \frac{dN_\Gamma}{dx_s} = & 2\pi \sum_{i=1}^N \left\{ \frac{1}{a} \frac{d}{dx_s} \left[\frac{a^3}{r_i} \cos \phi_i \left(\frac{\Gamma_i}{2-aV_\infty} \right) \right] - \frac{a}{r_i} \left(\frac{\Gamma_i}{2-aV_\infty} \right) \cos \phi_i \frac{da}{dx_s} \right\} \\
& + 2\pi \sum_{i=1}^N \frac{a^2}{r_i} \left(\frac{\Gamma_i}{2-aV_\infty} \right) \left[\frac{v}{V_\infty} \cos 2\phi_i + \frac{w}{V_\infty} \sin 2\phi_i \right]
\end{aligned}$$

(eq. (89) cont. on next page)

$$\begin{aligned}
& + 2\pi \sum_{i=1}^N \frac{a^3}{r_i (r_i^2 - a^2)} \left(\frac{\Gamma_i}{2\pi a V_\infty} \right)^2 \sin \phi_i \\
& - 2\pi \sum_{j=1}^{N-1} \sum_{i=j+1}^N \left[\frac{a}{r_i} \sin \phi_i + \frac{a}{r_j} \sin \phi_j + \psi(a, r_i, r_j, \phi_i, \phi_j) \right] \\
& \qquad \qquad \qquad \cdot \left(\frac{\Gamma_i}{2\pi a V_\infty} \right) \left(\frac{\Gamma_j}{2\pi a V_\infty} \right) \qquad (89)
\end{aligned}$$

where

$$\begin{aligned}
& \psi(a, r_i, r_j, \phi_i, \phi_j) \\
& = \frac{a}{\lambda} \left\{ (r_j^2 - r_i^2) \left[(a^2 + r_i^2) r_j \sin \phi_j - (a^2 + r_j^2) r_i \sin \phi_i \right] \right. \\
& \quad \left. + 2r_i r_j \sin (\phi_j - \phi_i) \left[(r_i^2 - a^2) r_j \cos \phi_j - (r_j^2 - a^2) r_i \cos \phi_i \right] \right\} \qquad (90)
\end{aligned}$$

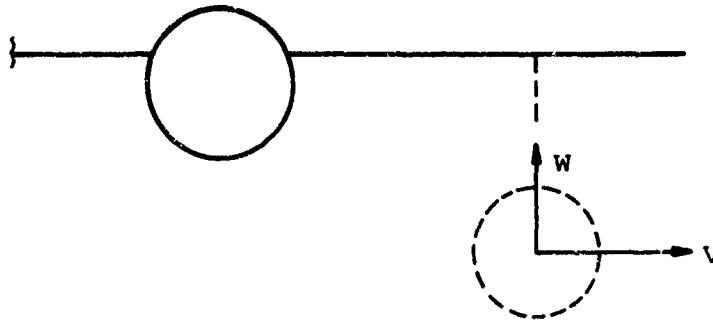
and λ in the above expression is

$$\begin{aligned}
\lambda & = (r_i^2 + r_j^2)(a^4 + r_i^2 r_j^2) - 2(a^2 + r_j^2)(a^2 + r_i^2) r_i r_j \cos (\phi_i - \phi_j) \\
& \quad + 4a^2 r_i^2 r_j^2 \cos^2 (\phi_i - \phi_j) \qquad (91)
\end{aligned}$$

The method of calculating the unknown vortex strengths Γ_i is given in Appendix II.

7.4 Boundary Condition for Store Under Pylon of Wing-Body Combination

For the case of an airplane represented by a wing-body combination with a number of external stores under wing or fuselage, the method of establishing the flow field has been presented in sections 4 and 5 of this report. Let this flow field be described by a three-dimensional potential ϕ_{3D} . Consider a cross section of the wing-body combination with a phantom pylon and a phantom detached store.



The potential ϕ_{3D} includes the effect of wing angle of attack, camber, twist, as well as thickness. It also includes the effects of wing-body interference and the volumetric effects of any other stores under the aircraft.

There are associated velocity components V and W at the center-line position of the phantom store. Besides the component due to ϕ_{3D} , these velocities include components due to translation of the store center of gravity, and angular velocities around the center of gravity. These factors are currently accounted for as described in section 6. We now consider the phantom store to materialize and to add flows to the field associated with da/dx , V , and W . Also, we let the phantom pylon materialize and it induces a further flow due to the fact that it is subject to a sidewash field associated with ϕ_{3D} and may have camber and twist of its own. The additional flows due to the store and pylon are associated with a slender-body interference potential, ϕ_{SB} . The complete potential for the problem is then

$$\phi_c = \phi_{3D} + \phi_{SB} \quad (92)$$

This scheme of setting up the potential has the advantage that the basic three-dimensional field is determined once, and need not be computed for each new position of the store during the trajectory. It is feasible to compute the changing part of the field due to the changing position of the store by this means because a small matrix is needed for a cross-flow calculation by the present method (of the order 10×10) rather than that for a complete airplane configuration including pylon and store (of the order 200×200).

In specifying the boundary conditions on the wing and pylon due to ϕ_{SB} , we must consider any normal velocities not already cancelled by ϕ_{3D} . On the pylon, for instance, we have the sidewash velocity induced by ϕ_{3D} , any effects of camber, twist, or incidence of the pylon, and the store flow field associated with V . The store flow fields associated with W and da/dx have no component normal to the pylon. Thus on the pylon, the boundary condition is

$$\frac{\partial \phi_{SB}}{\partial n} = V_{3D} + i_p V_\infty + V \frac{a^2}{z_s^2} \quad (93)$$

V_{3D} = sidewash induced at pylon surface by ϕ_{3D}

i_p = local incidence angle of pylon including effect of camber, twist, and incidence

$V = V_{3D}$ at store axis

At the pylon control points the boundary condition is thus

$$v_{P(k)} = V_{3D(k)} + i_{P(k)} V_\infty + \frac{Va^2}{\left[h_p - \frac{l}{2m} (2k - 1) \right]^2}; \quad k = 1, 2, \dots, m \quad (94)$$

With regard to the right wing panel, ϕ_{3D} includes any normal velocity on the wing due to its own incidence, camber, twist, and thickness, as well as any fuselage effects. If the wing angle of attack is α_w , then the normal velocity $V_\infty \alpha_w$ is accounted for by ϕ_{3D} . The velocity W determines the doublet strength on the store axis, and the normal velocity induced at the wing surface due to this doublet is the perturbation velocity which must be cancelled by the interference vortex system. The store flow field components associated with V and da/dx_s also produce normal velocities at the wing which must be cancelled. Accordingly, we have on the right or left wing panel

$$\frac{\partial \phi_{SB}}{\partial z_s} = \frac{Wa^2(y_s^2 - h^2)}{(y_s^2 + h^2)^2} - \frac{2Vay_s h}{(y_s^2 + h^2)^2} + \frac{aV_\infty \frac{da}{dx_s} h}{(y_s^2 + h^2)} \quad (95)$$

At the right wing panel control points, we thus have

$$w_{R(j)} = \frac{-2Va^2h \left(\frac{s}{2p}\right) (2j - 1)}{\left[\frac{s^2}{4p^2} (2j - 1)^2 + h^2\right]^2} + \frac{Wa^2 \left[\frac{s^2}{4p^2} (2j - 1)^2 - h^2\right]}{\left[\frac{s^2}{4p^2} (2j - 1)^2 + h^2\right]^2} + \frac{aV_\infty \frac{da}{dx_s} h}{\frac{s^2}{4p^2} (2j - 1)^2 + h^2}; \quad j = 1, 2, \dots, p \quad (96)$$

and on the left wing panel control points

$$w_{L(g)} = \frac{2Va^2h \left(\frac{t}{2n}\right) (2g - 1)}{\left[\frac{t^2}{4n^2} (2g - 1)^2 + h^2\right]^2} + \frac{Wa^2 \left[\frac{t^2}{4n^2} (2g - 1)^2 - h^2\right]}{\left[\frac{t^2}{4n^2} (2g - 1)^2 + h^2\right]^2} + \frac{aV_\infty \frac{da}{dx_s} h}{\frac{t^2}{4n^2} (2g - 1)^2 + h^2}; \quad g = 1, 2, \dots, n \quad (97)$$

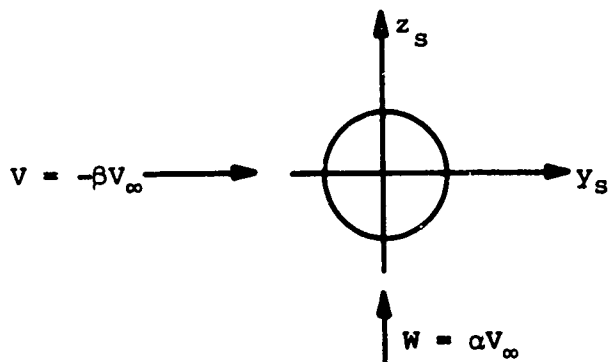
These boundary conditions, equations (94), (96), and (97), are used in equations (II-23) through (II-25) of Appendix II to determine the strengths of the vortices.

7.5 Application of the Method to Conical Configurations

7.5.1 Boundary conditions

Since conical configurations can be utilized to illustrate the importance of certain wing-pylon-store interference effects, some calculated results for such configurations will subsequently be shown. The boundary conditions will now be specified for such configurations.

Consider a conical store at angle of attack α and angle of sideslip β with crossflow planes normal to the store axis as shown



Consider now the positions which are to be occupied by wing and pylon. At these positions the store alone induces velocities by virtue of da/dx_s , V , and W . In order to determine the velocities normal to the pylon and wing, consider the total potential for the store flow

$$\phi_s = \text{R.P.} \left[V \left(\sigma + \frac{a^2}{\sigma} \right) + iW \left(-\sigma + \frac{a^2}{\sigma} \right) + aV_\infty \frac{da}{dx_s} \log \sigma \right] + x_s \sqrt{V_\infty^2 - V^2 - W^2} \quad (98)$$

$$v_B - iw_B = V \left(1 - \frac{a^2}{\sigma^2} \right) - iW \left(1 + \frac{a^2}{\sigma^2} \right) + aV_\infty \frac{da}{dx_s} \frac{1}{\sigma} \quad (99)$$

On the pylon where $\sigma = iz_s$, we have

$$v_p = V \left(1 + \frac{a^2}{z_s^2} \right) \quad (100)$$

The pylon control points have the coordinates (eq. (II-3))

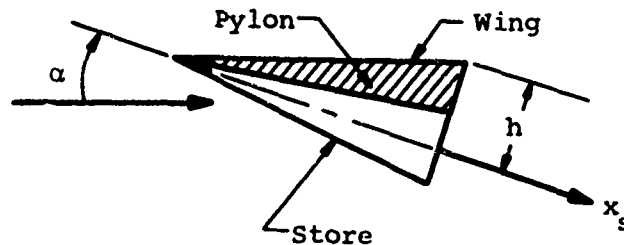
$$z_s = h_p - \frac{l}{2m} (2k - 1) \quad (101)$$

so that equation (100) becomes

$$v_{p(k)} = V + \frac{Va^2}{\left[h_p - \frac{l}{2m} (2k - 1) \right]^2} \quad k = 1, 2, \dots, m \quad (102)$$

This is the velocity to be cancelled by the vortex system at the m control points on the pylon.

On the wing, we have the value of w_B as given by equation (99), but we also have a normal velocity associated with the potential term $x_s \sqrt{v_\infty^2 - v^2 - w^2}$ unless the wing is parallel to x_s . Consider a side view of the conical configuration.



Neglecting $v^2 + w^2$ compared to v_∞^2 , the normal component due to the root term is $-v_\infty(dh/dx_s)$. On the wing $\sigma = y_s + ih$ so that

$$\begin{aligned}
 v_B - iw_B &= v \left[1 - \frac{a^2 (y_s^2 - h^2 - 2iy_s h)}{(y_s^2 + h^2)^2} \right] \\
 &\quad - iw \left[1 + \frac{a^2 (y_s^2 - h^2 - 2iy_s h)}{(y_s^2 + h^2)^2} \right] \\
 &\quad + a v_\infty \frac{da}{dx_s} \frac{(y_s - ih)}{y_s^2 + h^2}
 \end{aligned} \tag{103}$$

from which

$$w_B = \frac{-2Va^2 y_s h}{(y_s^2 + h^2)^2} + w \left[1 + \frac{a^2 (y_s^2 - h^2)}{(y_s^2 + h^2)^2} \right] + \frac{a v_\infty \frac{da}{dx_s} h}{y_s^2 + h^2} \tag{104}$$

At the right wing panel control points (see eq. (II-3))

$$y_s = \frac{s}{2p} (2j - 1) ; \quad j = 1, 2, \dots, p \tag{105}$$

Thus the velocity to be cancelled by the vortex system at the p control points on the right wing panel is

$$w_R(j) = - \frac{2Va^2h \left(\frac{s}{2p}\right) (2j - 1)}{\left[\frac{s^2}{4p^2} (2j - 1)^2 + h^2\right]^2} + \frac{aV_\infty \frac{da}{dx_s} h}{\frac{s^2}{4p^2} (2j - 1)^2 + h^2} + W + \frac{Wa^2 \left[\frac{s^2}{4p^2} (2j - 1)^2 - h^2\right]}{\left[\frac{s^2}{4p^2} (2j - 1)^2 + h^2\right]^2} - V_\infty \frac{dh}{dx_s}; j = 1, 2, \dots, p \quad (106)$$

At the left wing panel control points,

$$y_s = - \frac{t}{2n} (2g - 1); \quad g = 1, 2, \dots, n \quad (107)$$

so that the velocity to be cancelled at the n control points of the left panel by the vortex system is

$$w_L(g) = \frac{2Va^2h \left(\frac{t}{2n}\right) (2g - 1)}{\left[\frac{t^2}{4n^2} (2g - 1)^2 + h^2\right]^2} + \frac{aV_\infty \frac{da}{dx_s} h}{\frac{t^2}{4n^2} (2g - 1)^2 + h^2} + W + \frac{Wa^2 \left[\frac{t^2}{4n^2} (2g - 1)^2 - h^2\right]}{\left[\frac{t^2}{4n^2} (2g - 1)^2 + h^2\right]^2} - V_\infty \frac{dh}{dx_s}; g = 1, 2, \dots, n \quad (108)$$

It is of interest to consider the boundary conditions as composed of three basic cases:

$$\left. \begin{array}{l} \text{Case A: } V = 0 \quad W = 0 \quad \frac{da}{dx} \neq 0 \quad \frac{dh}{dx} \neq 0 \\ \text{Case B: } V \neq 0 \quad W = 0 \quad \frac{da}{dx} = 0 \quad \frac{dh}{dx} = 0 \\ \text{Case C: } V = 0 \quad W \neq 0 \quad \frac{da}{dx} = 0 \quad \frac{dh}{dx} = 0 \end{array} \right\} \quad (109)$$

The first case yields quantities due to the basic asymmetries, and establishes the angles of zero normal force and zero side force.

The boundary conditions associated with the three cases are

Case A: Basic Case

$$\left. \begin{aligned} w_{R(j)} &= \frac{aV_{\infty}h \frac{da}{dx_s}}{\frac{s^2}{4p^2} (2j-1)^2 + h^2} - V_{\infty} \frac{dh}{dx_s} \\ w_{L(g)} &= \frac{aV_{\infty}h \frac{da}{dx_s}}{\frac{t^2}{4n^2} (2g-1)^2 + h^2} - V_{\infty} \frac{dh}{dx_s} \\ v_{P(k)} &= 0 \end{aligned} \right\} \quad (110)$$

Case B: Angle of Sidewash Case

$$\left. \begin{aligned} w_{R(j)} &= - \frac{2Va^2h \left(\frac{s}{2p}\right) (2j-1)}{\left[\frac{s^2}{4p^2} (2j-1)^2 + h^2\right]^2} \\ w_{L(g)} &= \frac{2Va^2h \left(\frac{t}{2n}\right) (2g-1)}{\left[\frac{t^2}{4n^2} (2g-1)^2 + h^2\right]^2} \\ v_{P(k)} &= V + \frac{Va^2}{\left[h_p - \frac{l}{2m} (2k-1)\right]^2} \end{aligned} \right\} \quad (111)$$

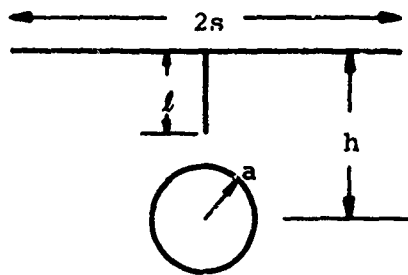
Case C: Angle of Attack Case

$$\left. \begin{aligned} w_{R(j)} &= W + \frac{Wa^2 \left[\frac{s^2}{4p^2} (2j-1)^2 - h^2\right]}{\left[\frac{s^2}{4p^2} (2j-1)^2 + h^2\right]^2} \\ w_{L(g)} &= W + \frac{Wa^2 \left[\frac{t^2}{4n^2} (2g-1)^2 - h^2\right]}{\left[\frac{t^2}{4n^2} (2g-1)^2 + h^2\right]^2} \\ w_{P(k)} &= 0 \end{aligned} \right\} \quad (112)$$

For Case A, the boundary conditions are symmetrical about the vertical axis, and a vortex system with mirror symmetry about the vertical axis is to be expected for left and right panels of equal span with no vortices on the pylon. For Case B, the vortex signs will not change between left and right panels for equal span panels, and there will be vortices on the pylon. The strengths will be equal on left and right panels and proportional to the sidewash angle. For Case C, the vortices will be similar to those for Case A. The physical significance of these cases will subsequently be discussed further.

7.5.2 Calculative example

In order to demonstrate the calculative method and to illustrate the nature of wing-store-pylon interference, a number of systematic calculations have been carried out for conical configurations of the general cross section shown below.



It is possible to show systematically the effects of the nondimensional quantities h/a , s/a , and l/a on the interference for such configurations, and thereby to shed light on the magnitude of the interference effects.

For a conical configuration in a uniform stream, the right-hand sides of equations (88) and (89) do not vary with x_s . Designating the part associated with the vortex system as Λ , we have from equation (87)

$$\frac{dN}{dx_s} = \frac{dN_s}{dx_s} + \rho_\infty V_\infty^2 a \Lambda \quad (113)$$

If we let the conical configuration have a store base radius a_{\max} and a length l_s and use the store base area as reference area, then

$$C_N = C_{N_s} + \frac{\Lambda}{\pi} \left(\frac{l_s}{a_{\max}} \right) \quad (114)$$

The quantity C_{N_s} is obtained from equation (I-13) and is found to be

$$C_{N_s} = 2 \frac{W}{V_\infty} = 2\alpha \quad (115)$$

Thus,

$$\begin{aligned} C_N = C_{N_s} + 2 \frac{l_s}{a_{\max}} & \left\{ \sum_{i=1}^N \frac{a}{r_i} \left(\frac{\Gamma_i}{2\pi a V_\infty} \right) \cos \phi_i \frac{da}{dx_s} \right. \\ & + \sum_{i=1}^N \frac{a^2}{r_i^2} \left(\frac{\Gamma_i}{2\pi a V_\infty} \right) \left[\left(\frac{V}{V_\infty} \right) \cos 2\phi_i + \left(\frac{W}{V_\infty} \right) \sin 2\phi_i \right] \\ & + \sum_{i=1}^N \frac{a^3}{r_i (r_i^2 - a^2)} \left(\frac{\Gamma_i}{2\pi a V_\infty} \right)^2 \sin \phi_i \\ & \left. - \sum_{j=1}^{N-1} \sum_{i=j+1}^N \left(\frac{\Gamma_i}{2\pi a V_\infty} \right) \left(\frac{\Gamma_j}{2\pi a V_\infty} \right) \left[\frac{a}{r_i} \sin \phi_i + \frac{a}{r_j} \sin \phi_j \right. \right. \\ & \left. \left. + \psi(a, r_i, r_j, \phi_i, \phi_j) \right] \right\} \quad (116) \end{aligned}$$

The quantity ψ is given by equations (90) and (91).

The boundary conditions for conical configurations were developed in the previous section, wherein three cases were differentiated. Case A included all terms not proportional to α or β ; Case B included terms proportional to β (or V); Case C included terms proportional to α (or W). Case A determines the lift and side force at zero α and β , and is not as interesting as the other two cases.

Consider the angle-of-attack case associated with vertical velocity W . The store alone has a normal-force curve slope of 2 for this case based on its base area as reference area. The presence of the wing above the store tends generally to dam up the crossflow above the store, and thereby to reduce the normal force. If we designated the normal-force coefficient of the store alone due to α as $C_{N_s(\alpha)}$ and that of the store in the presence of the wing and pylon as $C_{N_s, pw(\alpha)}$, we have

$$C_{N_s(\alpha)} \approx 2\alpha \quad (117)$$

$$C_{N_{s,pw}(\alpha)} = 2\alpha(1 + K_\alpha) \quad (118)$$

where

$$K_\alpha = \frac{C_{N_{s,pw}(\alpha)} - C_{N_s(\alpha)}}{C_{N_s(\alpha)}} \quad (119)$$

The interference factor K_α has the simple physical significance that it is the fractional amount that the store-alone normal force due to α is changed because of wing-store-pylon interference.

Inherent in the foregoing physical interpretation is the assumption that the nonlinear terms in equation (116) have no net contribution to C_N for the angle-of-attack case. Since the vortex strengths are proportional to W in this case, the last three terms of equation (116) yield contributions quadratic in α . For angles of attack of the order of a tenth of a radian, the numerical contributions from the nonlinear terms generally total less than one percent of the linear term. Whether the net contribution of the nonlinear terms should be identically zero on mathematical grounds is not known to the authors at this time. The residual nonlinear contribution could be the result of approximating a continuous vorticity distribution by a number of discrete vortices. In any event, it is small for the magnitude of the angles expected in practice, and it is therefore neglected.

A series of calculations has been made to determine how K_α varies with the nondimensional parameters h/a and s/a . Because the pylon is a streamline of the flow, no pylon vortices are required in the solution, and K_α does not depend on l/a . Since we are replacing a continuous vorticity distribution on the wing by a series of discrete vortices, the accuracy of the numerical results depends on the spacing of the vortices. The variation of K_α with h/a for $s/a = 2$ is shown in figure 24 for two uniform vortex spacings. For most practical purposes, a vortex spacing equal to a quarter of the body radius gives adequate results.

To illustrate further the convergence of the method for calculating K_α a systematic set of calculations was made varying the vortex spacing for $h/a = 1.25$ and $s/a = 10$. The following results were obtained:

<u>Vortex Spacing</u>	<u>K_α</u>
a	-0.57101
2a/3	-0.56515
a/2	-0.56238
2a/5	-0.56072
a/3	-0.55958
2a/7	-0.55876
a/4	-0.55816

For this case, a vortex spacing as great as a body radius gives adequate results for most practical purposes.

The effect of h/a on K_α for various values of s/a is shown in figure 25. For the limiting case $s/a = 0$, K_α is clearly zero. For the limiting case $s/a = \infty$, it is probable that $K_\alpha = -1$ based on the following argument. For a very large value of s/a , the flow under the central part of the wing is a stagnation region. Placing a store of radius small compared to s in this region will produce no normal force on the store, so that K_α will be -1 .

A significant point in connection with the angle-of-attack case is that no singularities arise. Such singularities occur when an external vortex comes in contact with the store. It is noted in equation (116) that the third term produces a singularity if $r_i = a$. From symmetry considerations, it is noted that the vorticity on one wing panel is equal and opposite to the other wing panel. Accordingly, no trailing vortex lies along the root chord of the wing. Thus when the store is in contact with the wing, there is no vortex in contact with the store to produce a singularity. It should be noted that as soon as the left and right wing panels are of unequal span or as soon as sidewash is introduced, the singularity arises.

For the angle-of-sidewash case, the last three terms of equation (116) are quadratic in β , and the linear term has no contribution to C_N . It is convenient to normalize the β^2 contribution to C_N in terms of a nondimensional normal-force ratio, K_β , which has a physical analogy with

a crossflow drag coefficient. Consider the side force on the store alone due to viscous crossflow with crossflow drag coefficient c_{d_c} .

$$Y_{cf} = c_{d_c} \beta^2 q_\infty S_n \quad (120)$$

For a conical body the area normal to the crossflow, S_n , is $l_s a_{max}$. It is possible to put the normal force due to β^2 , N_β , as obtained from equation (116), into the following form

$$N_\beta = K_\beta \beta^2 q_\infty S_n \quad (121)$$

The factor K_β has a simple physical significance. It is numerically equal to the crossflow drag coefficient which will yield a side force due to viscous crossflow. This side force is equal to the normal force N_β due to the angle of sidewash.

In figure 26, the value of K_β is shown versus h/a for $s/a = 2$ and $l/a = 1$ for two uniform vortex spacings on wing and pylon. It is noted that good agreement occurs for a gap between pylon and store as small as half a radius. However, as the gap gets smaller, the two results start to depart significantly. The difference is associated with the fact that as the lowest pylon vortex gets closer to the store, it approaches a singularity of the type previously discussed.

A systematic set of calculations has been made to see how K_β varies with vortex spacing for the same case for which the K_α calculations were made. The following results were obtained:

<u>Vortex Spacing</u>	<u>K_β</u>
a	2.2996
2a/3	1.6092
a/2	1.5043
2a/5	1.4892
a/3	1.4869
2a/7	1.4864
a/4	1.4864

For this case, with $h/a = 1.25$, $s/a = 10$, and $l/a = 1.0$, a vortex spacing of $a/2$ yields sufficiently accurate results for most practical purposes.

An exact solution for K_{β} has been obtained for the case of $s/a = \infty$ and $l/a = 0$ with the help of reference 14, page 174, example 25. It is of interest to compare the values of K_{β} for this case with those obtained by the present calculation method for $s/a = 10$ as a function of h/a . The comparison is shown below.

h/a	K_{β}	
	$s/a = \infty$ <u>Exact Solution</u>	$s/a = 10$ <u>Present Method</u>
1.05	6.2285	7.5549
1.10	3.5992	3.6009
1.15	2.5090	2.4806
1.20	1.8978	1.8750
1.25	1.5042	1.48640
1.50	.6550	.64724
1.75	.3658	.36024
2.00	.2298	.22662
2.50	.1102	.10802
4.00	.0254	.0239
5.00	.0128	.0114
8.00	.0031	.00205

Even for large values of h/a , where the difference in s/a may have some effect, the results are closely the same. For small values of h/a where the difference in s/a is of less significance, there is still very close agreement except at $h/a = 1.05$. At $h/a = 1.05$, the effect of the singularity at $h/a = 1.0$ in the present method is starting to make its influence felt. The vortex spacing for the calculation was $a/4$.

The general nature of the flow is as shown in the sketch of figure 26. High velocity flow through the gap creates a lower pressure there than at the bottom of the store so that a positive normal force is developed.

As the gap approaches zero, the lowest pylon vortex does not actually touch the store because of the way in which the pylon vortices have been distributed. The lowest vortex has been placed one-half of the pylon vortex spacing up from the pylon tip. This convention was followed for both vortex spacings. No analysis was made to determine how the lowest vortex should be located with respect to the tip, and the above conven-

tion represents a first approximation. Refinement of this convention would probably produce better convergence as the tip is approached.

Another theoretical point of significance is that the limit of the present case as the gap approaches zero is not the same as the zero-gap case. In the present case, the loading at the pylon tip falls to zero, and as the gap approaches zero this condition is not relaxed. However, if the gap becomes zero, then a load can be carried across the tip of the pylon. It appears that the positive normal force for the gap case could change to a negative normal force for the zero-gap case. For the purpose of calculating trajectories, we are interested in the gap case because the gap opens up immediately whenever the store is dropped or ejected. However, for determining attached-store loads, the zero-gap case could be of interest in special cases.

Figure 27 has been prepared to show how K_{β} varies with h/a for constant values of s/a . It is intuitively clear that after s/a reaches a certain value for a fixed value of h/a , it would not be expected that K_{β} would change significantly for further increases in s/a . Calculations bear out this supposition in that going from $s/a = 8$ to $s/a = 10$ did not change the calculated values of K_{β} significantly. In the foregoing sense there is an upper limit on K_{β} for a given value of h/a . The figure illustrates the rule of thumb that K_{β} is 0.1 or less if $h/a = 4$ to 5 for a short pylon.

8. COMPARISON OF CALCULATED LOAD DISTRIBUTION, FORCE, AND MOMENT WITH EXPERIMENT

This section of the report will present comparisons between the present theory and experimental data in order to assess the accuracy of the theory in predicting the store load distribution and also the total normal force and pitching moment acting on the store. Comparisons will first be made for the case of a single store under the wing of a wing-fuselage combination. These will be followed by comparisons for a single store under the pylon of a wing-fuselage-pylon combination. The last comparisons will be for a TER grouping under the wing of a wing-fuselage-pylon-rack combination.

8.1 Single Store Under Wing of Wing-Fuselage Combination

Some calculated normal-force distributions for the case of a single store under the left wing panel of a wing-fuselage combination are shown in the next three figures. The calculations and the data shown in the figures are for the configuration shown in figures 2 and 3 except that the store is one diameter, 0.75 inch, below the location shown in figure 3(a). This is the same case as for the flow-field calculations which were presented in figures 18 and 19. The data taken from Volume III of reference 1 are shown by the circles.

Figure 28 compares the primary interference normal force distribution, calculated as described in section 6, with the data taken at a Mach number of 0.25 at two angles of attack. The angle α_p is the angle at which the store and parent aircraft were placed relative to the wind-tunnel longitudinal axis. The angle α_w was used in the calculations. As was discussed in section 5.3.2, this angle reflects a partial correction for the wind-tunnel stream angle. Two theoretical curves are shown in figure 28. The solid curve in the figure is the primary interference normal-force distribution excluding store interference on the wing; that is, the store volume is not allowed to induce a wing camber. For the dashed curve, this induced camber is included. As can be seen in figure 28, the effect of the induced camber is small. At both angles of attack, the agreement between the experimental and calculated distributions is quite good.

The calculations shown by the dashed curves in figure 28 account for store interference on the wing, but not wing interference on the store, whereas the additional interference analysis of section 7 accounts for the mutual interference between these two components. Figure 29 shows the effect of including the additional interference, as calculated by the method of section 7, in the load distribution. These are the same cases as treated in figure 28. The solid curves are the primary interference load distributions. The store-induced wing camber has not been included since the store source distribution has been included in the boundary condition of the additional interference calculation, the da/dx_s terms in equations (96) and (97). The dashed curves in figure 29 include the additional interference. The only effect seen is in the nose region of the store. The effect appears to be much more pronounced for $\alpha_p = 0^\circ$

(fig. 29(a)) than for $\alpha_p = 6^\circ$. This is only because of the fact that the large slopes of the load distribution curve which exist near the nose for the $\alpha_p = 6^\circ$ case hide the change due to additional interference.

For $\alpha_p = 0^\circ$, the additional interference calculation produces an effect which is not seen in the data. This effect is due entirely to the store source terms, the da/dx_s terms, in equations (96) and (97). If these terms are not included in the boundary condition, the change due to additional interference cannot be seen on the plots of figure 29. It, therefore, appears that the two-dimensional source term produces an unrealistically large effect. The source effect calculated by slender-body theory is not accurate for reasons subsequently discussed, and the theory is modified accordingly.

The reason that the store source terms produce a large effect lies in a known limitation of slender-body theory. The term in the complex potential for the body source varies as $\log r$ and does not converge for distances far from the body in contrast to the doublet solution associated with body lift. However, an excellent approximation to the body volume effects on additional interference can be obtained very simply by using three-dimensional sources to represent the body and considering the wing to be a reflection plane. Alternately we could consider the modification of the wing vortex-lattice solution due to the effect of the three-dimensional body sources on the wing boundary conditions. The effect of store volume on the additional interference has been calculated both ways and compared. Both methods gave closely similar results for the present case and were negligible compared to the primary interference. Accordingly, the body volume effects will be calculated using three-dimensional source distributions. Except for stores very close to the wing they will be negligible.

Figure 30 presents comparisons between the primary interference theory and data for the same case as that of figure 28 except that the Mach number is 0.70. As in the Mach number 0.25 case, the calculations have been made taking into account the indicated tunnel-empty stream angle. The overall agreement between experiment and theory is not quite as good as that shown in figure 28 for a Mach number of 0.25. This is consistent with the results of the flow-field survey comparisons of figures 18 and 19 where it was found that better agreement was obtained for a Mach number of 0.25. The effects of tunnel stream angle on these comparisons should be recalled.

The primary interference theory is compared with the total normal-force and pitching-moment coefficients as a function of angle of attack in figure 31. This is the same configuration and store location as was considered in the previous figures. Figure 31(a) is for a Mach number of 0.25 and figure 31(b) is for a Mach number of 0.70. At both Mach numbers the calculated normal force is slightly high. This is to be expected, since in both figures 28 and 30 the calculated load distributions were generally above the experimental ones. The calculated pitching moment is in good agreement with the data. Since the overprediction of the store load distribution is generally around the store midpoint, the point about which the moment is taken, this overprediction has little effect on the moment.

8.2 Single Store Under Wing of Wing-Fuselage-Pylon Combination

Let us now consider the case of a single store below a pylon mounted at the 1/3 semispan position on the left wing panel of the wing-fuselage combination of figure 2. The details of the pylon are shown in figure 32. When mounted on the wing, the pylon centerline is located at 40 percent of the local wing chord. The store location if it were mounted on the pylon is shown in figure 3(a). The store location to be considered, however, is one diameter, 0.75 inch, below this location, the same position considered in the previous section. The store details are shown in figure 3(b). With the pylon present the store midpoint is directly below the pylon centerline.

In Volume III of reference 1, load distributions are presented which were measured both with and without the pylon present on the wing. By subtracting the data obtained without the pylon present from that obtained with the pylon on the wing, the incremental load distribution due to the addition of the pylon can be obtained. This has been done and the incremental loadings are plotted in figure 33. Data are shown for two angles of attack at a Mach number of 0.25. It can be seen from the two parts of the figure that the effect of angle of attack is small. Also, there is quite a large upstream influence of the pylon which the slender-body theory method of accounting for the pylon, section 7, will not predict.

For $\alpha_p = 6^\circ$, figure 33(b), an additional interference calculation has been made to see what portion of the experimental incremental load distribution is due to adding a pylon of zero thickness. The

result of the calculation is shown in the figure. As can be seen, only a small portion is accounted for. It is felt that the primary effect showing up in the data is one of pylon thickness which is not accounted for in either the primary or additional interference.

Even though the pylon thickness effect changes the store load distribution, its effect on C_N and C_m is small. If the curves of figure 33 are integrated over the store length, the resulting ΔC_N 's are approximately equal to the $2\sigma_s$ (two standard deviation) uncertainty of the data which was determined in Volume I of reference 1. Since the curves of figure 33 are fairly symmetrical about the store midpoint, the point about which the moments are to be taken, small values of ΔC_m are also obtained. These results may not be true in general even though the present pylon is excessively thick. It thus may be prudent to include the pylon thickness in the present prediction technique.

Another set of data for which comparisons between the present theory and experiment will be made is contained in reference 15. The configuration is shown in figure 34. This is the swept-wing model tested in reference 15. The store is located at the one-third semi-span approximately 18 percent of the local chord below the wing and is attached to the pylon. Comparisons with the measured normal force and pitching moment will be presented for both tail-on and tail-off stores. McKinnev and Polhamus, in reference 10, also have made calculations to compare with the same data. Their calculations were made using the flow field data of reference 5, which were taken under a slightly different wing-body combination, to determine the nonuniform flow field in the vicinity of the store. In the present work the flow field has been calculated by the methods described previously. Comparisons with their calculations will be presented, not only for the total normal force and pitching moment, but also for their components due to buoyancy and angle of attack.

The calculations to be presented are primary interference calculations only. As was discussed in section 7.5.2, in connection with the conical configuration, the additional interference analysis is not applicable to the case of zero gap between the store and pylon. In the present case, a very small gap exists since the store was tested in the carriage position with the balance supported through the pylon.

Before presenting the normal force and pitching moment determined by integrating over the store length, it is of interest to examine the magnitudes and distributions of the various components of the normal force over the length of the store shown in figure 34. The distributions to be shown are in figure 35 for the tail-off model at four angles of attack. At the top of each figure is a sketch of the wing-pylon-store cross section at the one-third semispan under the left wing, the semispan location where the calculations were made. For the purposes of this comparison only, the separation location has been assumed to be at 60 percent of the store length, $x_{s,c}/l_s = 0.60$. This region is shown by the shaded area on the store. This store, unlike the one for which the previous comparisons have been made is boattailed so that flow separation over the aft end of the store is to be expected. No method exists for determining the separation location on a body of revolution in a nonuniform flow field. The method of Hopkins, reference 12, which was mentioned earlier, applies only to a uniform flow field.

An examination of figure 35 shows that both the buoyancy and slender-body theory load distributions have regions where the loading is negative and regions where it is positive. The buoyancy distribution extends to the end of the body whereas the slender-body theory component ends at the assumed separation location. The component due to viscous crossflow theory acts only downstream of this point.

For all angles of attack, the buoyancy force distribution exhibits the same qualitative behavior. The loading near the wing leading edge is negative and becomes positive under the mid-portion of the wing. It becomes negative again near the wing trailing edge. The sign of this component of the loading changes as the sign of the pressure gradient across the store changes.

The slender-body theory loading curves are similar in behavior to the buoyancy curves except ahead of the wing leading edge where, at large angles of attack, a large positive loading exists. The behavior of the slender-body curves can be explained by examining the equation for the loading. From equation (59)

$$\frac{d(C_N)_{SB}}{d(x/l)_s} = \frac{2}{S_R} \frac{d}{d(x/l)_s} (a W_s^*)$$

or

$$\frac{d(C_N)_{SB}}{d(x/l)_S} = \frac{2\pi}{S_R} \left[2aW_S^* \frac{da}{d(x/l)_S} + a^2 \frac{dW_S^*}{d(x/l)_S} \right]$$

The sign of the first term depends on the sign of W_S^* as well as whether the body is expanding or contracting. The sign of the second term depends on the sign of the axial gradient of W_S^* . Thus, negative loadings due to slender-body theory can exist in regions where the body is expanding if

- (1) W_S^* and $dW_S^*/d(x/l)_S$ are both negative.
- (2) W_S^* is negative, $dW_S^*/d(x/l)_S$ is positive, but term 1 is larger in magnitude than term 2.
- (3) W_S^* is positive, $dW_S^*/d(x/l)_S$ is negative, and term 2 is larger in magnitude than term 1.

It is also possible to have nonzero loading on the cylindrical portion of the store because of the velocity gradient term, term 2. The store shown in figure 35 is cylindrical from $(x/l)_S = 0.315$ to $(x/l)_S = 0.617$.

The viscous crossflow theory loadings are small for the angles of attack shown since from equation (65) it is proportional to $aV_C^*W_S^*$. The product $V_C^*W_S^*$ is proportional to the square of the local angle of attack.

Let us now examine the normal force and pitching moment obtained by integrating the load distributions presented in figure 35 plus those calculated for two other angles of attack, -2° and 6° . The results are presented in figure 36. The nondimensionalizing length used in the pitching moment shown in figures 36 and 37 is the store length, not the maximum diameter used elsewhere in the report. The buoyancy component is shown in figure 36(a) with the results of McKinney and Polhamus (ref. 10) also shown. As was mentioned previously, their calculations were made using experimental downwash data from reference 5. These data were taken under a slightly different wing-body combination, see figure 9, from that shown in figure 34. The present calculations are entirely theoretical. The two calculations are in good agreement for both normal force and pitching moment.

A similar comparison is presented in figure 36(b) for the angle of attack component, that is, the sum of slender-body theory and viscous crossflow theory. Calculations using the present method are shown for

three assumed locations of separation. The results show the importance of knowing the separation point location in calculating the normal force, particularly at small angles of attack. It is not nearly as important in calculating the pitching moment since the region over which the normal force is affected by shifting the separation point is near the center of moments. For a particular value of the separation location, the present normal-force calculation coincides with the calculation of reference 10. It is not stated where separation was assumed in the calculations of reference 10. The pitching-moment calculations, however, do not agree. The reason for this is not understood. The presence of the pylon was also neglected in reference 10 since the experimental flow-field data used there were obtained under a wing-body combination without a pylon.

The total normal force and pitching moment, that is, the sums of the buoyancy and angle of attack components, are shown in figure 36(c). Also shown are the calculations of reference 10 and the data from reference 15. For the intermediate assumed separation location, $x_{s,0}/l_s$ equal to 0.47, the present calculations agree fairly well with the experimental data.

The comparisons between the total predicted and measured normal force and pitching moment for the external store with fins are shown in figure 37. Again, the theory shows an effect due to location of separation on the calculated normal force. In fact, these differences are precisely those shown in figure 36(c) for the store without fins since the calculated contribution of the fins does not depend on position of separation. For the intermediate position of separation, the normal-force theory and experiment are separated by a small increment up to about 6° angle of attack.

Above this angle of attack, the method overpredicts the tail contribution by an amount that increases as the angle of attack increases. In other words, the tail effectiveness decreases as the angle of attack increases. This nonlinear effect could well be the result of operating the tail in the presence of body vortices associated with viscous cross-flow. Methods for calculating this effect are known for uniform flow. For the present case of a store in a nonuniform flow, an approximate method should probably be developed to account for body vortex-tail interference. Methods for including such interference are available in reference .

The comparison between total moment coefficient as calculated and as measured for the store with fins is in good agreement up to about 6° angle of attack. For higher angles, there is less nose-down moment developed experimentally than predicted. This result is consistent with the fact that the tail normal force has been overestimated by a theory which neglects body vortex effects on tail effectiveness.

8.3 TER Stores Under Wing of Wing-Fuselage-Pylon-Rack Combination

An illuminating comparison can be made between the primary interference theory of section 6 and the data of Volume III of reference 1 for the incremental load distribution due to any stores remaining on the TER rack. Consider the TER grouping as shown in figure 20 and let us determine the incremental load distribution on store number 1, one store diameter below the position shown in the figure, due to the addition of stores 2 and 3 to the rack. Data are presented in Volume III of reference 1 with and without these stores present so that a subtraction of the two load distributions give the incremental loading due to the stores. This has been done, and the data are plotted in figure 38 for two angles of attack. Note that there is not a large change with angle of attack.

Also shown on the two parts of the figure are curves calculated using the primary interference theory of section 6. These curves were obtained by first calculating the loading produced by the velocity field due to fuselage volume, wing thickness, wing vorticity distribution including store-induced camber due to all three stores, and the volume distributions of stores 2 and 3. The calculation was then repeated excluding stores 2 and 3, including the wing camber induced by them, and the two load distributions subtracted. The resulting incremental load distribution is nearly independent of angle of attack since it is due primarily to the velocities induced by the volume distributions of stores 2 and 3, which are not functions of angle of attack. It can be seen from figure 38 that the incremental load distribution is predicted quite well at both angles of attack. The dominant store-store interference effect is clearly due to body sources.

The largest differences between experiment and theory occur at the aft end of the store. This region is influenced by the shape used to model the wakes of stores 2 and 3. In the present calculations, the wake was assumed to have the same shape as the store nose; that is, it

was taken to be an ogive 0.125 foot long (see the store details in figure 3(b)). If it had been taken more slender, then the values of $\Delta dC_N/dx_s$ near the store base would have been reduced. For blunt-based stores in TER or MER grouping, the modeling of the wake is, therefore, important.

Similar comparisons to those of figure 38 are presented in figure 39 except that the incremental load distribution on store 2 due to store 3 on the TER rack are shown. Store 1 is not present and store 2 is one diameter, 0.75 inch, below the position shown in figure 20. Again, the experimental distribution does not change much with angle of attack and is predicted quite well.

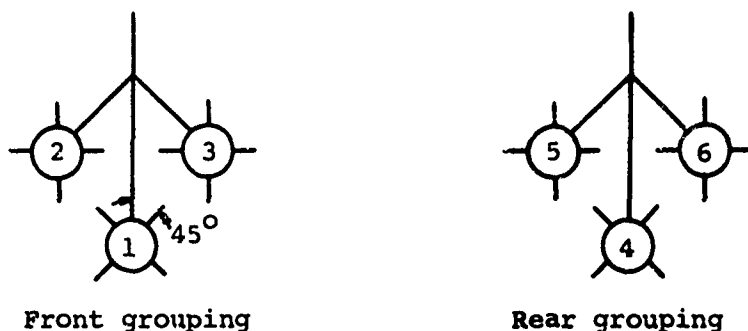
9. EXPERIMENTALLY DETERMINED MER INTERFERENCE EFFECTS

It is clear that the interference effects described in the previous section for ~~TER~~ configurations also exist as a large effect in MER configurations. However, there is in addition the interference between the front three stores and the rear three stores. Data are presented in Volume V of reference 1 in which the various interference effects associated with a multiple ejection rack (MER) installation have been isolated. This was accomplished by measuring forces and moments on a store in a fixed position relative to the wing-fuselage combination and building the remainder of the configuration up component by component. The wing-fuselage combination used in the tests is shown in figure 2. The stores are located as shown in figure 40(a) when in their carriage position on the rack. The details of the stores are shown in figure 40(b). The pylon details are shown in figure 32 and the MER rack details in figure 41.

On the following figures, abbreviations have been used to designate the various aircraft components. They are

WB	wing-fuselage
P	P ylon
M	M ER rack

The numbering system used to identify the six stores is shown in the following sketch as is the fin orientation.



The various stores will be designated as S_1 , S_2 , etc.

Data taken using finless stores are presented in figure 42. The finless stores used are identical to the finned one shown in figure 40(b) except that the fins have been removed. Increments in normal force ΔC_N and pitching moment ΔC_m are plotted against angle of attack for a Mach number of 0.40. In figure 42(a), data taken on MER store number 1 are presented. Similar data are presented in figure 42(b) for store number 4. These stores were located 0.375 inch below the position shown in figure 40(a) when data were taken.

Let us first consider the store number 1 data shown in figure 42(a). The increments plotted were obtained by differencing the data obtained with two parent aircraft configurations. Thus, the circles indicate the effect caused by adding the wing-fuselage combination to the flow field. Similarly, the squares show the change caused by adding the pylon; the diamonds, the MER rack; the equilateral triangles, stores S_2 and S_3 ; and the right triangles, stores S_5 and S_6 . It can be seen that the largest interference effects are caused by the wing-fuselage and stores S_2 and S_3 . The smallest change in force and moment is caused by the pylon. Since the wing and fuselage tend to align the flow with the fuselage, the store sees a smaller angle of attack than when it is in the stream by itself. Thus, the normal force on the store and the resulting pitching moment are reduced. The two stores S_2 and S_3 produce an effect similar to that seen in figure 38 for the TER racks. This is to be expected, since the MER rack is really two TER racks arranged one

behind the other. If the curves of figure 38 were integrated, we would find a positive ΔC_N but because of the negative loading at the nose the moment about the store midpoint would be negative. The addition of stores S_5 and S_6 produce a downwash over the aft end of S_1 since they are above and behind this store. This causes a negative ΔC_N and because this force is primarily generated on the aft end of the store a positive or nose-up pitching moment is produced.

Data taken on store number 4 are shown in figure 42(b). Again it is seen that the wing-fuselage and the two side stores in the same grouping, in this case S_5 and S_6 , have the largest effects. The front three stores produce no change in normal force; however, they do produce a negative increment in pitching moment.

Let us compare the effects of S_5 and S_6 on S_1 with the effects of S_2 and S_3 on S_4 . The stores are nearly symmetrical fore and aft so that the source distributions were nearly asymmetric fore and aft. Accordingly, the downwash produced at a point at a given distance in front of the trailing edge of store S_1 by S_5 and S_6 will be equal and opposite to that produced by S_2 and S_3 the same distance behind the leading edge of store S_4 . Such distributions will produce equal normal-force increments in the two curves, but opposite moment increments. Also the increments should not vary with angle of attack. The measured data exhibit these characteristics fairly well when consideration is given to the fact that the stores are not precisely symmetrical fore and aft, and in one case we are looking at the effect of adding S_5 and S_6 , and in the other S_1 , S_2 , and S_3 . Also, any effects of the wake entrainment would be present in one case but not the other. Based on these observations, it appears that the induced effect of one set of these stores on one of the other trio can be explained by three-dimensional source distributions neglecting wake entrainment.

In figure 43 data taken on the finned store shown in figure 40(b) are plotted against angle of attack. Data taken on store number 1 are presented in figure 43(a) and those taken on store number 4 in figure 43(b). The stores are located in the same positions as they were in the previous figure, that is, 0.375 inch below the locations shown in figure 40(a).

For both stores S_1 and S_4 , the addition of the wing-fuselage- pylon-MER configuration to the flow field adds a negative increment in

normal force over most of the angle-of-attack range. As in the case of the finless store, this is caused by the fuselage and wing tending to align the flow with the fuselage axis and thus reduce the angle of attack which the store sees. At small angles of attack a stabilizing moment increment is added while at large angles a destabilizing increment is added. This later effect is caused by the tail fins operating at a reduced angle of attack.

Adding the two side stores S_2 and S_3 above store S_1 , (fig. 43(a)) or S_5 and S_6 above S_4 (fig. 43(b)) produces the same effect, a positive ΔC_N and a negative ΔC_m . The magnitudes of the effects are nearly equal. This is the behavior expected from a TER grouping as was discussed in connection with figure 42.

The effect of the two stores S_5 and S_6 on store S_1 , figure 43(a), is to produce a small negative normal-force increment and a positive pitching-moment increment almost independent of angle of attack. Since stores S_5 and S_6 produce a downwash at the tail of S_1 , the local angle of attack is reduced which tends to reduce the stabilizing moment contributed by the tail. The effect of the front three stores, S_1 , S_2 , and S_3 , on S_4 can be seen in figure 43(b). There is little effect on normal force and a small stabilizing moment increment. This moment effect is not caused by the presence of the tail fins of store 4. A comparison of the curve indicated by the diamonds in figure 43(b) with the comparable curve for the finless store in figure 42(b), that given by the right triangles, shows the ΔC_m 's to be almost equal. Note the change of scales between the two figures.

In the computer program, the effect of store volume has been included, as it influences store-store interference in the TER configurations and the MER configurations.

10. STORE TRAJECTORIES

In the preceding sections of this report, methods have been presented which allow the calculation of the normal force and pitching moment acting on a store at any point in the aircraft flow field. Utilizing these tools a computer program has been written which will integrate the equation of motion of the store to determine its location and angular orientation as a function of time. For the present these equations are restricted to

three degrees of freedom representing motion in a vertical plane parallel to the airplane vertical plane of symmetry. The airplane is assumed to be in a straight uniform flight but may be climbing or diving.

In this section of the report, the equations of motion will first be derived. Then the computer program will briefly be described and, finally, a sample trajectory will be presented.

10.1 Equations of Motion

The equations of motion will be written in a coordinate system fixed in the aircraft fuselage. This system will have its origin at the fuselage nose and will move with the fuselage. The coordinate system is shown in figure 44 as the ξ, η system. The aircraft is flying at constant free-stream velocity, V_∞ , and at a constant flight path angle, γ_B , relative to the horizontal. The angle of attack of the aircraft, α_B , is also constant. At time $t = t_0$ the store is located as shown in figure 44. Its center of gravity is located at ξ_0, η_0 and its axis is inclined at some angle, θ_0 , measured with respect to a line parallel to the fuselage axis. Provision will be made for imposing an initial velocity relative to the aircraft, V_0 , and an initial angular velocity, $\dot{\theta}_0$.

The equations of motion of the store for the nonaccelerating coordinate system are:

$$\frac{m_s}{\frac{1}{2} \rho_\infty V_\infty^2 S_R} \ddot{z} = \frac{F_z}{\frac{1}{2} \rho_\infty V_\infty^2 S_R} \quad (122)$$

$$\frac{m_s}{\frac{1}{2} \rho_\infty V_\infty^2 S_R} \ddot{\eta} = \frac{F_\eta}{\frac{1}{2} \rho_\infty V_\infty^2 S_R} \quad (123)$$

$$\frac{m_s k^2}{\frac{1}{2} \rho_\infty V_\infty^2 S_R l_R} \ddot{\theta} = \frac{M_\theta}{\frac{1}{2} \rho_\infty V_\infty^2 S_R l_R} \quad (124)$$

The forces acting on the store are shown in figure 45. N_s is the normal force acting on the body and is the sum of three components

$$N_s = N_{BY} + N_{SB} + N_{CF} \quad (125)$$

where

N_{BY} = normal force due to buoyancy

N_{SB} = normal force due to slender-body theory

N_{CF} = normal force due to viscous crossflow

For stores with empennages, an additional normal force is developed. This is shown in figure 45 as N_E . These forces are the primary interference forces and the methods of evaluating them and their corresponding moments were presented in section 6. From here on, the total normal force, including the empennage force if an empennage is present, will be designated N and the corresponding moment, M .

The remaining two forces shown in figure 45 are the zero-lift drag force, D_o , and the gravitation force, $m_s g$. The zero-lift drag force will be taken to always act in the V_{∞_s} direction " the store center of gravity.

Referring to figures 44 and 45, the forces can be resolved into their components in the ξ and η directions to obtain

$$F_{\xi} = N \sin \theta + D_o \cos (\alpha_B + \gamma_B - \gamma_s) + m_s g \sin (\alpha_B + \gamma_B) \quad (126)$$

$$F_{\eta} = N \cos \theta + D_o \sin (\alpha_B + \gamma_B - \gamma_s) - m_s g \cos (\alpha_B + \gamma_B) \quad (127)$$

Thus, equations (122) and (123) can be rewritten as

$$\ddot{\xi} = \frac{1}{2} \rho_{\infty} V_{\infty_s}^2 \frac{S_R}{m_s} \left[C_N \sin \theta + C_{D,o} \cos (\alpha_B + \gamma_B - \gamma_s) \right] + g \sin (\alpha_B + \gamma_B) \quad (128)$$

and

$$\ddot{\eta} = \frac{1}{2} \rho_{\infty} V_{\infty_s}^2 \frac{S_R}{m_s} \left[C_N \cos \theta + C_{D,o} \sin (\alpha_B + \gamma_B - \gamma_s) \right] - g \cos (\alpha_B + \gamma_B) \quad (129)$$

Equation (124) can be written

$$\ddot{\theta} = \frac{1}{2} \rho_{\infty} V_{\infty_s}^2 \frac{S_R l_R}{m_s k^2} C_m \quad (130)$$

Equations (128), (129), and (130) are a set of three second-order differential equations which must be solved to determine the store motion relative to the moving aircraft. The six initial conditions are at $t = t_0$

$$\left. \begin{aligned} \xi &= \xi_0, \quad \eta = \eta_0, \quad \theta = \theta_0 \\ \dot{\xi} &= \dot{\xi}_0, \quad \dot{\eta} = \dot{\eta}_0, \quad \dot{\theta} = \dot{\theta}_0 \end{aligned} \right\} \quad (131)$$

The values of ξ_0 and η_0 are determined by specifying the location of the store center of gravity.

The initial pitch angle is obtained as follows

$$\theta_0 = i_w + i_s \quad (132)$$

wherein the wing incidence relative to the fuselage axis, i_w , and the store incidence relative to the wing root chord, i_s , are also input data.

The initial conditions on the velocities are to be specified as an initial rotational velocity, $\dot{\theta}_0$, positive in the nose-up direction, in radians per second, and an initial velocity, V_0 , in a direction normal to the store axis and positive as shown in figure 44. Then

$$\left. \begin{aligned} \dot{\xi}_0 &= -V_0 \sin \theta_0 \\ \dot{\eta}_0 &= -V_0 \cos \theta_0 \end{aligned} \right\} \quad (133)$$

In the equations of motion certain other quantities, which are constant with time, are required. They are

- a_{\max} = maximum radius of the store
- g = gravitational acceleration
- k = store radius of gyration
- l_R = reference length, taken as $2a_{\max}$
- m_s = mass of the store
- V_∞ = aircraft flight velocity
- α_B = the fuselage angle of attack
- γ_B = the fuselage flight path angle
- ρ_∞ = the free-stream mass density

In addition, the reference area, S_R , is needed. This is taken as the maximum cross-sectional area of the store

$$S_R = \pi a_{\max}^2 \quad (134)$$

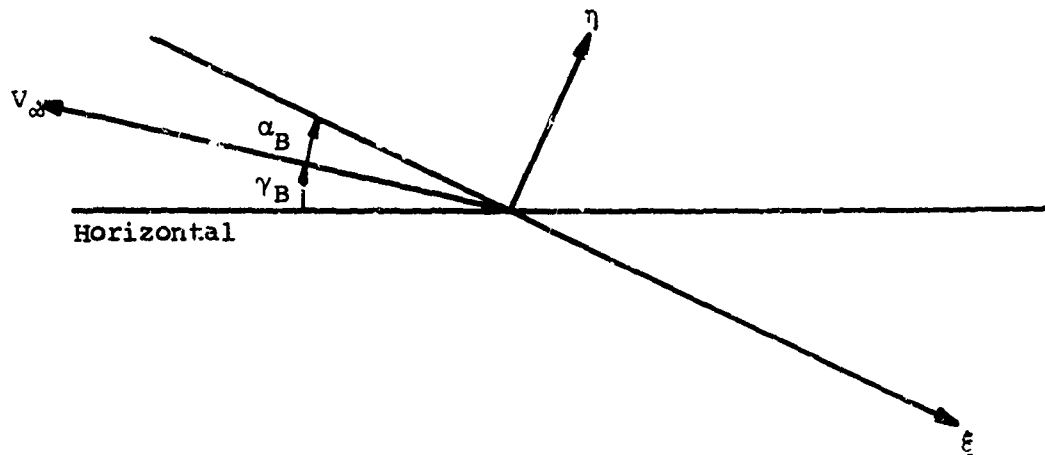
The last quantity which is not a function of time and which appears in the equations of motion is the store drag coefficient, $C_{D,o}$. This must be specified and is defined as

$$C_{D,o} = \frac{D_o}{\frac{1}{2} \rho_\infty V_\infty^2 S_R} \quad (135)$$

The remaining quantities in the equations of motion, V_s , γ_s , and the normal-force and pitching-moment coefficients, are functions of time. The store velocity relative to the atmosphere is

$$V_s = \left[(V_\infty \cos \alpha_B - \dot{h})^2 + (-V_\infty \sin \alpha_B + \dot{\eta})^2 \right]^{1/2} \quad (136)$$

The flight path angle of the store, γ_S , is found from the vertical and horizontal components of its velocity relative to the atmosphere. Consider the following sketch (also see figures 44 and 45).



The ξ, η coordinate system is moving at a velocity V_∞ . The store is moving in this ξ, η coordinate system at velocities $\dot{\xi}$ and $\dot{\eta}$. Thus, the horizontal and vertical velocities of the store relative to the atmosphere are

$$\left. \begin{aligned} V_{\text{hor}} &= V_\infty \cos \gamma_B - \dot{\xi} \cos (\gamma_B + \alpha_B) - \dot{\eta} \sin (\gamma_B + \alpha_B) \\ V_{\text{vert}} &= V_\infty \sin \gamma_B - \dot{\xi} \sin (\gamma_B + \alpha_B) + \dot{\eta} \cos (\gamma_B + \alpha_B) \end{aligned} \right\} \quad (137)$$

The flight path angle, γ_S in figure 45, is then

$$\gamma_S = \tan^{-1} \left(\frac{V_{\text{vert}}}{V_{\text{hor}}} \right) \quad (138)$$

The normal-force and pitching-moment coefficients are calculated by the methods presented in section 6.

10.2 Description of Computer Program

The computer program which calculates the trajectory of a store ejected from an aircraft actually consists of three separate programs in its present form. The three programs are

- (1) Axisymmetric and two-dimensional source distribution program
- (2) Vortex-lattice program
- (3) Trajectory program

For a given body or airfoil and a given Mach number, the first program needs to be run only once. For a given airplane-store configuration and Mach number, the second program needs to be run only once. The third program can be run for various angles of attack, altitudes, and store initial dynamical conditions without rerunning the first two programs. The extent to which the three programs should be incorporated into one program depends therefore on the particular problem at hand.

The first program calculates the source distributions which represent the fuselage and the stores, present on the aircraft, including the one to be ejected. Each shape is specified by a series of segmented polynomials and the program calculates and outputs the axial locations of the sources and their strengths.

This program also calculates the two-dimensional source distribution which represents the streamwise airfoil section of the wing at the spanwise station immediately above the store to be ejected. The airfoil section is also specified by a series of segmented polynomials, and the program calculates and outputs the source strengths and locations.

The second program, the vortex lattice program, computes the bound vorticity distributions which represent the wing camber and twist and angle of attack. The input data to this program consist of wing geometry and information which allows the program to locate the fuselage and all of the stores relative to the wing. In its present form, up to nine stores can be placed under the fuselage centerline and one wing panel. In addition to the above data, the source distributions representing the fuselage and stores are input as is the geometric camber and twist distribution of the wing. The first calculation performed by this program is to determine the velocities induced normal to the wing by the fuselage and the stores. These velocities are treated as an induced camber, and this

camber distribution is added to the wing geometric twist and camber. The program then solves for the two vorticity distributions. The first cancels the free-stream velocity component normal to the wing surface and the second cancels the twist and camber distribution. These vorticity distributions are output by the program.

The third program is the trajectory program. The input data to this program consist of all of the data read into the second program, the vorticity distribution output by the second program, and other information required for the force and moment and trajectory calculations. The additional information input includes the store mass, radius of gyration, center of gravity location, location of the tail, tail semispan, and tail lift-curve slope. Also, the aircraft flight conditions are input as are the store downward ejection velocity and the ejection pitching rate.

The trajectory calculation is begun with the store at a specified initial position. The velocity field is calculated over the store length, and using this field the forces and moments are calculated. The velocity field is found by adding to the free-stream velocity the velocities induced by the fuselage, wing, and all other stores. The integration of the equations of motion is accomplished by a standard numerical integration technique with the velocity field and the forces and moments being recalculated at each point required by the integration scheme.

10.3 Sample Trajectory

An example of the application of the trajectory program is shown in figure 46. This figure presents a comparison of two calculated trajectories with an experimental trajectory taken from reference 17 which was obtained using the captive trajectory system in the 4T Wind Tunnel at AEDC. At the top of figure 46(a) is a sketch of the aircraft, an F-105, showing the spanwise location of the store, an A/B45Y-4 spray tank. For the case shown, the simulated aircraft flight conditions were an altitude of 5,000 feet, horizontal flight, and an angle of attack of the aircraft of 6° . The wind-tunnel Mach number was 0.52. The calculations were made assuming incompressible flow and a free-stream velocity of 570 feet per second. The full-scale parameters used in the tests are given in Table I of reference 17. The same values were used in the calculations. At ejection, the store is pitched down at an angle of -3.0° relative to the

aircraft and given an initial downward velocity of 16 feet per second and pitching velocity of -0.29 radian per second.

Figure 46(a) shows as a function of time the change in pitch angle from its value in the attached position and figure 46(b) shows the change in the vertical location of the store center of gravity from its attached position. The wind-tunnel data are shown by the circles and two calculations using the present method are shown. One is labeled "free flight" and the other "captive store."

Consider the free-flight case in which the store, initially at 3° incidence with respect to the free stream, is given an initial downward velocity of 16 f.p.s. The angle of attack considering also the downward velocity of the center of gravity is then 4.6° . The initial value of $\dot{\theta}$ is -0.29 radians per second and corresponds to a nose-down angular velocity. The nose-down moment of the store tail fins corresponds to the above angle of attack of 4.6° , and a maximum pitch angle excursion of -9° is obtained before the oscillation reverses.

Consider now the captive store on a balance in the wind tunnel. It is not feasible to give the store the downward velocity so that its initial angle of attack is only 3° , and the initial nose-down moment due to the fins is less than in the free-flight case. The total angular excursion is only about -5° in this case. When the angle of attack due to the store's downward velocity was suppressed in the computer program, the trajectory shown by the dashed line was obtained. This trajectory is in agreement with that obtained in the wind tunnel (ref. 17).

This example illustrates the fact that the captive-store technique cannot reproduce the free-flight angle-of-attack history of the store and still maintain geometric similarity between free-flight and the wind tunnel.

11. CONCLUDING REMARKS

This report presents the results of a study directed toward developing a computer program for predicting the trajectories of external stores dropped from aircraft of the fighter-bomber type at speeds up to the critical speed. The stores can be located under the fuselage or under the wing and can be grouped together such as in TER or MER clusters. The present computer program is limited to three degrees of freedom; that is,

store motion in a vertical plane parallel to the airplane vertical plane of symmetry. The airplane is assumed to be in non-maneuvering flight, but may be climbing or diving. The methods presented can be readily extended to six degrees of freedom and maneuvering flight.

Methods are presented for modeling the fuselage and wing and the flow fields calculated utilizing these models agree quite well with experimental flow-field data obtained under wing-fuselage combinations.

Methods are presented for calculating the normal force and pitching moment due to primary interference and additional interference. Included in the primary interference are those interference effects which are dominant. The additional interference method includes minor components of the mutual interference between store, pylon, and wing. For the case of a single store beneath a wing-fuselage combination, the primary interference method predicts the normal force and pitching moment quite well. The additional interference method produces a negligible correction if the store source terms are included in the primary interference. It was found that including the source terms in the additional interference calculation greatly overestimated their effect because of a known limitation of slender-body theory.

The additional interference method was used to calculate the increment of normal force and pitching moment due to adding a pylon to a wing-fuselage combination. For the case considered, the increments were very small. This may not be true for side force and yawing moment. For the particular case for which comparisons were made, it was found that there was a significant change in the experimental load distribution near the pylon when it was added although the resulting effect on normal force and pitching moment was small. The change in the load distribution is attributed to pylon thickness effects. Even though in the case studied the pylon was excessively thick, the inclusion of a pylon thickness model in the primary interference may be desirable.

For a cluster of stores grouped on a TER rack under the wing of a wing-fuselage combination, it was found that the predominant interference effect was due to the volumes of the other stores and the incremental load distribution due to adding the other stores could be predicted quite well by representing their volumes with a distribution of three-dimensional sources. An examination of experimental MER data indicates the same to be true.

Comparisons made with data obtained on a single store with tail fins under the wing of a wing-fuselage combination indicates that it may be necessary to include body-vortex effects in estimating the tail effectiveness. At high angles of attack, the store with an empennage exhibited the characteristic lift and moment curves associated with the loss of tail effectiveness.

The location of flow separation from a store with boattail is also important at high angles of attack. Methods exist for estimating this location for a store in a uniform flow. A means of estimating separation in a nonuniform flow should be developed.

The one trajectory comparison presented shows that the trajectory is well predicted only if pitch damping is included. The method of accounting for pitch damping is thus considered satisfactory and is readily extended to include yaw and roll damping.

TABLE I
BODY-OF-REVOLUTION STORE COORDINATES

Station, inches	Radius, inches
0	0
0.112	0.067
0.212	0.108
0.312	0.139
0.412	0.161
0.512	0.180
0.612	0.195
0.712	0.209
0.812	0.222
0.912	0.232
1.012	0.241
1.112	0.248
1.212	0.254
1.312	0.258
1.412	0.262
1.512	0.265
1.612	0.266
1.712	0.267
1.812	0.267
1.912	0.268
2.312	0.268
2.412	0.266
2.512	0.264
2.612	0.259
2.712	0.254
2.812	0.248
2.912	0.241
3.012	0.234
3.173	0.222
3.812	0.175
4.430	0.175

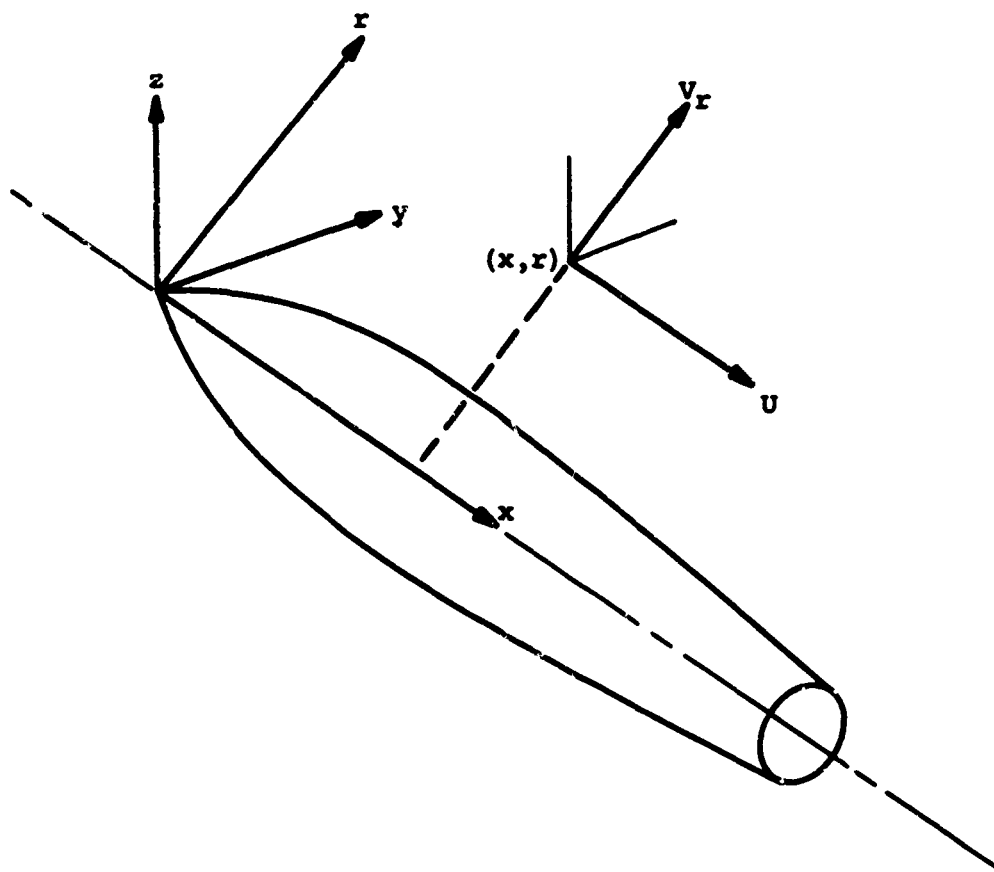


Figure 1.- Coordinate system for axisymmetric body.

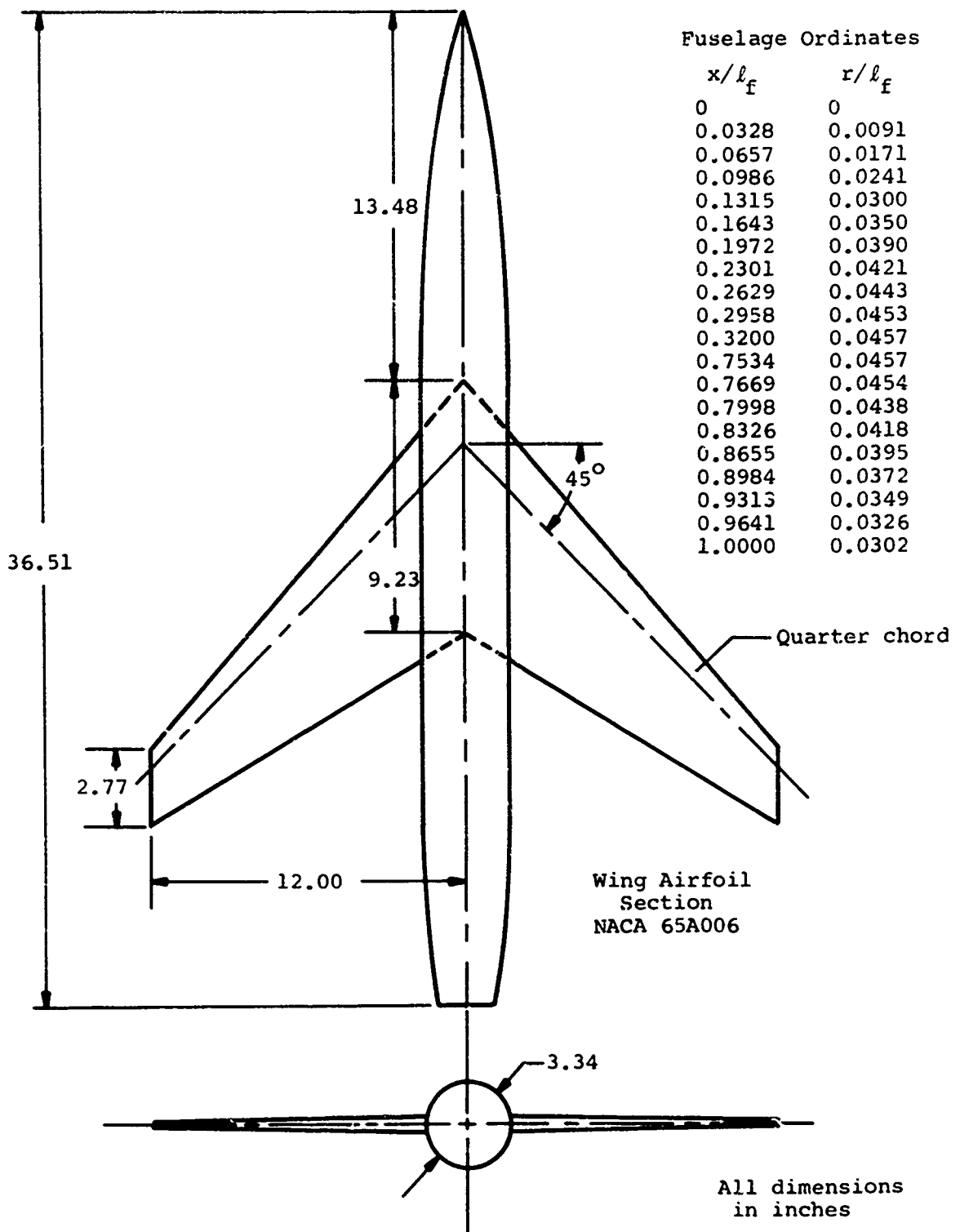
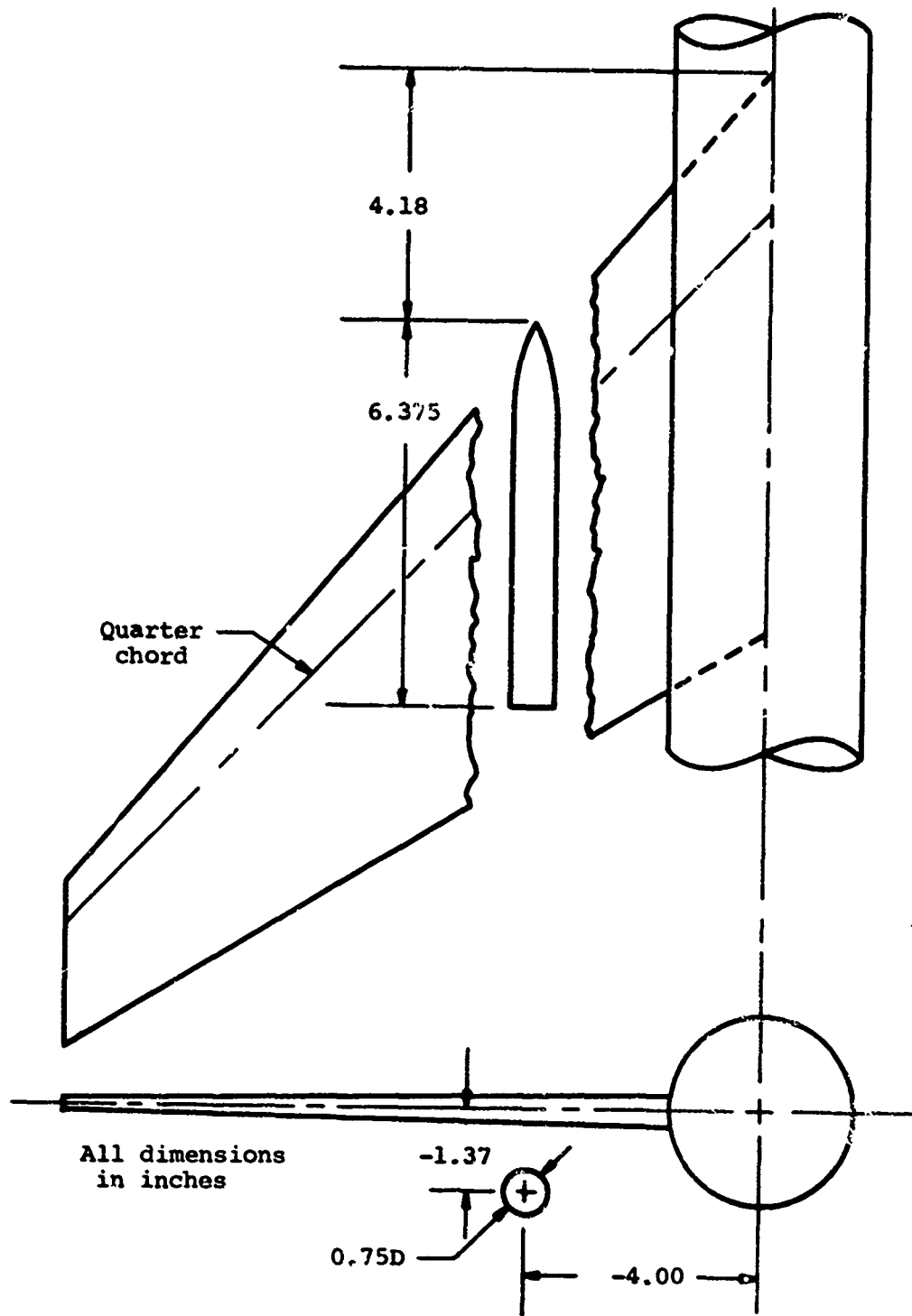
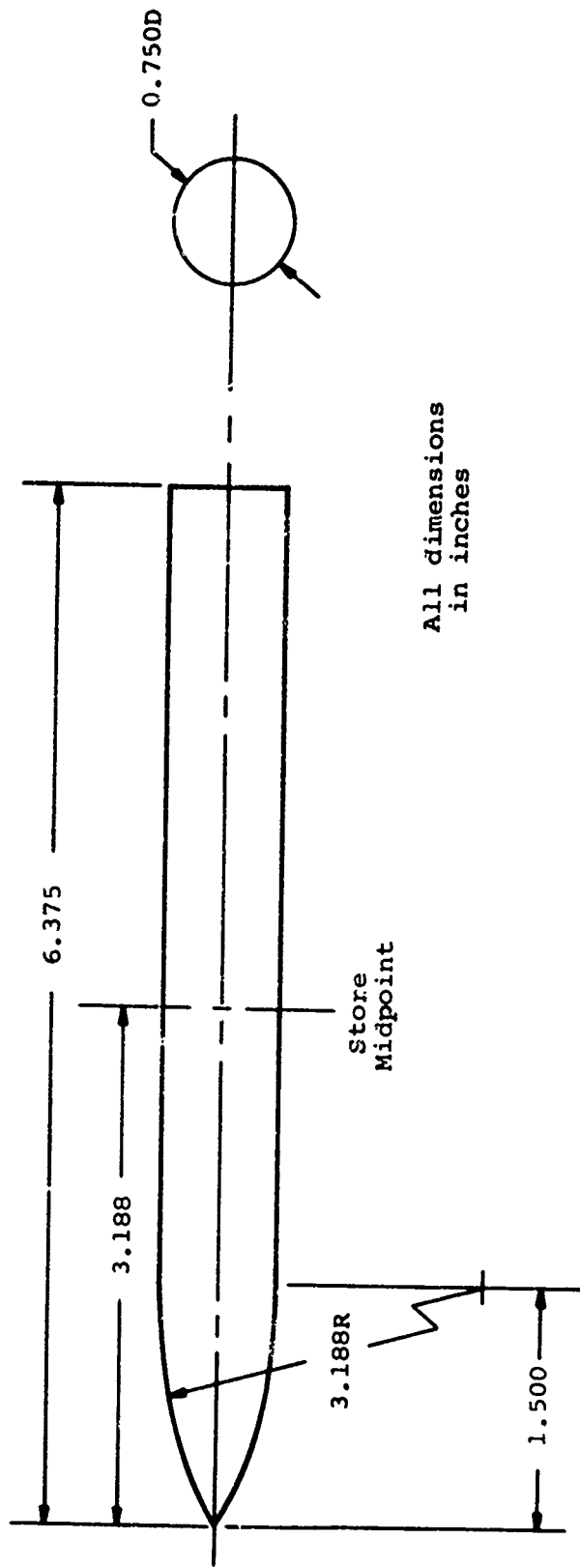


Figure 2.- Wing-fuselage combination used in reference 1.



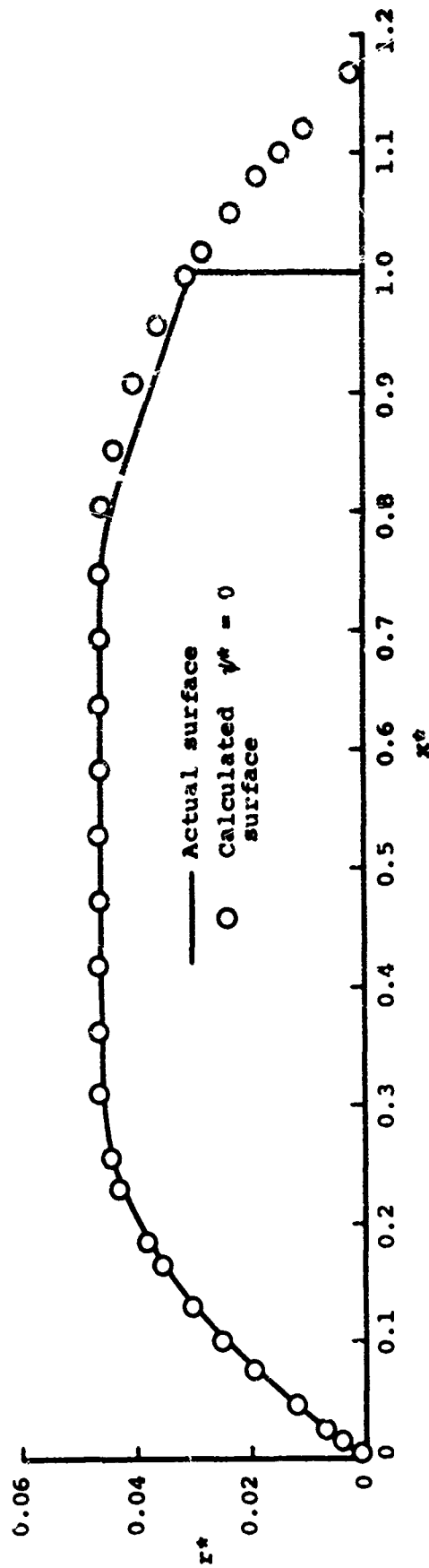
(a) Store location.

Figure 3.- Single store in the presence of the wing-fuselage combination of reference 1.

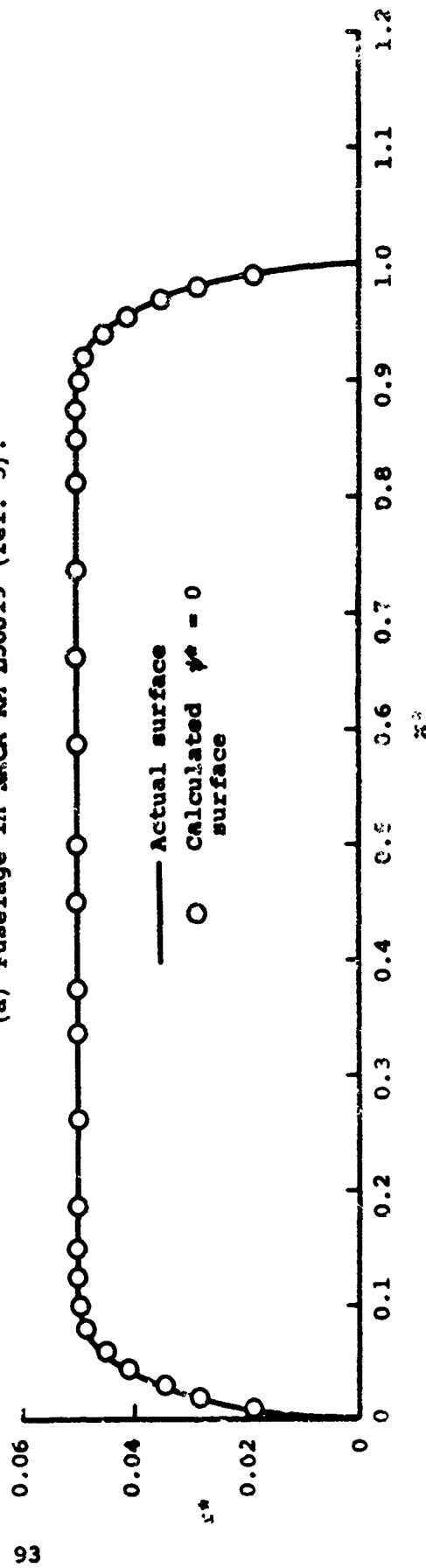


(b) Store details.

Figure 3.- Concluded.



(a) Fuselage in NACA RM L56J19 (ref. 5).



(b) Cylinder with ellipsoidal ends.

Figure 4.- Comparison between actual and calculated shapes for two axisymmetric bodies. (Note differences in x^* and r^* scales.)

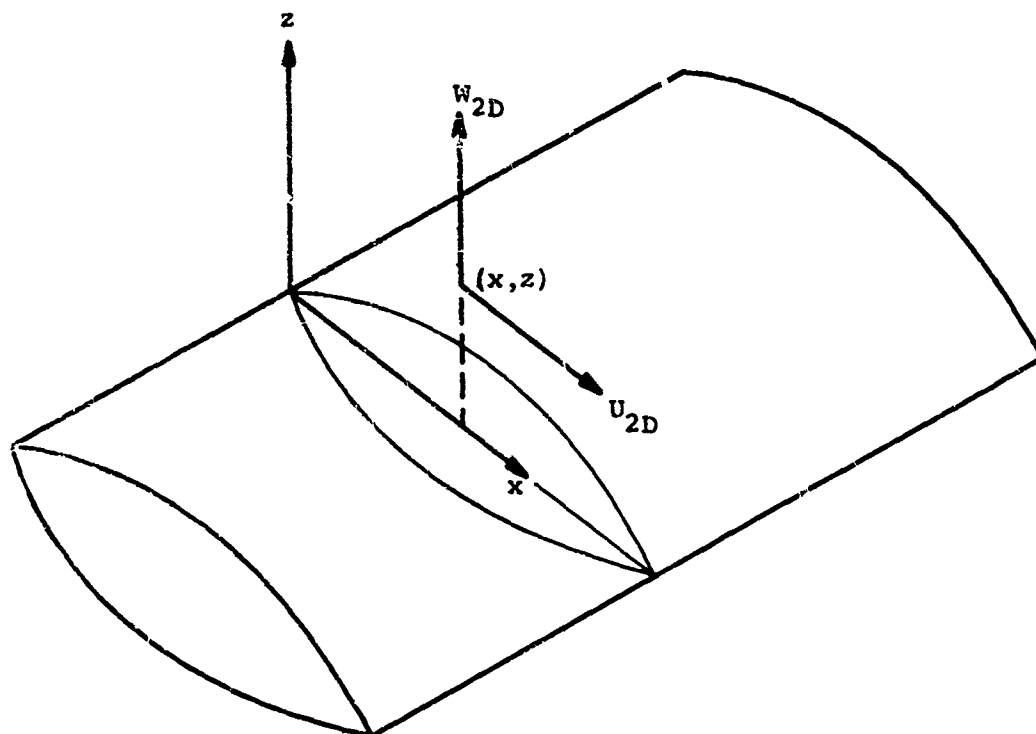


Figure 5.- Coordinate system for two-dimensional wing.

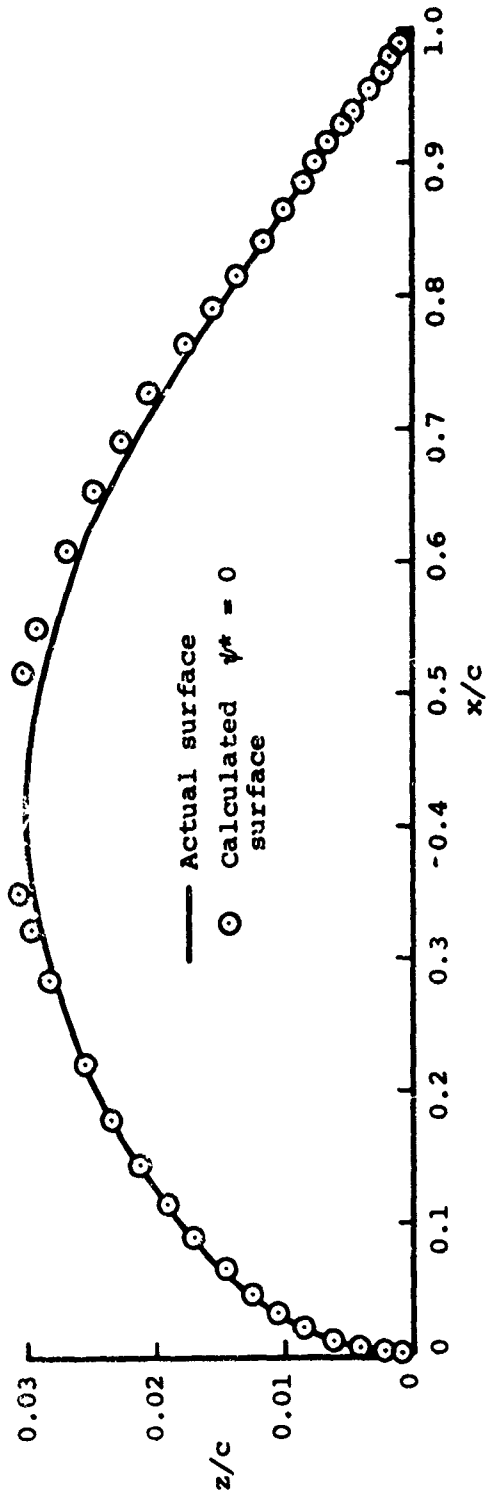


Figure 6.- Comparison between actual and calculated shapes for NACA 65A006 airfoil. (Note difference in z/c and x/c scales.)

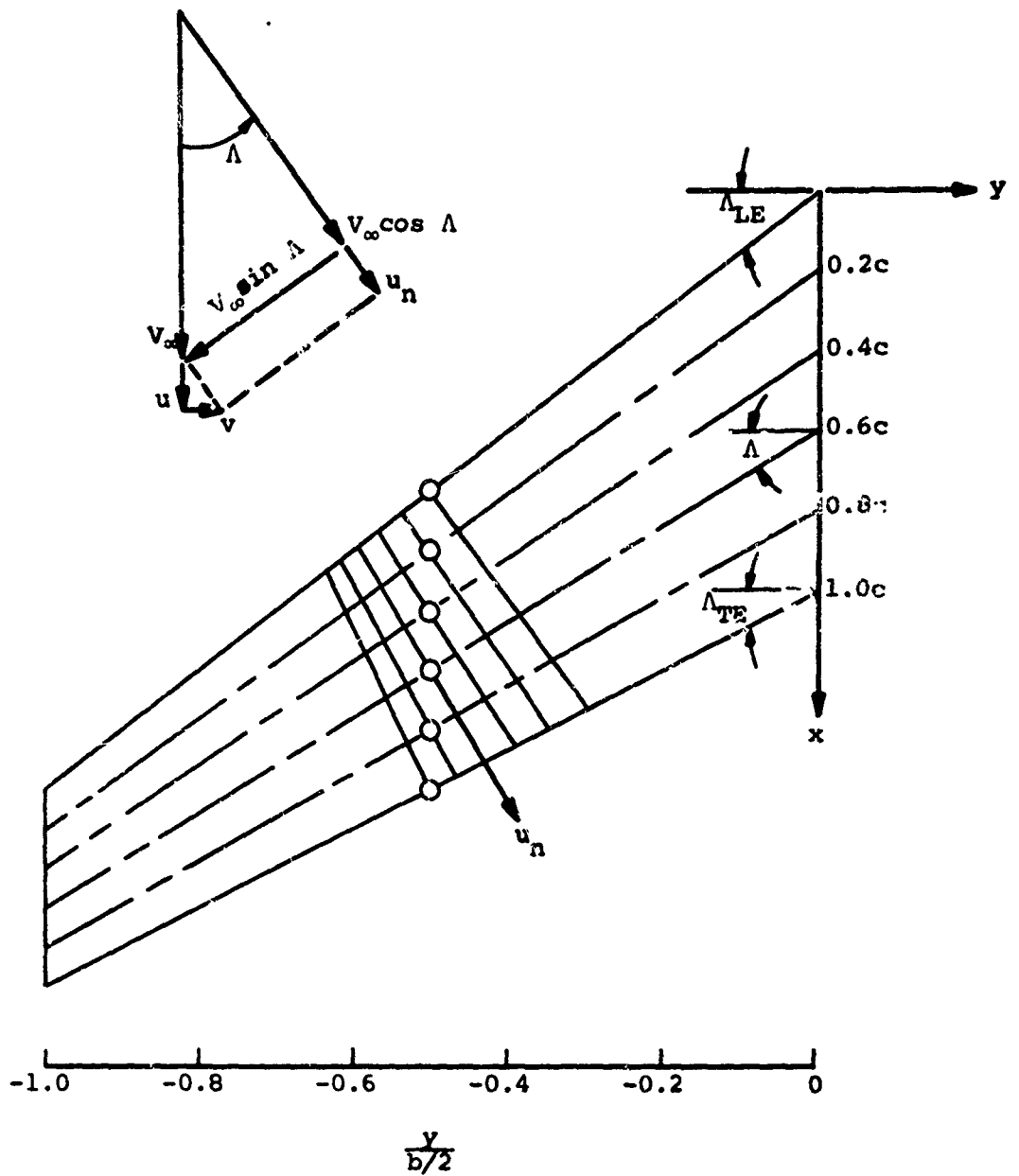


Figure 7.- Swept-wing configuration and flow velocities.

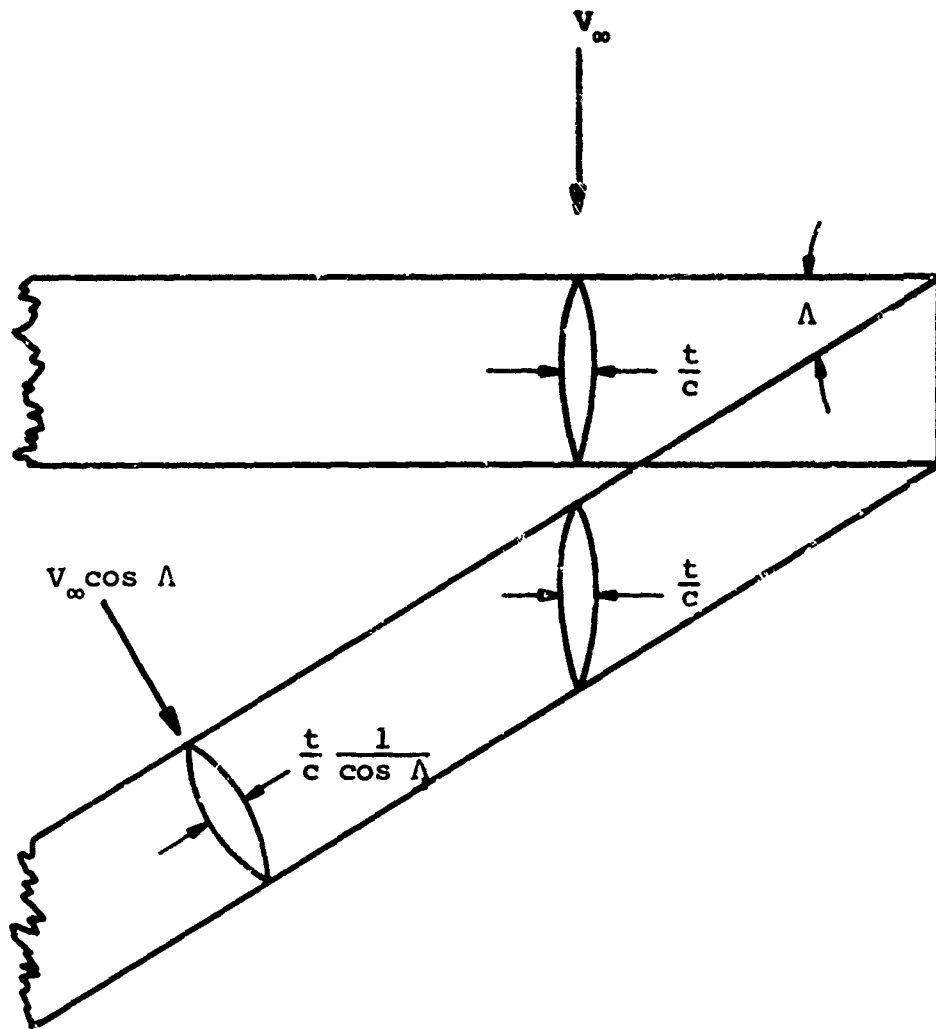


Figure 8.- Swept and unswept constant chord wings.

16

All dimensions in feet
Streamwise airfoil section, NACA 65A006

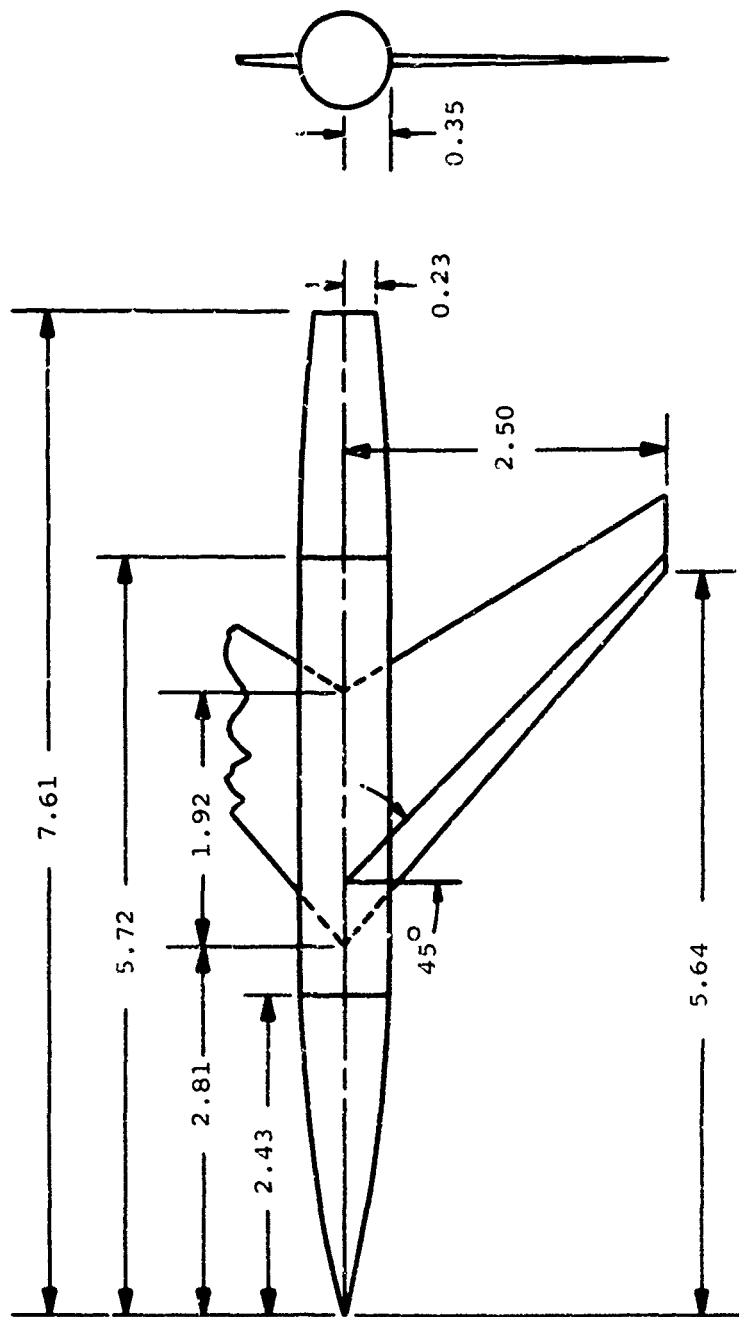
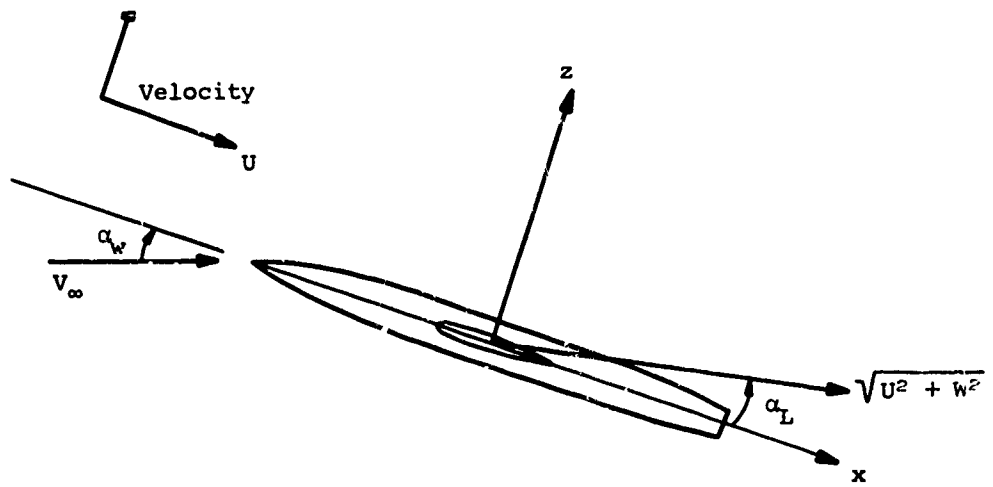
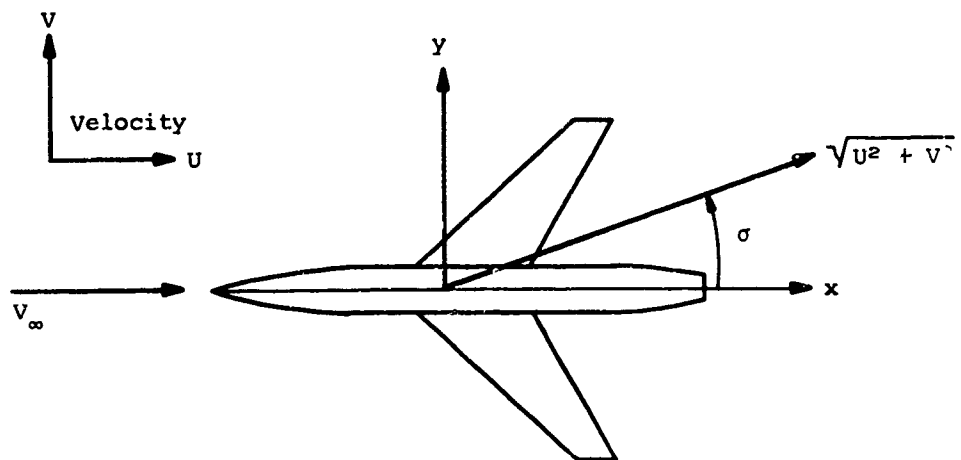


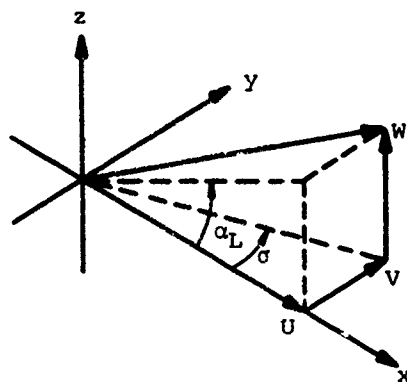
Figure 9.- Dimensions of wing-body configuration
of references 5 and 6.



(a) Local angle of attack.

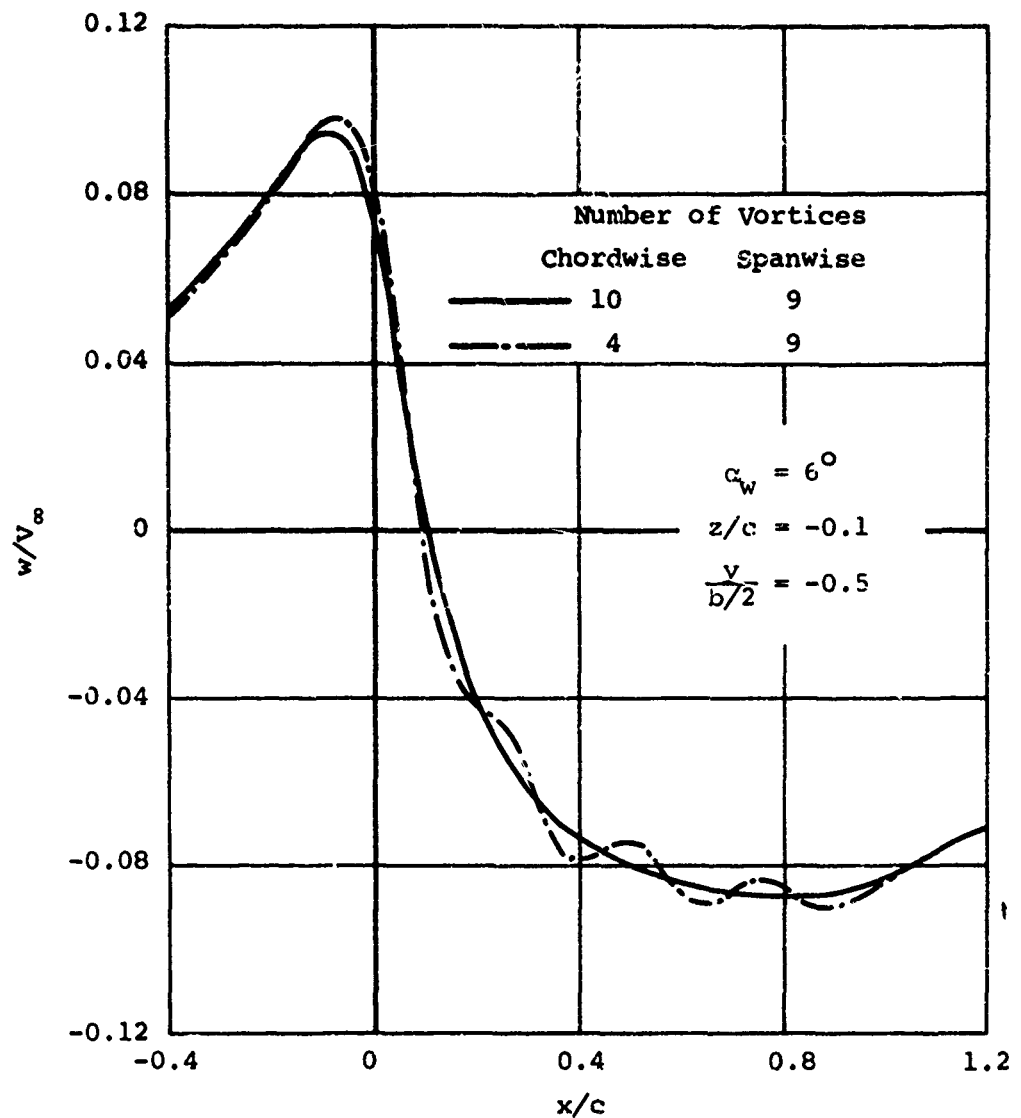


(b) Sidewash angle.



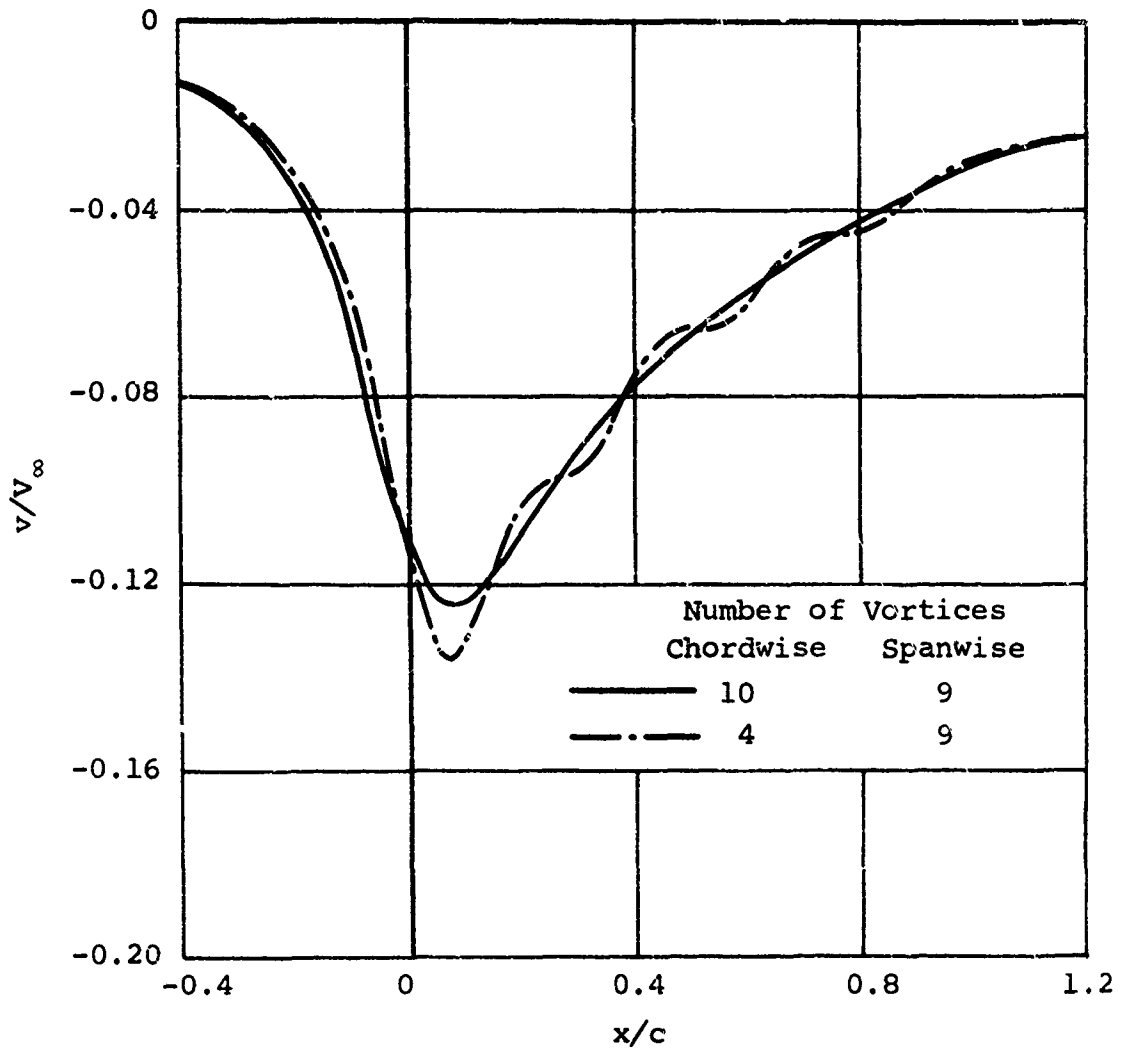
(c) Composite velocity diagram.

Figure 10.- Definitions of local angle of attack and sidewash angle.



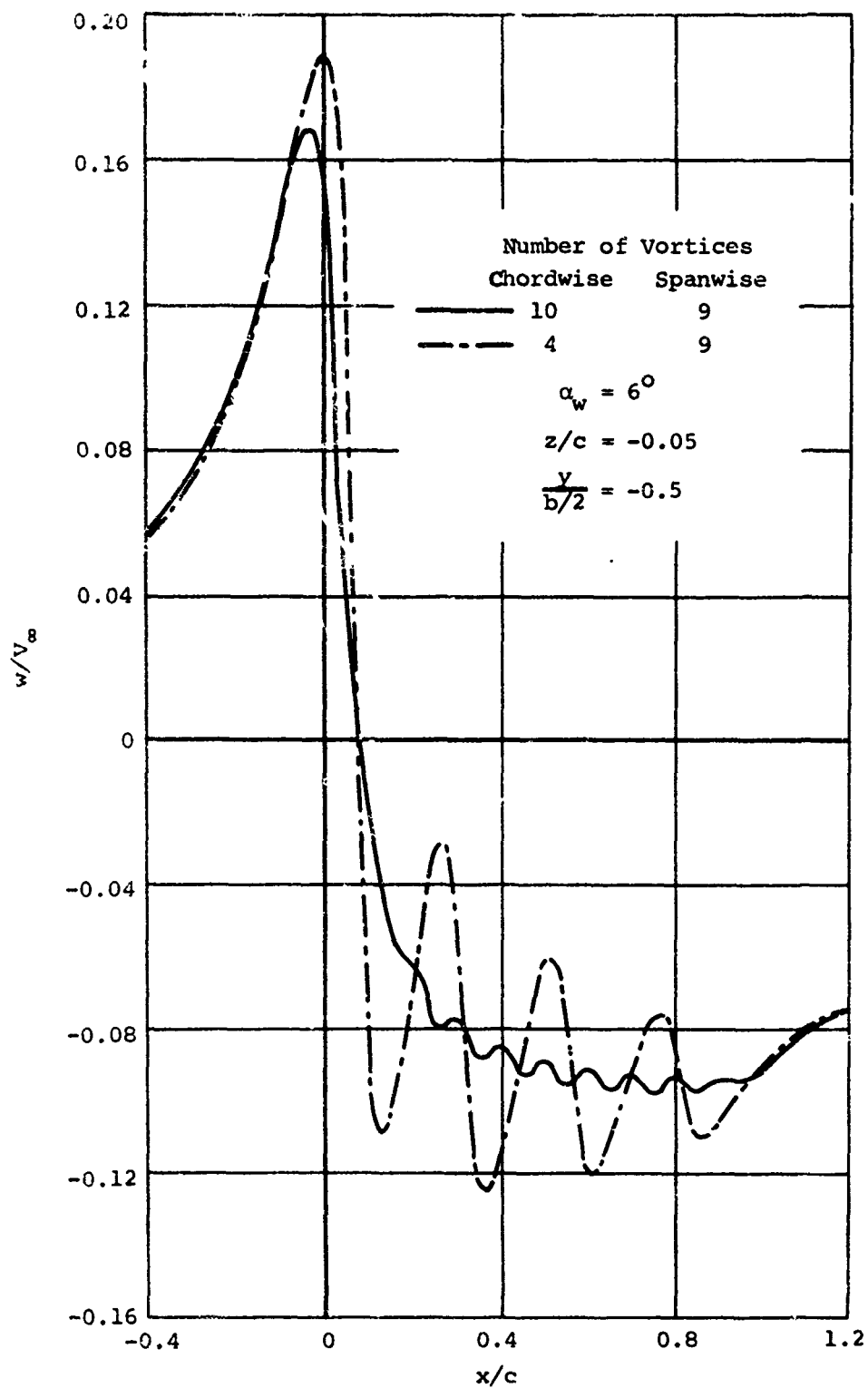
(a) Upwash perturbation velocity.

Figure 11.- Perturbation velocities due to angle of attack 10 percent of local chord beneath wing of example wing-body combination.



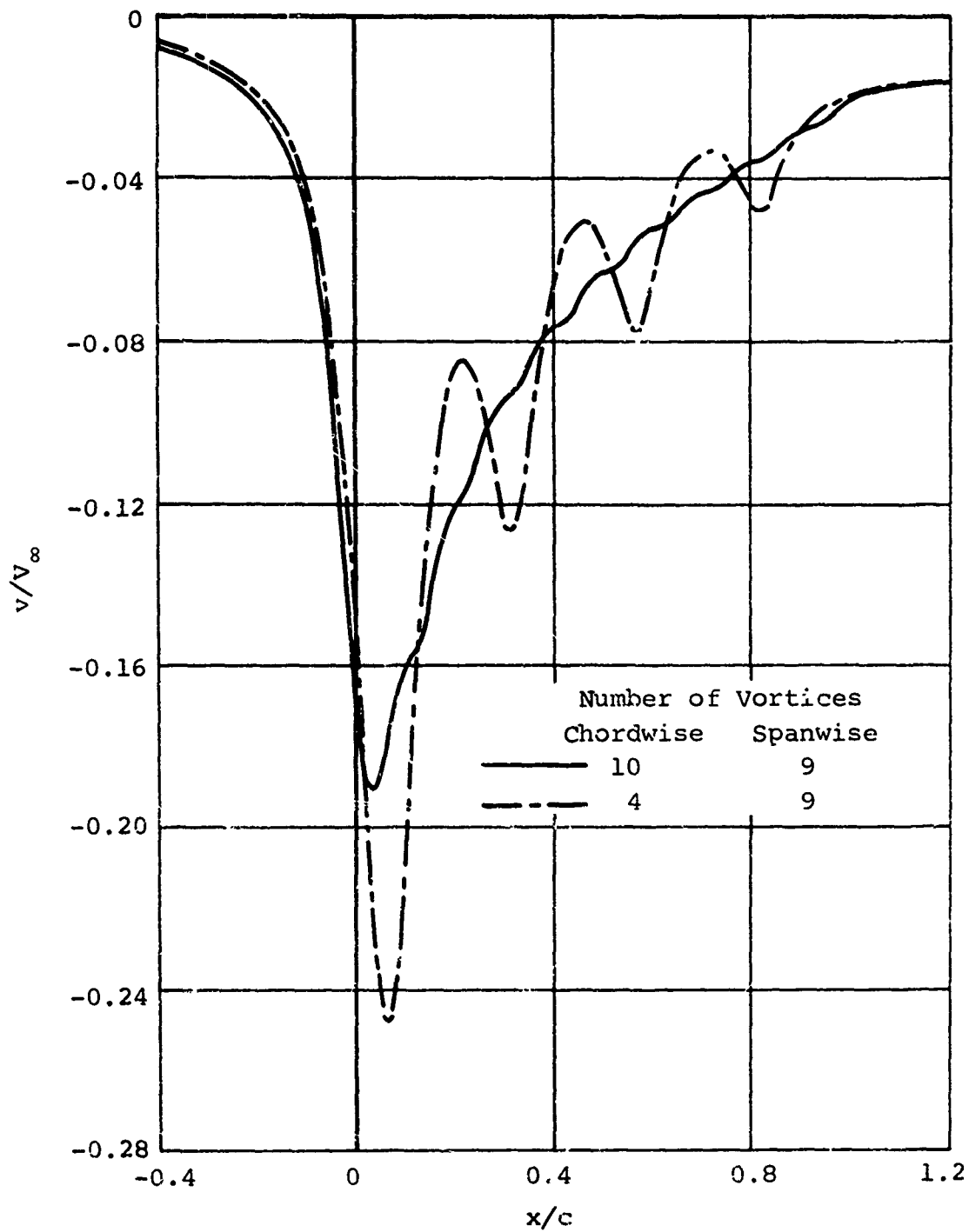
(b) Sidewash perturbation velocity.

Figure 11.- Continued.



(a) Upwash perturbation velocity.

Figure 12.- Perturbation velocities due to angle of attack 5 percent of the local chord beneath wing of example wing-body combination.

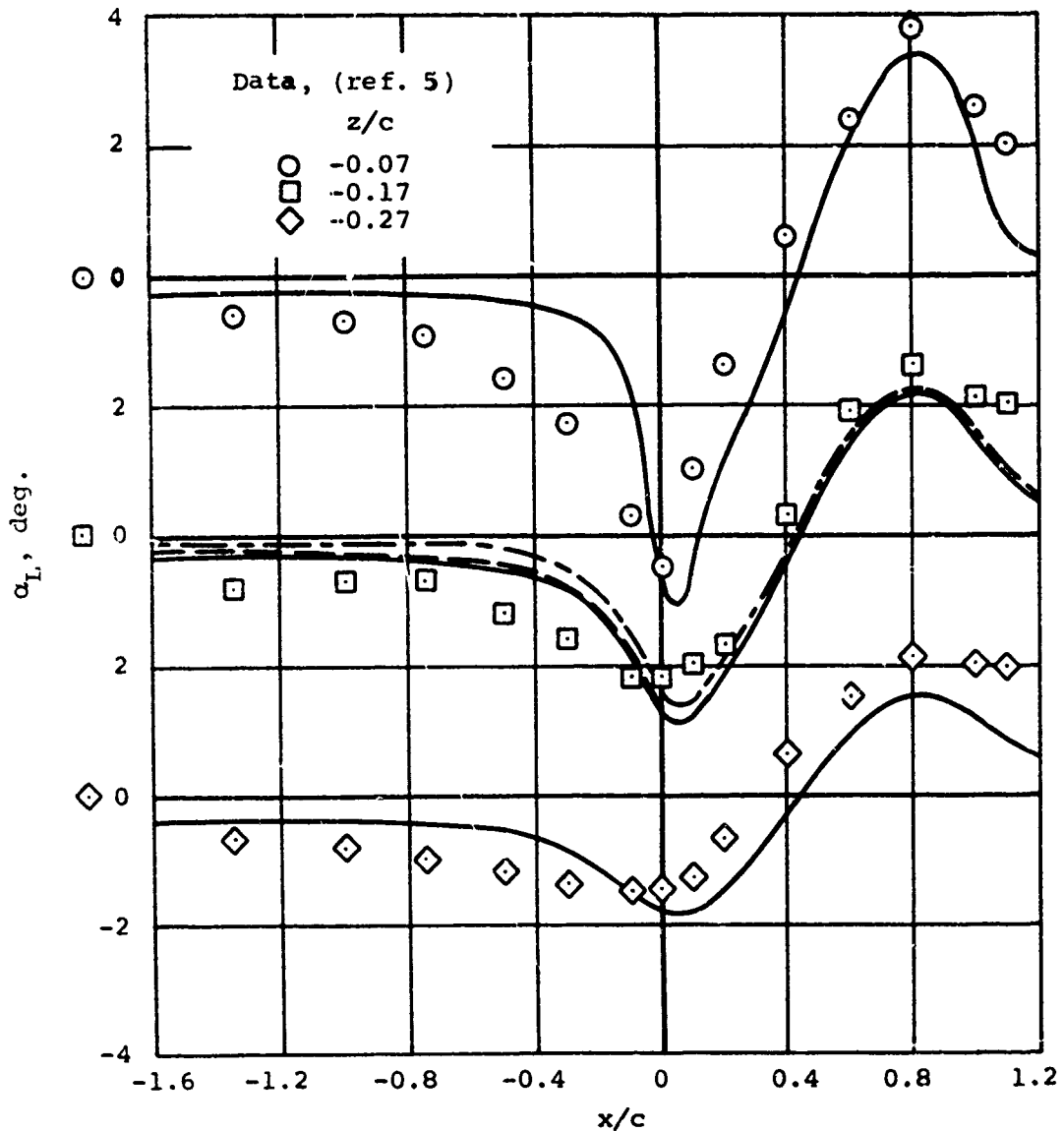


(b) Sidewash perturbation velocity.

Figure 12.- Concluded.

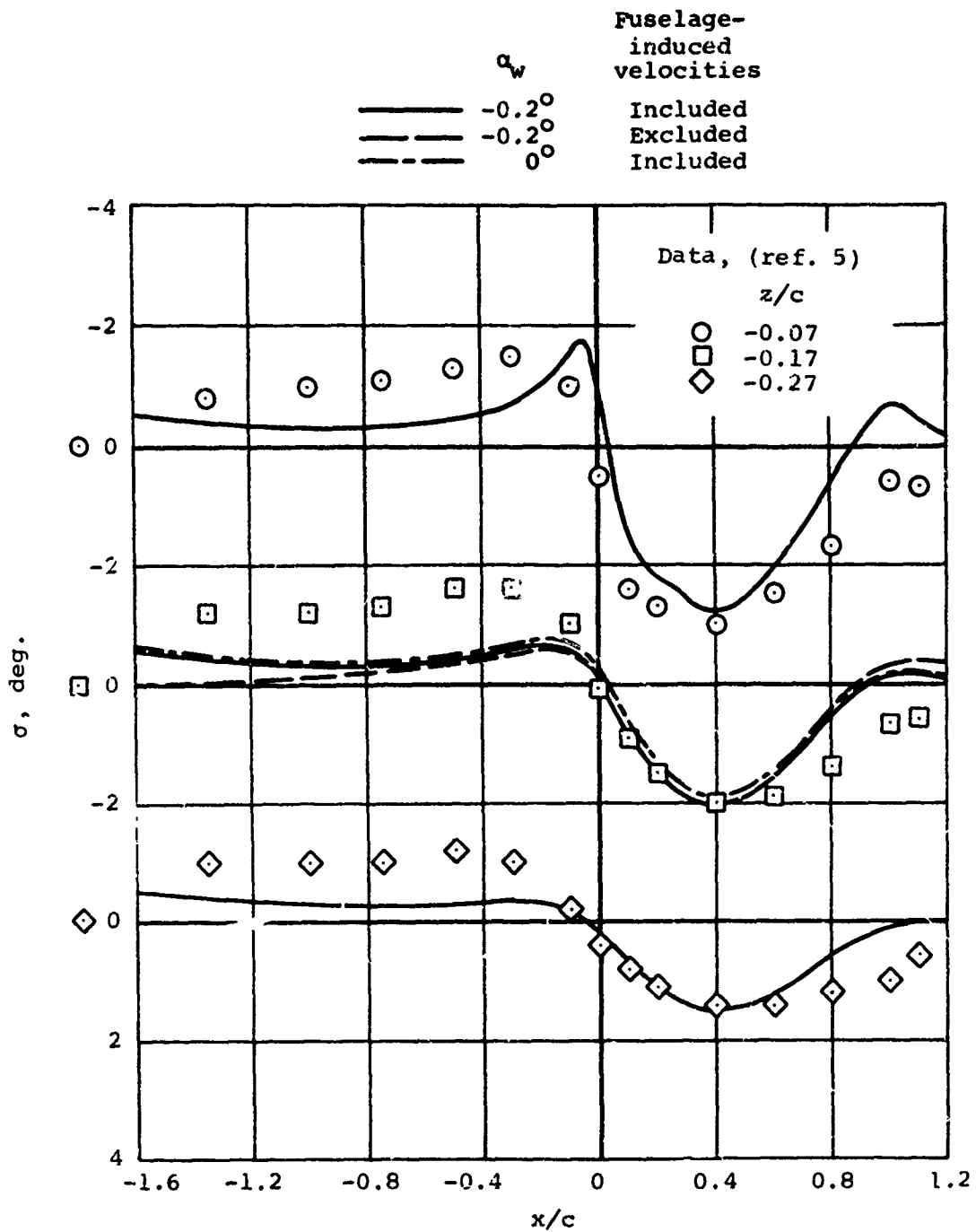
Calculations

	α_w	Fuselage-induced velocities
————	-0.2°	Included
-----	-0.2°	Excluded
- - - -	0°	Included



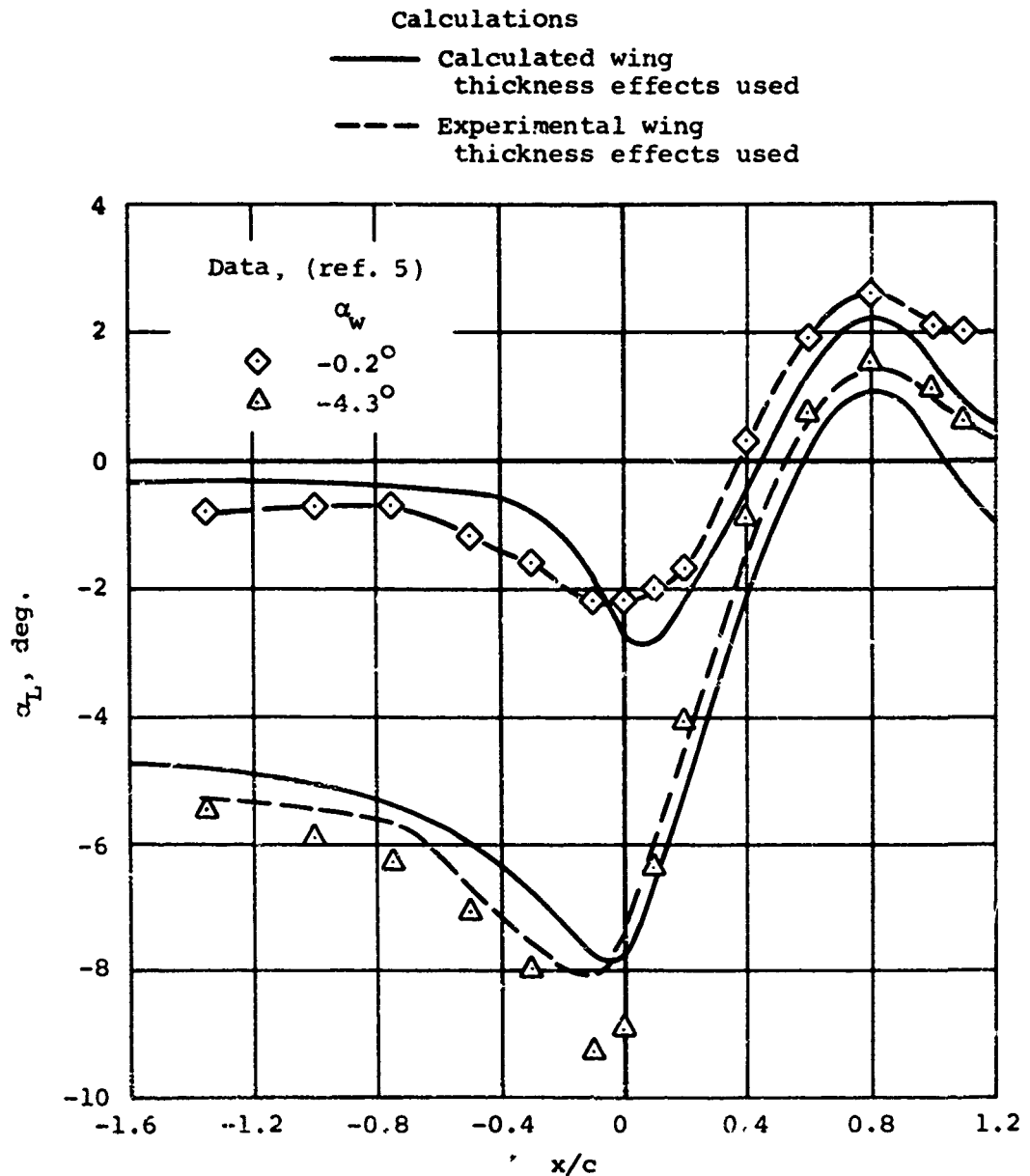
(a) Local angle of attack.

Figure 13.- Comparison between calculated and experimental local angle of attack and sidewash angle under the mid-semispan of wing-body configuration of figure 9; $\alpha_w = -0.2^\circ$.



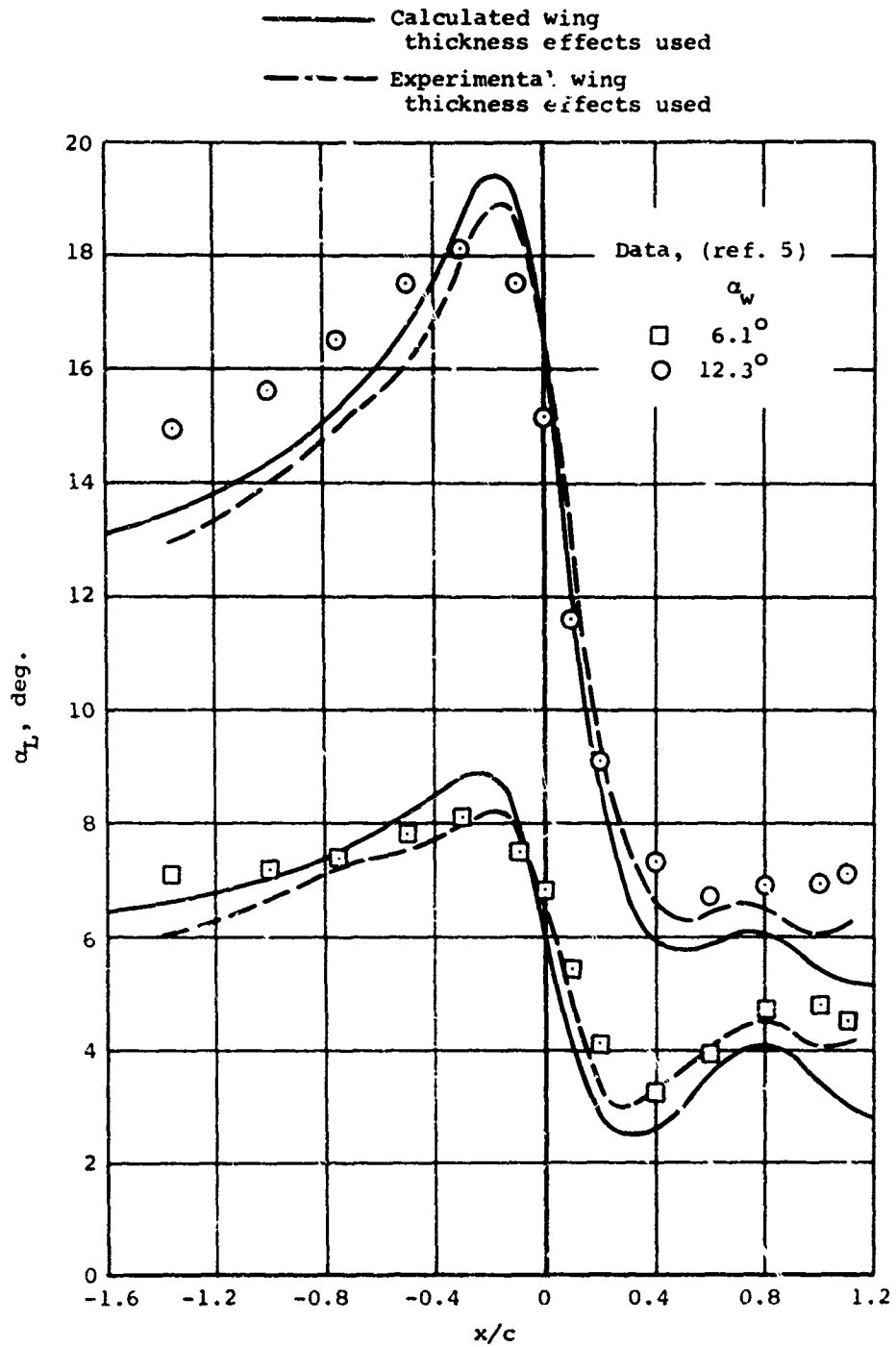
(b) Sidewash angle.

Figure 13.- Concluded.



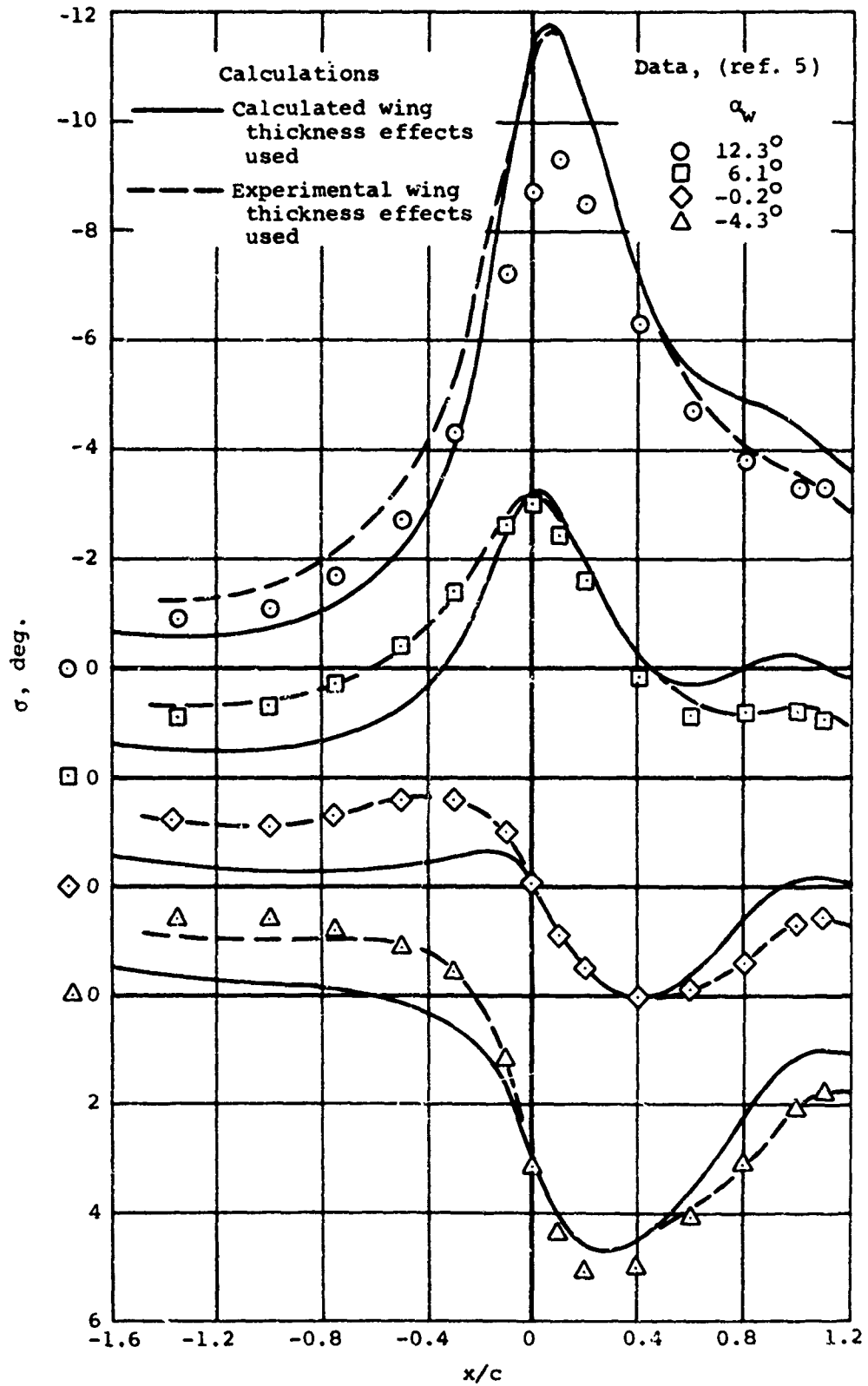
(a) Local angle of attack with $\alpha_w = -0.2^\circ$ and -4.3° .

Figure 14.- Comparison between calculated and experimental local angle of attack and sidewash angle under wing-body configuration of figure 9 at the mid-semispan 17 percent of the local chord below the wing for various angles of attack.



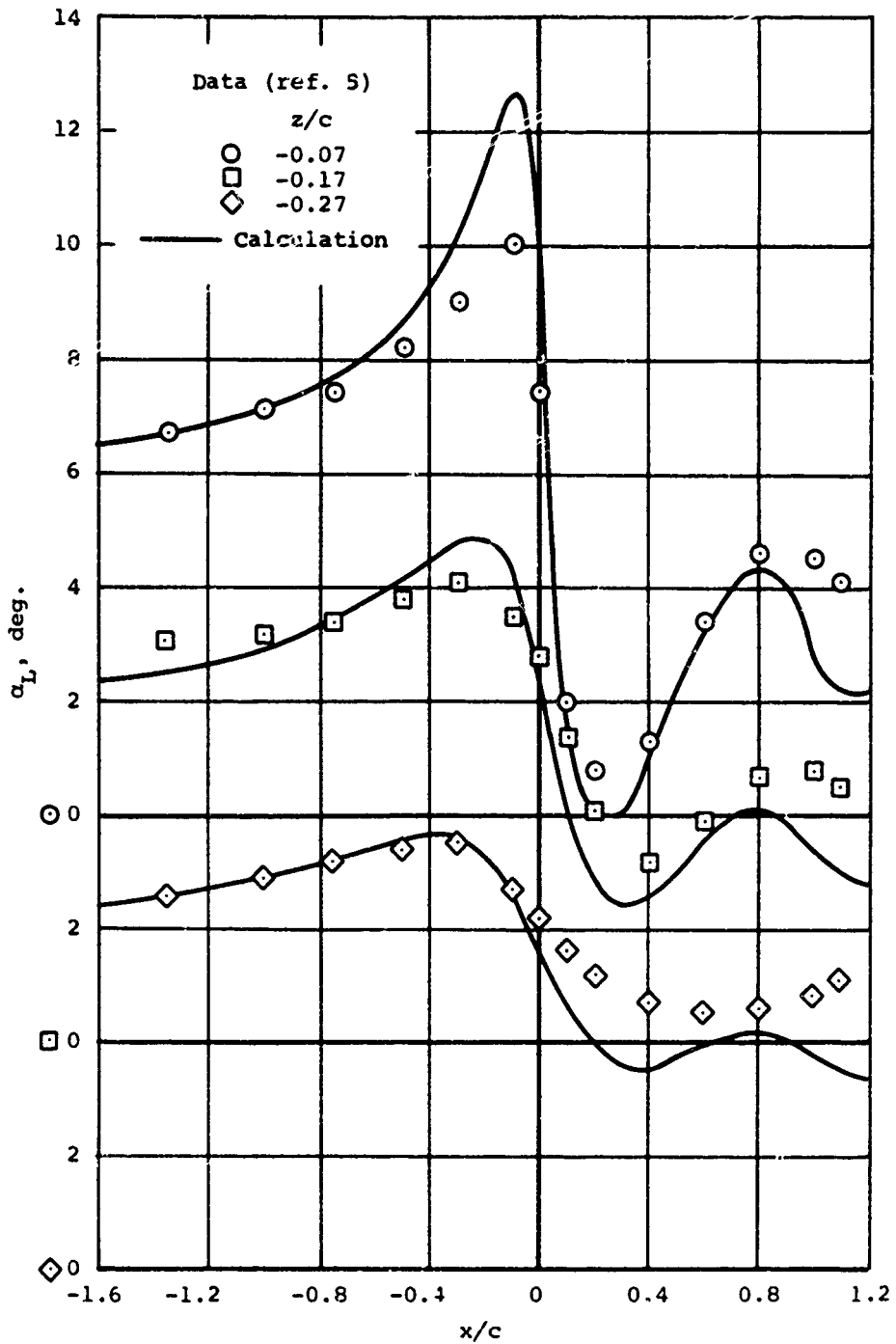
(b) Local angle of attack with $\alpha_w = 6.1^\circ$ and 12.3° .

Figure 14.- Continued.



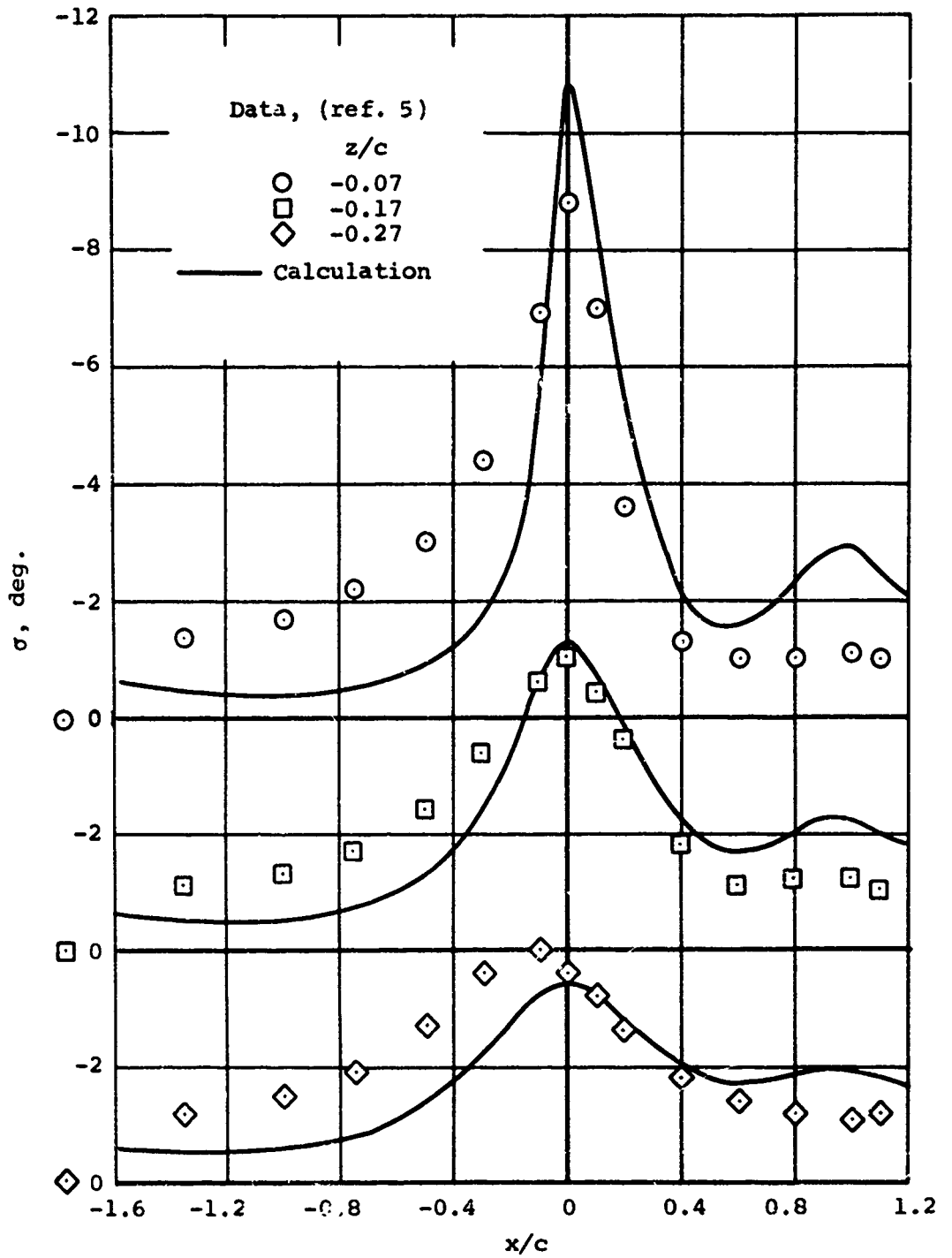
(c) Sidewash angle.

Figure 14.- Concluded.



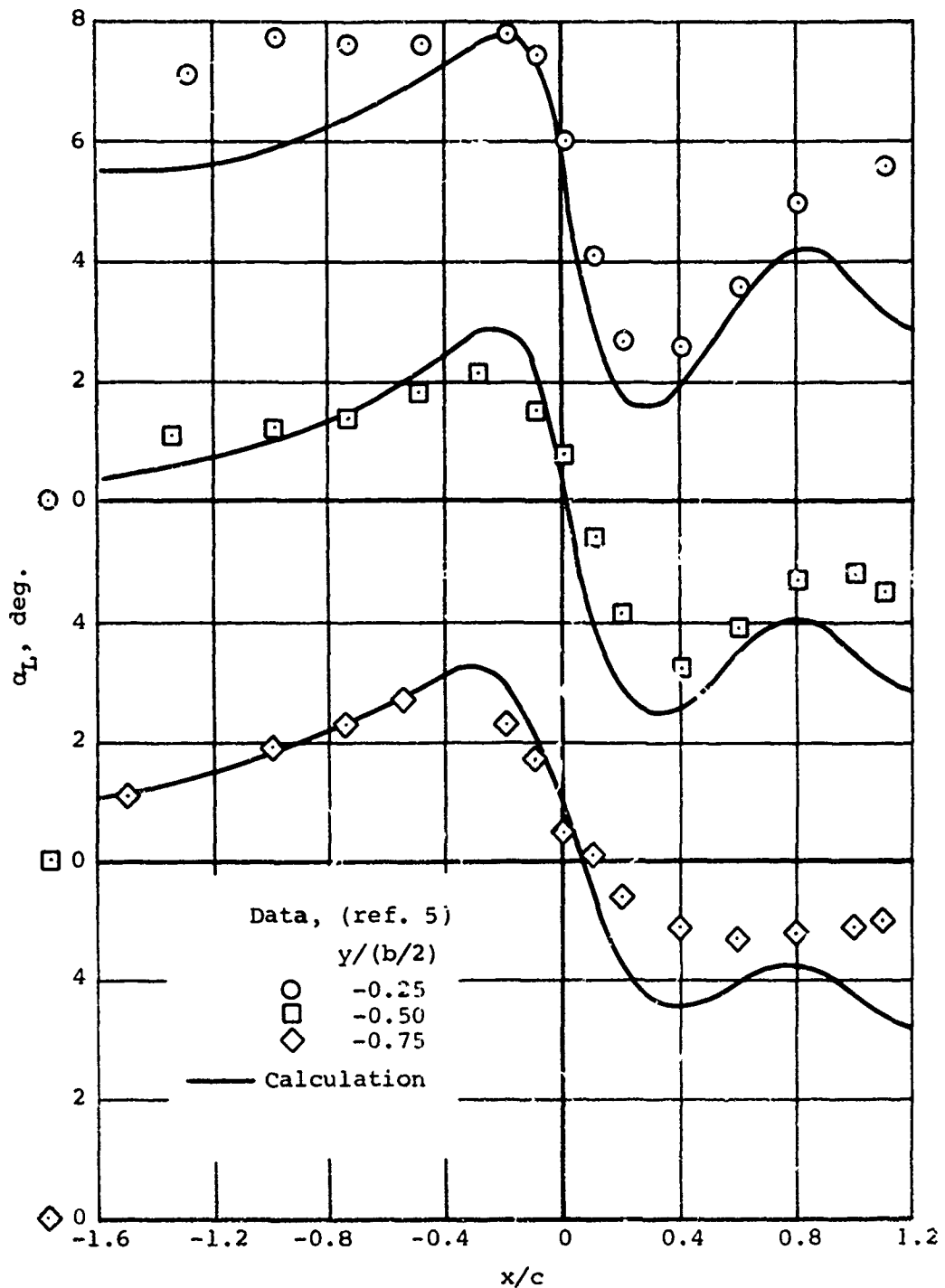
(a) Local angle of attack.

Figure 15.- Comparison between calculated and experimental local angle of attack and sidewash angle under wing-body configuration of figure 9 at the mid-semispan at an angle of attack of 6.1° .



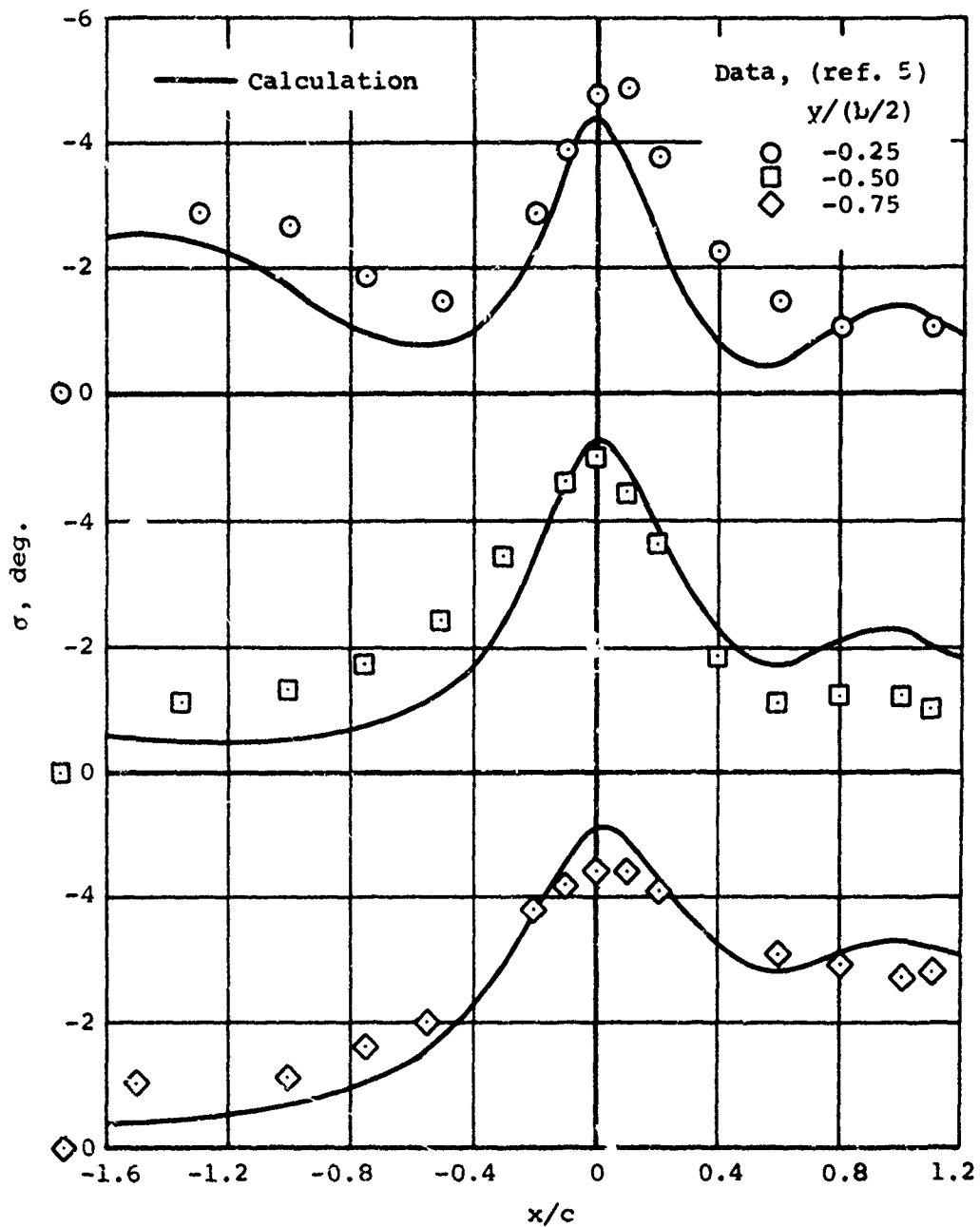
(b) Sidewash angle.

Figure 15.- Concluded.



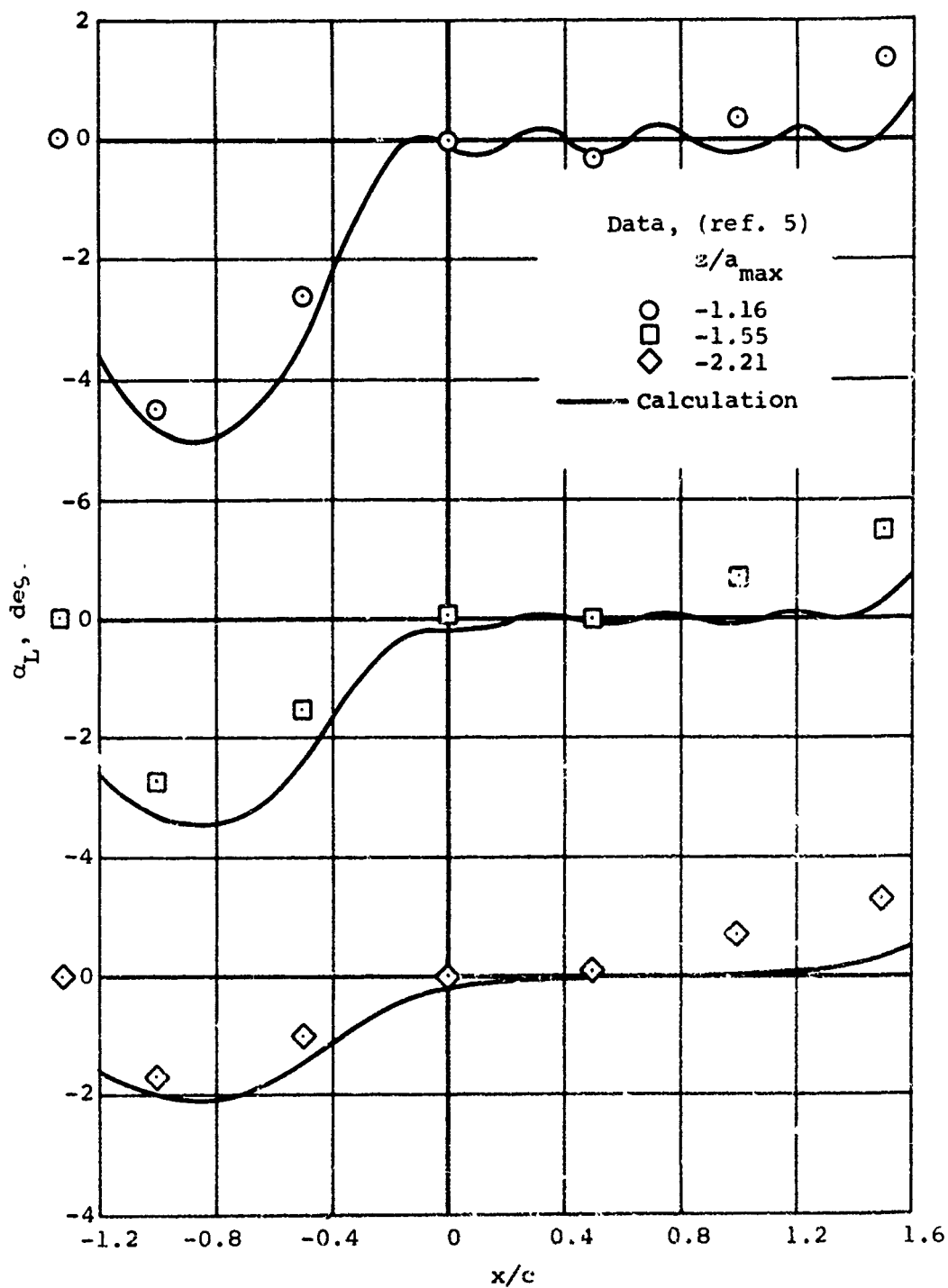
(a) Local angle of attack.

Figure 16.- Comparison between calculated and experimental local angle of attack and sidewash angle under wing-body configuration of figure 9 at 17 percent of the local chord below the wing at an angle of attack of 6.1° .



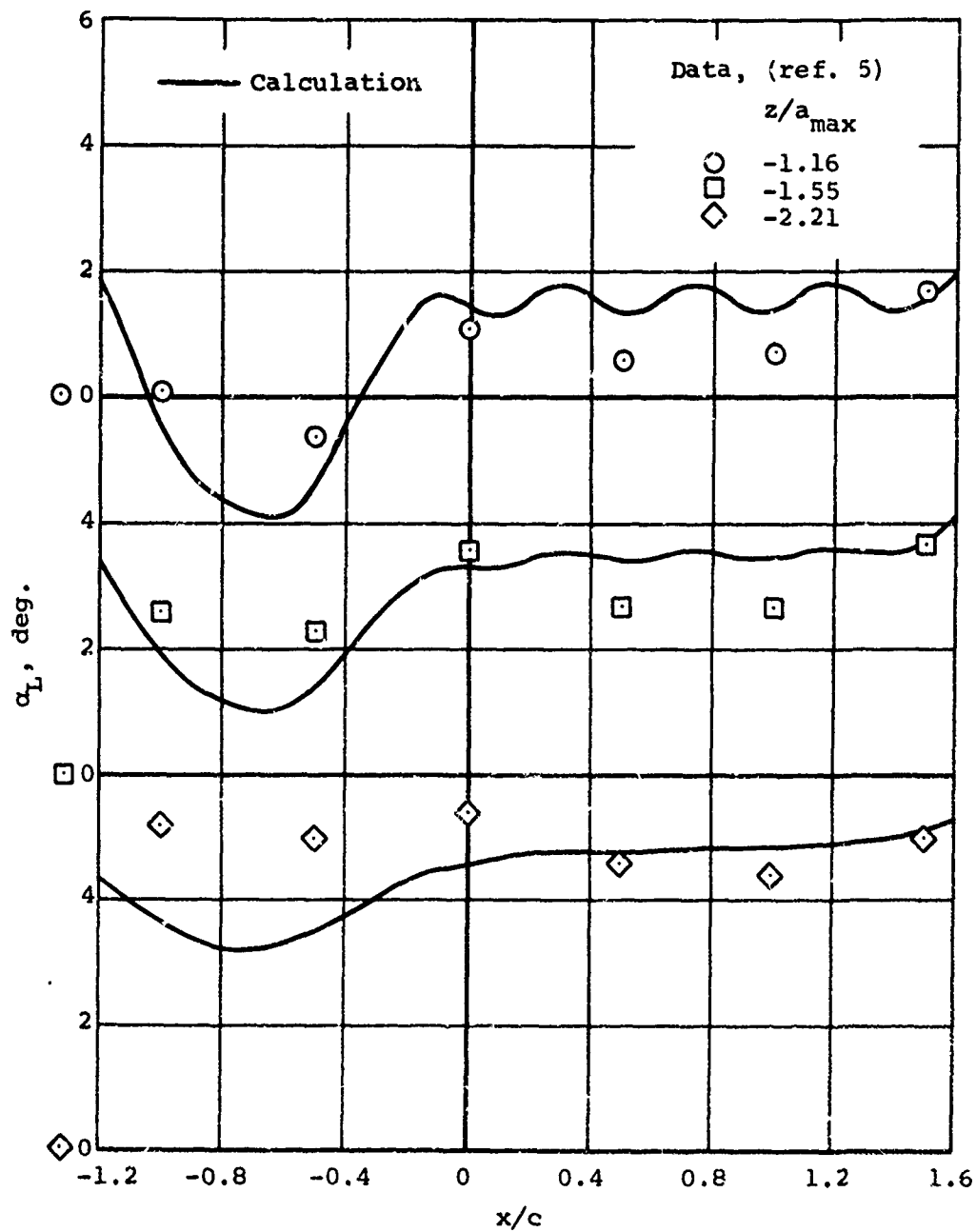
(b) Sidewash angle.

Figure 16.- Concluded.



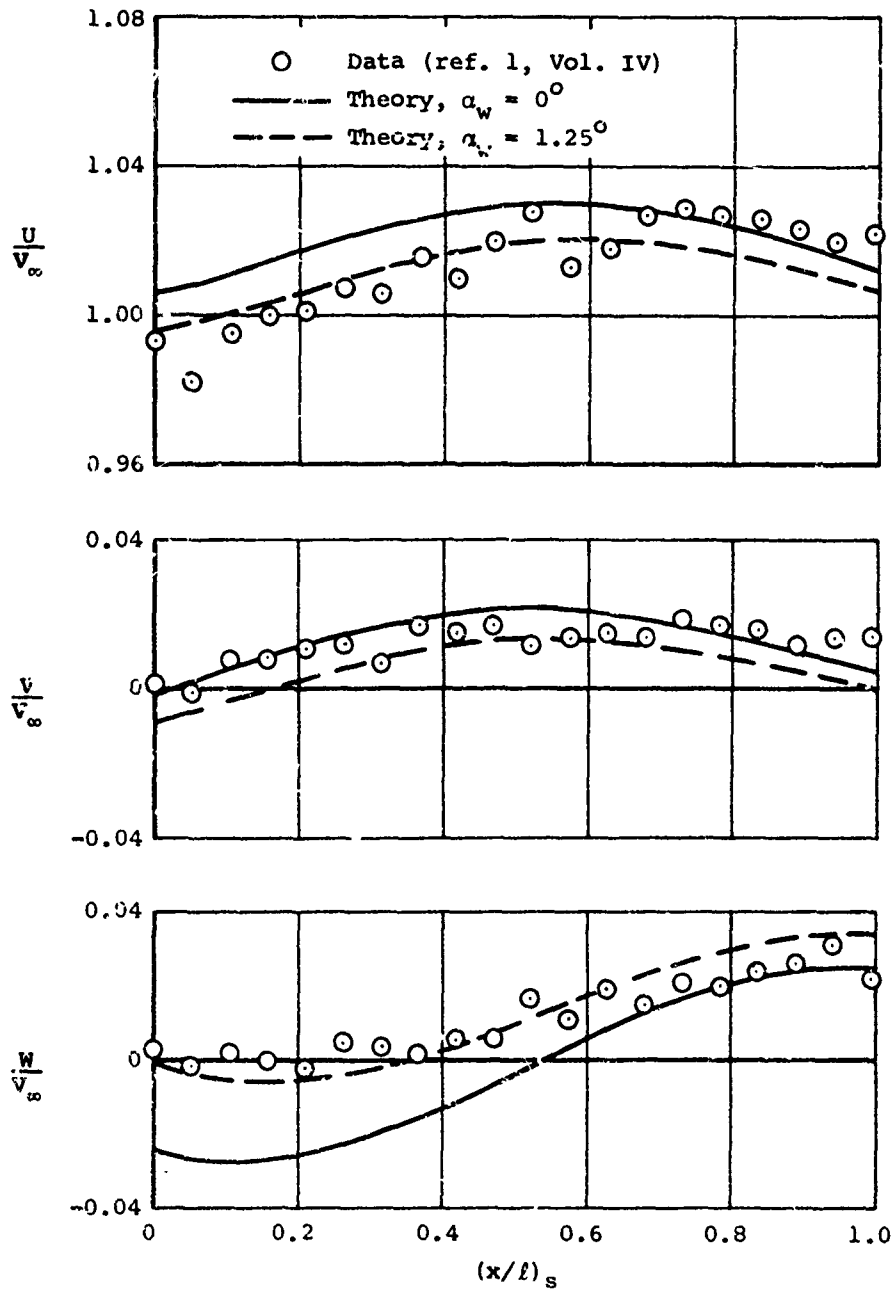
(a) $\alpha_w = -0.2^\circ$.

Figure 17.- Comparison between calculated and experimental local angle of attack under the fuselage centerline of wing-body configuration of figure 9 for various distances below the fuselage.



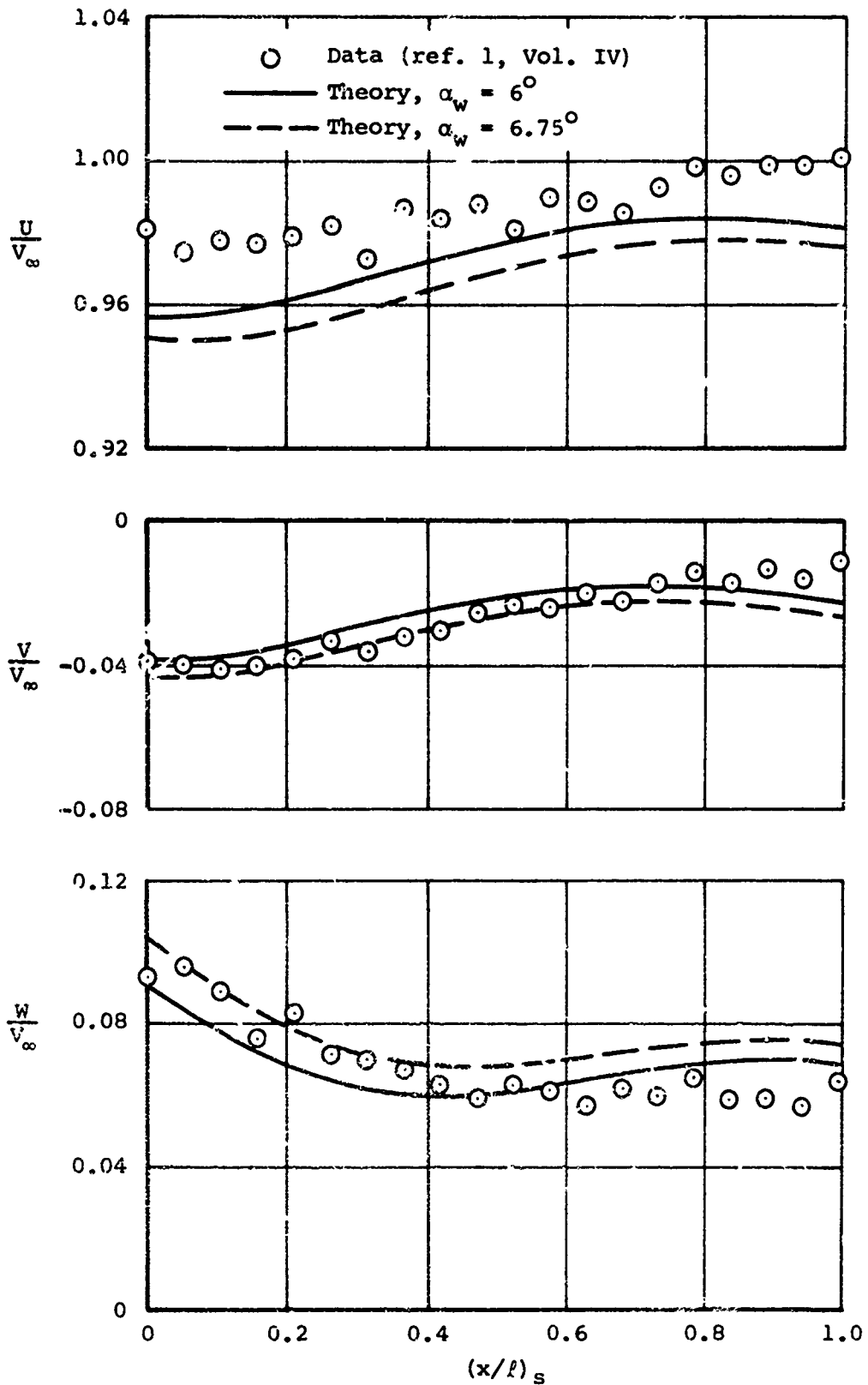
(b) $\alpha_w = 6.1^\circ$.

Figure 17.- Concluded.



(a) $\alpha_p = 0^\circ$.

Figure 18.- Comparison between calculated and experimental velocity field at the 1/3 semispan of the left wing panel of wing-body configuration of figure 1; $M_\infty = 0.25$, $z/c = -0.30$.



(k) $\alpha_p = 6^\circ$.

Figure 18.- Concluded.

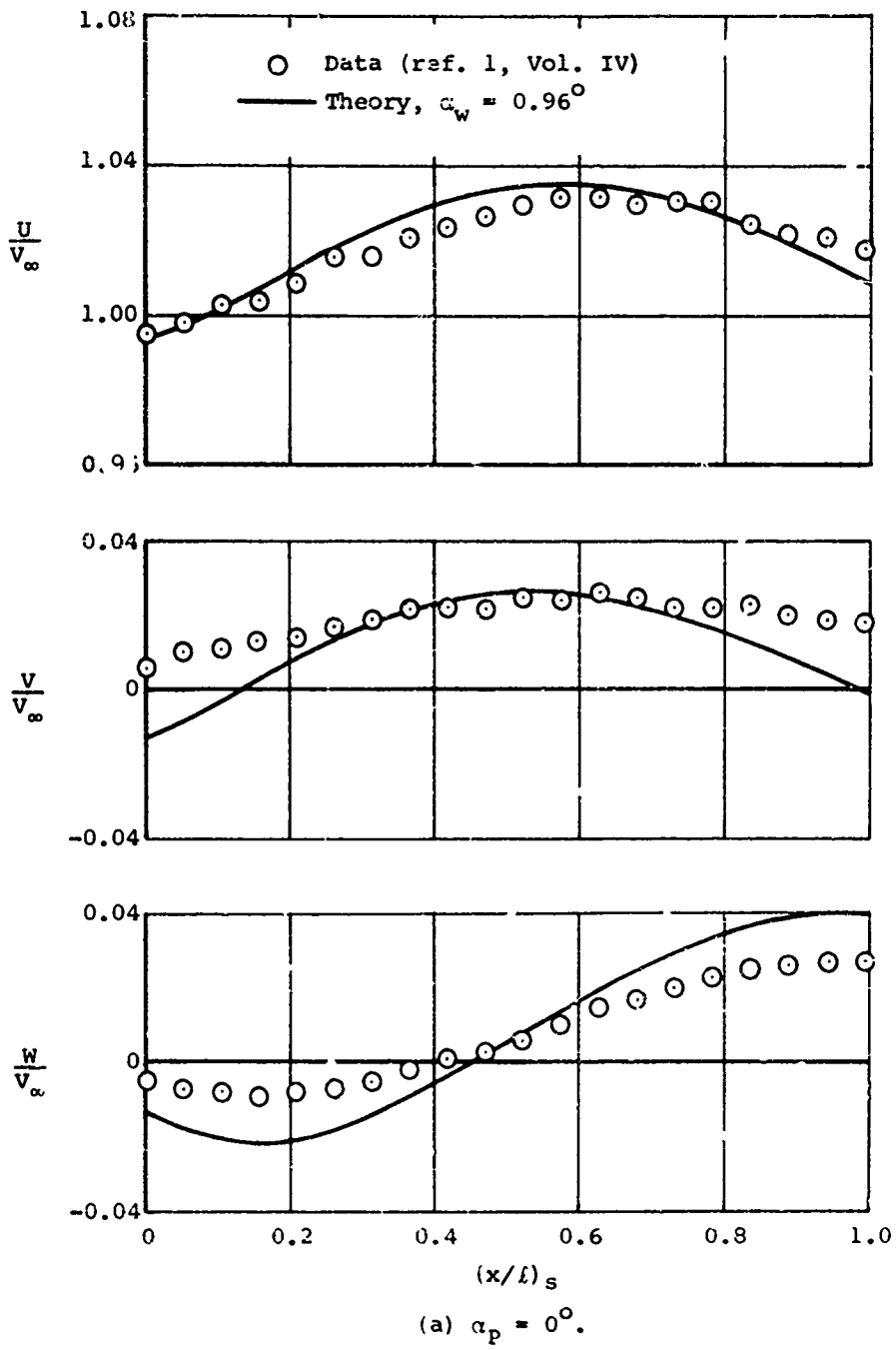
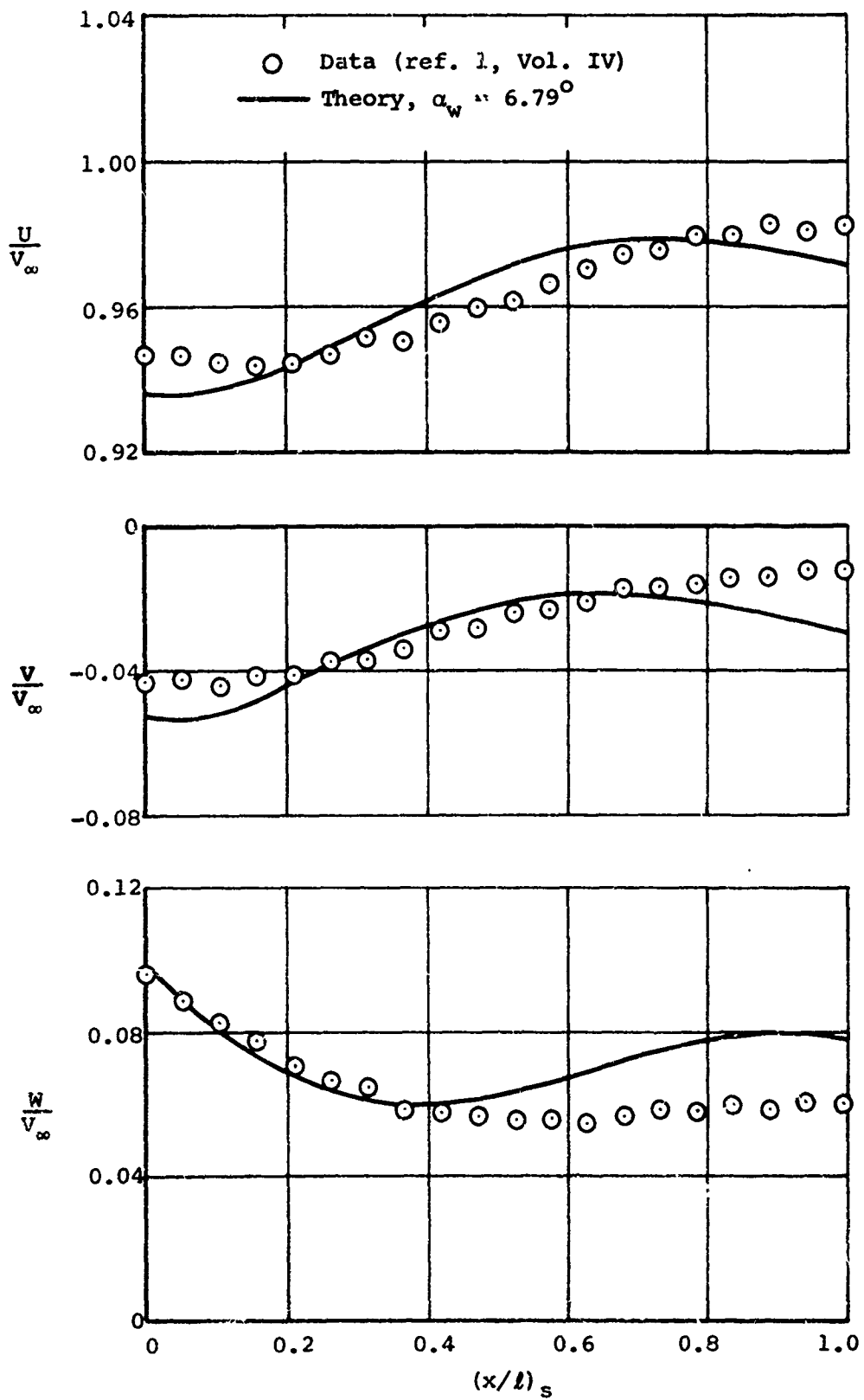


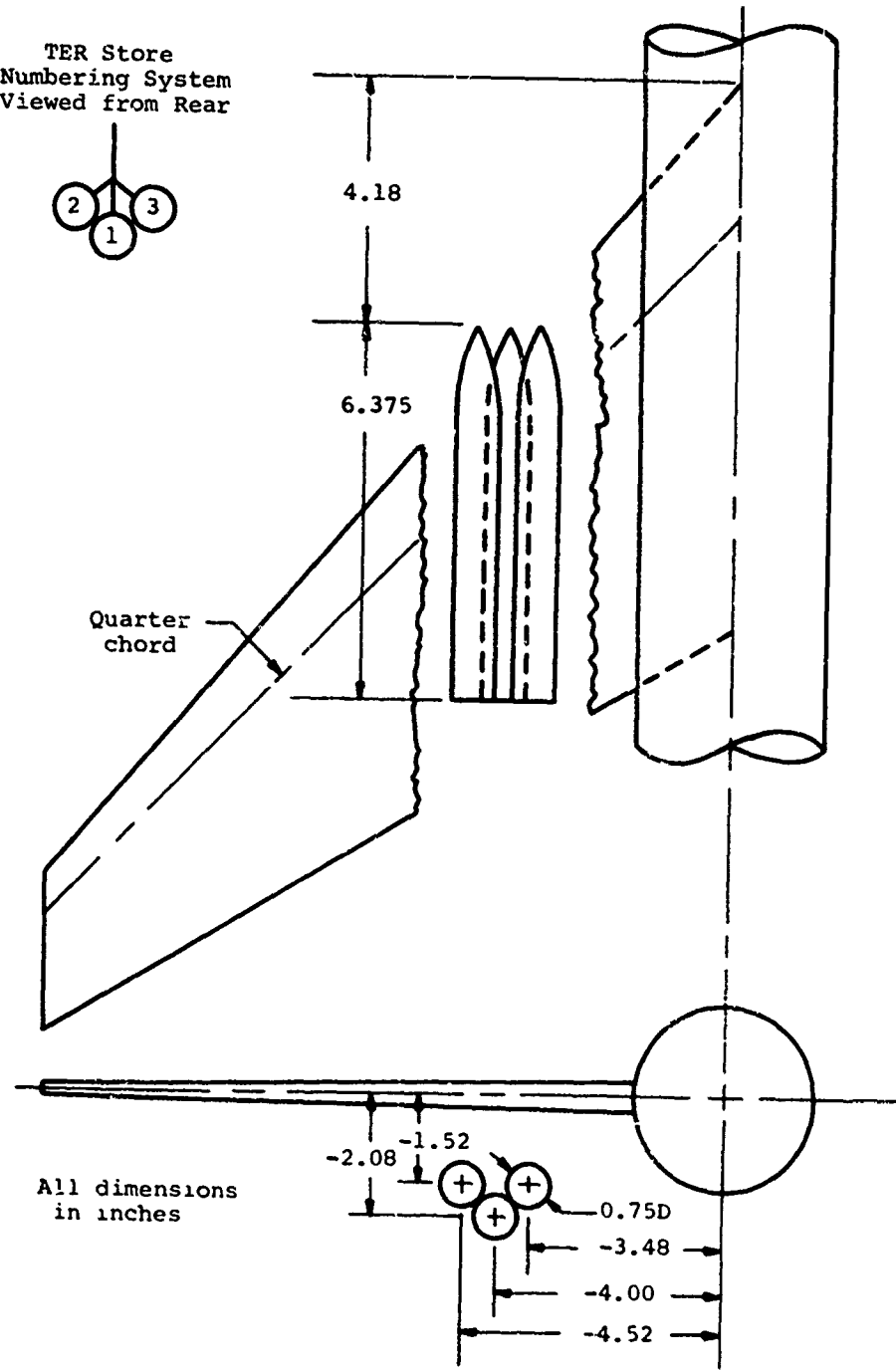
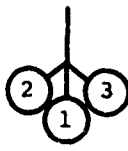
Figure 19.- Comparison between calculated and experimental velocity field at the 1/3 semispan of the left wing panel of wing-body configuration of figure 1; $M_\infty = 0.70$, $z/c = -0.30$.



(b) $\alpha_p = 6^\circ$.

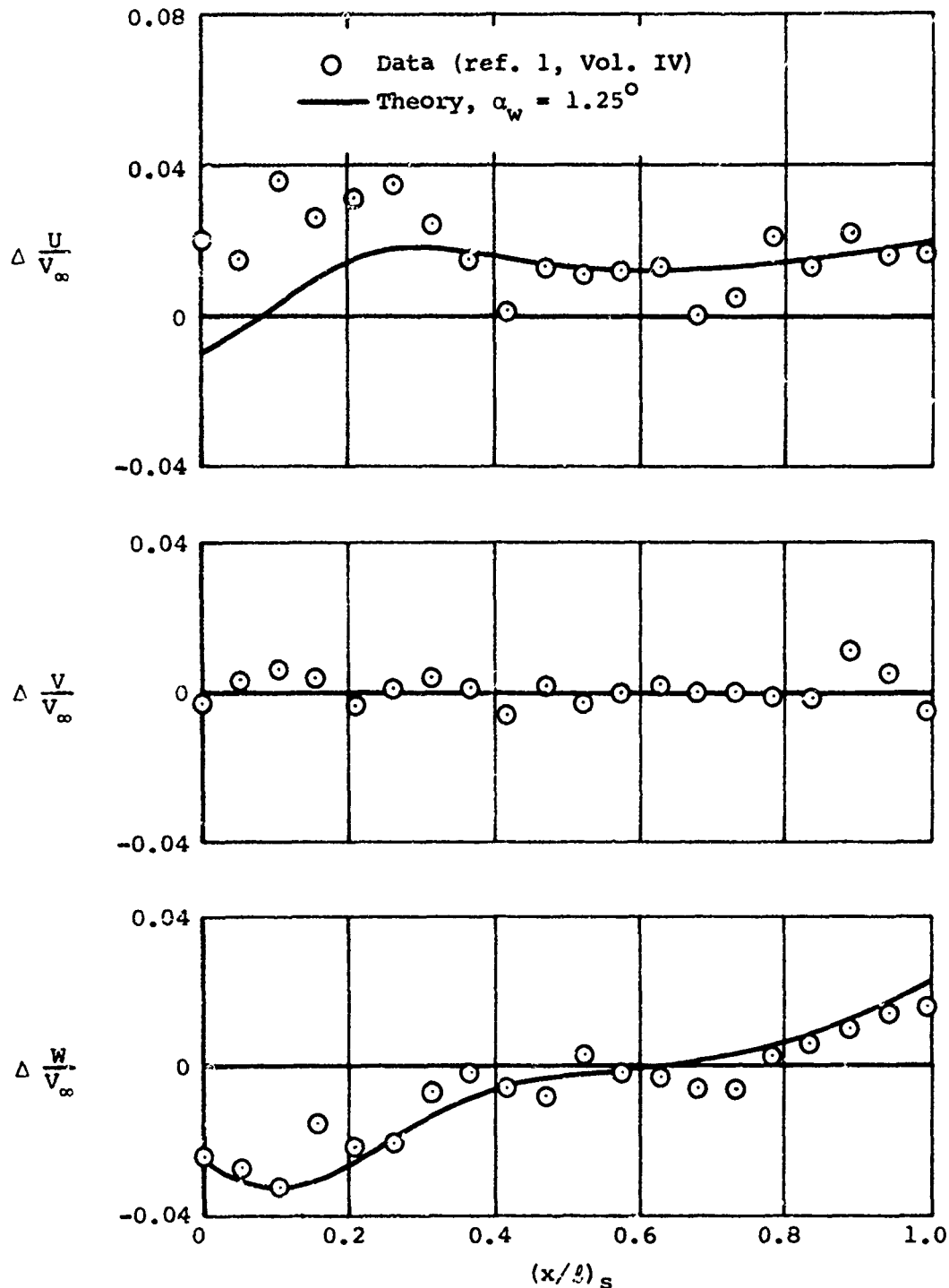
Figure 19.- Concluded.

TER Store
Numbering System
Viewed from Rear



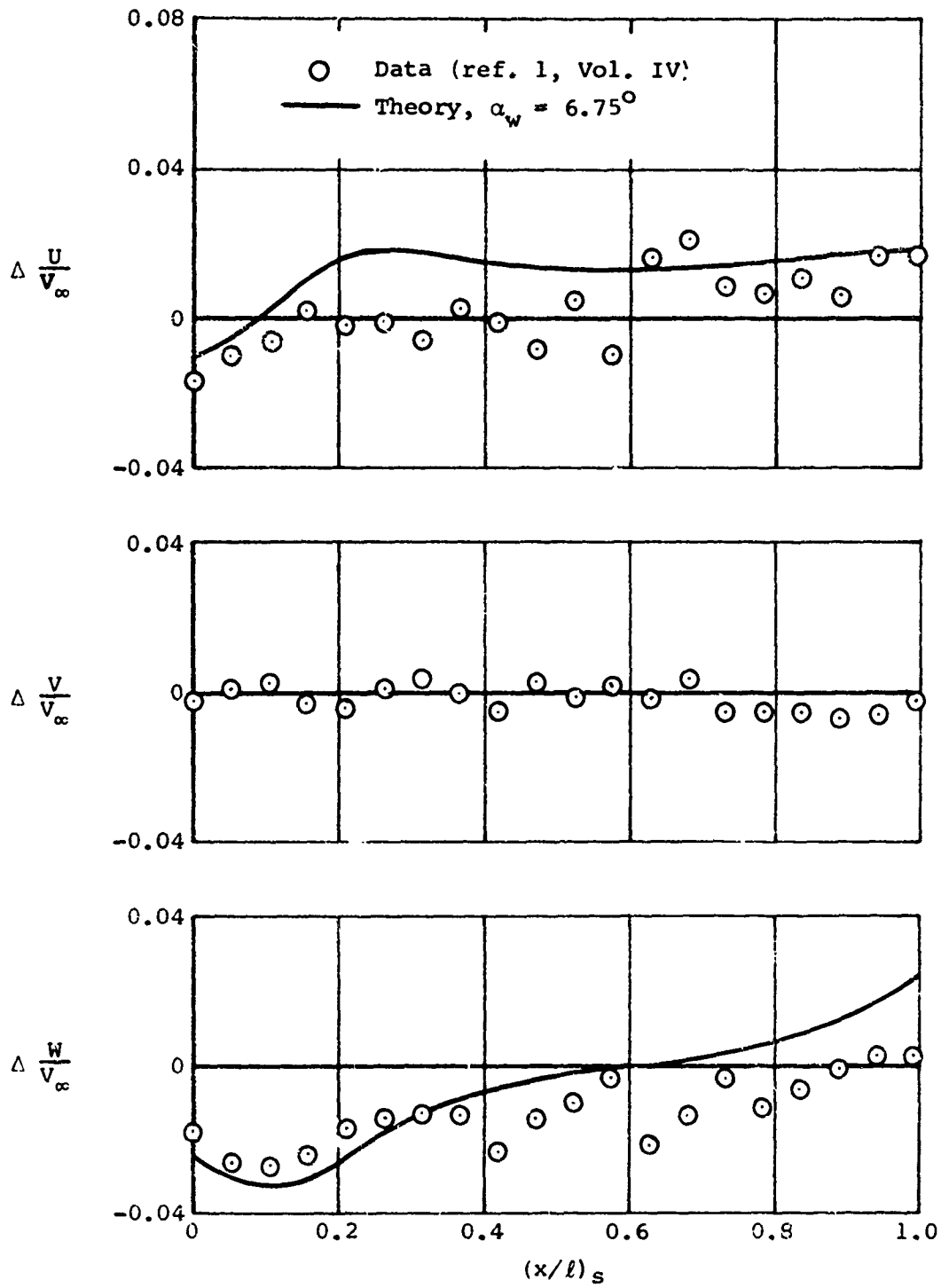
All dimensions
in inches

Figure 20.- TER grouping of stores in the presence of the wing-fuselage combination of reference 1.



(a) $\alpha_p = 0^\circ$.

Figure 21.- Comparison between calculated and experimental velocity increments due to addition of two shoulder stores to TER rack; $M_\infty = 0.25$, $y/s = -0.333$, $z/c = -0.40$.



(b) $\alpha_p = 6^\circ$.

Figure 21.- Concluded.

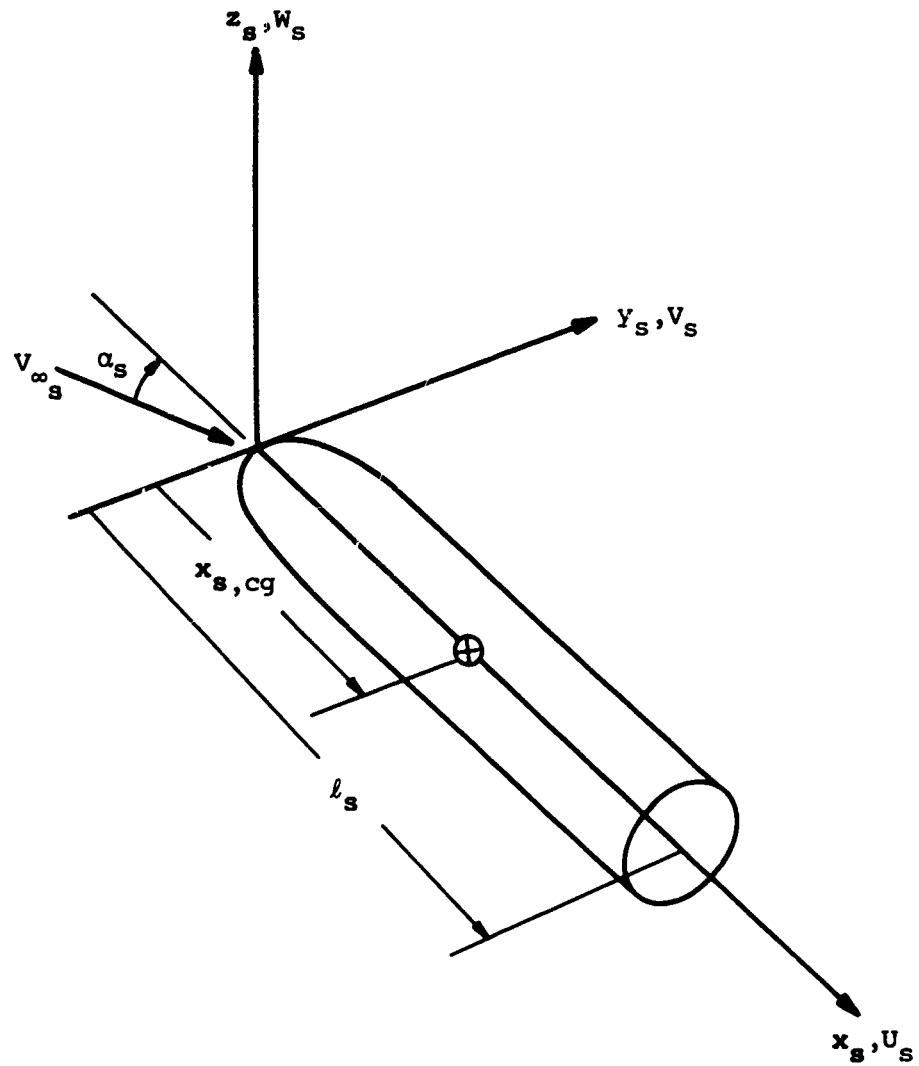


Figure 22.- Coordinate system fixed in ejected store.

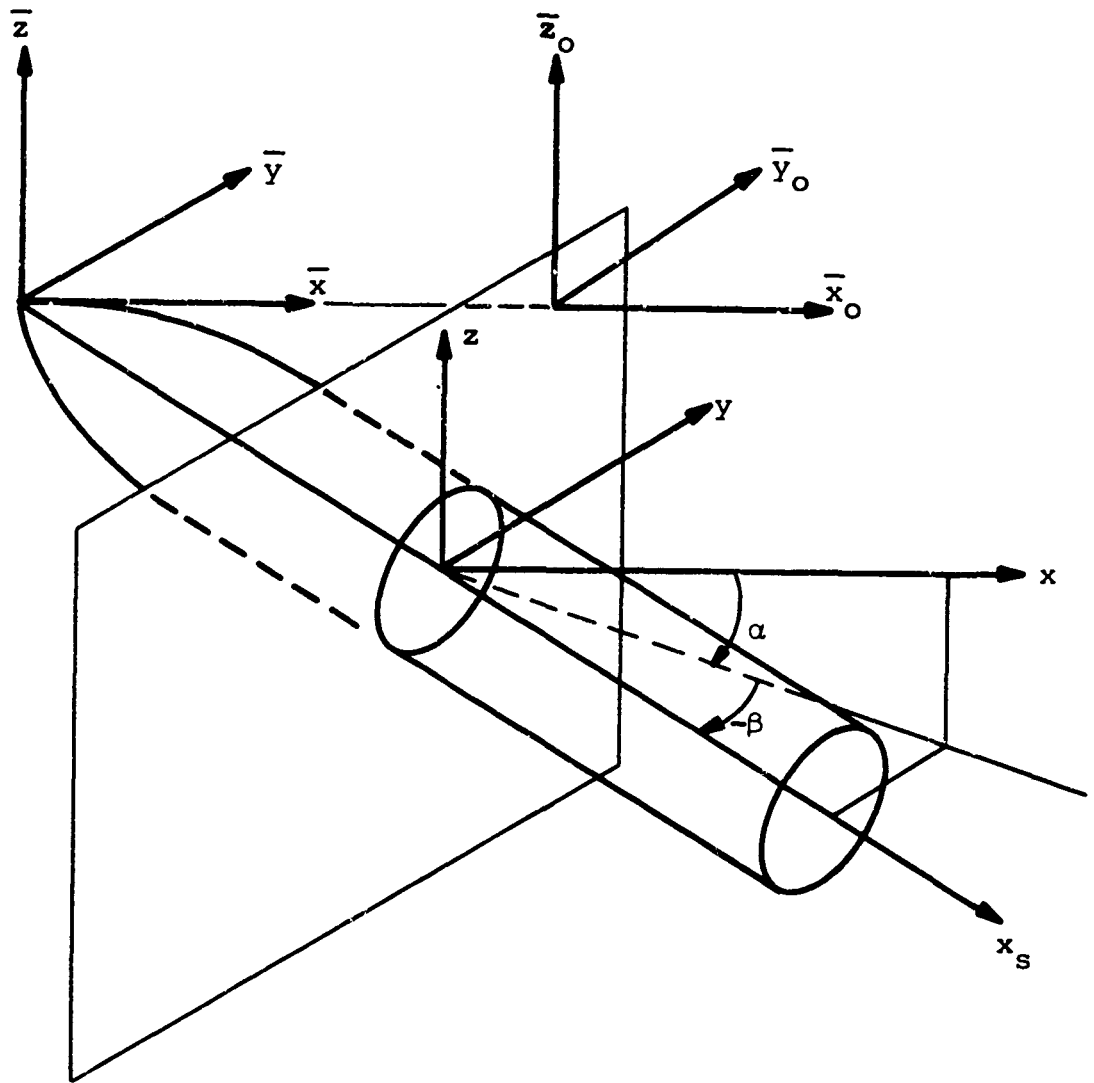


Figure 23.- Axis systems used in mutual interference analysis.

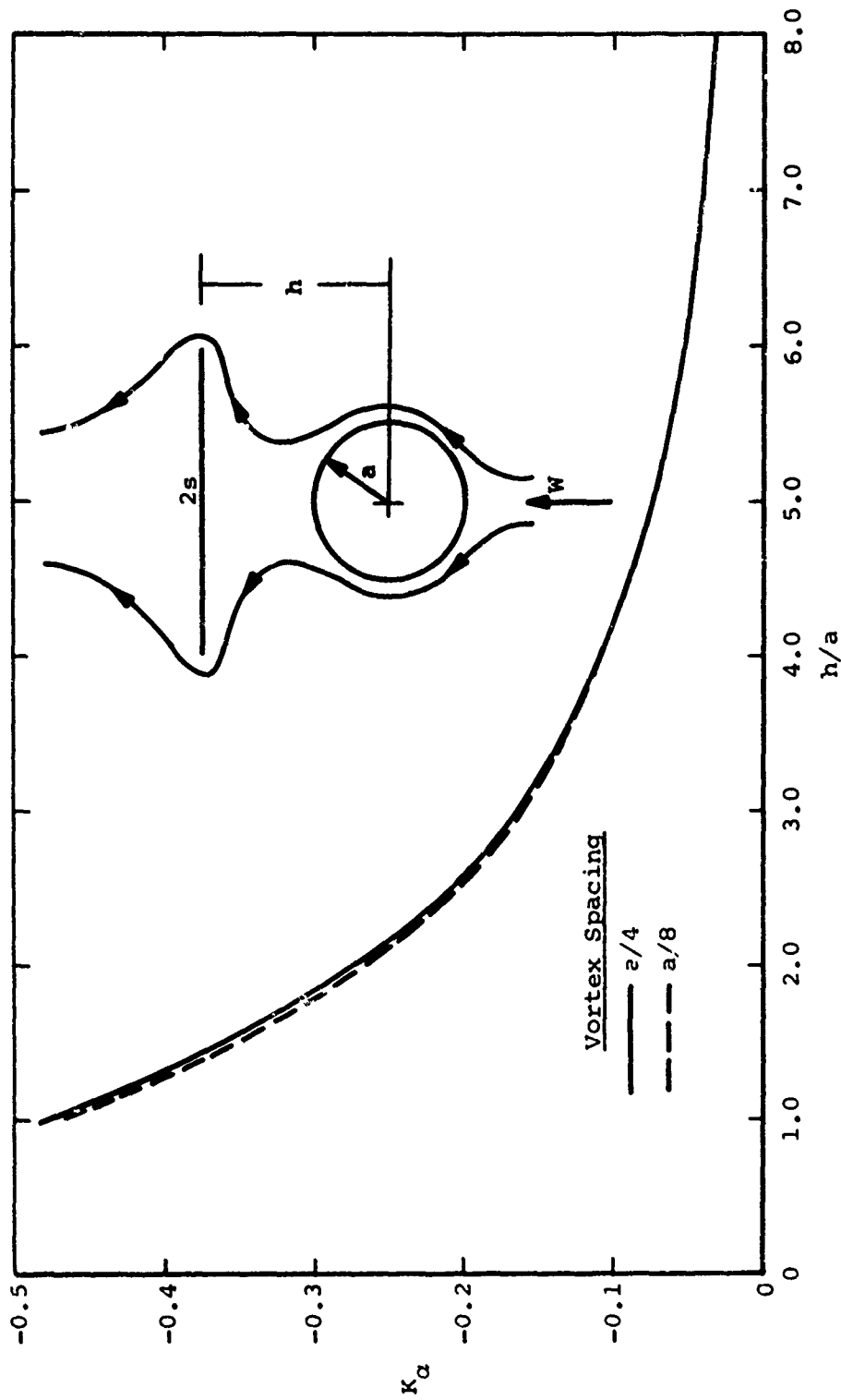


Figure 24.- Effect of vortex spacing on calculated values of K_α for conical wing-store-pylon configuration.

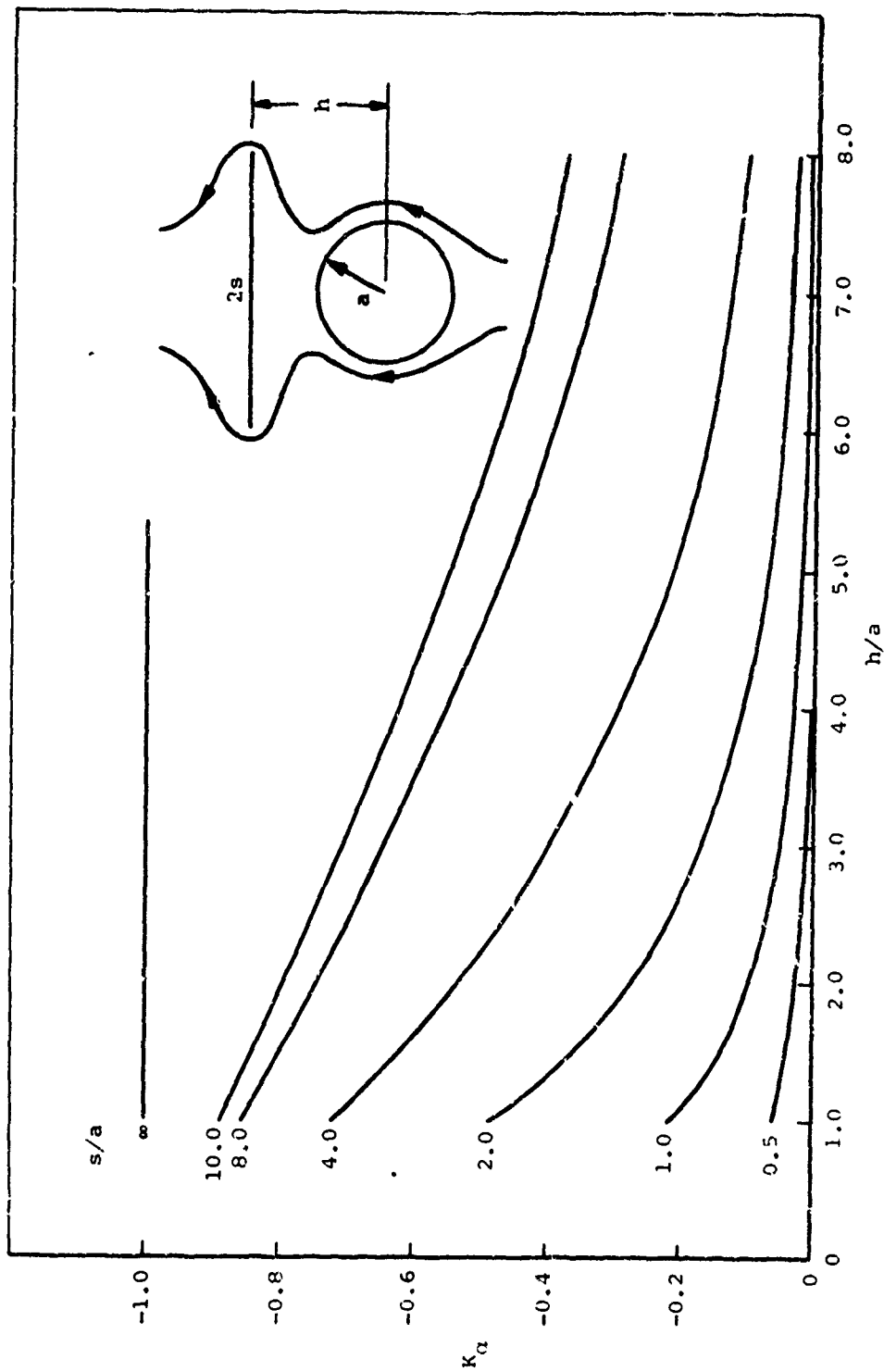


Figure 25.- Variation of K_α with geometric parameters of conical wing-store-pylon configuration.

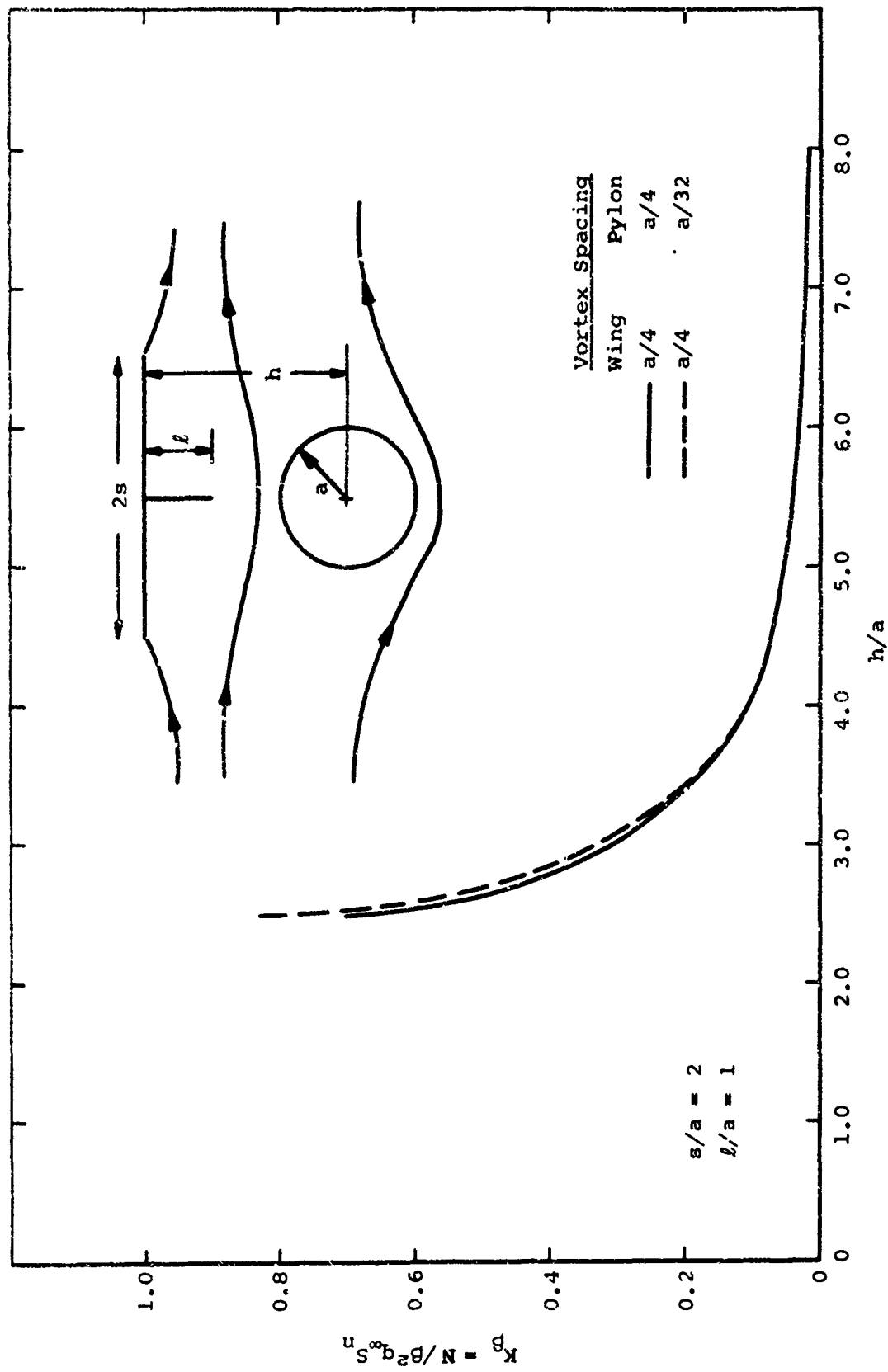


Figure 26.- Effect of vortex spacing on calculated values of K_B for conical wing-store-pylon configuration.

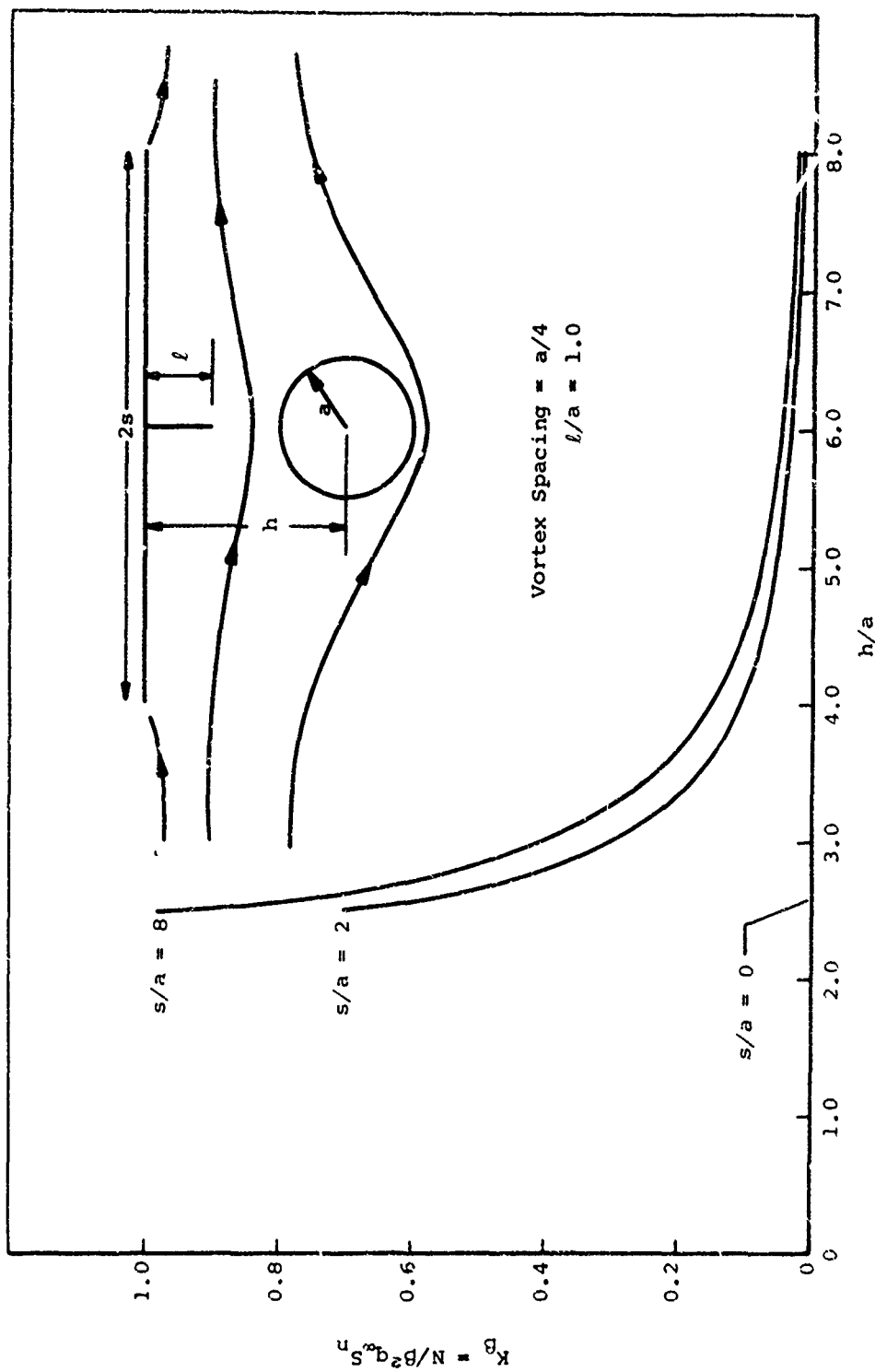
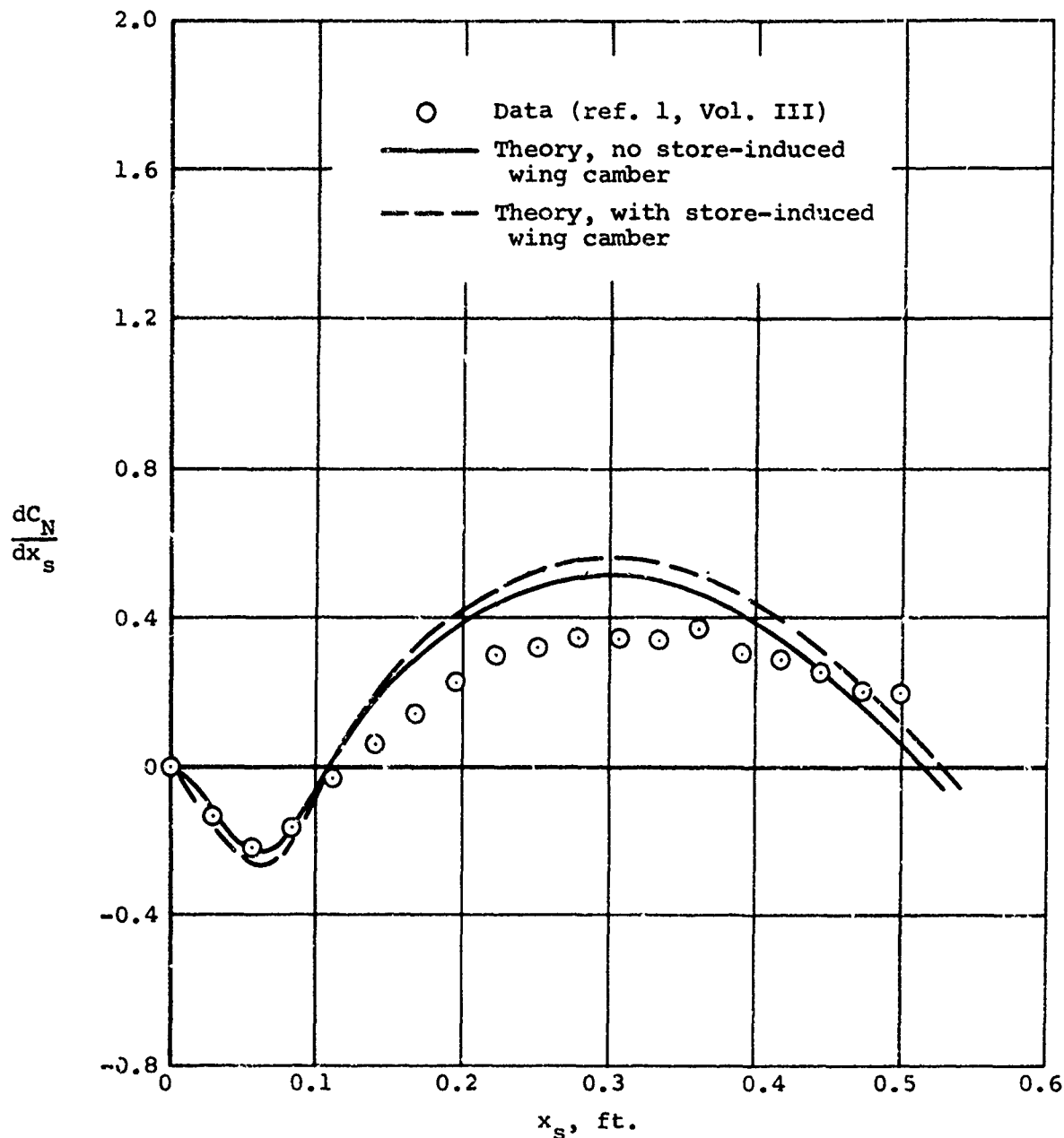
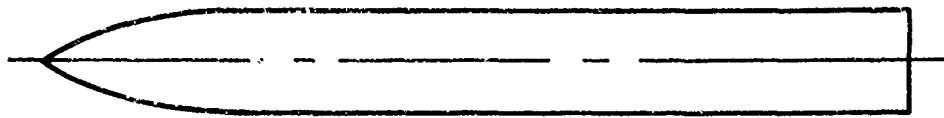
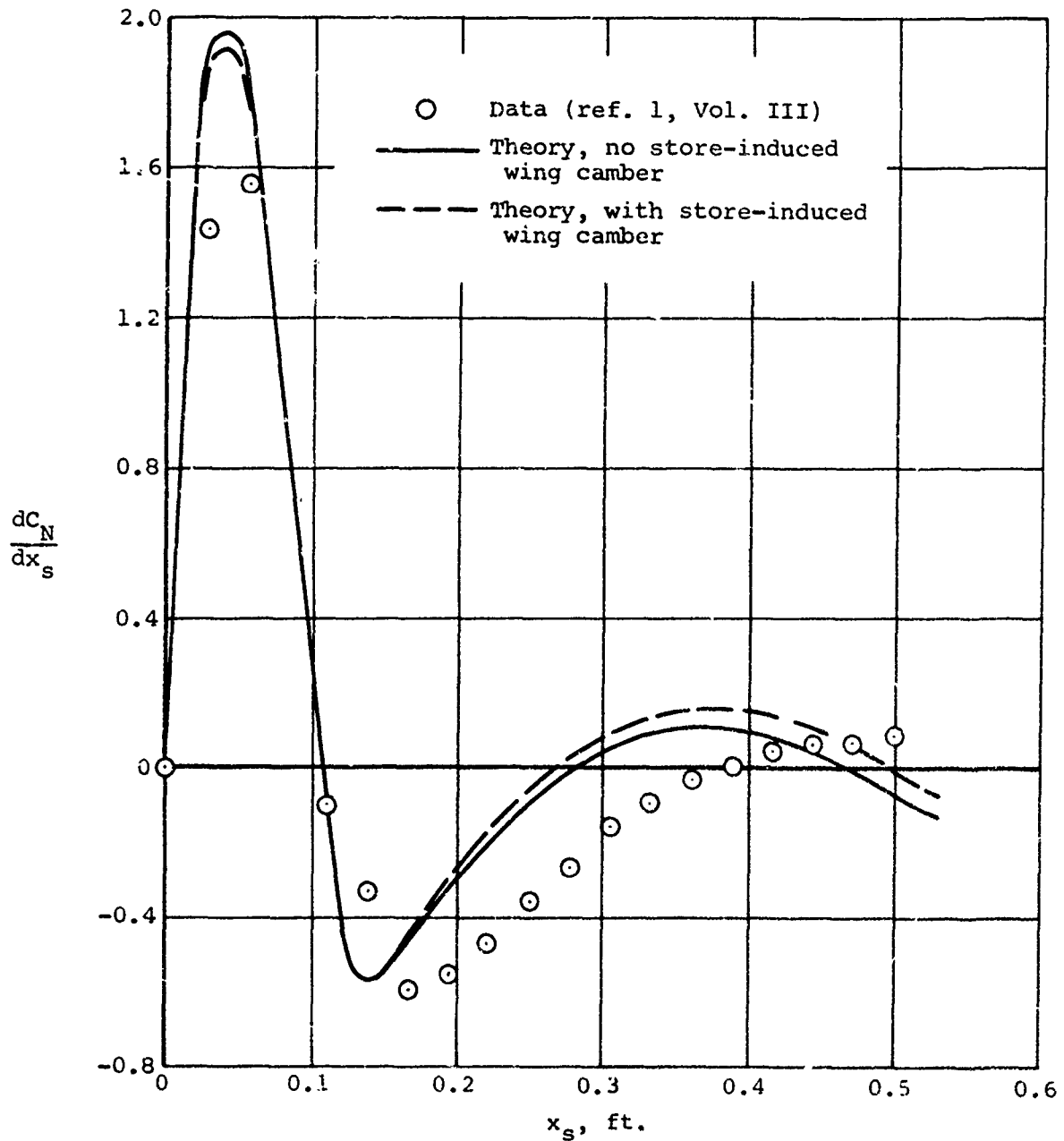


Figure 27.- Variation of normal force due to sidewash with geometric parameters of conical wing-store-pylon configuration.



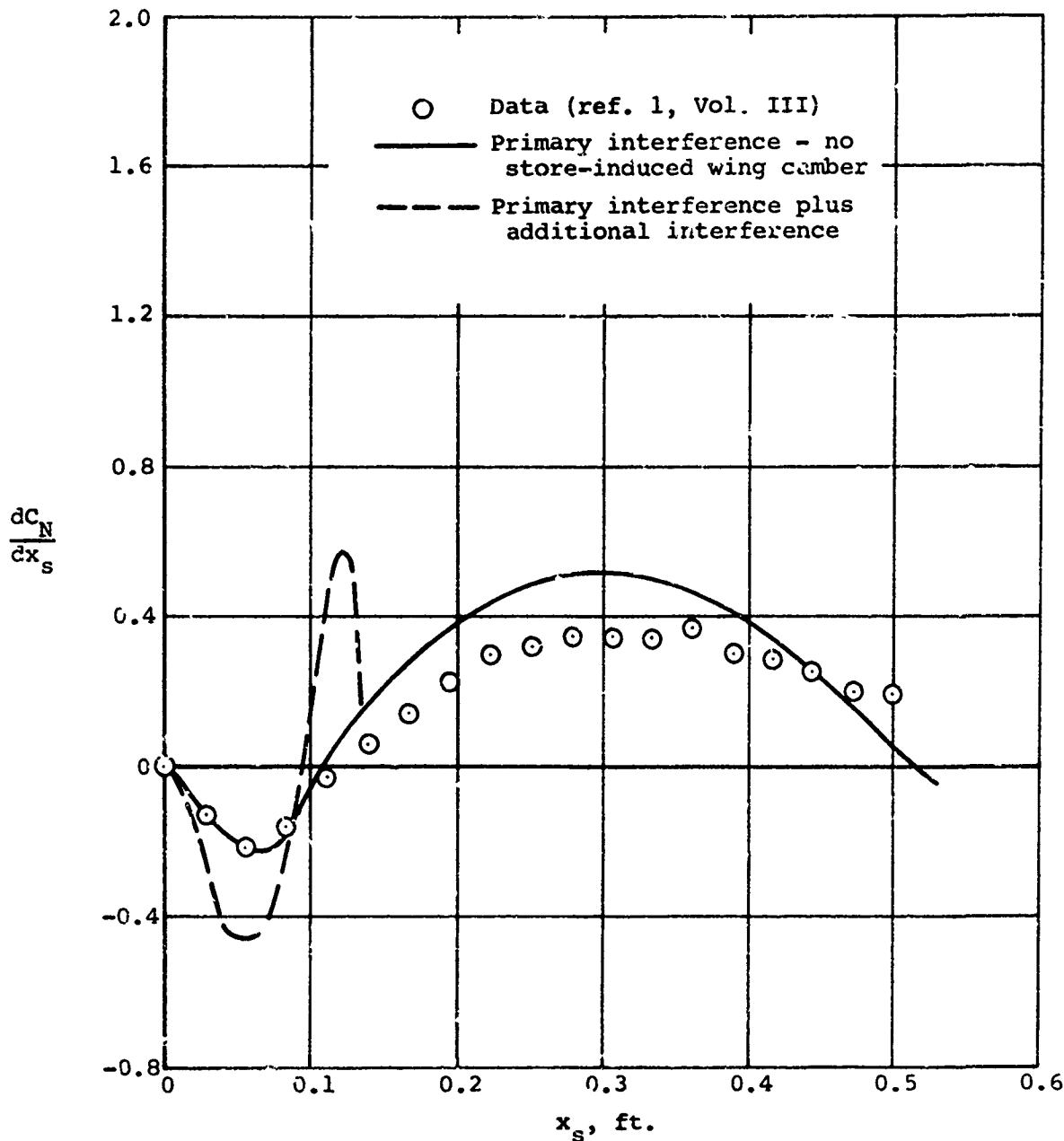
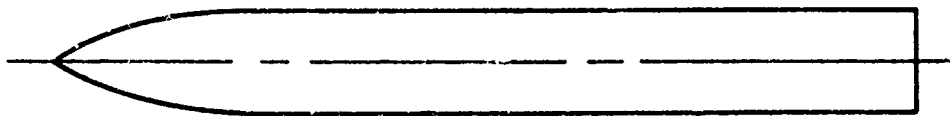
(a) $\alpha_p = 0^\circ$, $\alpha_w = 1.25^\circ$.

Figure 28.- Primary interference normal force distribution on a single store below the left wing panel of a wing-fuselage combination; $M_\infty = 0.25$, $y/s = -0.333$, $z/c = -0.30$.



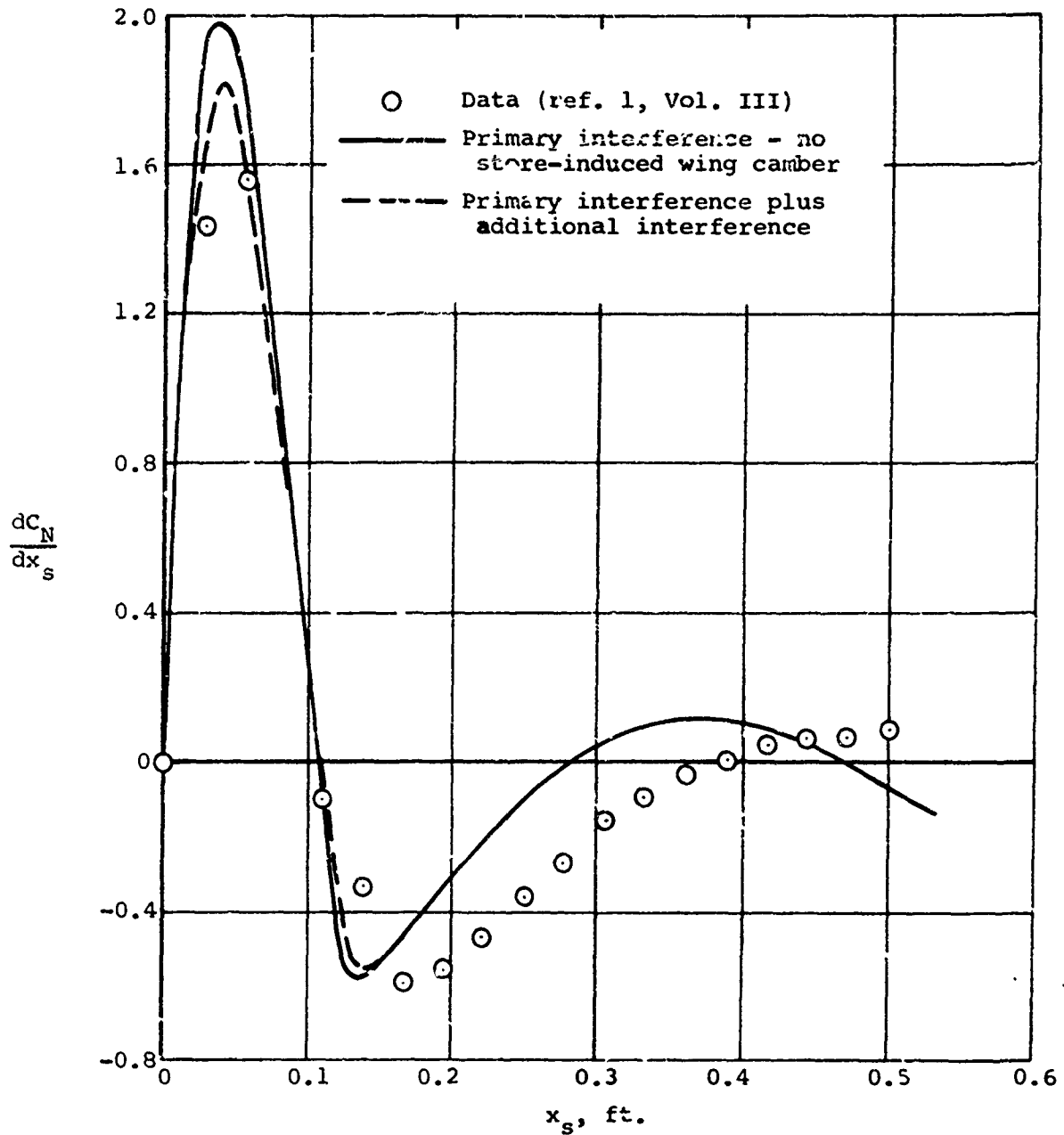
(b) $\alpha_p = 6^\circ$, $\alpha_w = 6.75^\circ$.

Figure 28.- Concluded.



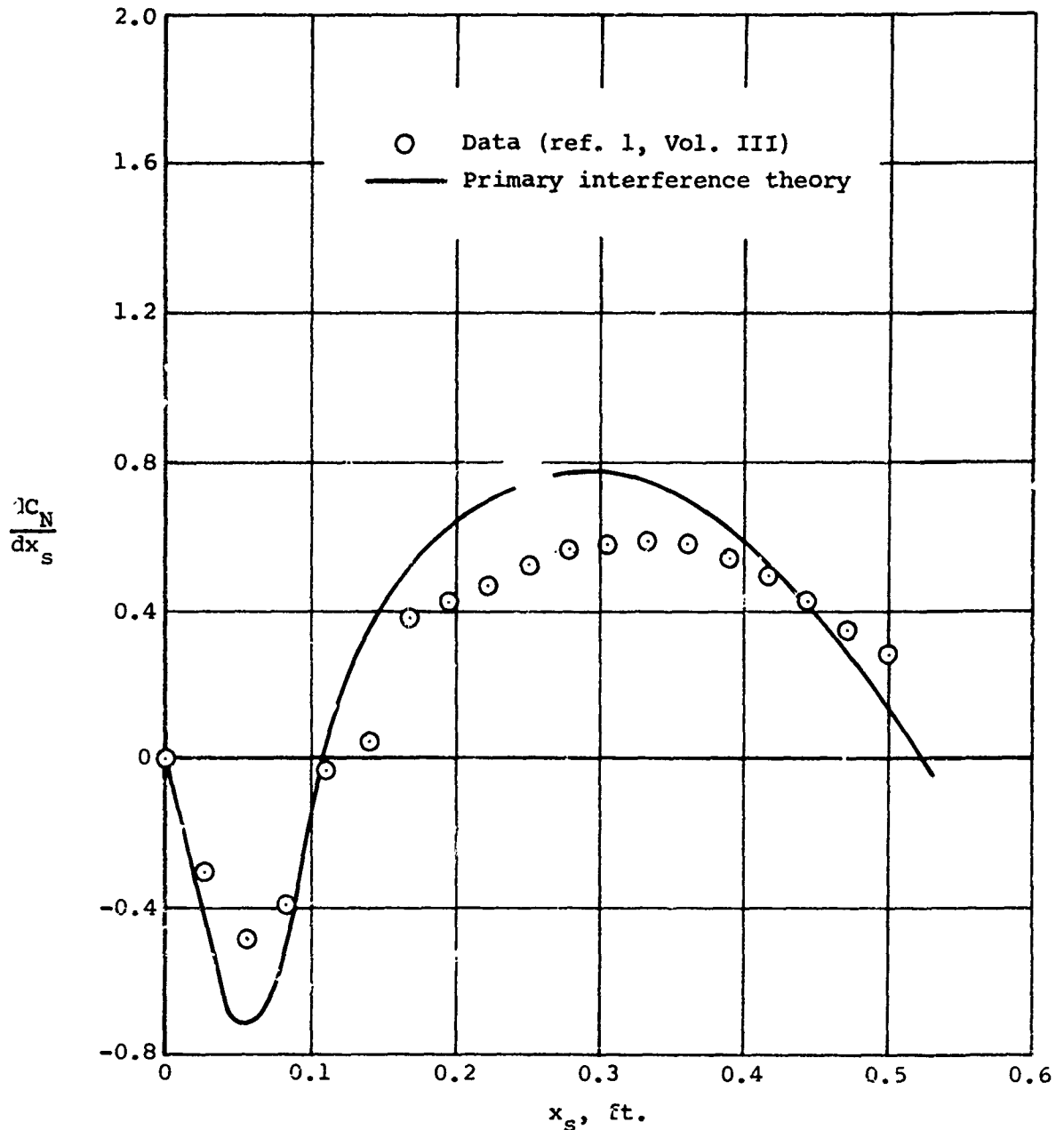
(a) $\alpha_p = 0^\circ, \alpha_w = 1.25^\circ$.

Figure 29.- Effect of additional interference on normal-force distribution on a single store below the left wing panel of a wing-fuselage combination;
 $M_\infty = 0.25, y/s = -0.333, z/c = -0.30$.



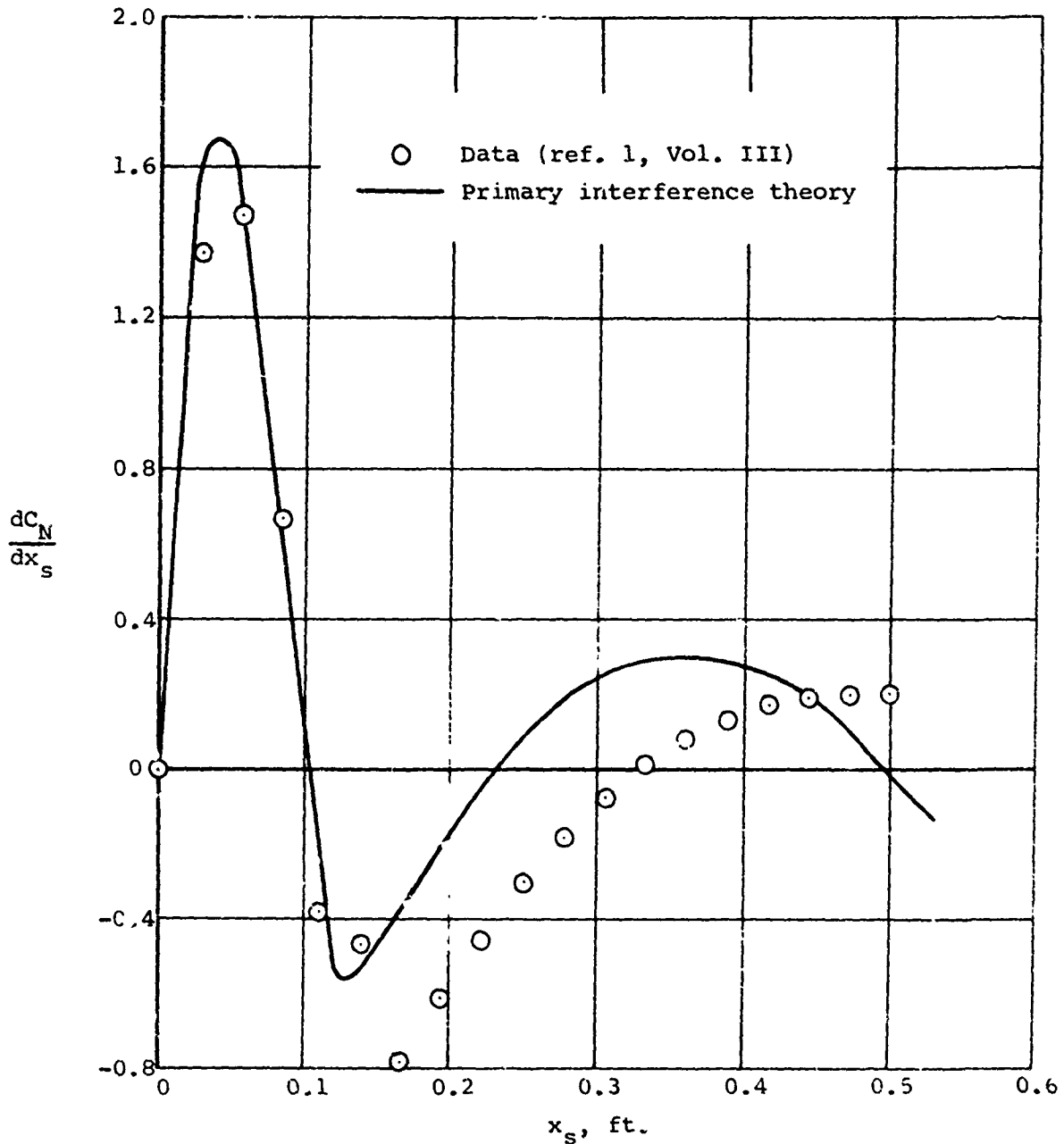
(b) $\alpha_p = 6^\circ$, $\alpha_w = 6.75^\circ$.

Figure 29.- Concluded.



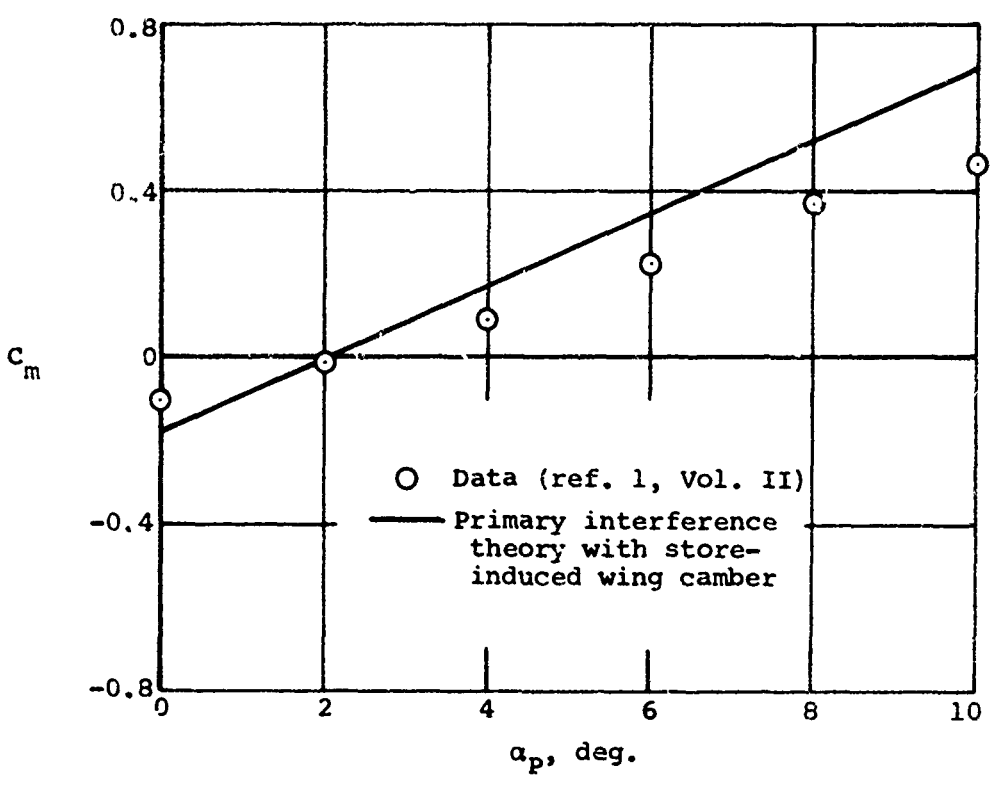
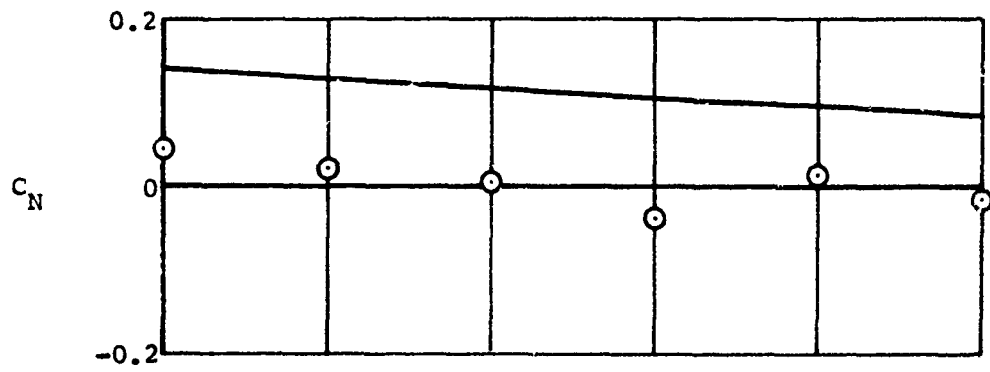
(a) $\alpha_p = 0^\circ$, $\alpha_w = 0.96^\circ$.

Figure 30.- Primary interference normal-force distribution on a single store below the left wing panel of a wing-fuselage combination; $M_\infty = 0.70$, $y/s = -0.333$, $z/c = -0.30$.



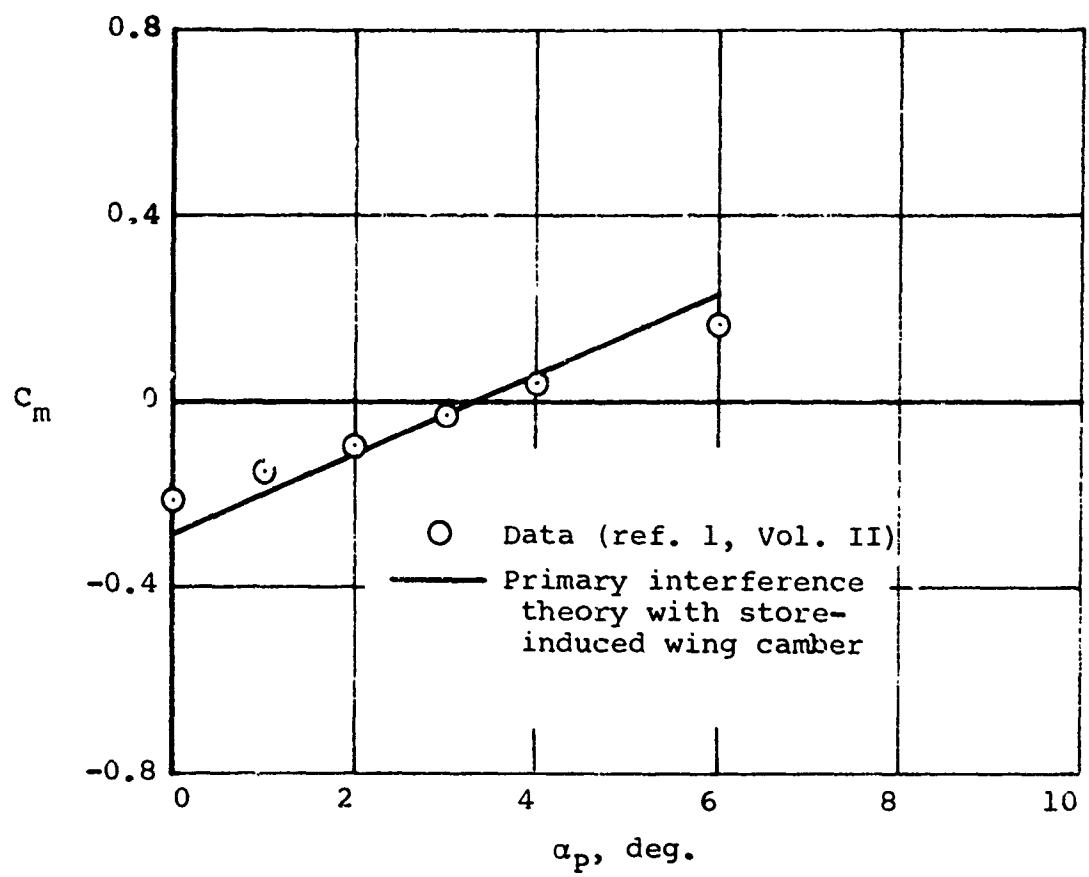
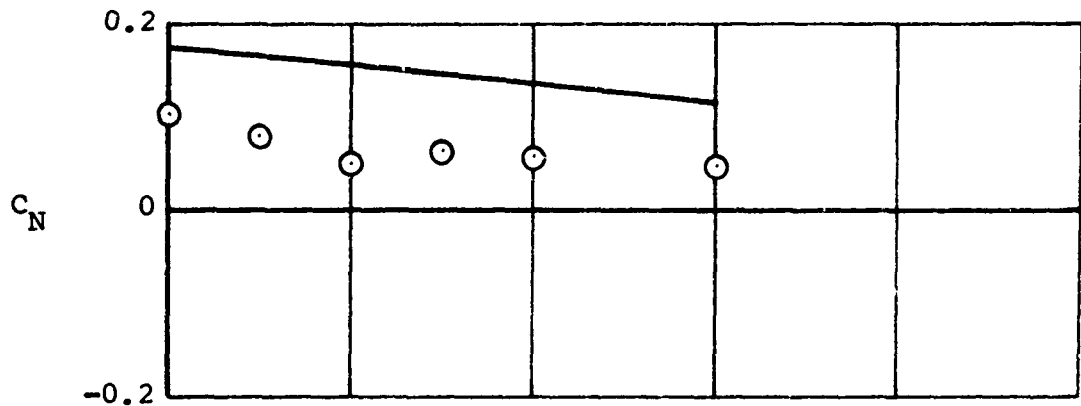
(b) $\alpha_p = 6^\circ$, $\alpha_w = 6.79^\circ$.

Figure 30.- Concluded.



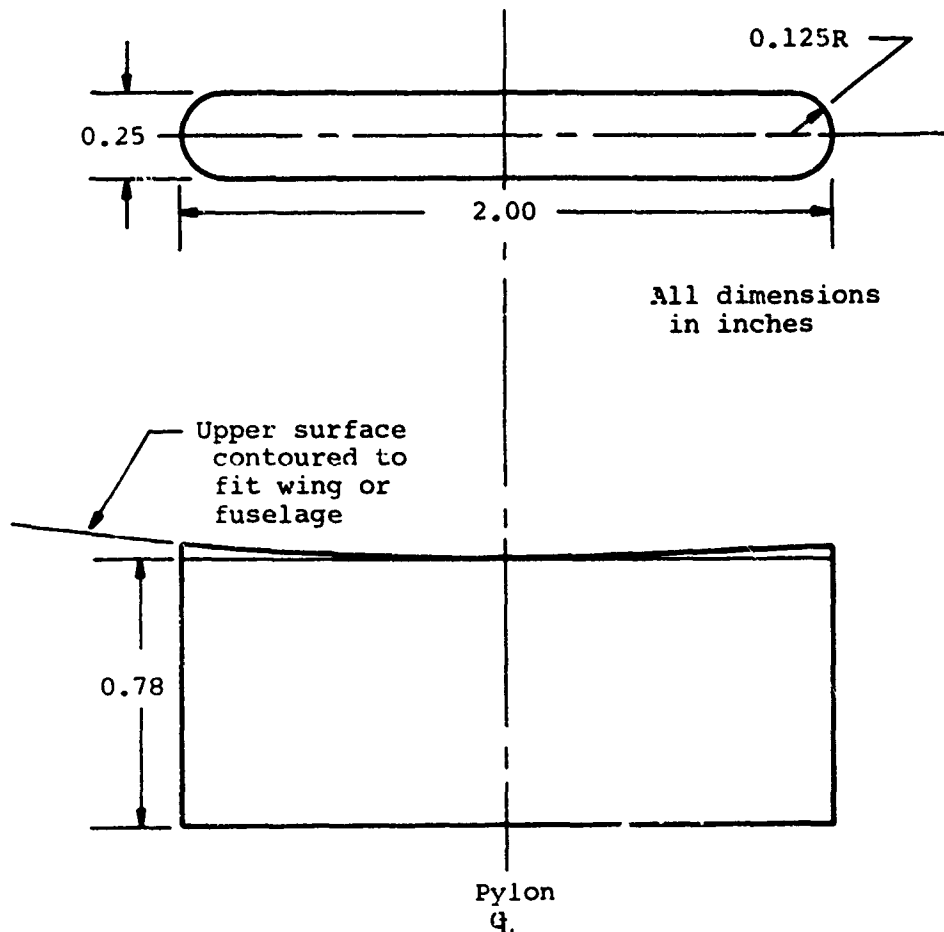
(a) $M_\infty = 0.25$.

Figure 31.- Primary interference normal force and pitching moment on a single store below the left wing panel of a wing-fuselage combination; $y/s = -0.333$, $z/c = -0.30$.



(b) $M_\infty = 0.70$.

Figure 31.- Concluded.

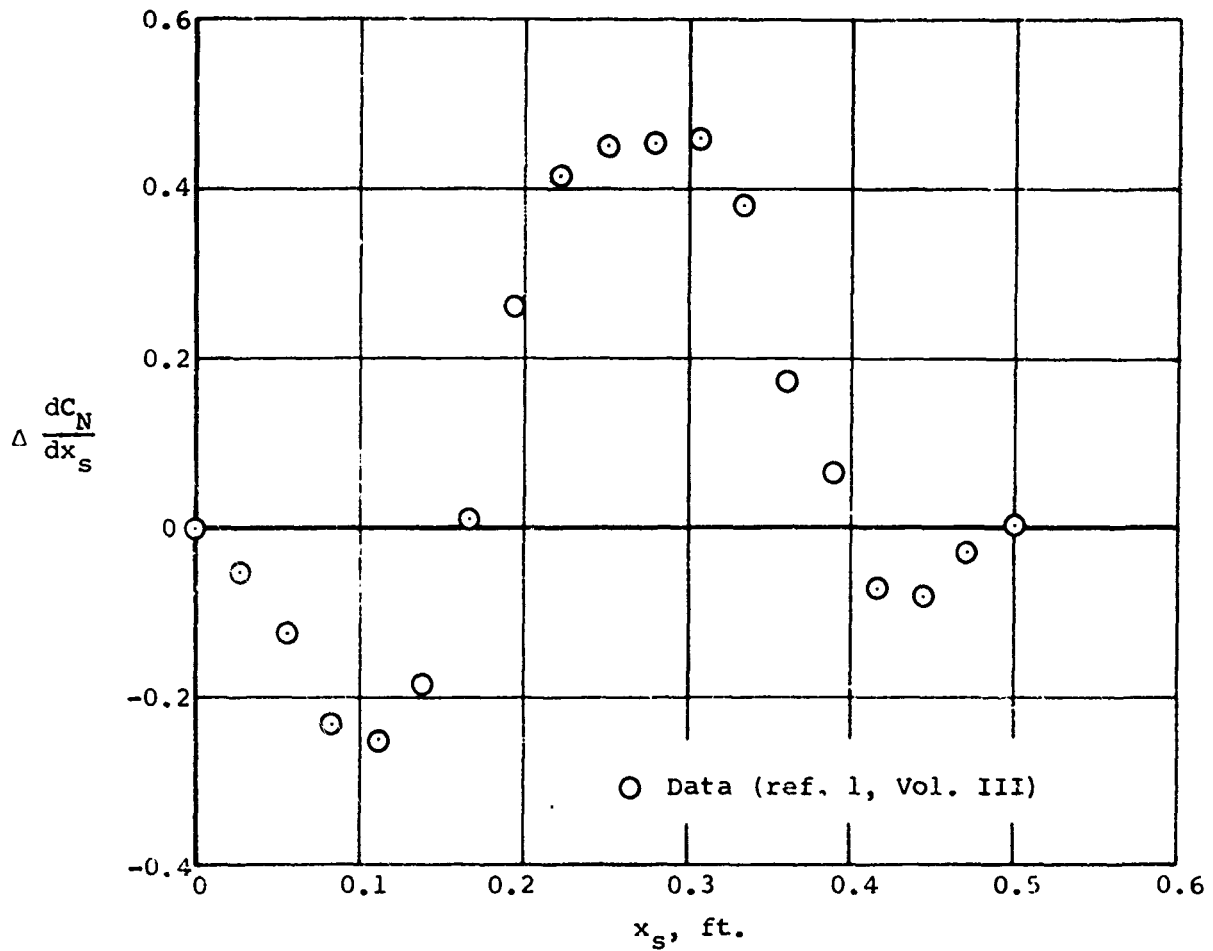


For wing pylons, pylon centerline located at 40% wing chord.

For fuselage pylon, pylon centerline located 19.43 inches aft of fuselage nose.

Figure 32.- Details of pylons used in experimental investigation of reference 1.

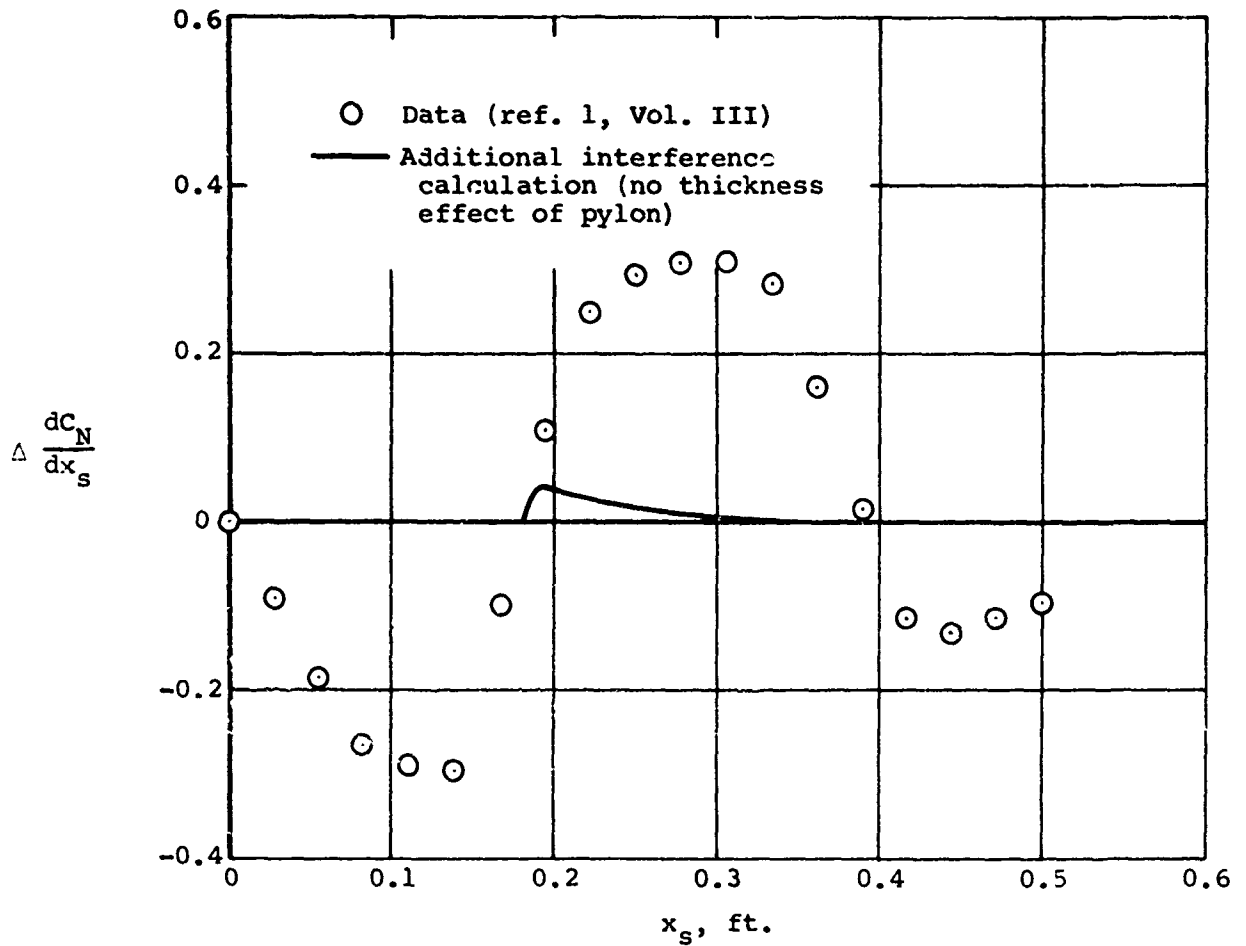
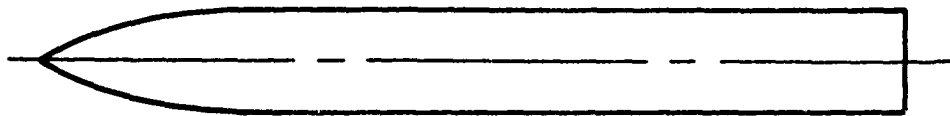
Pylon



(a) $\alpha_p = 0^\circ$.

Figure 33.- Incremental loading on single store at 1/3 semispan location caused by addition of pylon to wing-fuselage combination; $M_\infty = 0.25$, $z/c = -0.30$.

Pylon



(b) $\alpha_p = 6^\circ$.

Figure 33.- Concluded.

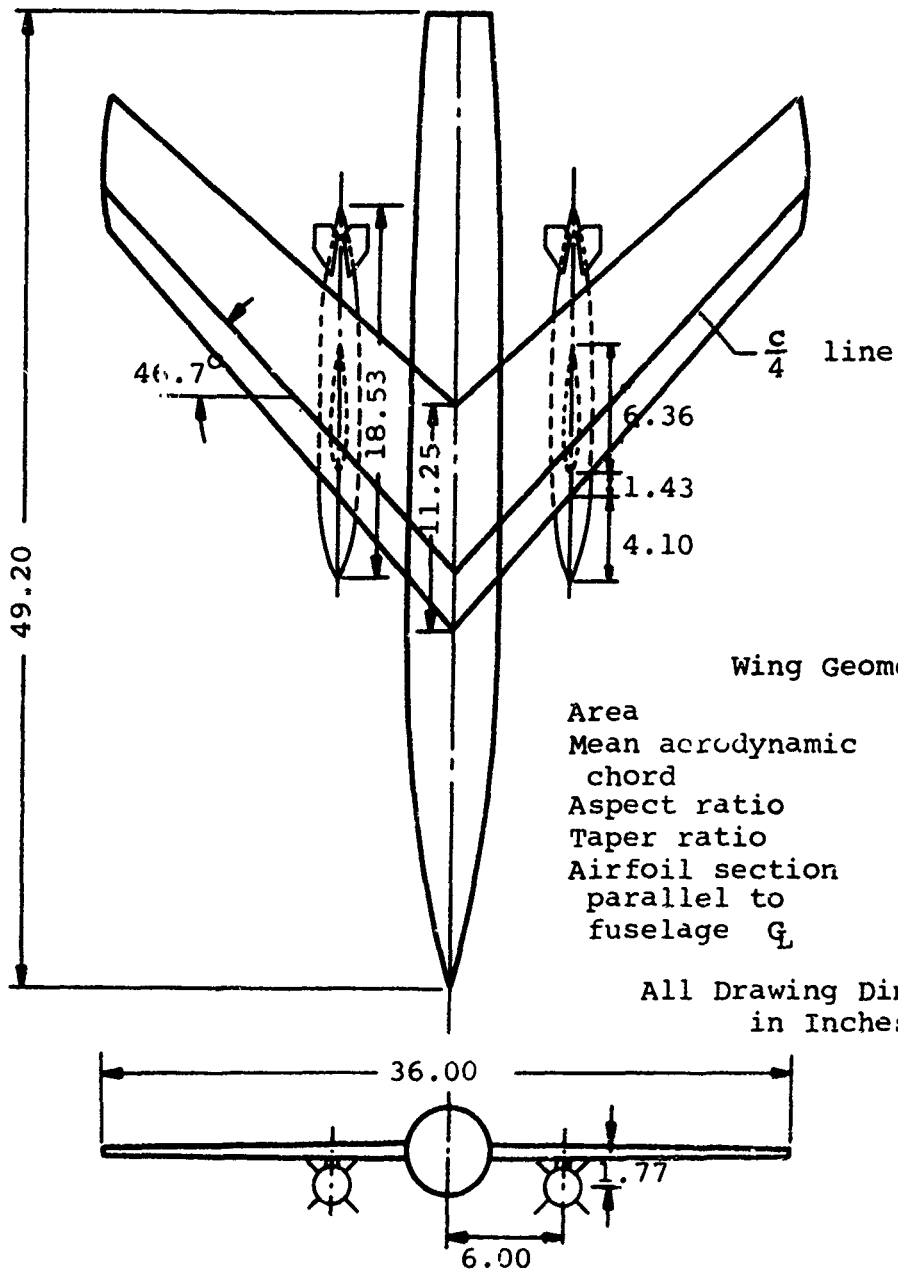
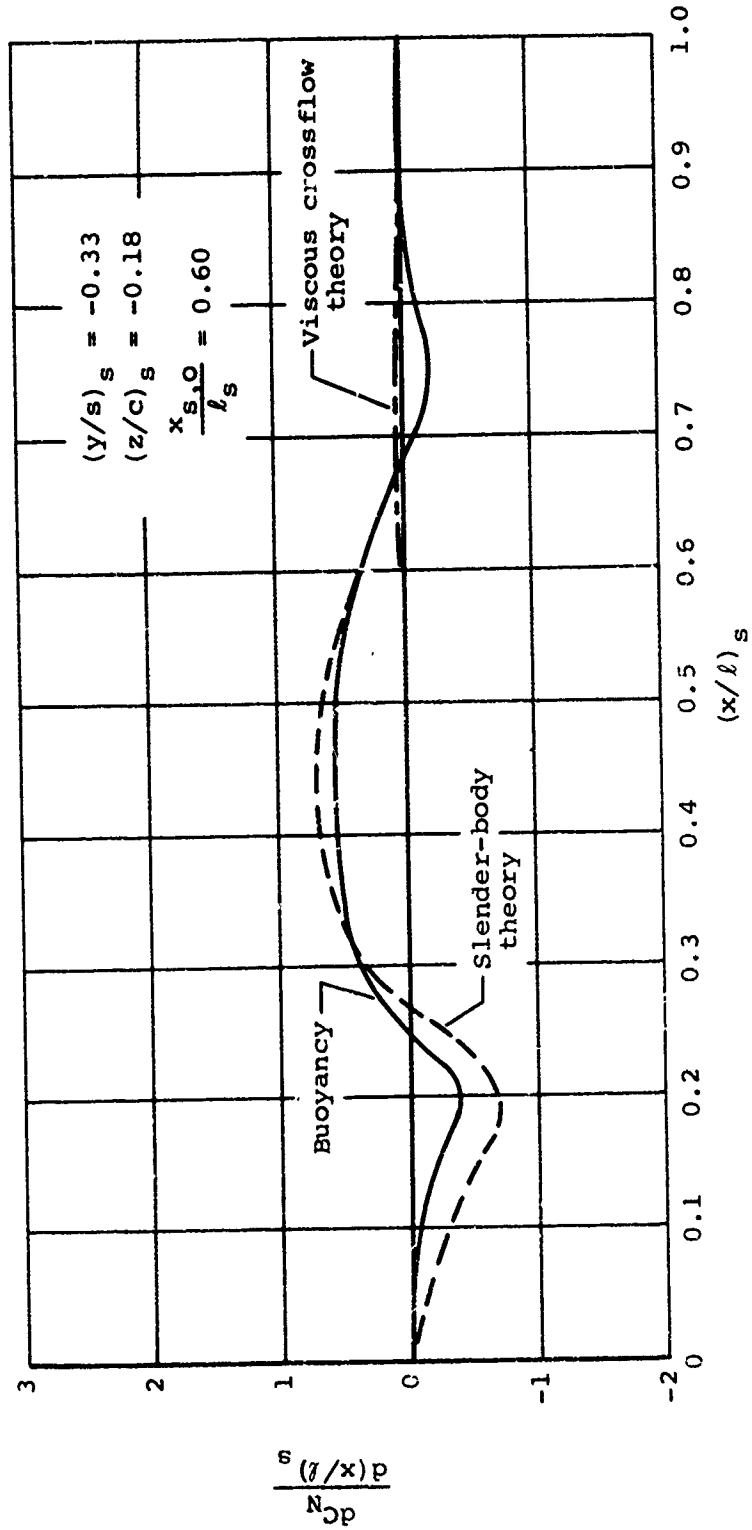
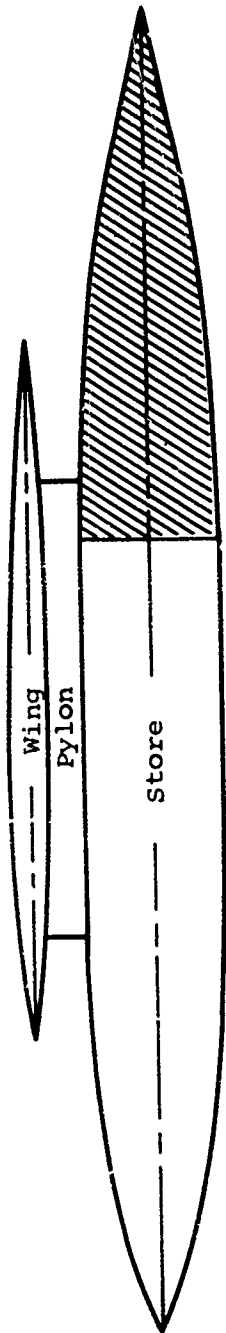
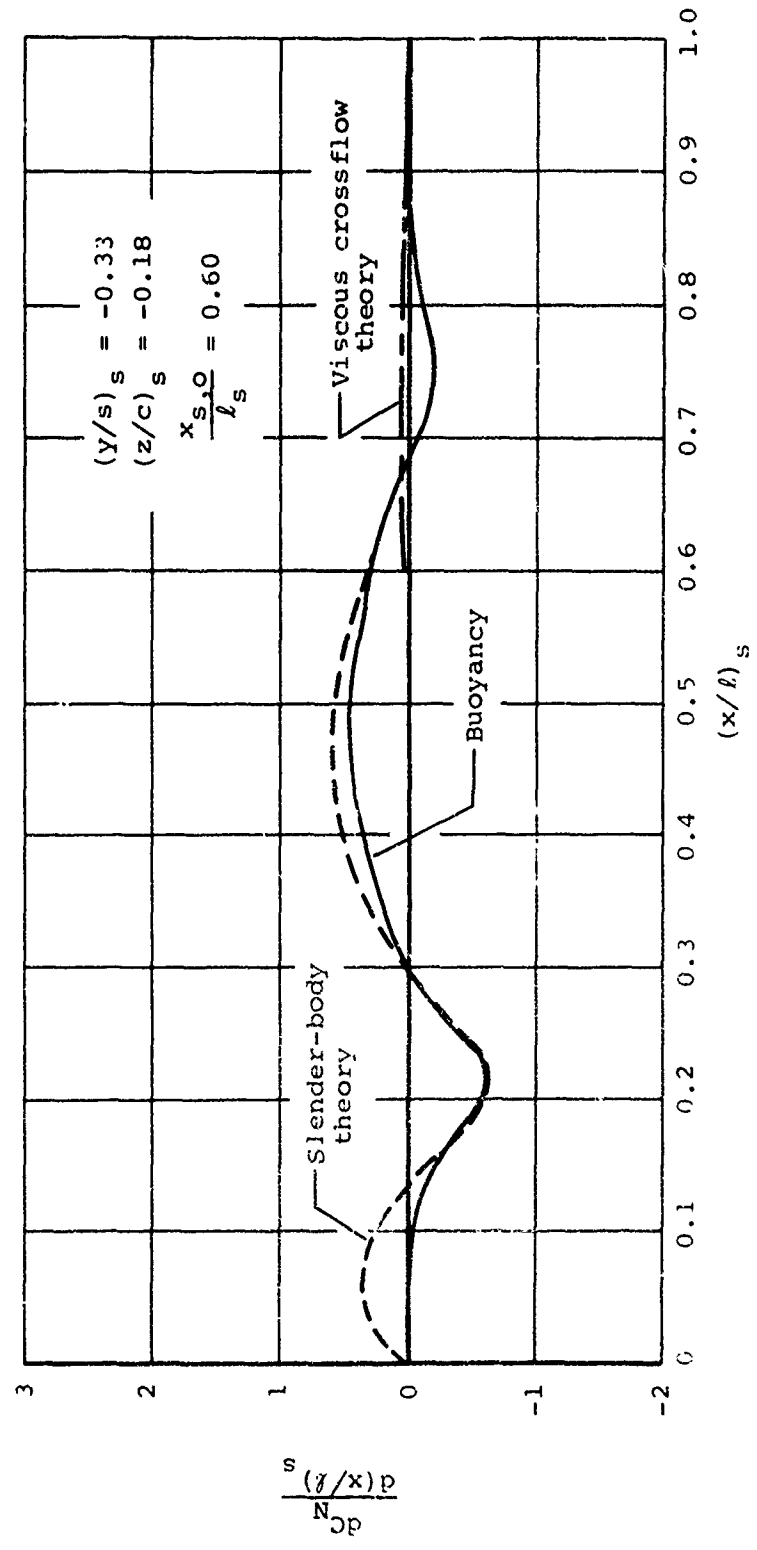
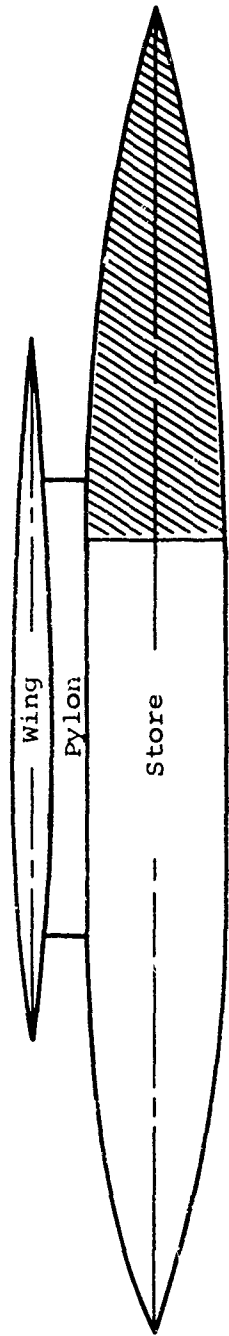


Figure 34.- Swept-wing model of NACA RM L54B18 (ref. 15).



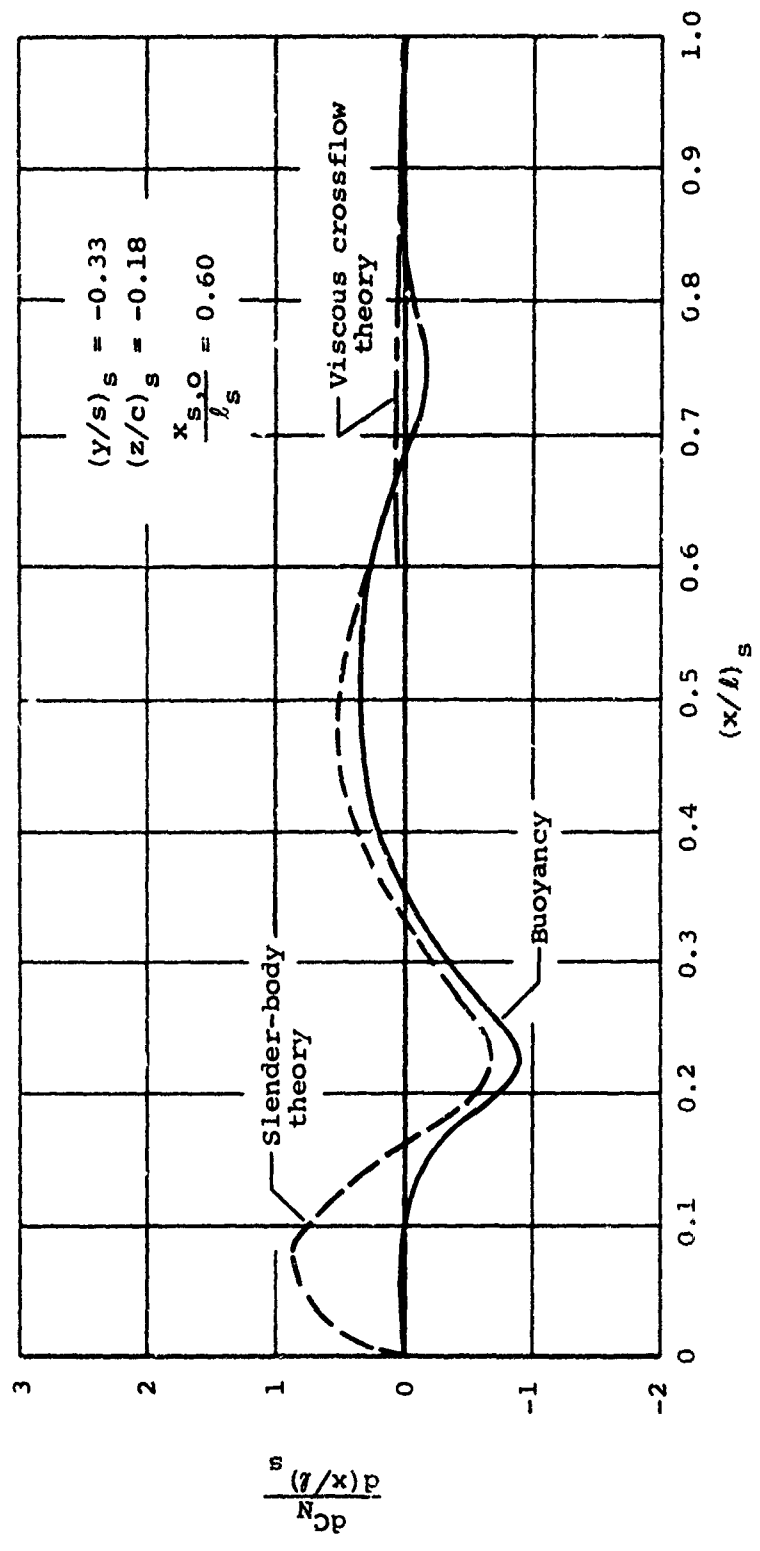
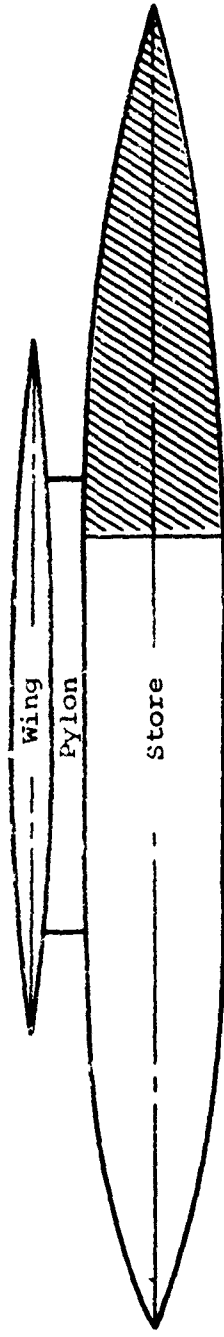
(a) $\alpha_w = \alpha_s = 0^\circ$.

Figure 35.- Distribution of the various components of normal force on a store in a nonuniform flow field.



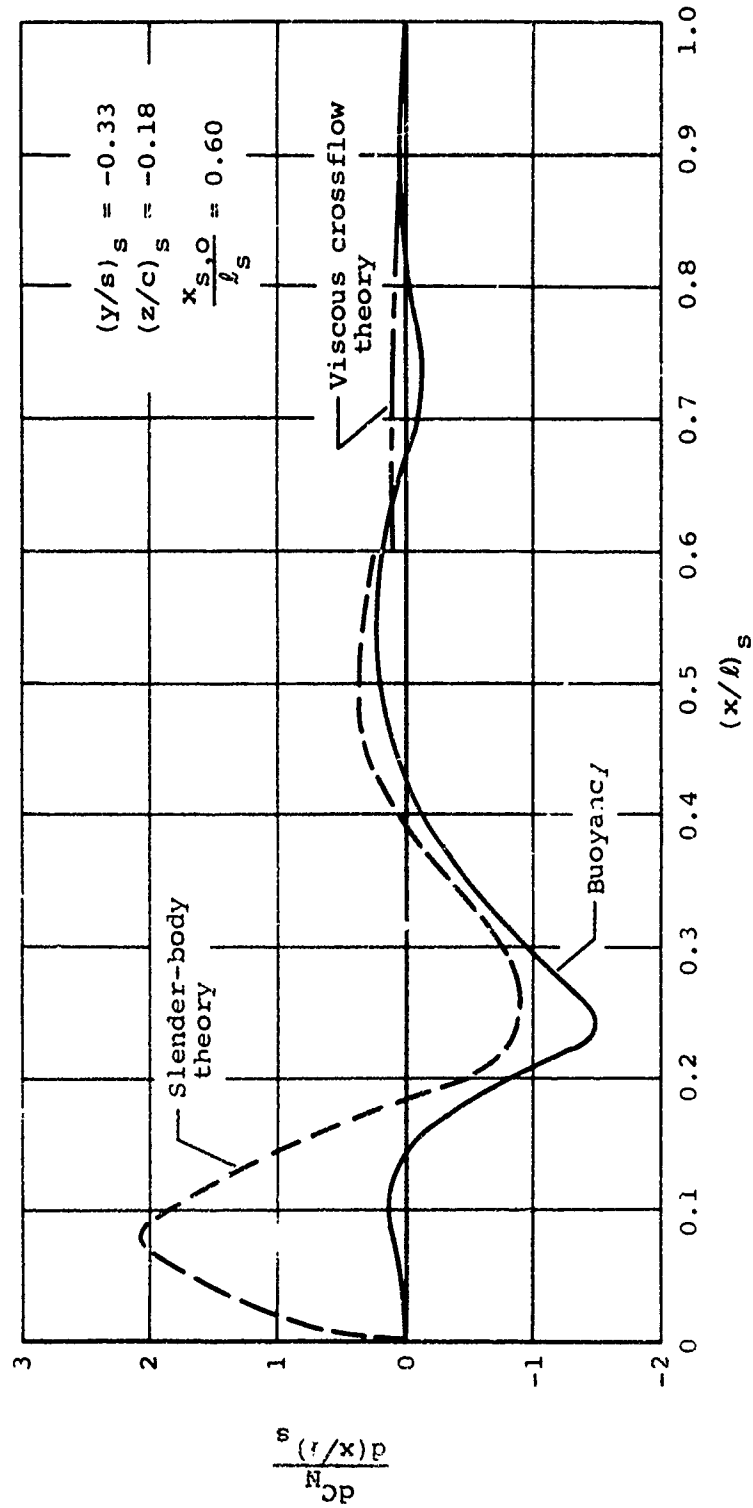
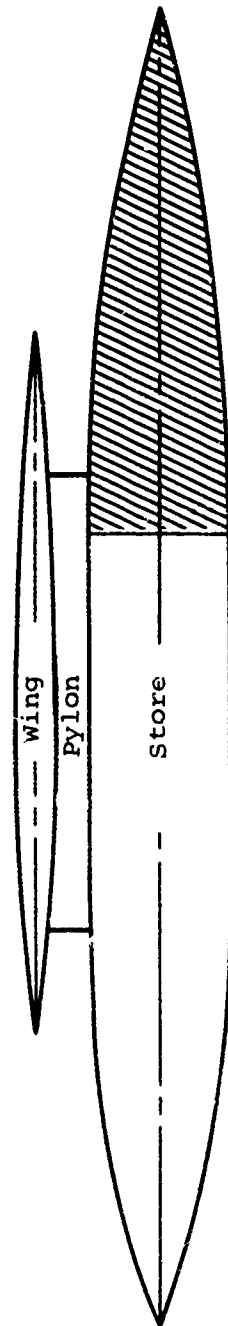
(b) $\alpha_w = \alpha_s = 2^\circ$.

Figure 35.- Continued.



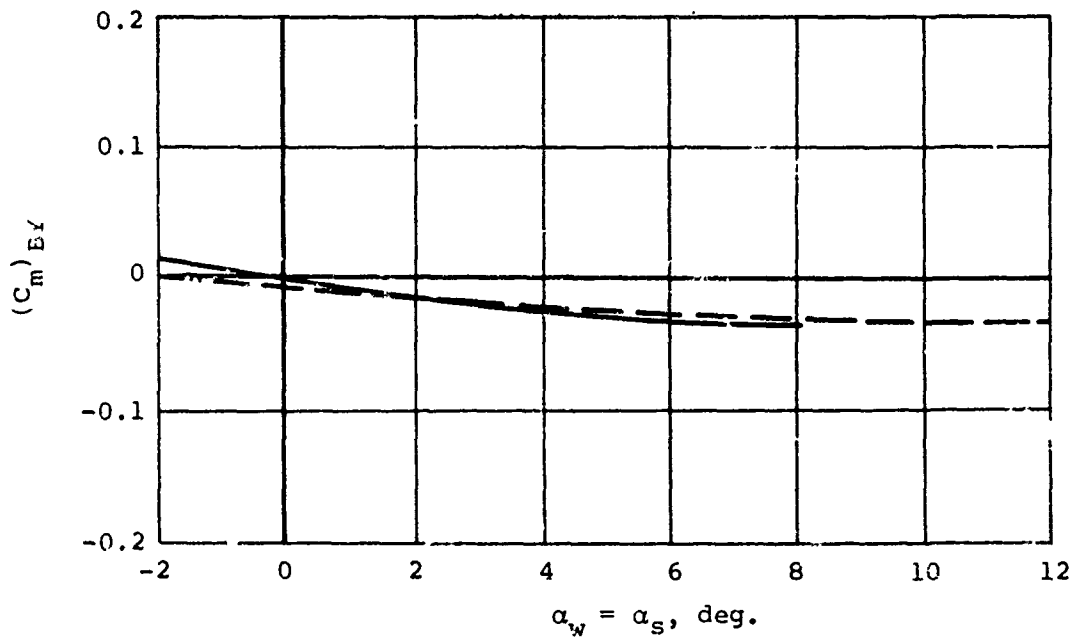
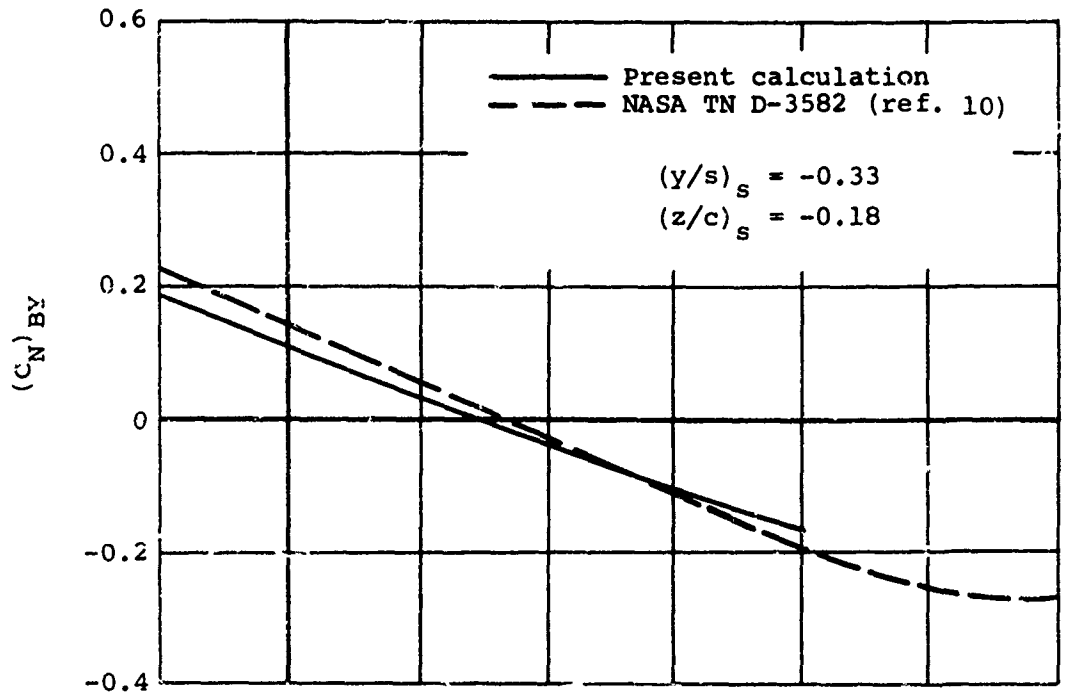
(c) $\alpha_w = \alpha_s = 4^\circ$.

Figure 35.- Continued.



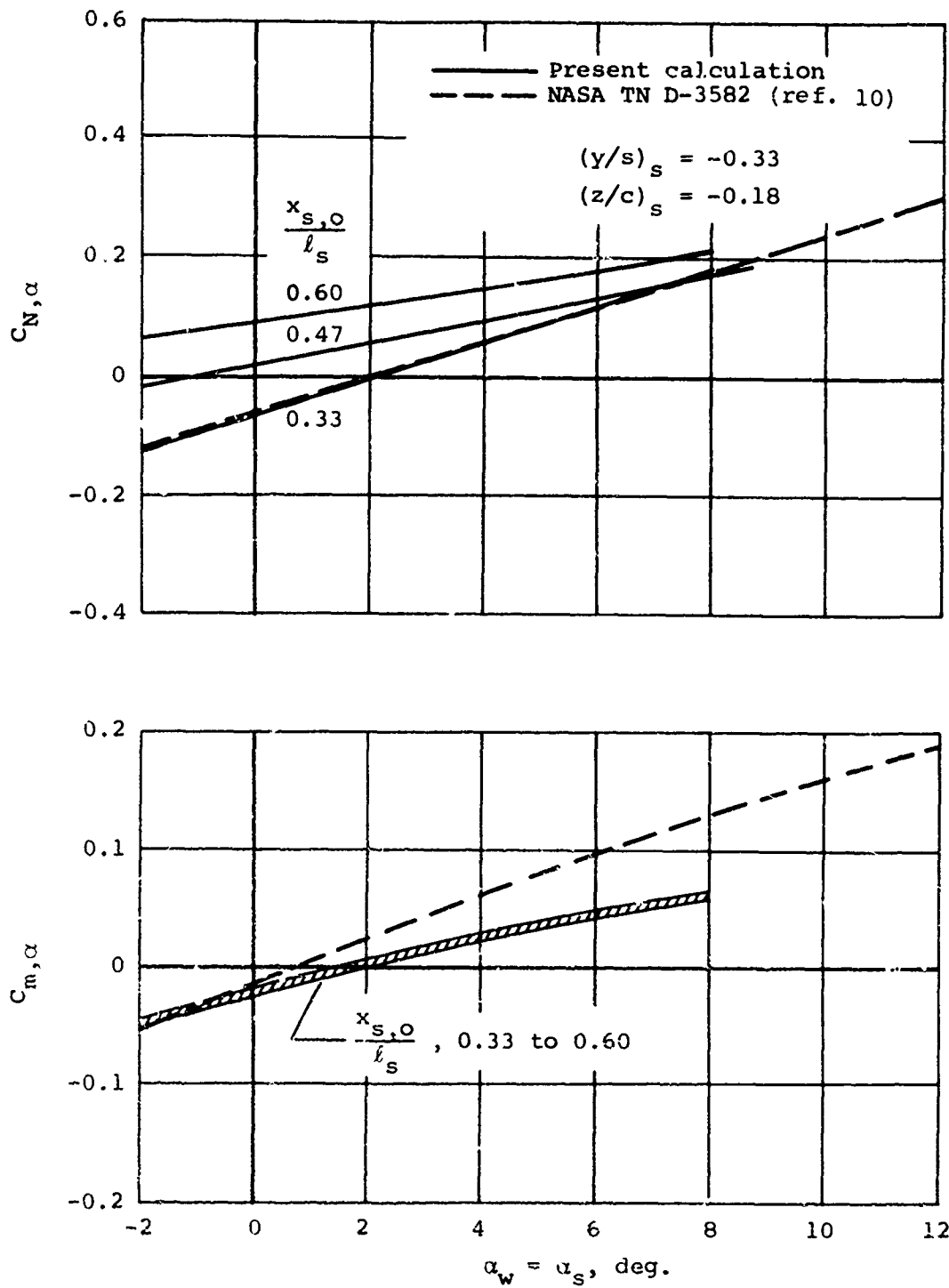
(d) $\alpha_w = \alpha_s = 8^\circ$.

Figure 35.- Concluded.



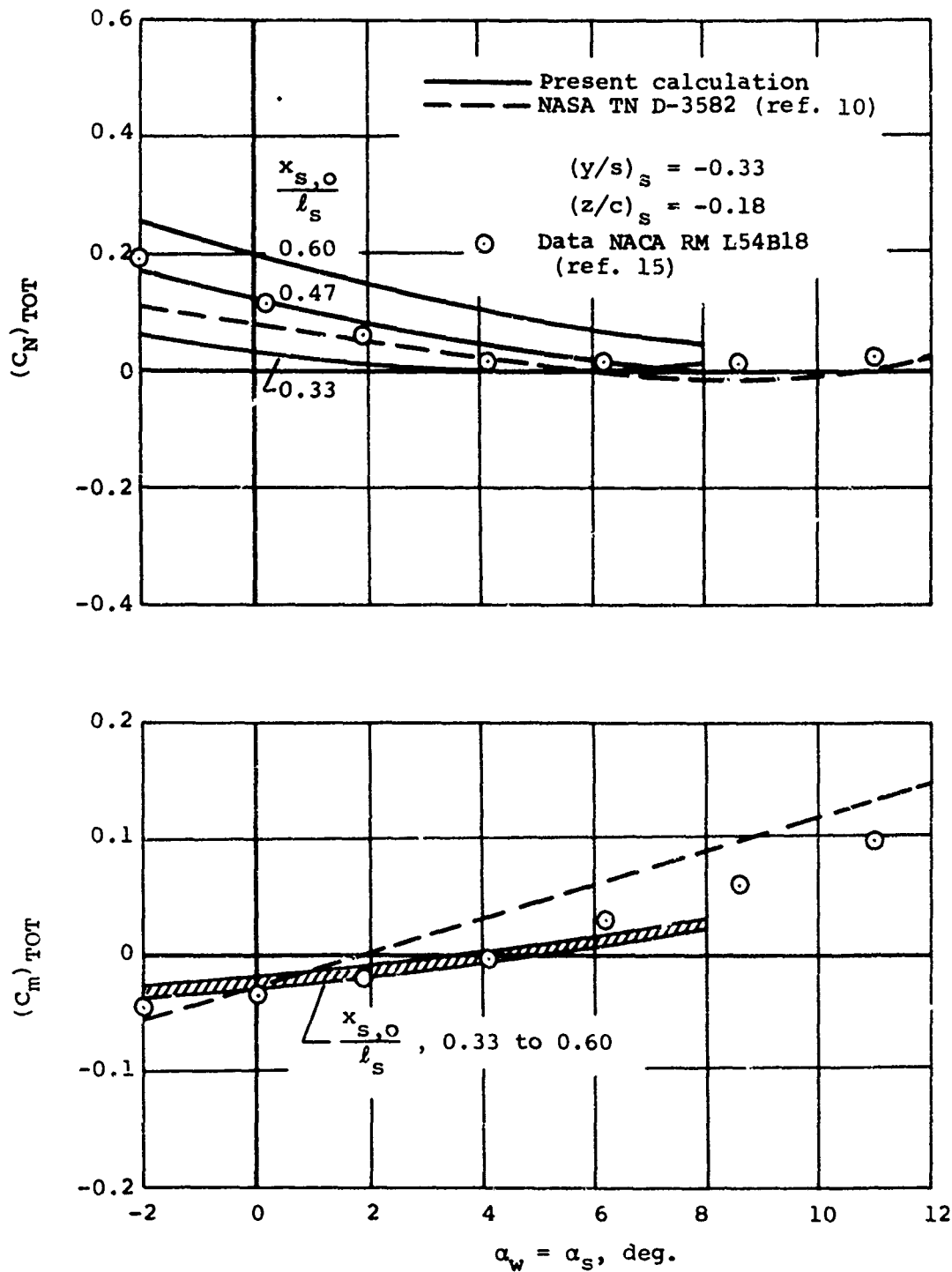
(a) Buoyancy component.

Figure 36.- Normal force and pitching moment on store without tail fins.



(b) Angle of attack component.

Figure 36.- Continued.



(c) Total force and moment.

Figure 36.- Concluded.

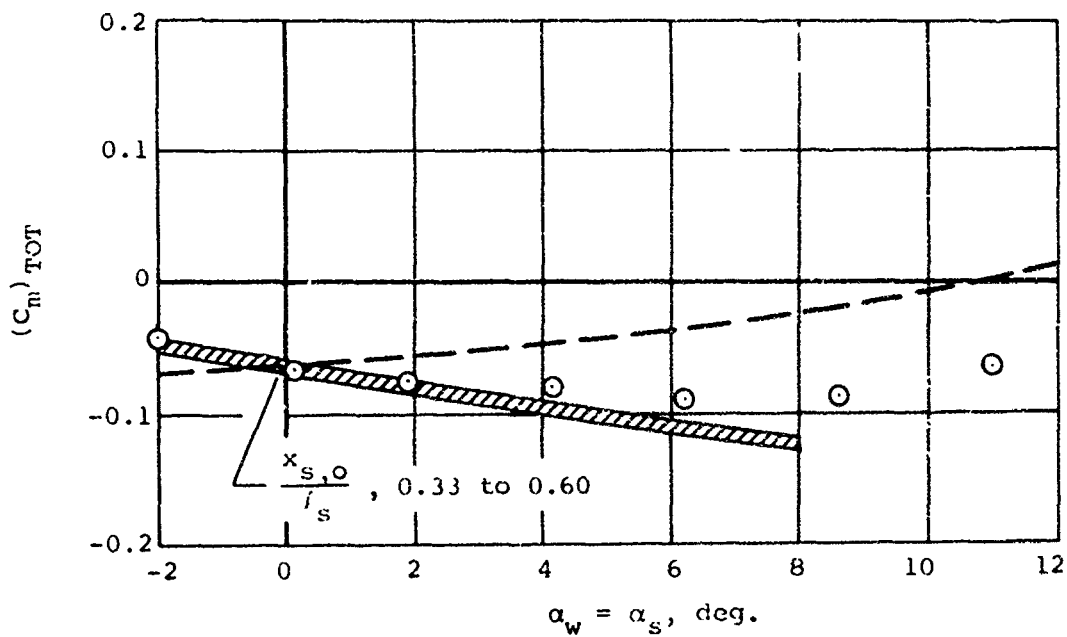
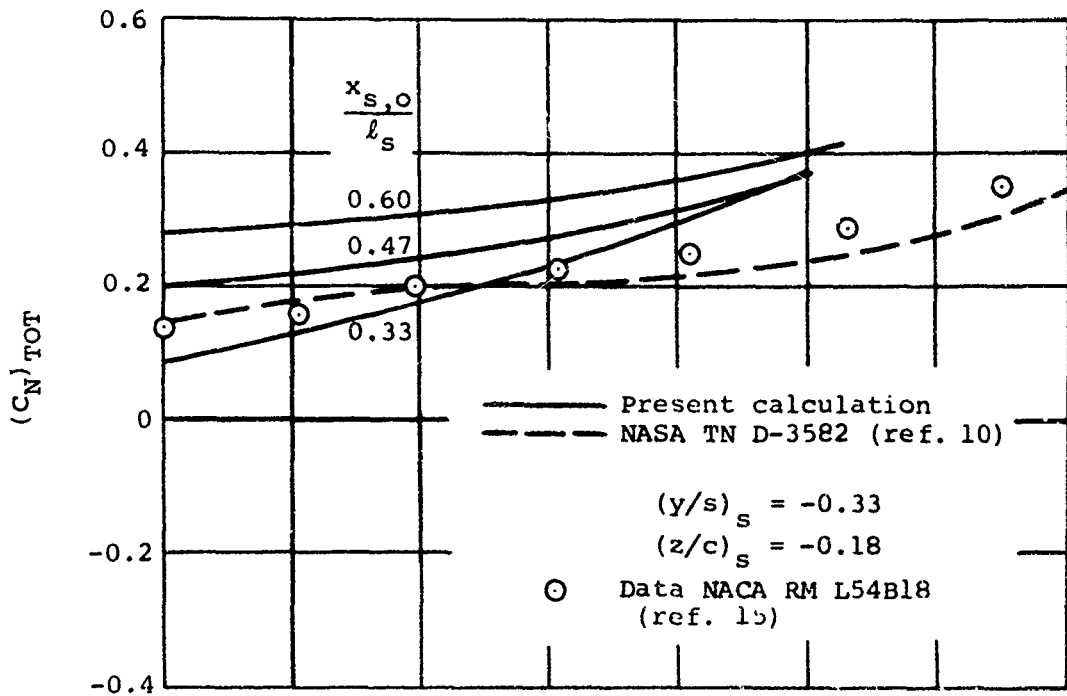


Figure 37.- Total normal force and pitching moment on store with tail fins.

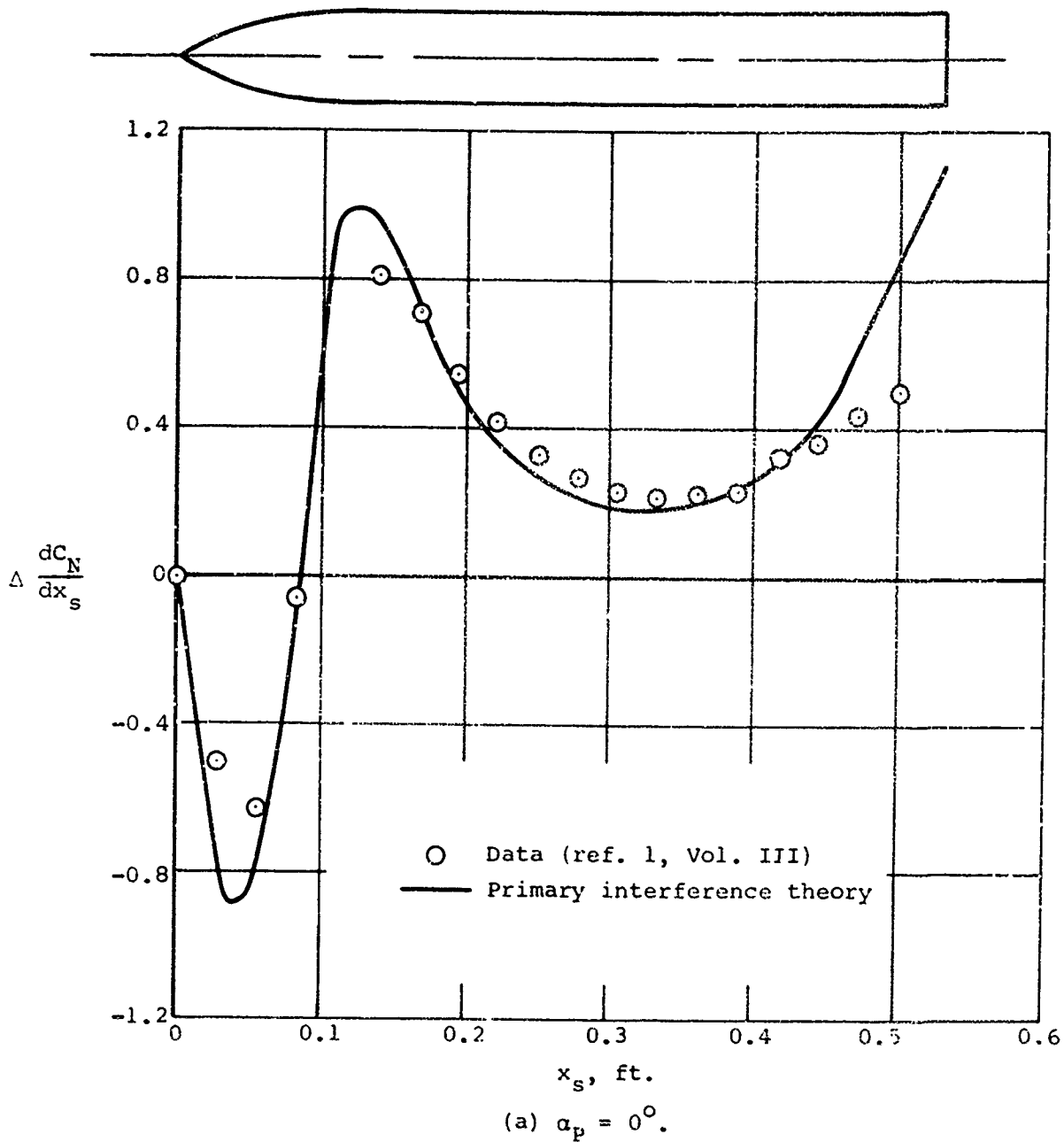
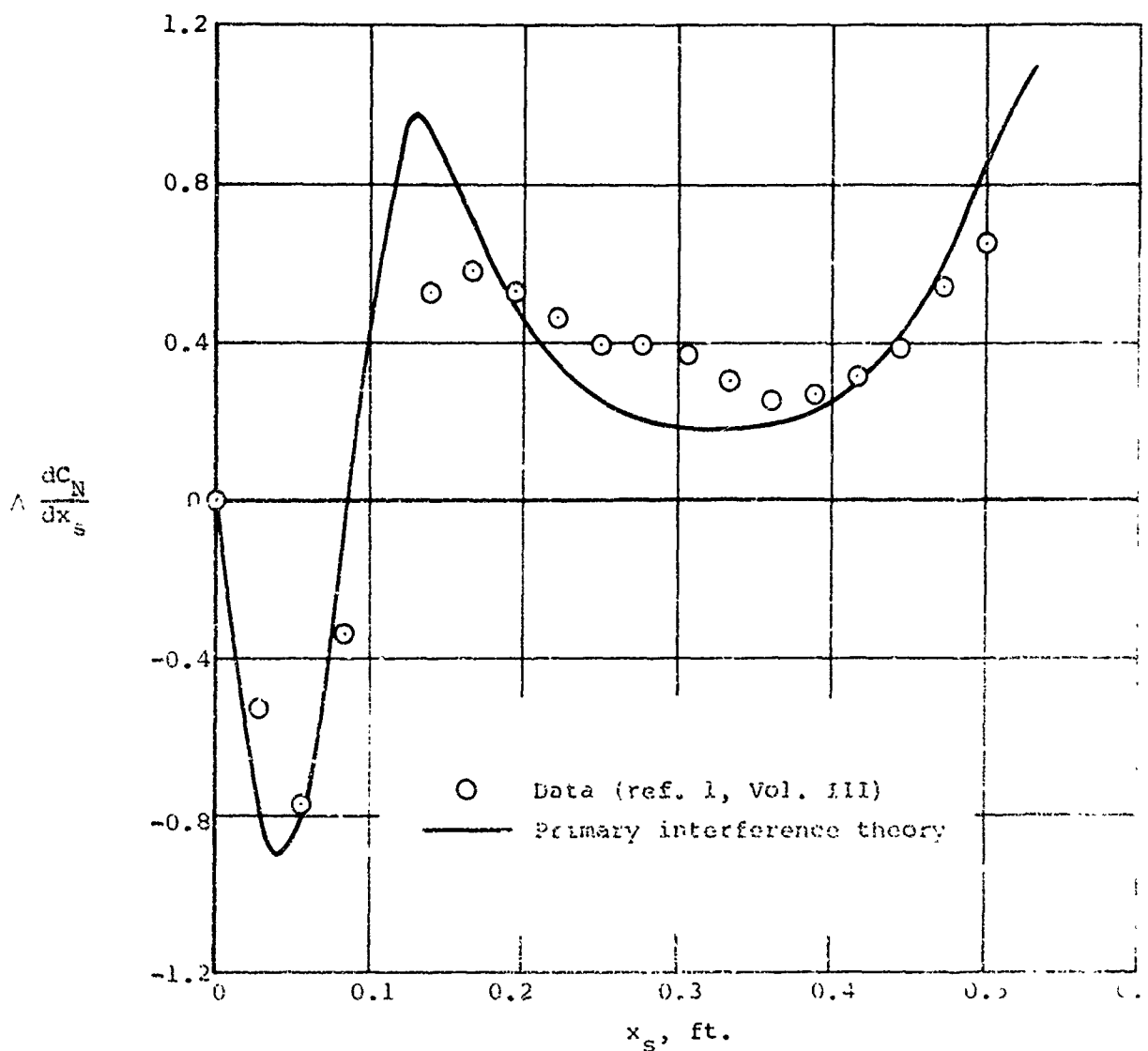
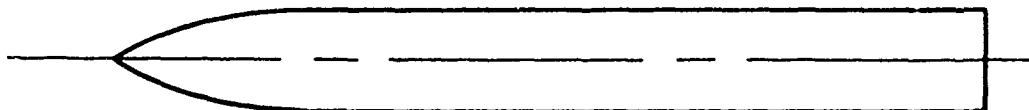
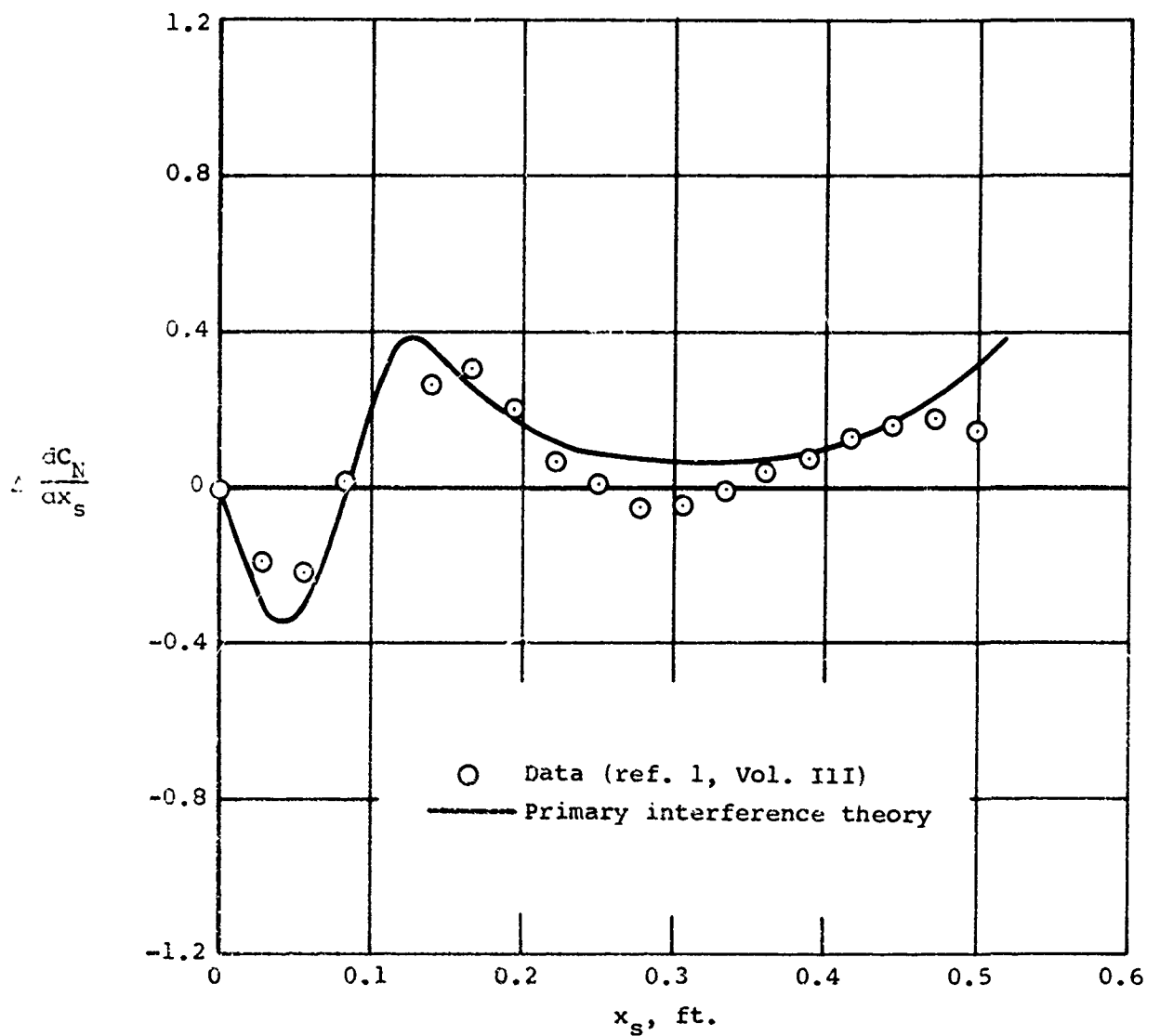


Figure 38.- Incremental loading on bottom store on TER rack at 1/3 semispan caused by addition of two side stores; $M_\alpha = 0.25$, $z/c = -0.40$.



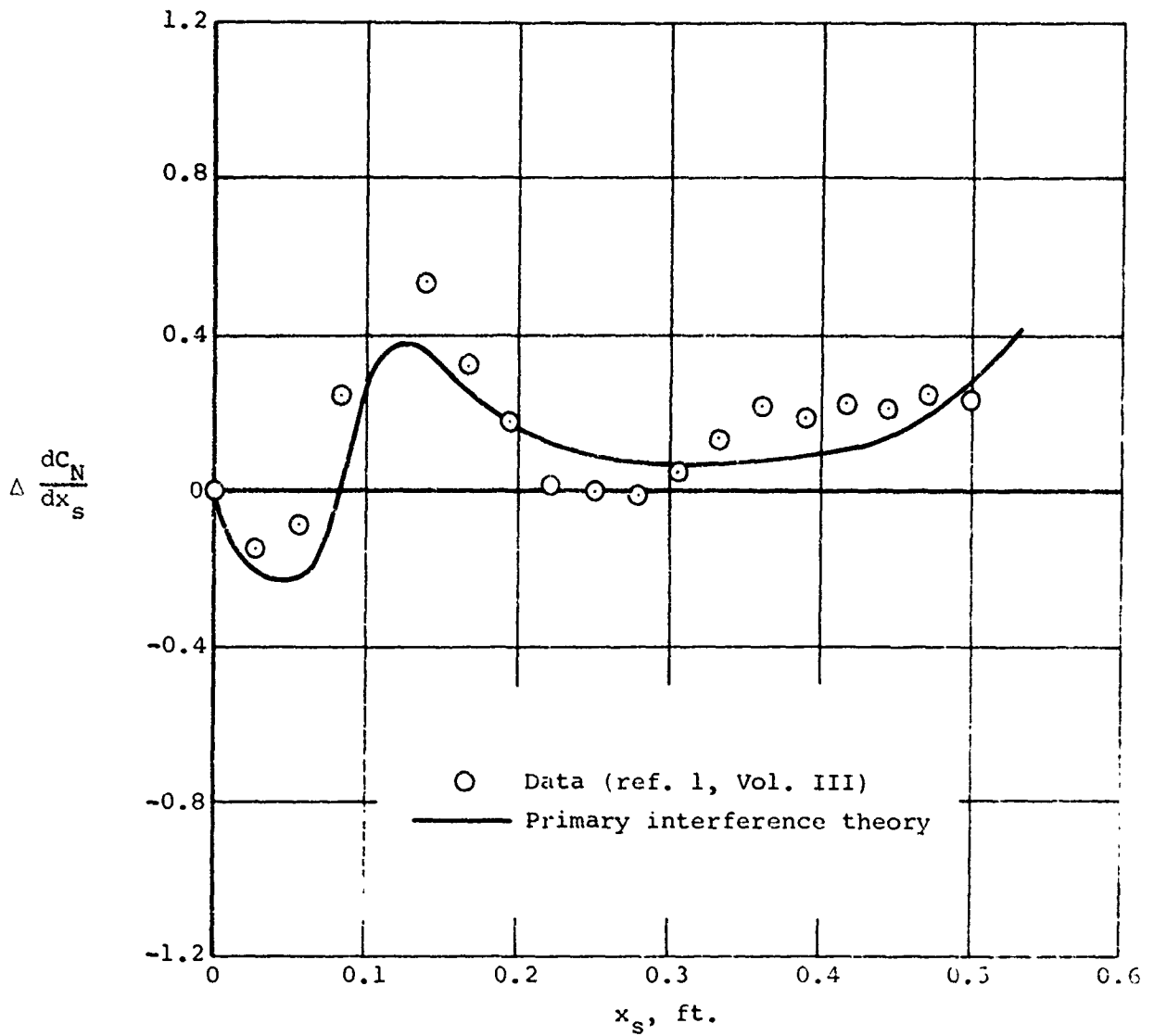
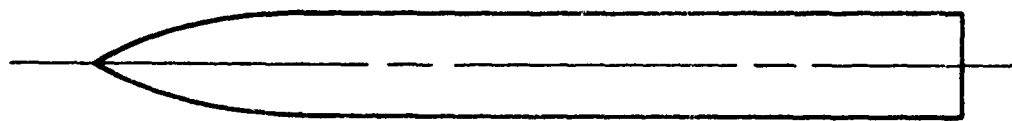
(b) $\alpha_p = 6^\circ$.

Figure 38.- Concluded.



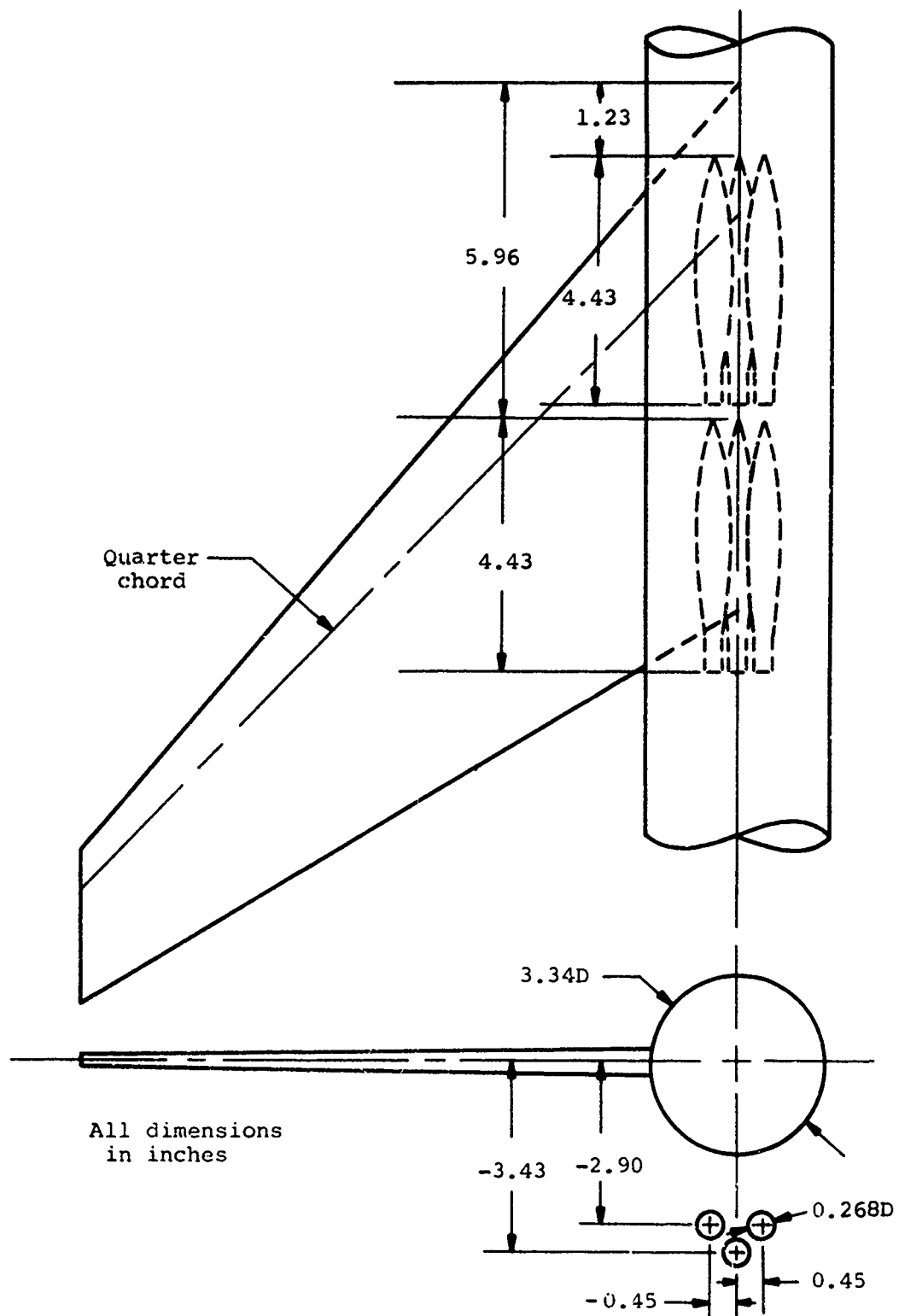
(a) $\alpha_p = 0^\circ$.

Figure 39.- Incremental loading on store no. 2 on TER rack at 1/3 span caused by addition of store no. 3; $M_\infty = 0.25$, $z/c = -0.333$.



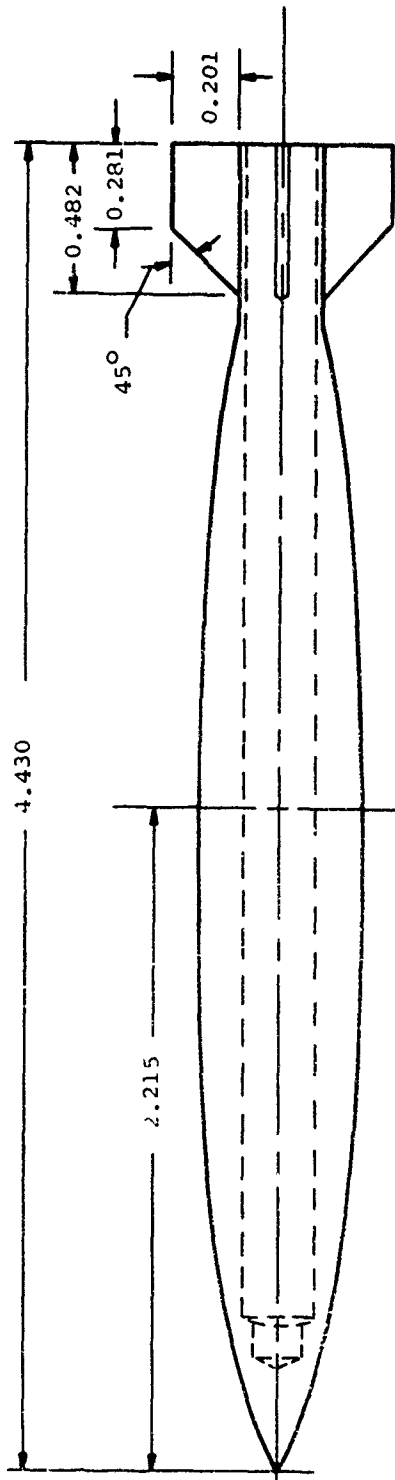
(b) $\alpha_p = 6^\circ$.

Figure 39.- Concluded.

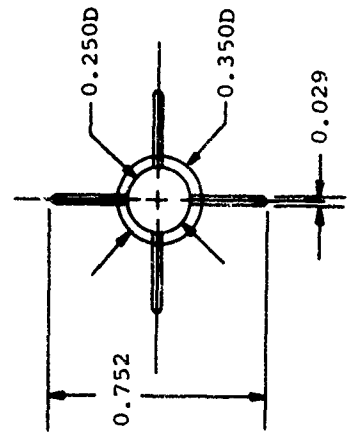


(a) Store locations.

Figure 40.- MER grouping of stores in the presence of the wing-fuselage combination of reference 1.



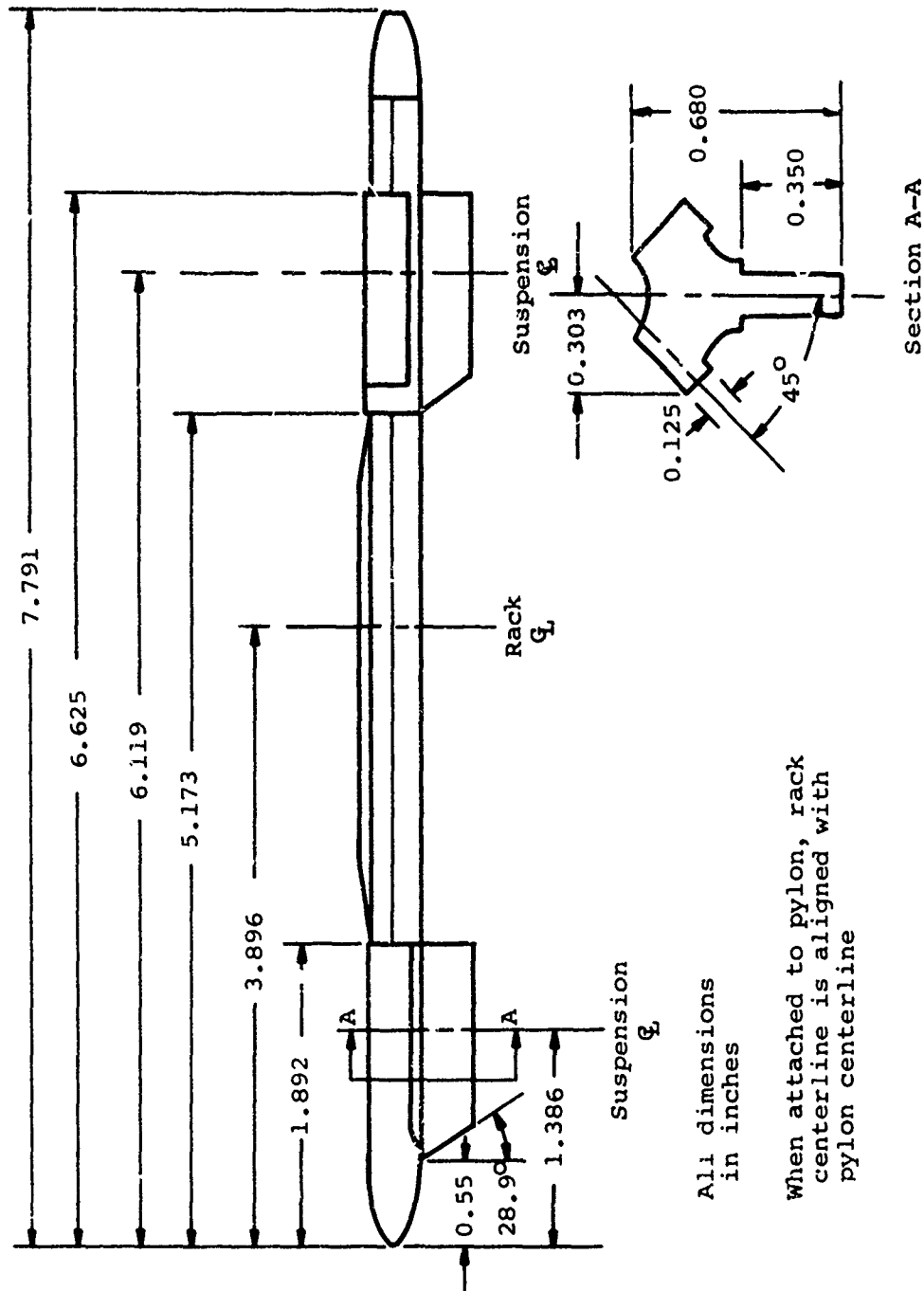
All dimensions
in inches



Store
Midpoint

Store midpoint aligned with suspension centerline on NER rack when in carriage position.
 Unfinned force and moment model same as finned model except for omission of fins.
 Finned and unfinned dummy stores same as respective force and moment stores except for omission of center bore for balance mount in J.
 See Table I for body coordinates.

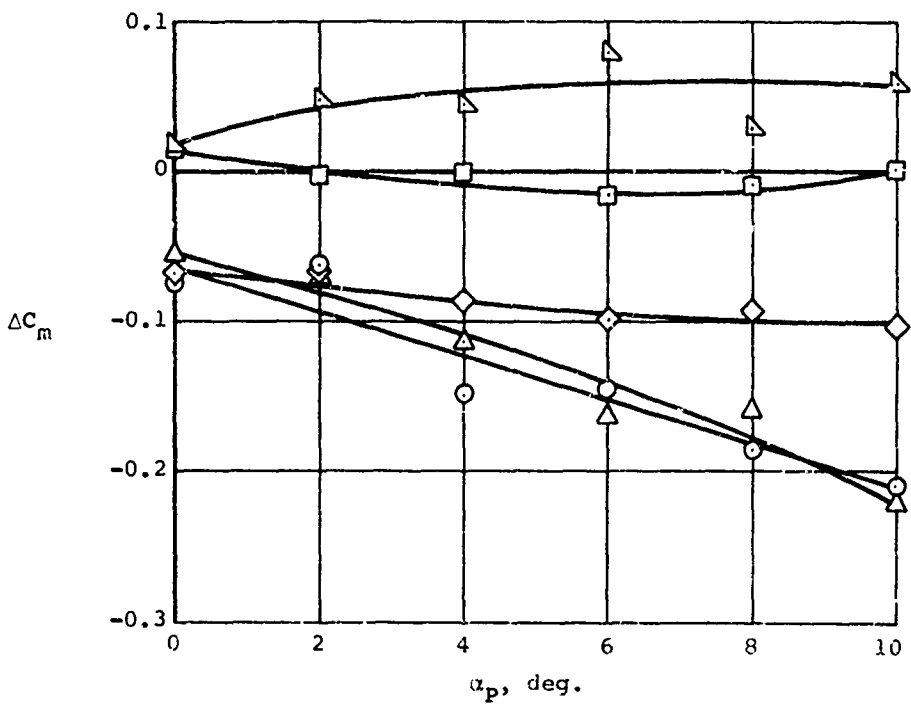
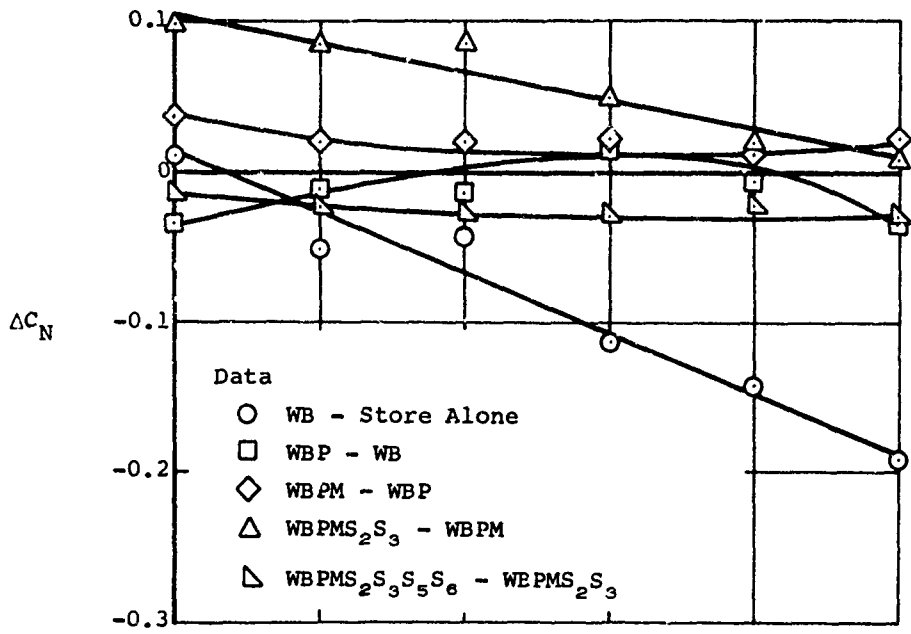
(b) Store details.
 Figure 40.- Concluded.



All dimensions in inches

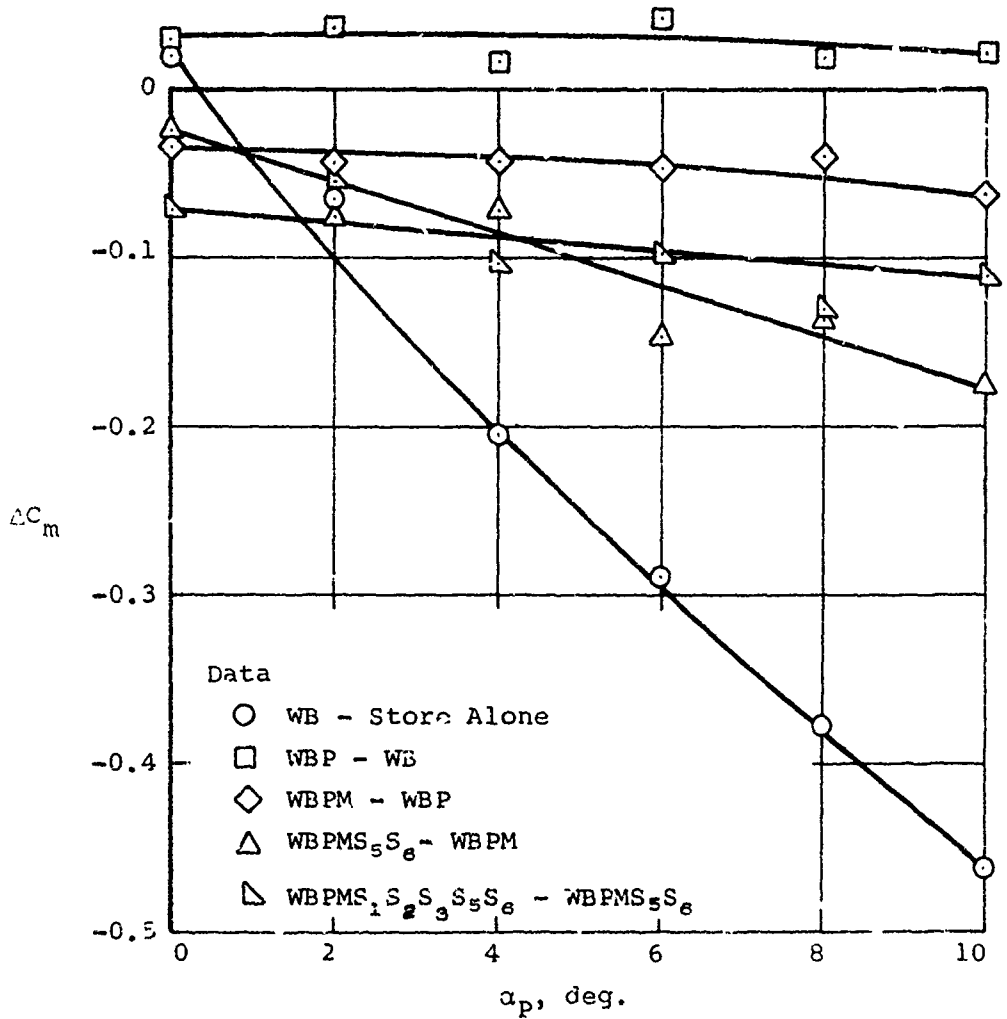
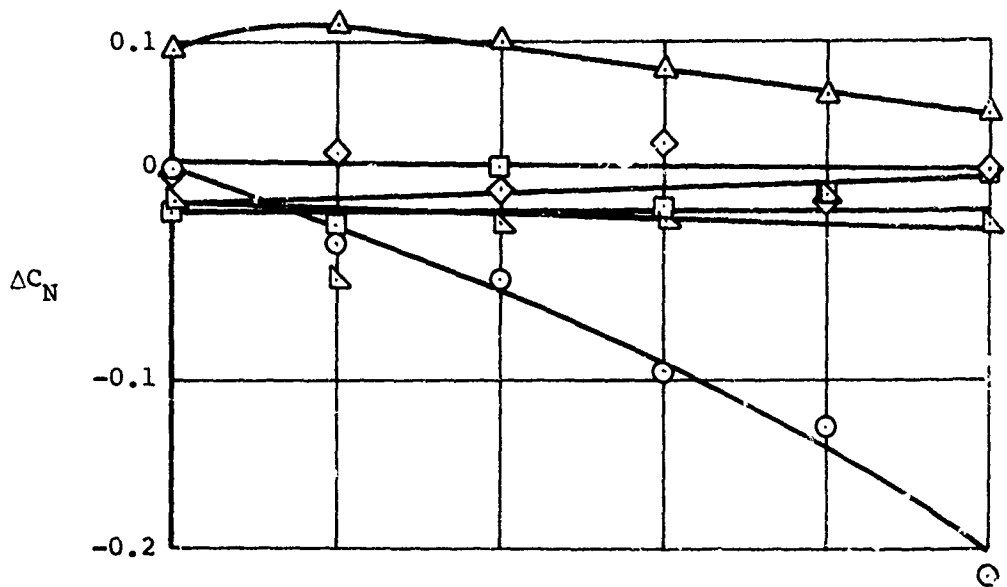
When attached to pylon, rack centerline is aligned with pylon centerline

Figure 41.- MER rack details.

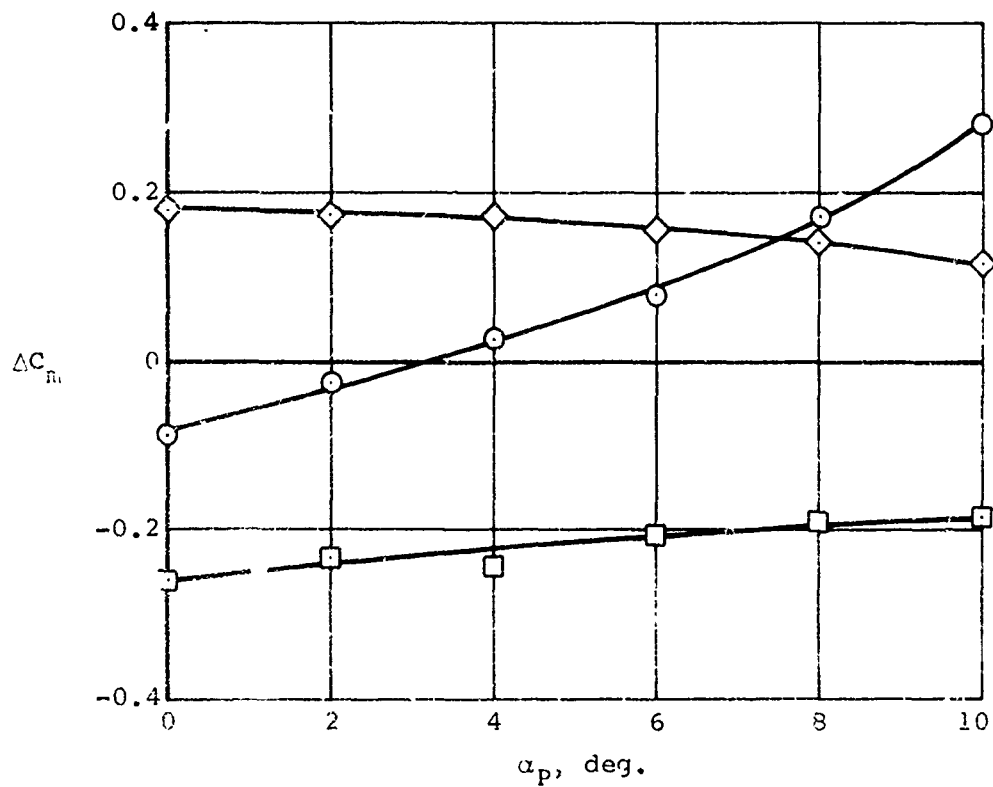
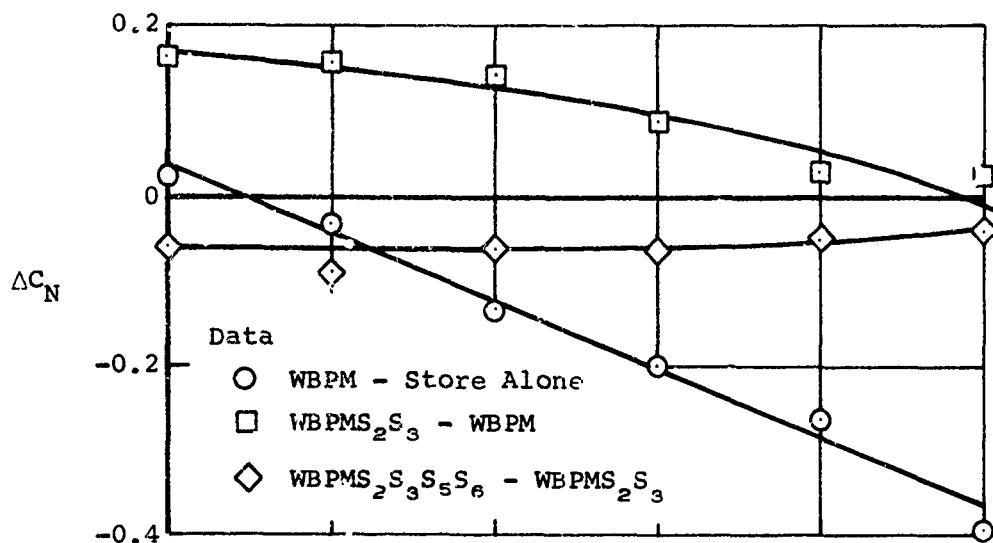


(a) Store number 1.

Figure 42.- Incremental interference force and moment on finless MER stores; $M_{on} = 0.40$, $z = -3.80$ inches.

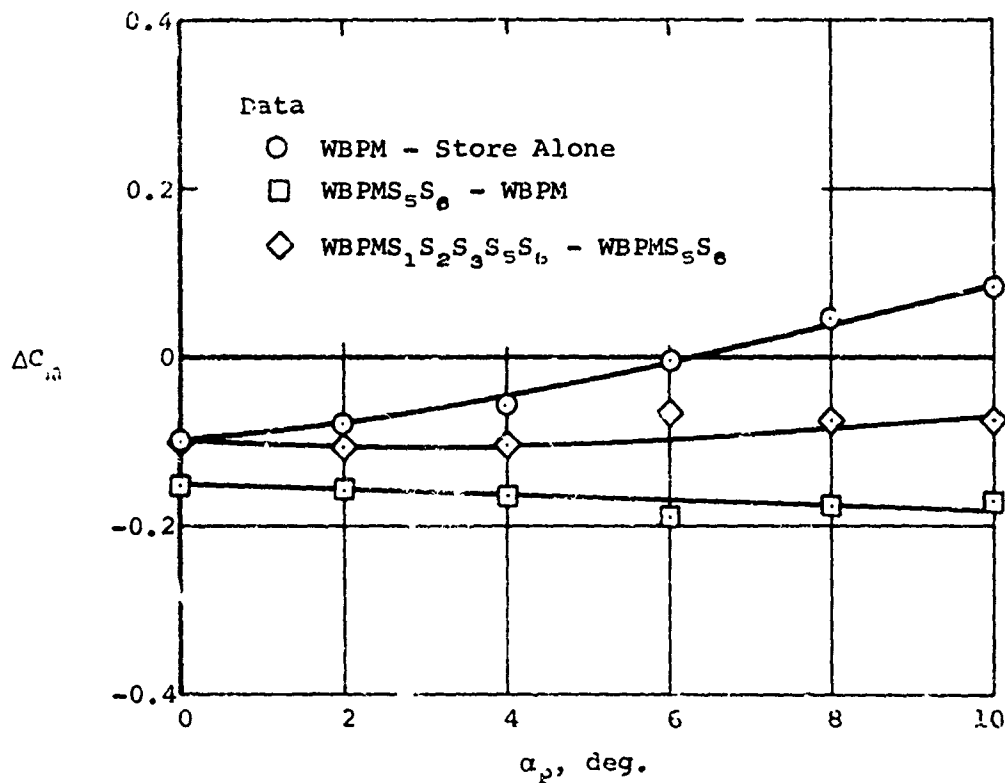
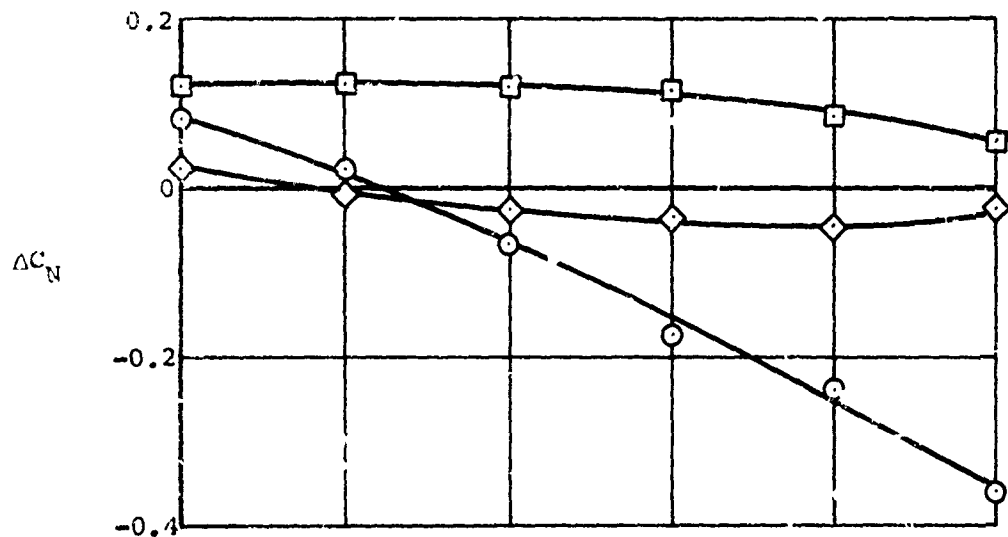


(b) Store number 4.
Figure 42.- Concluded.



(a) Store number 1.

Figure 43.- Incremental interference force and moment of finned MER stores; $M_\infty = 0.40$, $z = -3.80$ inches.



(b) Store number 4.
Figure 43.- Concluded.

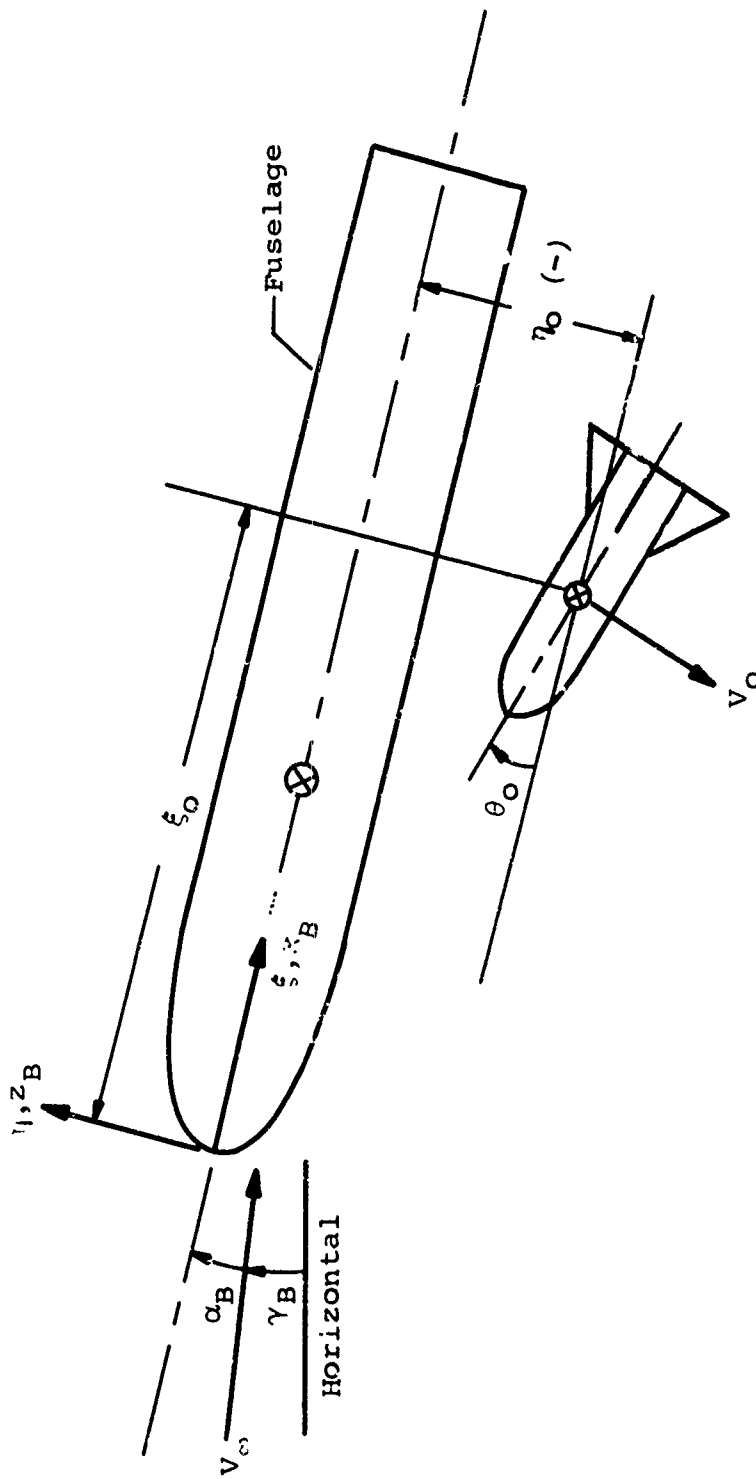


Figure 44.- Coordinate systems and angle definitions used in trajectory calculations.

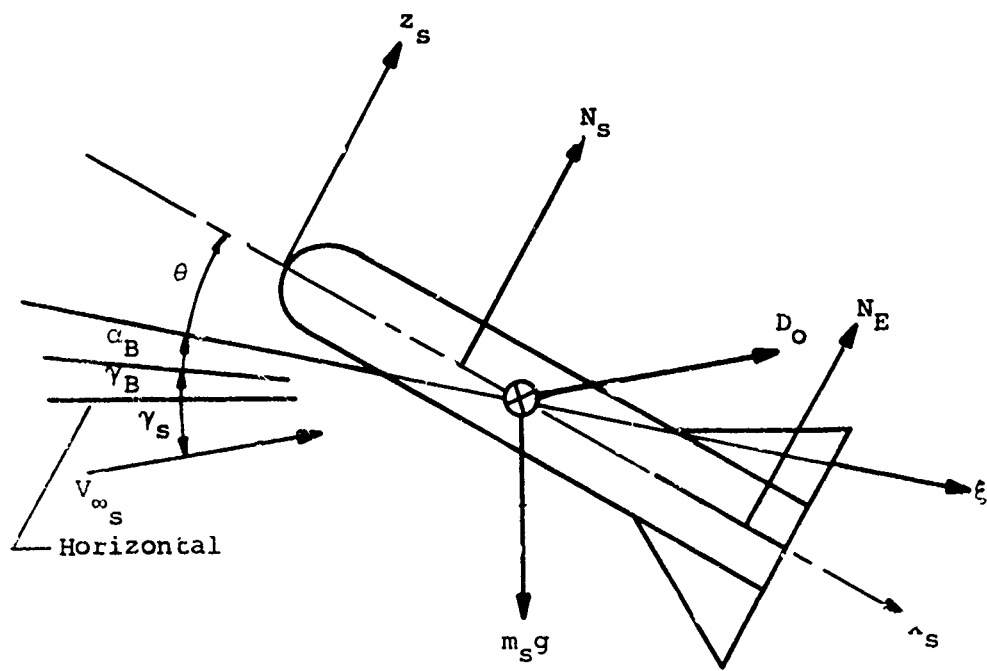
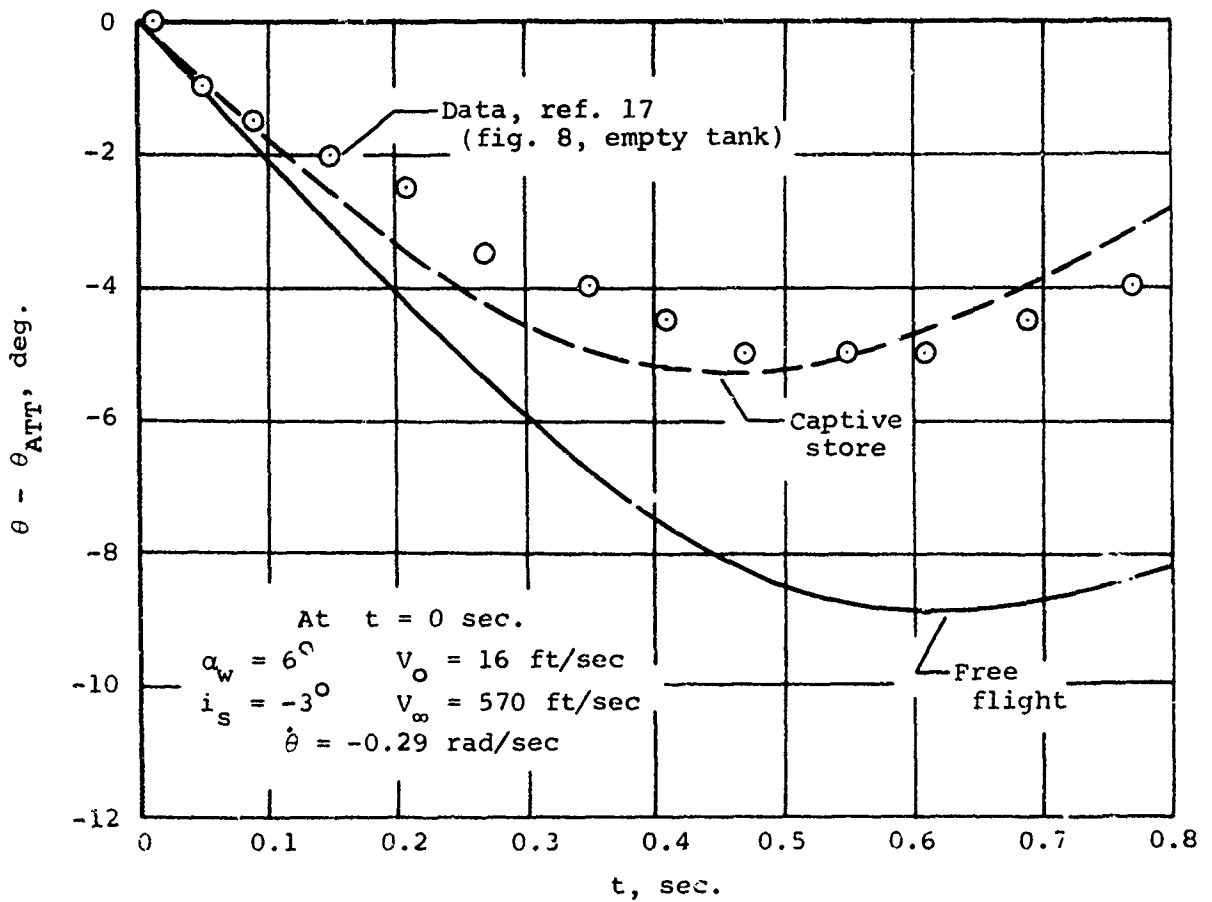
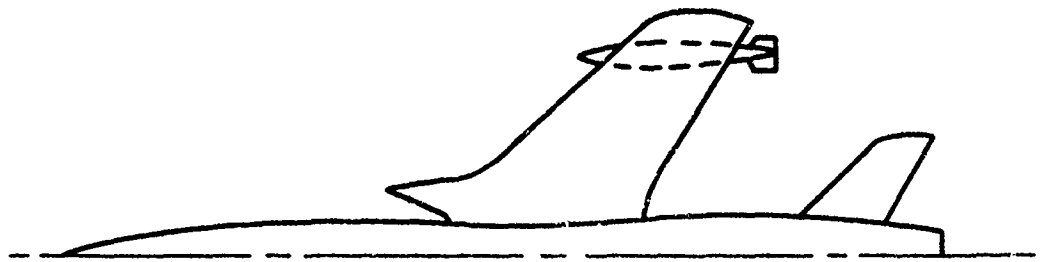
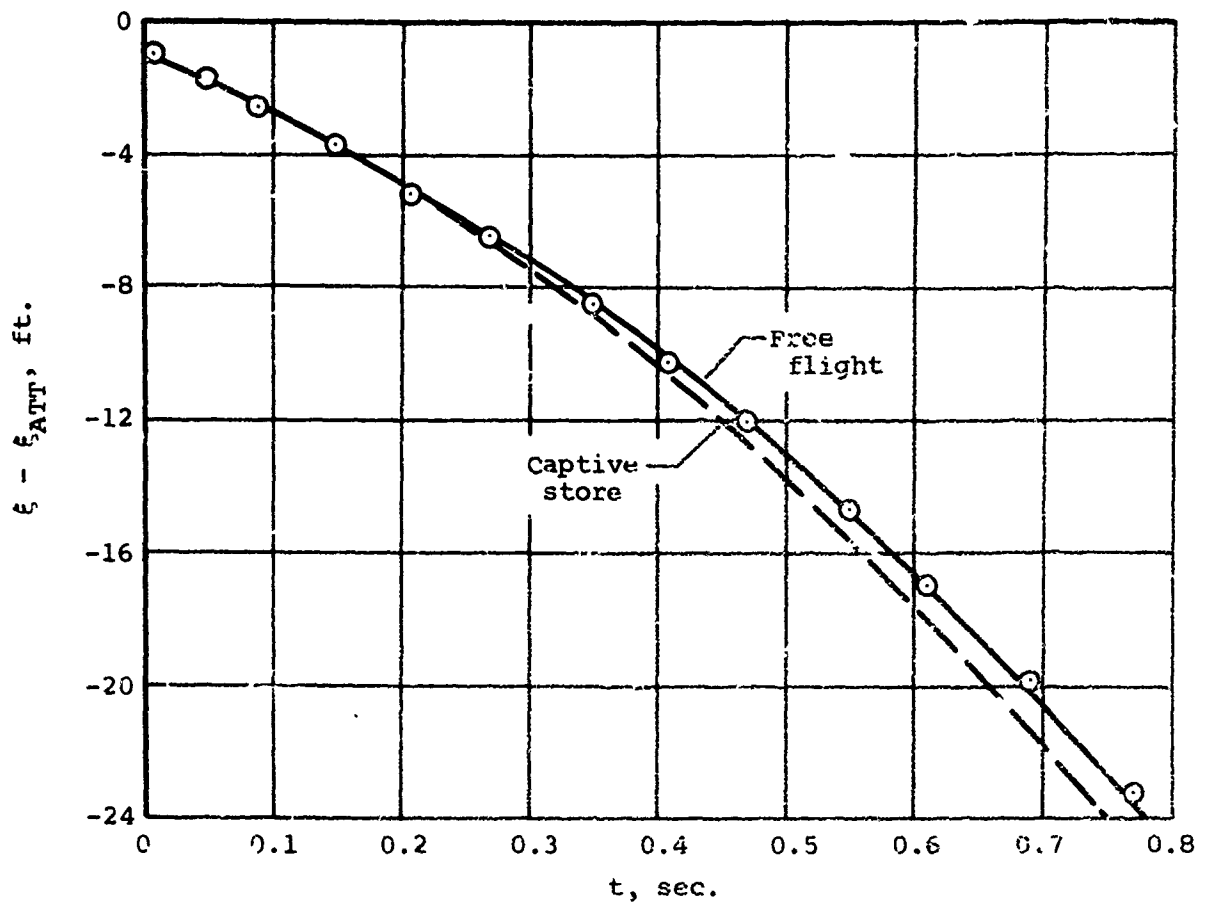


Figure 45.- Forces acting on store.



(a) Pitch angle.

Figure 46.- Sample trajectory calculation.



(b) Vertical location of store center of gravity.

Figure 46.- Concluded.

APPENDIX I

INTEGRATION OF THE LOADING EQUATION

The integration of the loading equation, equation (86), will be carried out in this appendix. It will be done in two steps. The first step will be to integrate the first two integrals to obtain the load distribution on the store alone in the nonuniform flow field. This constitutes the primary interference. Following this the last five integrals will be integrated to determine the load distribution due to the additional interference between the wing, pylon, and store.

To obtain the store-alone pressure coefficient, we must evaluate u_s , v_s , and w_s from equations (77) and (78). Since on the store

$$\sigma = ae^{i\theta} \tag{I-1}$$

equation (78) yields

$$\left. \begin{aligned} v_s &= -W \sin 2\theta - V \cos 2\theta + V_\infty \frac{da}{dx_s} \cos \theta \\ w_s &= W \cos 2\theta - V \sin 2\theta + V_\infty \frac{da}{dx_s} \sin \theta \end{aligned} \right\} \tag{I-2}$$

To obtain u_s we need the perturbation potential ϕ_s which can be obtained from equation (77). Ordinarily, we can just take the derivative of the perturbation potential to obtain u_s when the components of the free-stream potential V and W are not functions of x_s . However, in this case a component of u_s is associated with the crossflow potentials Vy_s and Wz_s . Accordingly,

$$u_s = \frac{\partial}{\partial x_s} (\phi_s + Vy_s + Wz_s) \tag{I-3}$$

Since ϕ_s is the real part of $W_s(\sigma)$ we find at some field point P where

$$\sigma_p = re^{i\gamma} \tag{I-4}$$

that equations (77) and (I-3) give

$$u_s = \frac{\sin \gamma}{r} \frac{d}{dx_s} (Wa^2) + \frac{\cos \gamma}{r} \frac{d}{dx_s} (Va^2) + \frac{V_\infty}{2} \log r \frac{d^2}{dx_s^2} (a^2) + y_s \frac{dV}{dx_s} + z_s \frac{dW}{dx_s} \quad (\text{I-5})$$

On the store where $r = a$, $\gamma = \theta$, this becomes

$$u_s = 2 \sin \theta \frac{d}{dx_s} (Wa) + 2 \cos \theta \frac{d}{dx_s} (Va) + \frac{V_\infty}{2} \log a \frac{d^2 a^2}{dx_s^2} \quad (\text{I-6})$$

From equations (75), (76), and (83)

$$\frac{\bar{u}_s}{V_\infty} = \frac{u_s}{V_\infty} - \beta \left(\frac{v_s}{V_\infty} \right) + \alpha \left(\frac{w_s}{V_\infty} \right) \quad (\text{I-7})$$

Since

$$\left. \begin{aligned} \alpha &= \frac{W}{V_\infty} \\ \beta &= -\frac{V}{V_\infty} \end{aligned} \right\} \quad (\text{I-8})$$

the perturbation velocity \bar{u}_s is

$$\begin{aligned} \frac{\bar{u}_s}{V_\infty} &= 2 \sin \theta \frac{d}{dx_s} \left(\frac{Wa}{V_\infty} \right) + 2 \cos \theta \frac{d}{dx_s} \left(\frac{Va}{V_\infty} \right) + \frac{1}{2} \log a \frac{d^2 a^2}{dx_s^2} \\ &+ \left[\left(\frac{W}{V_\infty} \right)^2 - \left(\frac{V}{V_\infty} \right)^2 \right] \cos 2\theta - 4 \left(\frac{V}{V_\infty} \right) \left(\frac{W}{V_\infty} \right) \sin 2\theta \\ &+ \frac{da}{dx_s} \left[\left(\frac{V}{V_\infty} \right) \cos \theta + \left(\frac{W}{V_\infty} \right) \sin \theta \right] \end{aligned} \quad (\text{I-9})$$

Thus, the first integral in equation (86) is

$$\int_0^{2\pi} \frac{\bar{u}_s}{V_\infty} \sin \theta \, d\theta = 2\pi \frac{d}{dx_s} \left(\frac{Wa}{V_\infty} \right) + \pi \frac{da}{dx_s} \left(\frac{W}{V_\infty} \right) \quad (\text{I-10})$$

The second integral in equation (86) involves the square terms

$$\left(\frac{v_s}{V_\infty} \right)^2 + \left(\frac{w_s}{V_\infty} \right)^2 = \left(\frac{W}{V_\infty} \right)^2 + \left(\frac{v}{c_1} \right)^2 + \left(\frac{da}{dx_s} \right)^2 - 2 \frac{da}{dx_s} \left[\frac{W}{V_\infty} \sin \theta + \frac{v}{V_\infty} \sin \theta \right] \quad (\text{I-11})$$

The second integral is thus

$$\frac{1}{2} \int_0^{2\pi} \left[\left(\frac{v_s}{V_\infty} \right)^2 + \left(\frac{w_s}{V_\infty} \right)^2 \right] \sin \theta \, d\theta = -\pi \frac{da}{dx_s} \left(\frac{W}{V_\infty} \right) \quad (\text{I-12})$$

The store normal force without the vortex system is the sum of these two integrals

$$\frac{dN_s}{dx_s} = 2\pi\rho V_\infty^2 a \frac{d}{dx_s} \left(\frac{Wa}{V_\infty} \right) \quad (\text{I-13})$$

It is of interest that the foregoing expression can be interpreted in terms of normal forces associated with apparent mass and buoyancy. Let us rewrite equation (I-13) as

$$\frac{dN_s}{dx_s} = V_\infty \frac{d}{dx_s} (\pi\rho a^2 W) + V_\infty (\pi\rho a^2) \frac{dW}{dx_s} \quad (\text{I-14})$$

The additional apparent mass of the store per unit length is

$$m = \pi\rho a^2 \quad (\text{I-15})$$

so that equation (I-14) can be rewritten

$$\frac{dN_s}{dx_s} = \frac{d}{dt} (mW) + V_\infty \pi\rho a^2 \frac{dW}{dx_s} \quad (\text{I-16})$$

The first term has a clear momentum interpretation. The second term is a buoyant force as will now be shown. For irrotational plane flow, we have¹

$$\frac{\partial p}{\partial n} = - \frac{\rho V_L^2}{R} \quad (\text{I-17})$$

n = direction normal to streamline
 V_L = velocity along streamline
 R = radius of curvature of streamline

The buoyant force dN_s/dx_s per unit length is

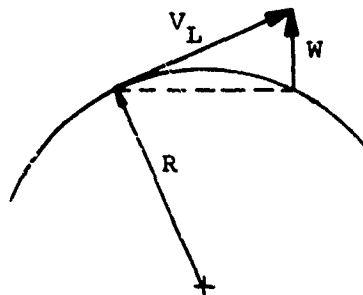
$$\frac{dN_s}{dx_s} = 2 \int_0^{\pi/2} (p_\ell - p_u) a \sin \theta \, d\theta \quad (\text{I-18})$$

wherein

$$p_\ell - p_u = 2 \frac{\partial p}{\partial n} a \sin \theta \quad (\text{I-19})$$

The radius of curvature of the flow sketched below is

$$\frac{1}{R} = - \frac{d(W/V_L)}{dx_s} \quad (\text{I-20})$$



¹Milne-Thomson, L. M.: Theoretical Hydrodynamics. Second ed., The MacMillan Company, New York, 1950.

Thus,

$$\begin{aligned} \frac{dN_s}{dx_s} &= 4a^2 \frac{\partial p}{\partial n} \int_0^{\pi/2} \sin^2 \theta \, d\theta \\ &= \pi a^2 \rho V_L \frac{dW}{dx_s} \end{aligned} \quad (I-21)$$

It is seen that except for a negligible cosine term, the buoyant normal force per unit length is the same as the last term of equation (I-16).

The normal-force distribution calculated in accordance with equation (I-16) was the basis of the store force calculations in sections 6.1 and 6.2. The buoyant force was calculated there from actual pressure calculations rather than the simple expression in equation (I-16).

The remaining terms in equation (86), the third through seventh integrals, are the additional interference and will now be evaluated in terms of the strengths Γ_i of the external vortices which remain to be determined.

In evaluating the third through sixth integrals of equation (86), we note that they are linear sums over the external vortices so that we can carry out the integration for one external vortex Γ_1 and sum over the external vortices. For one external vortex and its image system, the complete potential is from equation (79)

$$W_1(\sigma) = \frac{i\Gamma_1}{2\pi} \left[\log(\sigma - \sigma_1) - \log\left(\sigma - \frac{a^2}{\sigma_1}\right) + \log \sigma \right] \quad (I-22)$$

where σ , the field point, is

$$\sigma = \zeta e^{i\theta} \quad (I-23)$$

and σ_1 , the vortex position, is

$$\sigma_1 = r_1 e^{i\phi_1} \quad (I-24)$$

The velocities v_1 and w_1 on the store are given by

$$v_1 - iw_1 = \left. \frac{dW_1(\sigma)}{d\sigma} \right|_{\zeta=a} \quad (I-25)$$

from which we find

$$\left. \begin{aligned} v_1 &= \frac{\Gamma_1 \sin \theta}{2\pi a} \left[1 + \frac{a^2 - r_1^2}{R_1} \right] \\ w_1 &= - \frac{\Gamma_1 \cos \theta}{2\pi a} \left[1 + \frac{a^2 - r_1^2}{R_1} \right] \end{aligned} \right\} \quad (I-26)$$

wherein

$$R_1 = a^2 + r_1^2 - 2ar_1 \cos(\phi_1 - \theta) \quad (I-27)$$

To obtain u_1 on the store, we must extract ϕ_1 from equation (I-22).

$$\phi_1 = \text{R.P. } W_1(\sigma)$$

or

$$\phi_1 = - \frac{\Gamma}{2\pi} \left[\arg(\sigma - \sigma_1) - \arg\left(\sigma - \frac{a^2}{\sigma_1}\right) + \arg \sigma \right] \quad (I-28)$$

Carrying out the differentiation in the manner shown in reference 13, we find

$$\begin{aligned} u_1 = \left. \frac{\partial \phi_1}{\partial x_s} \right|_{\zeta=a} &= - \frac{1}{2\pi} \frac{d\Gamma_1}{dx_s} \left[\tan^{-1} \left(\frac{a \sin \theta - r_1 \sin \phi_1}{a \cos \theta - r_1 \cos \phi_1} \right) \right. \\ &\quad \left. - \tan^{-1} \left(\frac{a \sin \theta - \frac{a^2}{r_1^2} \sin \phi_1}{a \cos \theta - \frac{a^2}{r_1^2} \cos \phi_1} \right) + \theta \right] \end{aligned}$$

(eq. (I-29) cont. on next page)

$$\begin{aligned}
& - \frac{\Gamma_1}{2\pi} \left[\frac{(a \sin \theta - z_v) \frac{dy_v}{dx_s} - (a \cos \theta - y_v) \frac{dz_v}{dx_s}}{R_1} \right] \\
& + \frac{\Gamma_1}{2\pi} \left(\frac{r_1^2}{a^2} \right) \left[\frac{\left(a \sin \theta - \frac{a^2}{r_1^2} z_v \right) \frac{d}{dx_s} \left(\frac{a^2}{r_1^2} y_v \right)}{R_1} \right. \\
& \quad \left. - \frac{\left(a \cos \theta - \frac{a^2}{r_1^2} y_v \right) \frac{d}{dx_s} \left(\frac{a^2}{r_1^2} z_v \right)}{R_1} \right] \tag{I-29}
\end{aligned}$$

where the vortex coordinates are

$$\left. \begin{aligned} z_v &= r_1 \sin \phi_1 \\ y_v &= r_1 \cos \phi_1 \end{aligned} \right\} \tag{I-30}$$

The third integral is evaluated by performing the integration using equation (I-29) in the manner shown in reference 13 to obtain

$$\begin{aligned}
& \sum_{i=1}^N \int_0^{2\pi} \left(\frac{u_i}{V_\infty} \right) \sin \theta \, d\theta \\
& = 2\pi \sum_{i=1}^N \left\{ \frac{1}{a} \frac{d}{dx_s} \left[\frac{a^3}{r_i} \cos \phi_i \left(\frac{\Gamma_i}{2\pi a V_\infty} \right) \right] - \frac{a}{r_i} \left(\frac{\Gamma_i}{2\pi a V_\infty} \right) \cos \phi_i \frac{da}{dx_s} \right\} \tag{I-31}
\end{aligned}$$

The fourth, fifth, and sixth integrals are evaluated using equations (I-2), (I-8), and (I-26) and yield (ref. 13)

$$\begin{aligned}
& \sum_{i=1}^N \int_0^{2\pi} \left(\frac{\alpha w_i - \beta v_i}{V_\infty} \right) \sin \theta \, d\theta \\
& = \pi \sum_{i=1}^N \left(\frac{\beta^2}{r_i^2} \right) \left(\frac{\Gamma_i}{2\pi a V_\infty} \right) \left[\left(\frac{V}{V_\infty} \right) \cos 2\phi_i + \left(\frac{W}{V_\infty} \right) \sin 2\phi_i \right] \tag{I-32}
\end{aligned}$$

$$\sum_{i=1}^N \int_0^{2\pi} \left[\left(\frac{v_i}{V_\infty} \right) \left(\frac{v_s}{V_\infty} \right) + \left(\frac{w_i}{V_\infty} \right) \left(\frac{w_s}{V_\infty} \right) \right] \sin \theta \, d\theta$$

$$= \pi \sum_{i=1}^N \left(\frac{a^2}{r_i^2} \right) \left(\frac{\Gamma_i}{2\pi a V_\infty} \right) \left[\frac{V}{V_\infty} \cos 2\phi_i + \frac{W}{V_\infty} \sin 2\phi_i \right] \quad (\text{I-33})$$

$$\frac{1}{2} \sum_{i=1}^N \int_0^{2\pi} \left[\left(\frac{v_i}{V_\infty} \right)^2 + \left(\frac{w_i}{V_\infty} \right)^2 \right] \sin \theta \, d\theta = 2\pi a^3 \sum_{i=1}^N \left(\frac{\Gamma_i}{2\pi a V_\infty} \right)^2 \frac{\sin \phi_i}{r_i (r_i^2 - a^2)} \quad (\text{I-34})$$

In evaluating the seventh integral of equation (86) we can perform the integration for a pair of external vortices Γ_1 and Γ_2 and then sum over all pairs. In summing over i and j as specified in equation (86), we are summing over the nondiagonal terms of the ij matrix. If i and j are interchanged, the value of the integral is unchanged. Accordingly, we can sum over only half of the nondiagonal terms and double the sum. Performing the integration in the manner of reference 13, we find

$$\sum_{i=1}^N \sum_{\substack{j=1 \\ i \neq j}}^N \int_0^{2\pi} \left[\left(\frac{v_i}{V_\infty} \right) \left(\frac{v_j}{V_\infty} \right) + \left(\frac{w_i}{V_\infty} \right) \left(\frac{w_j}{V_\infty} \right) \right] \sin \theta \, d\theta$$

$$= -4\pi \sum_{j=1}^{N-1} \sum_{i=j+1}^N \left[\frac{a}{r_i} \sin \phi_i + \frac{a}{r_j} \sin \phi_j \right. \\ \left. + \psi(a, r_i, r_j, \phi_i, \phi_j) \right] \left(\frac{\Gamma_i}{2\pi a V_\infty} \right) \left(\frac{\Gamma_j}{2\pi a V_\infty} \right) \quad (\text{I-35})$$

where

$$\psi(a, r_i, r_j, \phi_i, \phi_j)$$

$$= \frac{a}{r} \left\{ (r_j^2 - r_i^2) \left[(a^2 + r_i^2) r_j \sin \phi_j - (a^2 + r_j^2) r_i \sin \phi_i \right] \right. \\ \left. + 2r_i r_j \sin (\phi_j - \phi_i) \left[(r_i^2 - a^2) r_j \cos \phi_j - (r_j^2 - a^2) r_i \cos \phi_i \right] \right\} \quad (\text{I-36})$$

and λ in the above expression is

$$\begin{aligned} \lambda = & (r_i^2 + r_j^2) (a^4 + r_i^2 r_j^2) - 2(a^2 + r_i^2) (a^2 + r_j^2) r_i r_j \cos (\phi_i - \phi_j) \\ & + 4a^2 r_i^2 r_j^2 \cos^2 (\phi_i - \phi_j) \end{aligned} \quad (\text{I-37})$$

The five integrals just evaluated determine the store normal force per unit length due to the vortex system. That is,

$$\begin{aligned} \frac{1}{\rho V_\infty^2 a} \frac{dN_\Gamma}{dx_s} = & 2\pi \sum_{i=1}^N \left\{ \frac{1}{a} \frac{d}{dx_s} \left[\frac{a^3}{r_i} \cos \phi_i \left(\frac{\Gamma_i}{2\pi a V_\infty} \right) \right] \right. \\ & \left. - \frac{a}{r_i} \left(\frac{\Gamma_i}{2\pi a V_\infty} \right) \cos \phi_i \frac{da}{dx_s} \right\} \\ & + 2\pi \sum_{i=1}^N \frac{a^2}{r_i^2} \left(\frac{\Gamma_i}{2\pi a V_\infty} \right) \left[\frac{V}{V_\infty} \cos 2\phi_i + \frac{W}{V_\infty} \sin 2\phi_i \right] \\ & + 2\pi \sum_{i=1}^N \frac{a^3}{r_i (r_i^2 - a^2)} \left(\frac{\Gamma_i}{2\pi a V_\infty} \right)^2 \sin \phi_i \\ & - 2\pi \sum_{j=1}^{N-1} \sum_{i=j+1}^N \left[\frac{a}{r_i} \sin \phi_i + \frac{a}{r_j} \sin \phi_j + \psi(a, r_i, r_j, \phi_i, \phi_j) \right] \\ & \cdot \left(\frac{\Gamma_i}{2\pi a V_\infty} \right) \left(\frac{\Gamma_j}{2\pi a V_\infty} \right) \end{aligned} \quad (\text{I-38})$$

The total normal force per unit length given by equation (86) is the sum of the two components given by equations (I-13) and (I-38) That is,

$$\frac{1}{\rho V_\infty^2 a} \frac{dN}{dx_s} = \frac{1}{\rho V_\infty^2 a} \left(\frac{dN_s}{dx_s} + \frac{dN_\Gamma}{dx_s} \right) \quad (\text{I-39})$$

The first term on the right-hand side is the normal force acting on the store due to a known nonuniform flow field and is evaluated using the methods of sections 6.1 through 6.3. The remaining term is the force due to mutual interference between the wing, pylon, and store. To evaluate this term the strengths of the vortices Γ_i must be determined. This determination is described in Appendix II.

APPENDIX II

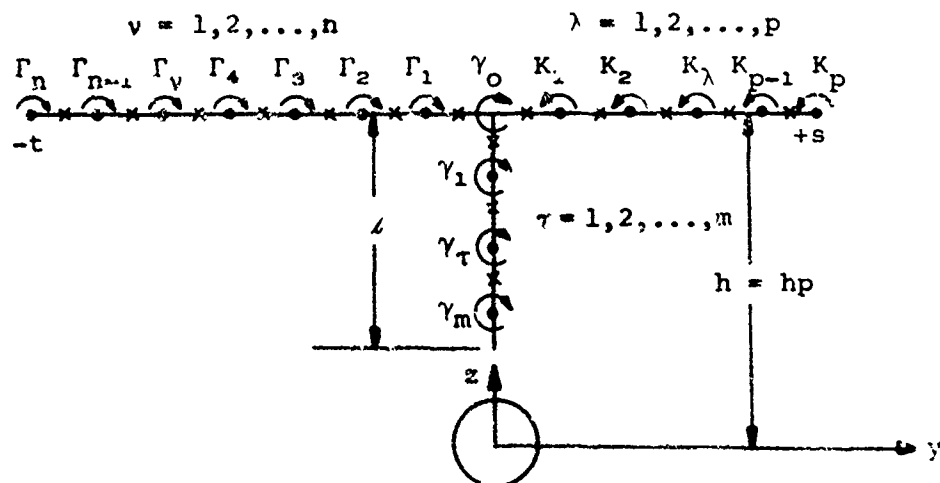
CALCULATION OF VORTEX STRENGTHS

II-1. INTRODUCTION

The determination of the vortex strengths is simple in principle, but is complicated from the bookkeeping point of view. Vortices are placed at selected locations on the wing and pylon together with their image systems within the store. The velocities induced by the vortex system normal to the wing and pylon at selected control points are calculated in the form of a linear combination of the vortex strengths. These normal induced velocities are then equated to the normal velocities at these points which are to be cancelled, thereby giving enough equations to determine the vortex strengths. The velocities to be cancelled, which are considered the boundary conditions, depend on the configuration under consideration.

II-2. VORTEX NOTATION, POSITIONS, AND CONTROL POINTS

The general array of vortices on wing and pylon is as shown in the sketch below. The left and right wing panels may be of unequal length. On the right wing panel we will place equally spaced vortices of strength K_λ , $1 \leq \lambda \leq p$; on the left wing panel we place equally spaced vortices Γ_v , $1 \leq v \leq n$; and on the pylon vortices γ_τ , $1 \leq \tau \leq m$. The control points are located midway between the vortices. Positive circulation of the various vortices is as shown.



The vortex centers are thus located as follows with respect to the store axis:

$$\left. \begin{array}{lll}
 \text{Left panel: } \Gamma_v & v = 1, 2, \dots, n & \sigma_v = -\frac{t v}{n} + ih \\
 \text{Right panel: } K_\lambda & \lambda = 1, 2, \dots, p & \sigma_\lambda = \frac{s \lambda}{p} + ih \\
 \text{Pylon: } \gamma_\tau & \tau = 1, 2, \dots, m & \sigma_\tau = 0 + i\left(h_p - \frac{\tau l}{m}\right)
 \end{array} \right\} \quad (\text{II-1})$$

No vortex is placed at the bottom of the pylon because it would be identically cancelled by its image in the store attached position.

Each vortex as sketched above has a trailing leg of opposite sign at the pylon-wing juncture. Accordingly,

$$\tau_0 = - \sum_{\tau \neq 0} \gamma_\tau - \sum K_\lambda - \sum \Gamma_v \quad (\text{II-2})$$

The control points are located as follows:

$$\left. \begin{array}{lll}
 \text{Left panel: } \sigma_g = -\frac{t}{2n} (2g - 1) + ih; & g = 1, 2, \dots, n \\
 \text{Right panel: } \sigma_j = \frac{s}{2p} (2j - 1) + ih; & j = 1, 2, \dots, p \\
 \text{Pylon: } \sigma_k = i\left[h_p - \frac{l}{2m} (2k - 1)\right]; & k = 1, 2, \dots, m
 \end{array} \right\} \quad (\text{II-3})$$

We must satisfy boundary conditions on the left panel, the right panel, and the pylon. Let us define the following vortex-induced velocities:

$w_L(\Gamma)$	normal velocity on left panel induced by Γ vortex
$w_L(K)$	" " " " " " " " K "
$w_L(\gamma)$	" " " " " " " " γ "
$w_R(\Gamma)$	normal velocity on right panel induced by Γ vortex
$w_R(K)$	" " " " " " " " K "
$w_R(\gamma)$	" " " " " " " " γ "

$v_P(\Gamma)$	normal velocity on pylon induced by Γ vortex
$v_P(K)$	" " " " " " K "
$v_P(\gamma)$	" " " " " " γ "

Vortex velocities include those induced by their images including the center vortex.

At each control point, we will obtain equations of the following types which satisfy the condition of no flow through the control point.

Left panel control points:

$$\sum_v w_L(\Gamma_v) + \sum_\lambda w_L(K_\lambda) + \sum_\tau w_L(\gamma_\tau) + w_L(g) = 0 \quad (\text{II-4})$$

Right panel control points:

$$\sum_v w_R(\Gamma_v) + \sum_\lambda w_R(K_\lambda) + \sum_\tau w_R(\gamma_\tau) + w_R(j) = 0 \quad (\text{II-5})$$

Pylon:

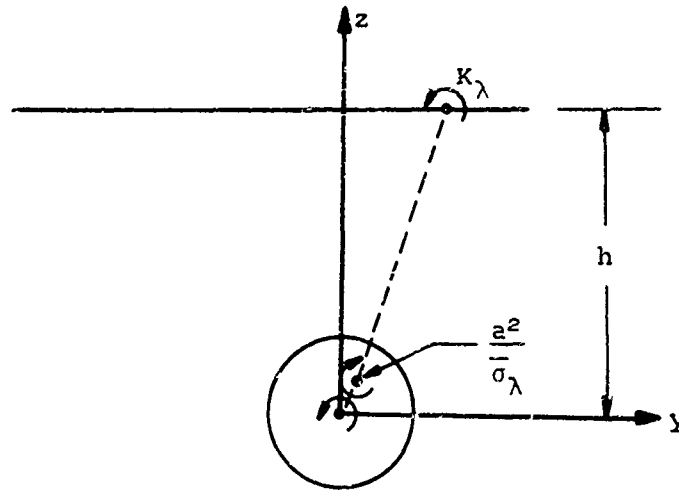
$$\sum_v v_P(\Gamma_v) + \sum_\lambda v_P(K_\lambda) + \sum_\tau v_P(\gamma_\tau) + v_P(k) = 0 \quad (\text{II-6})$$

In these equations $w_L(g)$, $w_R(j)$, and $v_P(k)$ are interference velocities at the control points to be cancelled by the vortex system.

II-3. DETERMINATION OF VORTEX-INDUCED VELOCITIES

The expressions for the vortex-induced velocities will now be determined. The derivation of only one of the nine will be presented, since they all proceed in a similar manner. The derivation of all nine is carried out in reference 13.

Let us consider the velocity induced on a right wing panel control point by a right wing panel vortex plus its images.



The direction of positive K_λ is shown in the above sketch. The location of the external vortex is σ_λ . For the external vortex plus its images, the complex potential is

$$w_{K_\lambda}(\sigma) = -\frac{iK_\lambda}{2\pi} \left[\log(\sigma - \sigma_\lambda) - \log\left(\sigma - \frac{a^2}{\sigma_\lambda}\right) + \log \sigma \right] \quad (\text{II-7})$$

from which we obtain

$$\frac{dw_{K_\lambda}}{d\sigma} = (v - iw)_{K_\lambda} = -\frac{iK_\lambda}{2\pi} \left[\frac{1}{\sigma - \sigma_\lambda} - \frac{1}{\sigma - \frac{a^2}{\sigma_\lambda}} + \frac{1}{\sigma} \right] \quad (\text{II-8})$$

Let

$$\sigma_\lambda = y_\lambda + ih \quad (\text{II-9})$$

and for the wing control point

$$\sigma = y + ih \quad (\text{II-10})$$

Then the normal velocity induced at a wing control point by a vortex on the right wing panel is

$$w_{K_\lambda} = \frac{K_\lambda}{2\pi} \left\{ \frac{1}{y - y_\lambda} - \frac{(y_\lambda^2 + h^2) [y(y_\lambda^2 + h^2) - y_\lambda a^2]}{[y(y_\lambda^2 + h^2) - a^2 y_\lambda]^2 + h^2 [y_\lambda^2 + h^2 - a^2]^2} + \frac{y}{y^2 + h^2} \right\} \quad (\text{II-11})$$

For a specific vortex equation (II-1) gives

$$y_\lambda = \frac{s\lambda}{p} \quad (\text{II-12})$$

and for a specific right panel control point (eq. (II-3))

$$y = \frac{s}{2p} (2j - 1) \quad (\text{II-13})$$

Therefore, the velocity induced by a right panel vortex on a right panel control point is

$$w_{R(K_\lambda)} = \frac{K_\lambda}{2\pi} \left\{ \frac{1}{\frac{s}{p} (j - \lambda - \frac{1}{2})} + \frac{\frac{s}{2p} (2j - 1)}{\frac{s^2}{4p^2} (2j - 1)^2 + h^2} - \frac{\left(\frac{s^2}{p^2} \lambda^2 + h^2 \right) \left[\frac{s}{2p} (2j - 1) \left(\frac{s^2}{p^2} \lambda^2 + h^2 \right) - \frac{s}{p} a^2 \lambda \right]}{\left[\frac{s}{2p} (2j - 1) \left(\frac{s^2}{p^2} \lambda^2 + h^2 \right) - \frac{s}{p} a^2 \lambda \right]^2 + [h^2] \left[\frac{s^2}{p^2} \lambda^2 + h^2 - a^2 \right]^2} \right\} \quad (\text{II-14})$$

In a similar manner the other eight vortex-induced velocities are found to be

$$w_L(K_\lambda) = \frac{K_\lambda}{2\pi} \left\{ \frac{-1}{\frac{t}{2n}(2g-1) + \frac{s}{p}\lambda} - \frac{\frac{t}{2n}(2g-1)}{\frac{t^2}{4n^2}(2g-1)^2 + h^2} \right. \\ \left. - \frac{\left(\frac{s^2}{p^2}\lambda^2 + h^2\right) \left[-\frac{t}{2n}(2g-1)\left(\frac{s^2\lambda^2}{p^2} + h^2\right) - \frac{s}{p}a^2\lambda\right]}{\left[-\frac{t}{2n}(2g-1)\left(\frac{s^2}{p^2}\lambda^2 + h^2\right) - \frac{s}{p}a^2\lambda\right]^2 + h^2\left[\frac{s^2\lambda^2}{p^2} + h^2 - a^2\right]^2} \right\} \quad (\text{II-15})$$

$$w_R(\Gamma_v) = -\frac{\Gamma_v}{2\pi} \left\{ \frac{1}{\frac{s}{2p}(2j-1) + \frac{t}{n}v} + \frac{\frac{s}{2p}(2j-1)}{\frac{s^2}{4p^2}(2j-1)^2 + h^2} \right. \\ \left. - \frac{\left(\frac{t^2}{n^2}v^2 + h^2\right) \left[\frac{s}{2p}(2j-1)\left(\frac{t^2v^2}{n^2} + h^2\right) + \frac{t}{n}a^2v\right]}{\left[\frac{s}{2p}(2j-1)\left(\frac{t^2v^2}{n^2} + h^2\right) + \frac{t}{n}a^2v\right]^2 + h^2\left[\frac{t^2}{n^2}v^2 + h^2 - a^2\right]^2} \right\} \quad (\text{II-16})$$

$$w_L(\Gamma_v) = -\frac{\Gamma_v}{2\pi} \left\{ \frac{1}{\frac{t}{n}\left(-g + v + \frac{1}{2}\right)} - \frac{\frac{t}{2n}(2g-1)}{\frac{t^2}{4n^2}(2g-1)^2 + h^2} \right. \\ \left. - \frac{\left(\frac{t^2}{n^2}v^2 + h^2\right) \left[-\frac{t}{2n}(2g-1)\left(\frac{t^2}{n^2}v^2 + h^2\right) + \frac{t}{n}v\right]}{\left[-\frac{t}{2n}(2g-1)\left(\frac{t^2}{n^2}v^2 + h^2\right) + \frac{t}{n}v\right]^2 + h^2\left[\frac{t^2}{n^2}v^2 + h^2 - a^2\right]^2} \right\} \quad (\text{II-17})$$

$$\begin{aligned}
w_R(\gamma_\tau) = & -\frac{\gamma_\tau \frac{s}{2p} (2j-1)}{2\pi} \left\{ \frac{1}{\left(\frac{s}{2p}\right)^2 (2j-1)^2 + \left(\frac{\tau\ell}{m} + h - h_p\right)^2} \right. \\
& - \frac{\left(h_p - \frac{\tau\ell}{m}\right)^2}{\left[h\left(h_p - \frac{\tau\ell}{m}\right) - a^2\right]^2 + \left(\frac{s}{2p}\right)^2 (2j-1)^2 \left(h_p - \frac{\tau\ell}{m}\right)^2} \\
& \left. + \frac{1}{\frac{s^2}{4p} (2j-1)^2 + h^2} \right\} \tag{II-18}
\end{aligned}$$

$$\begin{aligned}
w_L(\gamma_\tau) = & \frac{\gamma_\tau \left(\frac{t}{2n}\right) (2g-1)}{2\pi} \left\{ \frac{1}{\left(\frac{t}{2n}\right)^2 (2g-1)^2 + \left(\frac{\tau\ell}{m} + h - h_p\right)^2} \right. \\
& - \frac{\left(h_p - \frac{\tau\ell}{m}\right)^2}{\left[h\left(h_p - \frac{\tau\ell}{m}\right) - a^2\right]^2 + \left(\frac{t}{2n}\right)^2 (2g-1)^2 \left(h_p - \frac{\tau\ell}{m}\right)^2} \\
& \left. + \frac{1}{\frac{t^2}{4n^2} (2g-1)^2 + h^2} \right\} \tag{II-19}
\end{aligned}$$

$$\begin{aligned}
v_P(K_\lambda) = & -\frac{K_\lambda}{2\pi} \left\{ \frac{h_p - \frac{\ell}{2m} (2k-1) - h}{\left(\frac{s}{p} \lambda\right)^2 + \left[h_p - h - \frac{\ell}{2m} (2k-1)\right]^2} \cdot \frac{1}{h_p - \frac{\ell}{2m} (2k-1)} \right. \\
& \left. + \frac{\left\{ ha^2 - \left(\frac{s^2}{p^2} \lambda^2 + h^2\right) \left[h_p - \frac{\ell}{2m} (2k-1)\right] \right\}}{\left\{ a^2 - h \left[h_p - \frac{\ell}{2m} (2k-1)\right] \right\}^2 + \frac{s^2}{p^2} \lambda^2 \left[h_p - \frac{\ell}{2m} (2k-1)\right]^2} \right\} \tag{II-20}
\end{aligned}$$

$$v_{P(\Gamma_v)} = \frac{\Gamma_v}{2\pi} \left\{ \frac{h_p - \frac{l}{2m}(2k-1) - h}{\frac{t^2 v^2}{n^2} + \left[h_p - h - \frac{\ell k}{m} + \frac{l}{2m} \right]^2} + \frac{1}{h_p - \frac{l}{2m}(2k-1)} \right. \\ \left. + \frac{\left[ha^2 - \left(h_p - \frac{\ell k}{m} + \frac{l}{2m} \right) \left(\frac{t^2 v^2}{n^2} + h^2 \right) \right]}{\left[a^2 - h \left(h_p - \frac{\ell k}{m} + \frac{l}{2m} \right) \right]^2 + \left[\frac{t v}{n} \left(h_p - \frac{\ell k}{m} + \frac{l}{2m} \right) \right]^2} \right\} \quad (\text{II-21})$$

$$v_{P(\gamma_\tau)} = \frac{\gamma_\tau}{2\pi} \left\{ \frac{1}{\frac{\tau l}{m} - \frac{l}{2m}(2k-1)} + \frac{1}{\left[h_p - \frac{l}{2m}(2k-1) \right]} \right. \\ \left. + \frac{\left(h_p - \frac{\tau l}{m} \right)}{a^2 - \left(h_p - \frac{\tau l}{m} \right) \left(h_p - \frac{l k}{m} + \frac{l}{2m} \right)} \right\} \quad (\text{II-22})$$

II-4. EQUATIONS FOR VORTEX STRENGTHS

In writing the equations for the vortex strengths, we start first with equation (II-5) for the right panel. The value of $w_{R(\Gamma)}$ is given by equation (II-16), $w_{R(K)}$ by equation (II-14), and $w_{R(\gamma)}$ by equation (II-18). In writing these equations, we will also consider a trailing leg in the wing-pylon juncture having the opposite sign from that of the other trailing leg. As a consequence, the vortices at the center of the store will be equal and opposite and thus cancel. The induced velocity due to the trailing leg at the wing-pylon juncture can be obtained from that for the other trailing leg by setting γ , v , or τ equal to zero (as the case may be) and reversing the sign of the result. Thus for control points on the right panel we obtain the following equations.

$$\begin{aligned}
& - \sum_{v=1}^n \frac{\Gamma_v}{2\pi} \left\{ \frac{1}{\left(\frac{s}{2p}\right)(2j-1) + \frac{t}{n}v} - \frac{1}{\frac{s}{2p}(2j-1)} + \frac{\frac{s}{2p}(2j-1)h^2}{\frac{s^2}{4p^2}(2j-1)^2 h^2 + (a^2 - h^2)^2} \right. \\
& \quad \left. - \frac{\left(\frac{t^2 v^2}{n^2} + h^2\right) \left[\frac{s}{2p}(2j-1) \left(\frac{t^2 v^2}{n^2} + h^2\right) + \frac{t}{n} a^2 v \right]}{\left[\frac{s}{2p}(2j-1) \left(\frac{t^2 v^2}{n^2} + h^2\right) + \frac{t}{n} a^2 v \right]^2 + h^2 \left[\frac{t^2 v^2}{n^2} + h^2 - a^2 \right]^2} \right\} \\
& + \sum_{\lambda=1}^p \frac{K_\lambda}{2\pi} \left\{ \frac{1}{\frac{s}{p} \left(j - \lambda - \frac{1}{2}\right)} - \frac{1}{\frac{s}{2p}(2j-1)} + \frac{\frac{s}{2p}(2j-1)h^2}{\frac{s^2}{4p^2}(2j-1)^2 h^2 + (a^2 - h^2)^2} \right. \\
& \quad \left. - \frac{\left(\frac{s^2}{p^2} \lambda^2 + h^2\right) \left[\frac{s}{2p}(2j-1) \left(\frac{s^2}{p^2} \lambda^2 + h^2\right) - \frac{s}{p} a^2 \lambda \right]}{\left[\frac{s}{2p}(2j-1) \left(\frac{s^2}{p^2} \lambda^2 + h^2\right) - \frac{s}{p} a^2 \lambda \right]^2 + h^2 \left(\frac{s^2}{p^2} \lambda^2 + h^2 - a^2\right)^2} \right\} \\
& - \sum_{\tau=1}^m \frac{\gamma_\tau}{2\pi} \frac{s}{2p}(2j-1) \left\{ \frac{1}{\left(\frac{s}{2p}\right)^2 (2j-1)^2 + \left(\frac{\tau \ell}{m} + h - h_p\right)^2} - \frac{1}{\left[\frac{s}{2p}(2j-1)\right]^2} \right. \\
& \quad \left. + \frac{h^2}{(h - a^2)^2 + \left[\frac{s}{2p}(2j-1)h\right]^2} \right. \\
& \quad \left. - \frac{\left(h_p - \frac{\tau \ell}{m}\right)^2}{\left[h\left(h_p - \frac{\tau \ell}{m}\right) - a^2\right]^2 + \left(\frac{s}{2p}\right)^2 (2j-1)^2 \left(h_p - \frac{\tau \ell}{m}\right)^2} \right\}
\end{aligned}$$

$$= -w_R(j) ; j = 1, 2, \dots, p \quad (\text{II-23})$$

The equations for the n left panel control points are obtained from equation (II-4) with $w_L(\Gamma)$ from equation (II-17), $w_L(K)$ from equation (II-15), and $w_L(\gamma)$ from equation (II-19). There results

$$\begin{aligned}
& - \sum_{v=1}^n \frac{\Gamma_v}{2\pi} \left\{ \frac{1}{\frac{t}{n} \left(v - g + \frac{1}{2} \right)} + \frac{1}{\frac{t}{2n} (2g - 1)} - \frac{\frac{t}{2n} (2g - 1) h^2}{\frac{t^2}{4n^2} (2g - 1)^2 h^2 + (a^2 - h^2)^2} \right. \\
& \quad \left. - \frac{\left(\frac{t^2 v^2}{n^2} + h^2 \right) \left[-\frac{t}{2n} (2g - 1) \left(\frac{t^2 v^2}{n^2} + h^2 \right) + \frac{t}{n} a^2 v \right]}{\left[-\frac{t}{2n} (2g - 1) \left(\frac{t^2 v^2}{n^2} + h^2 \right) + \frac{t}{n} v a^2 \right]^2 + h^2 \left[\frac{t^2 v^2}{n^2} + h^2 - a^2 \right]^2} \right\} \\
& - \sum_{\lambda=1}^p \frac{K_\lambda}{2\pi} \left\{ \frac{1}{\frac{t}{2n} (2g - 1) + \frac{s}{p} \lambda} - \frac{1}{\frac{t}{2n} (2g - 1)} + \frac{\frac{t}{2n} (2g - 1) h^2}{\frac{t^2}{4n^2} (2g - 1)^2 h^2 + (a^2 - h^2)^2} \right. \\
& \quad \left. + \frac{\left(\frac{s^2}{p^2} \lambda^2 + h^2 \right) \left[-\frac{t}{2n} (2g - 1) \left(\frac{s^2}{p^2} \lambda^2 + h^2 \right) - \frac{s}{p} \lambda a^2 \right]}{\left[-\frac{t}{2n} (2g - 1) \left(\frac{s^2}{p^2} \lambda^2 + h^2 \right) - \frac{s}{p} \lambda a^2 \right]^2 + h^2 \left[a^2 - \left(\frac{s^2}{p^2} \lambda^2 + h^2 \right) \right]^2} \right\} \\
& + \sum_{\tau=1}^m \frac{\gamma_\tau \left(\frac{t}{2n} \right) (2g - 1)}{2\pi} \left\{ \frac{1}{\left(\frac{t}{2n} \right)^2 (2g - 1)^2 + \left(\frac{\tau l}{m} + h - h_p \right)^2} - \frac{1}{\left[\frac{t}{2n} (2g - 1) \right]^2} \right. \\
& \quad \left. + \frac{h^2}{(h^2 - a^2)^2 + \left[\frac{t}{2n} (2g - 1) h \right]^2} \right. \\
& \quad \left. - \frac{\left(h_p - \frac{\tau l}{m} \right)^2}{\left[h \left(h_p - \frac{\tau l}{m} \right) - a^2 \right]^2 + \left(\frac{t}{2n} \right)^2 (2g - 1)^2 \left(h_p - \frac{\tau l}{m} \right)^2} \right\} \\
& = -w_L(g) ; \quad g = 1, 2, \dots, n \quad (\text{II-24})
\end{aligned}$$

The equations for the m pylon control points are obtained from equation (II-6) with $v_{P(\Gamma)}$ from equation (II-24), $v_{P(K)}$ from equation (II-20), and $v_{P(\gamma)}$ from equation (II-22).

$$\begin{aligned}
 & \sum_{v=1}^n \frac{\Gamma_v}{2\pi} \left\{ \frac{h_p - h - \frac{\ell}{2m} (2k - 1)}{\left(\frac{tv}{n}\right)^2 + \left[h_p - h - \frac{\ell}{2m} (2k - 1)\right]^2} - \frac{1}{h_p - h - \frac{\ell}{2m} (2k - 1)} \right. \\
 & \quad - \frac{h}{a^2 - h \left[h_p - \frac{\ell}{2m} (2k - 1)\right]} \\
 & \quad \left. + \frac{ha^2 - \left(h_p - \frac{\ell k}{m} + \frac{\ell}{2m}\right) \left(\frac{t^2 v^2}{n^2} + h^2\right)}{\left[a^2 - h \left(h_p - \frac{\ell k}{m} + \frac{\ell}{2m}\right)\right]^2 + \left[\frac{tv}{n} \left(h_p - \frac{\ell k}{m} + \frac{\ell}{2m}\right)\right]^2} \right\} \\
 & - \sum_{\lambda=1}^p \frac{K_\lambda}{2\pi} \left\{ \frac{h_p - h - \frac{\ell}{2m} (2k - 1)}{\left(\frac{s\lambda}{p}\right)^2 + \left[h_p - h - \frac{\ell}{2m} (2k - 1)\right]^2} - \frac{1}{h_p - h - \frac{\ell}{2m} (2k - 1)} \right. \\
 & \quad - \frac{h}{a^2 - h \left[h_p - \frac{\ell}{2m} (2k - 1)\right]} \\
 & \quad \left. + \frac{ha^2 - \left(h_p - \frac{\ell k}{m} + \frac{\ell}{2m}\right) \left(\frac{s^2 \lambda^2}{p^2} + h^2\right)}{\left[a^2 - h \left(h_p - \frac{\ell k}{m} + \frac{\ell}{2m}\right)\right]^2 + \frac{s^2 \lambda^2}{p^2} \left[h_p - \frac{\ell k}{m} + \frac{\ell}{2m}\right]^2} \right\} \\
 & + \sum_{\tau=1}^m \frac{\gamma_\tau}{2\pi} \left\{ \frac{1}{\frac{\tau \ell}{m} - \frac{\ell}{2m} (2k - 1)} - \frac{1}{h_p - \frac{\ell}{2m} (2k - 1) - h} - \frac{h}{a^2 - \left[h_p - \frac{\ell}{2m} (2k - 1)\right] h_p} \right. \\
 & \quad \left. + \frac{h_p - \frac{\tau \ell}{m}}{a^2 - \left(h_p - \frac{\tau \ell}{m}\right) \left(h_p - \frac{\ell k}{m} + \frac{\ell}{2m}\right)} \right\} \\
 & = -v_{P(k)} ; \quad k = 1, 2, \dots, m \quad (\text{II-25})
 \end{aligned}$$

These equations, equations (II-23), (II-24), and (II-25), are a set of simultaneous linear algebraic equations which can be solved for the unknown circulations once the boundary conditions $w_L(g)$, $w_R(j)$, and $v_P(k)$ are specified. These circulations can then be used in the loading equation, equation (89), to determine the normal force due to the vortex system. The sign convention on the circulations so obtained is consistent with that of equation (89).

REFERENCES

1. Bergrun, N. R. and Goodwin, F. K.: Data Report for the External Stores Test Program. Volume I - Summary Report for First Tunnel Entry, Volume II - First Tunnel Entry Force and Moment Data, Volume III - First Tunnel Entry Pressure and Load Distribution Data, Volume IV - First Tunnel Entry Flow-Field Survey Data, Volume V - Second Tunnel Entry Force and Moment Data, Volume VI - Second Tunnel Entry Flow-Field Survey Data. Nielsen Engineering & Research, Inc., NEAR Rep. TR 24, Oct. 1970.
2. Summers, W. E.: Flow Field Characteristics and Aerodynamic Loads on External Stores Near the Fuselage and Wing Pylon Positions of a Swept-Wing/Fuselage Model at Mach Numbers of 0.25 and 0.70. AEDC-TR-70-202, Sept. 1970.
3. Roberts, R. H.: Flow-Field Characteristics and Aerodynamic Loads on External Stores Near the Fuselage and Wing Pylon Positions of a Swept-Wing/Fuselage Model at Mach Numbers of 0.25, 0.40, and 0.70 - Phase II. AEDC-TR-70-279, Jan. 1971.
4. Vallentine, H. R.: Applied Hydrodynamics. Plenum Press, New York, N. Y., 1967.
5. Alford, W. J., Jr. and King, T. J., Jr.: Experimental Investigation of Flow Fields at Zero Sideslip Near Swept- and Unswept-Wing-Fuselage Combinations at Low Speed. NACA RM L56J19, 1957.
6. Alford, W. J., Jr.: Theoretical and Experimental Investigation of the Subsonic-Flow Fields Beneath Swept and Unswept Wings with Tables of Vortex-Induced Velocities. NACA Rep. 1327, 1957.
7. Margason, R. J. and Lamar, J. E.: Wing Aerodynamic Characteristics Calculated by a Vortex Lattice Lifting Surface Computer Program for Fixed Wings with Dihedral and Variable-Sweep Wings at Subsonic Speeds. NASA LWP-493, 1967.
8. Margason, R. J. and Lamar, J. E.: Calculation of the Flow Field Characteristics in the Vicinity of a Lifting Wing at Subsonic Speeds. NASA LWP-446, 1967.
9. Nielsen, J. N.: Missile Aerodynamics. McGraw-Hill Book Co., Inc., New York, N. Y., 1960.
10. McKinney, I. W. and Polhamus, E. C.: A Summary of NASA Data Relative to External-Store Separation Characteristics. NASA TN D-3582, 1966.
11. Pai, S.: Introduction to the Theory of Compressible Flow. D. Van Nostrand Co., Inc., Princeton, New Jersey, 1959.
12. Hopkins, E. J.: A Semi-Empirical Method for Calculating the Pitching Moment of Bodies of Revolution at Low Mach Numbers. NACA RM A51C14, May 1951.

13. Nielsen, J. N., Goodwin, F. K., and Dillenius, M. F. E.: A Calculative Method for Predicting Store Separation Trajectories at Speeds up to the Critical Speed - Phase II Interim Report. NEAR Rep. TR 22, June 1970.
14. Milne-Thomson, L. M.: Theoretical Hydrodynamics. Second ed., The MacMillan Company, New York, N. Y., 1950.
15. Alford, W. J., Jr. and Silvers, H. N.: Investigation at High Subsonic Speeds of Finned and Unfinned Bodies Mounted at Various Locations from the Wings of Unswept- and Swept-Wing Fuselage Models, Including Measurements of Body Loads. NACA RM L54B18, Apr. 1954.
16. Pitts, W. C., Nielsen, J. N., and Kaattari, G. E.: Lift and Center of Pressure of Wing-Body-Tail Combinations at Subsonic, Transonic, and Supersonic Speeds. NACA Rep. 1307, 1957.
17. Price, E. A., Jr.: Wind Tunnel Studies of the A/B45Y-4 Spray Tank Separation Characteristics from the Left Outboard Pylon of the F-105 Aircraft. AEDC-TR-85-185, Aug. 1968.